



MONASH University

**Design, fabrication and characterisation
of topological interlocking structures
utilising additive manufacturing**

Lee Djumas
BSc BE(Hons)

Supervisors:
Dr. Andrey Molotnikov
Prof. Yuri Estrin
Prof. George Simon

A thesis submitted for the degree of *Doctor of Philosophy* at
Monash University in 2018
Department of Materials Science & Engineering

Copyright notice

© Lee Djumas 2018

I certify that I have made all reasonable efforts to secure copyright permissions for third-party content included in this thesis and have not knowingly added copyright content to my work without the owner's permission.

Abstract

In the search for materials with improved combinations of properties, materials scientists and engineers are increasingly turning to composite or hybrid materials which satisfy these demands, due to their ability to combine the advantageous properties of their constituents. The spatial arrangements of these constituents become crucial for achieving these combinations of properties, and the design and control of the topology of the building blocks has become a key focus. Materials designed in this fashion are often referred to as “architected materials”. Some structures and materials found in Nature possess many of these characteristics and have served as an inspiration for much of the development in this ever-growing field. Furthermore, with the advent of new advanced fabrication techniques, such as additive manufacturing, intricate topologies of architecture materials have become far more accessible.

In this work, a particular class of architected materials is studied, based on the concept of *topological interlocking*. In this approach, a structural component is tessellated in identical discrete blocks, which are held in place owing to their specially designed geometry and mutual arrangement. This distinct form of segmentation allows interlocking to occur in three dimensions, providing the structure with an out-of-plane load bearing capacity and controllable flexural compliance amongst many other favourable properties. This approach to materials development unlocks new design variables including geometry and size of the building blocks, as well as their interfacial properties.

This thesis contributes to two main areas in the field of topological interlocking: Firstly, the characterisation of a broad range of mechanical properties of planar assemblies of topologically interlocked blocks with non-planar contact surfaces under concentrated

point loading utilising experimental and numerical techniques. Secondly, the design, development, fabrication, and testing of a range of novel, bioinspired architected topologically interlocking structures, including hierarchically interlocking and multi-material structures. This work provides a better understanding of the complex deformation mechanisms related to such topological interlocking materials and structures.

A number of variables which are known to affect the mechanical properties of topological interlocking assemblies have been studied. A finite element model was developed and supported by experimental results, in order to understand the relationship between intrinsic material properties, including elastic modulus and coefficient of friction, and extrinsic parameters such as the constraining forces and size parameters on the mechanical response of assemblies of topologically interlocked blocks to which concentrated, out-of-plane point loadings are applied. Using this model, numerical characterisation is undertaken, which details the relationships and correlations of the various mechanical properties with these parameters, before linking mechanical properties to these parameters through mathematical formula established by using an Artificial Neural Network. In particular, the relationship between peak load and stiffness with varying block and assembly size was shown to agree with previous analytical and theoretical results, while extending these relationships to include higher deformations such as deflection to peak load and point of failure. The effect of friction on the mechanical response was of particular interest, highlighting the ability to modify the softening behaviour.

The bio-inspired concept of structural hierarchy is explored experimentally and numerically in this work, alongside topological interlocking, to create hierarchically interlocked structure in three dimensions. The introduction of a secondary interlocking surface geometry provides insights in to the deformation mechanisms of topological interlocking structures, in particular the role of slip of the central block under load and tilt/bend of the assembly to the overall failure of the structure. Slip was found to be linked to the softening behaviour of the assembly through numerical results, and was further tested by modifications to the block geometry whereby a new block geometry, termed the “H+” block is introduced to suppress the ability for blocks to slip past one

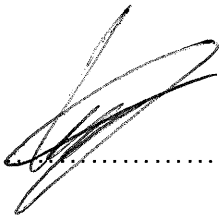
another. The results show that such geometrical modifications enable the control of the failure mechanisms, and thus the mechanical response, of this class of architected material.

Finally, multi-material design concepts, inspired by natural materials such as nacre, are realised in the form of novel topological interlocking specimens. This work extends the design principles of combining hard building blocks with a soft interfacial material between blocks, with the topological interlocking paradigm to create three-dimensional specimens with improved mechanical properties under two failure modes. Using a combination of experimental and numerical techniques, it is demonstrated that these novel materials exhibit a superior combination of stiffness, load bearing capacity and energy absorption which, due to their three-dimensional design, have an increased ability to shift the stress concentrations to alternating sides of the block geometry, thereby resisting crack propagation through the stiff phase. The benefits of multi-material topological interlocking structures is also demonstrated in the out-of-plane loading direction, whereby assemblies with sufficiently thin soft phases are able to maintain a high deflection to failure, while also increasing their load bearing capacity. Multi-material topological interlocking structures provide a promising avenue for future development of hybrid materials.

Declaration

This thesis contains no material which has been accepted for the award of any other degree or diploma at any university or equivalent institution and that, to the best of my knowledge and belief, this thesis contains no material previously published or written by another person, except where due reference is made in the text of the thesis.

Signature:



Print Name:

Lee Djumas

Date:

19/07/2018

Publications

Djumas, L., Molotnikov, A., Simon, G. P. & Estrin, Y. Enhanced Mechanical Performance of Bio-Inspired Hybrid Structures Utilising Topological Interlocking Geometry. *Scientific Reports* **6**, 26706, doi:10.1038/srep26706 (2016).

Djumas, L., Simon, G. P., Estrin, Y. & Molotnikov, A. Deformation mechanics of non-planar topologically interlocked assemblies with structural hierarchy and varying geometry. *Scientific Reports* **7**, doi:10.1038/s41598-017-12147-3 (2017).

To Mum & Dad,
For Everything

Acknowledgements

First and foremost, I would like to thank my supervisors, Dr. Andrey Molotnikov, Prof. George Simon and Prof. Yuri Estrin for the immense amount of support, guidance and invaluable expertise they have provided me. Since the start of 2013, when I began working with them as an undergraduate student, they have been nothing but generous with their time and efforts. It has been a distinct and absolute pleasure to work with them. They have taught me a lot, both professionally and personally, and my development would not be the same without them.

I would like to thank Monash University and the Department of Materials Science & Engineering more broadly, for all that has been offered to me over the last nine years. The experience and people here have made this journey incredibly special for me, and while listing them all is nearly impossible, I would like to acknowledge and thank a few individually. Prof. Nick Birbilis, Head of Department, for his insightful suggestions, feedback and advice, particularly in relation to Chapter 4 of this thesis, as well as all the valuable opportunities he has provided me; Mr. Brett Williams, Mr. Daniel Curtis and Mr. Silvio Mattievich for their technical support; Mr. Ian Wheeler, Ms. Edna Tan and Ms. Kris Wirthensohn for all their administrative support and Prof. Chris Davies and Dr. Laurence Brassart for their discerning discussions and recommendations. I would also like to thank Dr. Ehsan Bafekrpour for his help and assistance learning FE, additive manufacturing and experimental techniques.

To the many, many colleagues and friends that have helped, listened and been there for a chat and coffee when needed, I would like to extend my thanks. These include Dr. Alexander Medvedev, Dr. Yuanshen Qi, Mr. Marten Jurg, Mr. Alessandro Bevacqua, Ms. Ezgi Onal, Ms. Erin Brodie, Dr. Oumaïma Gharbi, Mr. Darren Feenstra, Mr. Guilhaume Sander Malab, Mr. Will Nash and Ms. Malaika Ingram.

Finally, I would like to thank my family and friends for their ongoing love and support while completing my PhD. In particular, special thanks must be given to my parents, Harry and Des, and sister, Kate, for their never-ending encouragement and understanding. And last but not least to my wonderful wife, Karen, who has always been there for me, to endure my frustrations and celebrate my successes. Your love, dedication and patience have made this journey truly worthwhile.

Table of Contents

Abstract	iii
Publications	vii
Acknowledgements	ix
Table of Contents	xi
Abbreviations	xiv
List of Tables	xv
List of Figures	xvi
1. Introduction	1
1.1 Background and Motivation	1
1.2 Research Objectives	2
1.3 Structure of Thesis	3
2. Literature Review	6
2.1 Hybrid Materials	6
2.2 Bioinspired Materials	9
2.2.1 Nacre	9
2.2.2 Interlocking Suture Joints.....	11
2.2.3 Hierarchical Structures.....	13
2.3 Topological Interlocking	14
2.3.1 Background.....	14
2.3.2 Platonic bodies.....	16
2.3.3 Non-planar block geometries	19
2.3.4 Mechanical properties	21
2.3.5 Size effects	29
2.3.6 Geometry effects.....	34
2.4 Fabrication	36
2.4.1 Additive Manufacturing	37
2.5 Computational Techniques	39
2.6 Summary	44
3. Methodology	46
3.1 CAD Design	46
3.2 Fabrication	48

3.3	Materials	49
3.3.1	Hardness	49
3.3.2	Mechanical Properties	50
3.3.3	Thermal Properties	52
3.4	Mechanical Testing	53
3.4.1	Out-of-plane point loading	53
3.4.2	Mode I tensile	54
3.5	Numerical Modelling	55
3.6	Artificial Neural Network	56
3.7	Summary	57
4.	Characterisation of the mechanical behaviour of non-planar topological interlocking blocks within planar assemblies	58
4.1	Introduction	58
4.2	Study Design and Setup	59
4.3	Finite Element Model Development and Validation	63
4.3.1	Software Environment	63
4.3.2	Quasi-static Modelling	63
4.3.3	Material Properties	65
4.3.4	Interaction	65
4.3.5	Mesh	66
4.3.6	Boundary Conditions	67
4.3.7	Validation	70
4.4	Results	73
4.4.1	Assembly Parameters	73
4.4.1.1	Elastic Modulus	73
4.4.1.2	Boundary Conditions	76
4.4.1.3	Friction	79
4.4.2	Size Parameters	82
4.4.2.1	Variable block size and constant assembly size	82
4.4.2.2	Variable assembly size and constant block size	84
4.4.2.3	Variable block size and assembly size with constant size ratio	87
4.4.3	Discussion	90
4.4.4	Artificial Neural Network Model	92
4.5	Discussion	99
4.6	Conclusions	104
5.	Deformation mechanics of non-planar topologically interlocked assemblies with structural hierarchy and varying geometry	106
5.1	Introduction	106
5.2	Methods	107
5.2.1	Design of structures	107
5.2.2	Experimental	112
5.2.3	Computational	112

5.3	Results	114
5.3.1	Hierarchically interlocking assemblies	114
5.3.2	Modified geometries to adjust slip characteristics	121
6.	Mechanical Performance of Bioinspired Hybrid Structures Utilising Topological Interlocking Geometry	129
6.1	Introduction	129
6.2	Design and Motivation	131
6.3	Results	136
6.3.1	Out-of-plane Loading	136
6.3.2	Mode I Tensile Loading.....	140
6.4	Discussion	148
6.5	Conclusions.....	150
7.	Conclusions and Future Work.....	152
7.1	Conclusions.....	152
7.1.1	Characterisation of Mechanical Properties	153
7.1.2	Geometry variation and hierarchical structure	155
7.1.3	Bioinspired, multi-material structures	155
7.2	Future Work.....	157
7.2.1	Geometrical optimisation	157
7.2.2	Interfacial design.....	158
7.2.3	Topological interlocking design utilising computational techniques.....	159
	References	161

Abbreviations

VW+	VeroWhitePlus
TB+	TangoBlackPlus
DM	Digital Material
E	Elastic modulus
S	Type A Shore hardness
σ_y	Yield strength
T_g	Glass transition temperature
t	Block thickness (or size)
s	Assembly span (or size)
μ	Coefficient of friction
K	Stiffness (N/mm)
F_P	Peak Force (N)
δ_P	Deflection to peak force
δ_f	Deflection to failure
ANN	Artificial Neural Network
F_L	Lateral pre-load (N)
ν	Poisson's ratio
ρ	Density
κ	Spring stiffness
δ_s	Spring displacement
δ	Displacement
BC	Boundary conditions
FEA	Finite Element Analysis
a	Block size
h	Block curvature variable 1
Δh	Block curvature variable 2

List of Tables

Table 3.1 - Shore hardness type A values with Young's modulus approximations. Note the last two numbers of the material code refers to the supplier value for Shore Hardness (Type A).	50
Table 4.1 – Reference assembly numerical input parameters.....	60

List of Figures

Figure 2.1 – Combining components and materials in multiple ways - with shape, scale and configuration becoming key design variables to fill material property space [1]	7
Figure 2.2 - Various families of hybrid or architected materials including segmentation in 1, 2 and 3 dimensions [25]	8
Figure 2.3 - Hierarchical structure of nacre [8]	10
Figure 2.4 - Overview of printing and testing bio-inspired composites, after Dimas et al. [16]	11
Figure 2.5 - A selection of suture joints found in Nature [9]	12
Figure 2.6 - Hierarchical structure of bone, leading to outstanding mechanical properties [80]	14
Figure 2.7 - Examples of Abeille (left) and Truchet (right) vaulted geometries [89]	16
Figure 2.8 - A selection of platonic bodies capable of topological interlocking including tetrahedra and cube structures. Schematic of planar assembly orientations. Adapted from [15]	17
Figure 2.9 - Mechanical response of (a) bio-inspired tensegrity structure [14] and (b) responsive structures utilising a shape memory alloy as tensioning wires [93]	18
Figure 2.10 - "Negative stiffness" effect with associated deformation mechanism. Adapted from [101] and [81]	18
Figure 2.11 – Non-planar osteomorphic geometries with curved and flat contact surfaces. Adapted from [15]	20
Figure 2.12 - Various osteomorphic geometries studied by Yong [98]	21
Figure 2.13 - Comparison of force-displacement curves for varying coefficient of friction values obtained via DEM [106]	22
Figure 2.14 - FEM predictions of point indentation curves showing the effect of Young's modulus on cube-shaped (left) and osteomorphic (right) assemblies [15]	23

Figure 2.15 - FEM predictions of point indentation curves showing the effect of friction on cubic (left) and osteomorphic (right) assemblies [15]	23
Figure 2.16 - FEM predictions of point indentation curves showing the effect of lateral load on cubic (left) and osteomorphic (right) assemblies [14].....	24
Figure 2.17 - Relationship between peak force, stiffness and elastic modulus as shown by Schaare [13]. The x-axis is given as Elastic Modulus in GPa	24
Figure 2.18 - Effect of lateral load, friction and elastic modulus on peak load F_{\max} [13]. The x-axis (right plot) is given as coefficient of friction (μ)	25
Figure 2.19 – Comparison of thrust-line model predictions with experimental results for force-stiffness and force-work relations with varying density of tetrahedral blocks in a planar assembly under point loading [99]	27
Figure 2.20 - FEM prediction of the effect of friction on the mechanical response of a planar assembly of tetrahedron-shaped blocks [92]	28
Figure 2.21 - Comparison of loading curves for planar assemblies of interlocking ice tetrahedra for different temperatures, with lower temperatures corresponding to higher values of the coefficient of friction [107].....	28
Figure 2.22 - Comparison of the effect of block size on load-displacement curves for assemblies of cube-shaped blocks for a fixed assembly size [106].....	29
Figure 2.23 - FEM predictions of point indentation curves showing the effect of block size on cubic (left) and osteomorphic (right) assemblies [14]	30
Figure 2.24 FEM predictions of point indentation curves showing the effect of assembly size on cubic (left) and osteomorphic (right) assemblies [14]	30
Figure 2.25 - Schematic overview of size and scale study conducted by Khandelwal et al. [104].....	31
Figure 2.26 - Overview of impact testing conducted by Mirkhalaf et al. [105] showing impact energy of architected glass structures	34
Figure 2.27 - Effect of amplitude and block geometry on the force-displacement curves for non-planar interlocked assemblies [98]. Refer to Figure 2.12 for abbreviations and geometries.....	35
Figure 2.28 - Applying random surface roughness to FE simulation [98]	36
Figure 2.29 - A selection of printing processes - a) stereolithography, b) selective laser sintering, c) polymer jetting, d) and e) extrusion based techniques [111]	37
Fig. 2.30 - PolyJet printing process [112]	38

Figure 2.31 – Various modelling techniques ranging in size and time scales with comparative experimental techniques [126]	40
Figure 2.32 – Overview of combined DEM-FEM employed by Brugger et al. and Duguè et al. [108].....	41
Figure 2.33 - Comparison of DEM v FEM for assembly of cube-shaped blocks [103]	42
Figure 2.34 - FE and experimental curves for a planar assembly of interlocked tetrahedra [92]	42
Figure 2.35 - Basic example of an ANN structure with two inputs, one hidden layer (with two nodes) and one output [129].....	44
Figure 3.1 - Design of osteomorphic block showing progression from function generated edge curves through to full osteomorphic solid geometry	47
Figure 3.2 - a) Connex500 used for fabrication of experimental specimens. b) Schematic of polymer jetting process used by Connex500 [112]	48
Figure 3.3 - Plot of elastic modulus obtained from tensile testing of the various printed materials. Rubber-like samples shown in blue, rigid shown in red	51
Figure 3.4 - Representative true stress-strain curve of VW+ under uniaxial tension	51
Figure 3.5 - Normalized tan delta plots for TB+ and VW+ highlighting difference in T_g	52
Figure 3.6 – a) Mechanical test set-up for osteomorphic assembly, with indenter and force sensors shown. Indenter moves down through the assembly to apply a concentrated point load to the centre of the assembly, b) Post-failure specimen with steel inserts shown for variable sized assemblies.....	53
Figure 3.7 – Image of basic mechanical testing set up for Mode I single edge notched tensile testing. Grips are shown in black at the top and bottom of the image, moving up and down, respectively, to impart a tensile load on the hybrid samples	55
Figure 4.1 - Schematic of assembly studies in Chapter 4, a) experimental and b) computational. – 1) elastic modulus: a) modified material, b) changes to elastic modulus of green bodies 2) boundary condition: a) lateral pre-load controlled by screws, measured by force sensors, b) modified spring constants highlighted in pink 3) friction: b) modified penalty coefficient of friction between blocks.....	61

Figure 4.2 - Schematic of size and scale studies in chapter 4, a) variable block size (t) with constant assembly size (s), b) variable assembly size (s) with constant block size (t), c) variable block size (t) and assembly size (s) with constant size ratio (s/t). The red box indicates the constant reference assembly. t is given as the block thickness and s defines the length or span of the assembly. Values are given in mm	62
Figure 4.3 – An example of a smooth step amplitude used for applying displacement in the model. The numbers given here are indicative only [133].....	64
Figure 4.4 – Plot of the ratio of kinetic energy to internal energy vs time. Note that block removal occur at time = 0.082. Ratio is less than 1% throughout time period ...	65
Figure 4.5 – Uniform quad meshing utilised in ABAQUS for reference osteomorphic assembly	67
Figure 4.6 - Simulation set up showing a planar block assembly, indenter, frame and idealised elastic springs.....	68
Figure 4.7 - Plot of force v displacement as a function frame inertia for the reference assembly. Inertia values are relative to the material density	69
Figure 4.8 - Comparison of force v displacement curves for experimental and simulation of the reference assembly	70
Figure 4.9 - Example of post-failure damage observed for mechanical testing of reference assembly	71
Figure 4.10 - FE validation of assembly variables. Experimental results shown with dashed lines. F_L denotes the value of the applied lateral load in N.....	72
Figure 4.11 - FE validation of size parameters. Experimental results shown with dashed lines. t represents the thickness of a sample in mm	73
Figure 4.12 - Plot of force vs displacement (normalised to reference t) for various elastic moduli (0.9 – 200 GPa) when $F_L = 1\text{ kN}$ and $\mu = 0.3$. Experimental results are shown with dotted lines	74
Figure 4.13 – Plots of mechanical properties for various moduli (GPa), including K (N/mm^2), F_P (N), δ_P (mm), and δ_f (mm). $F_L = 1\text{ kN}$ and $\mu = 0.3$. A strong logarithmic trend is observed for K and F_P , while no trend is observed for the two deflection values. E axis plotted on logarithmic scale.....	75

Figure 4.14 – Plot of force vs displacement (normalised to reference t) for various lateral forces (0.1 – 10 kN) when $E = 1.7$ GPa and $\mu = 0.3$. Experimental results shown with dotted lines	77
Figure 4.15 - Plots of mechanical properties for various lateral forces, including K (N/mm ²), F_P (N), δ_P (mm) and δ_f (mm). $E = 1.7$ GPa and $\mu = 0.3$. A strong, positive logarithmic trend is observed for K and F_P , while the deflection values show a weak negative trend between lateral force and deflection to peak force and failure...	78
Figure 4.16 - Plot of force vs displacement (normalised to reference t) for various coefficient of friction ($\mu = 0.01 - 100$), when $E = 1.7$ GPa and $F_L = 1$ kN. Experimental results shown with dotted lines	80
Figure 4.17 - Plots of mechanical properties for various coefficients of friction, including K (N/mm ²), F_P (N), δ_f (mm) and δ_P (mm). $F_L = 1$ kN and $E = 1.7$ GPa. Strong, broadly linear, positive trends are observed for K , F_P and δ_P , while δ_f appears to be approximately constant.....	81
Figure 4.18 – Plot of force vs displacement with varying t and constant s . Experimental results shown with dotted lines.....	82
Figure 4.19 - Plots of mechanical properties for varying t (mm) and constant s (mm), including K (N/mm ²), F_P (N), δ_P (mm) and δ_f (mm). Strong, positive power law relationships were observed for K and F_P . δ_f and δ_P show a positive, weaker trend with t	84
Figure 4.20 - Plot of force vs displacement with varying s and constant t . Experimental results shown with dotted lines.....	85
Figure 4.21 - Plots of mechanical properties for varying s and constant t , including K (N/mm ²), F_P (N), δ_P (mm) and δ_f (mm). K shows a negative second-degree power law trend with F_P displaying a similar trend. δ_f and δ_P show a positive, weaker relationship with s	86
Figure 4.22 - Plot of force vs displacement with varying s and t , with constant s/t . Experimental results shown as dotted lines.....	87
Figure 4.23 - Plot of normalised (t) force vs normalised (t) displacement with varying s and t , with constant s/t . Experimental results shown with dotted lines	88
Figure 4.24 - Plots of mechanical properties for varying s and t , with constant s/t ratio, including K (N/mm ²), F_P (N), δ_P (mm) and δ_f (mm). K , F_P , δ_f and δ_P show a weaker positive power law trend with t (or s)	89

Figure 4.25 - Plot of δ_f vs δ_P for the three size case studies presented in this chapter as well as for μ . A clear positive trend is observed between the two properties when related to size, while δ_P approaches δ_f with variable friction.....	91
Figure 4.26 – Plot of K vs F for all variables. Linear relationship fitted between the two properties. Trend line given as: $K = 1.74F + 147$, $R^2 = 0.947$. E = orange, μ = red, F_L = green, size = blue	92
Figure 4.27 - Diagram of ANN structure. The five input parameters are shown on the left with elastic modulus (E) and lateral load (BC) adapted to a logarithmic scale, as the values are not well distributed on a linear scale. A single layer with five hidden nodes utilising tanh functions are shown in the centre. Predicted output variables (stiffness, peak force deflection to failure and deflection to peak load) are shown on the right.....	93
Figure 4.28 - Plots of actual v ANN predicted values for training and validation sets across four outputs.....	95
Figure 4.29 - Predicted contour plots for four outputs with the five corresponding variables. These plots show the predicted values (y-axis) of the reference assembly input variables (x-axis). The shape of each contour represents the relative effect of each input on the corresponding output.....	96
Figure 4.30 - Surface plots of selected variables with largest impact on outputs. Scale for colour gradients are not uniform across plots.....	98
Figure 4.31 – Multiple views of the progression of the von Mises stress distribution for the reference assembly during point loading. “Rings” of stress concentration are observed on the top of the assembly in A. A “X” pattern is observed on the back of the plate in B. C-E) Various angles highlighting deformation mechanisms of the assembly. Scale for all images ranges from 0 (Blue) to 65 (Red) MPa. Max range exceeded in (4) and (5) in confined regions. Values above 65 MPa not shown in red, as they are considered unrepresentative due to the exclusion of plasticity or damage in the simulations.....	100
Figure 4.32 – Von Mises stress distribution of a solid plate at representative displacement of 7 mm. A) top, B) bottom, C) side and D) cross section of solid plate. Scale for all images ranges from 0 (Blue) to 65 (Red) MPa. Values above max are shown in red	102

Figure 4.33 – Various experimental specimens post-failure. a) – d) reference assembly, e) and f) solid plate.....	103
Figure 5.1 - Schematic view of Grasshopper script in Rhinoceros 3D to generate hierarchical interlocking blocks in Chapter 5. Progression from the same curved surface to gridded mesh, checker board pattern and point generation, allowing implementation of pyramidal surfaces features on solid block geometry.....	109
Figure 5.2 – Overview of the hierarchical approach to block geometries and piece-wise planar block assemblies used – a) experimental setup showing assembled osteomorphic blocks, indenter, screw-driven frame and lateral force sensors. b) Computational setup with the same dimensions as the experimental one (160 mm x 150 mm) and the block size of 20 mm x 20 mm x 10 mm. (c) Two-dimensional representation of shapes used for non-planar interlocking curves for block geometries, orange: square, black: osteomorphic, dark yellow: triangle. (d) As-fabricated and designed individual blocks with various geometries. (e) Representation of pyramidal surface modifications to an osteomorphic block. (f) As-fabricated and designed individual blocks, with various hierarchically interlocked surfaces. (g) Pyramidal profile design, individual pyramids approx. 1 – 2 mm in size	110
Figure 5.3 – Variable tetra meshing utilised in Hypermesh for central blocks. The same quad meshing regime, from Chapter 4 was used for the outer assembly blocks	113
Figure 5.4 - Load-displacement curves for hierarchically interlocked assemblies. Load F is normalised with respect to the peak load F^* for the assembly of reference osteomorphic blocks, while displacement is normalised with respect to the plate thickness. The solid lines represent experimental results and the dashed lines represent computational results, which are presented up to the displacements at which a divergence from the experimental results occurs. Experimental testing was conducted in triplicate as a minimum	115
Figure 5.5 – Experimental peak load vs. stiffness for assemblies with hierarchal interlocking, normalised with respect to the peak load and stiffness of a reference assembly of osteomorphic blocks. The error bars indicate the scatter in the data. Peak load error bar for the case referred to as “planar” are small and are contained	

within the symbol. Stiffness is taken as the tangent at 0.01 normalised displacement. Experimental testing was conducted in triplicate as a minimum	116
Figure 5.6 – Displacement of central block relative to neighbouring blocks as measured by average distance of two edges shown in purple squares: a) plotted as a function of normalised displacement, b) images of computational output for central block at 1.0 normalised displacement (as shown by the purple line in Figure 5.6a). Colour borders correspond to curve colours in Figure 5.6b. Displacements have been normalised in the same way as in Figures 5.2 and 5.5.....	120
Figure 5.7 - a) Normalised load-displacement curves for assemblies of interlocked blocks with non-planar surfaces. The load and the displacement have been normalised in the same manner as in Figure 5.4. The solid lines correspond to the experimental curves and dashed lines to the computational curves. b) Damage to osteomorphic and square assemblies after mechanical testing	122
Figure 5.8 – Experimental peak load and stiffness for assemblies with modified geometry, normalised with respect to the peak load and stiffness of a reference assembly of osteomorphic blocks. The error bars indicate the scatter in the data. Stiffness is taken as the tangent at 0.01 normalised displacement	124
Figure 6.1 – Outline of geometries and assemblies tested in section 6.2.2, all images show printed samples, white = stiff, black = soft. a) multiple individual osteomorphic blocks with a soft phase coating on interlocking interfaces, varying in thickness between 0.05 mm – 0.5 mm. Coating thickness of 0.4 mm was selected as an optimum one. Block size 20 mm x 20 mm x 10 mm. b) assemblies with a soft interface layer of 0.8 mm between blocks, achieved either through discrete blocks with 0.4 mm coating or single piece printed assembly. c) single piece assembly with minimum achievable interface thickness of 0.25 mm. d) monolithic plate with hierarchical interlocking geometry from Chapter 5 with 0.25 mm soft interface. b) to d) assembly size approx. 160 mm x 150 mm, small variation with different thickness interface	132
Figure 6.2 – Principal building block geometries used in specimens for testing in Section 6.2.3. (a) rectangle or standard brick used as a reference in the brick-and-mortar structures printed; (b) “hourglass” and (c) “smooth honeycomb” represent the two opposite faces of the osteomorphic block shown in (d). The size of each block pictured is 6.25 mm in length and 3.125 mm in width, however the physical	

dimensions could be chosen arbitrarily, as the property of interlocking is size-independent. Note that the cross-sections of the blocks in figures (b) and (c) do not change along the straight lines drawn in the figures. Assemblies based on these geometries are therefore referred to as two-dimensional. By contrast, the cross-section of the osteomorphic block (d) transforms along the direction normal to its face: a crest at the front face corresponds to a minimum at the back face. The shape presented in (d) provides the structure with the three-dimensionality that is crucial for its mechanical performance..... 134

Figure 6.3 - Images of additively manufactured specimens used for Mode I fracture testing. The dimensions of specimens are 64.75 mm x 58.5 mm with a thickness of 3.125 mm. The volume fraction of the soft phase is approximately 13.5 ± 0.1 % for all samples. (a) Bricks-and-mortar sample, representing a simplified nacre structure; (b) and (c) “hourglass” and “smooth honeycomb” samples: the respective motifs of the surface tessellations of these samples correspond to the two opposite faces of an osteomorphic block, as seen in Figure 5.2d. Further details of the samples are given in Section 0. Note that the sample consisting of interlayered interlocked osteomorphic blocks, which was also tested, is not shown, as it appears identical to the samples in (b) or (c) depending on which side is viewed 135

Figure 6.4 – Plot of load vs displacement for out-of-plane loading of various multi-material assemblies. Reference assembly (as used in Chapter 4) shown in dark yellow. Discrete blocks coated with 0.4mm soft phase sample shown in green, with monolithic comparison (0.8mm soft phase) shown in blue. Monolithic sample with 0.25mm thick soft phase shown in red, with hierarchical comparison (same soft phase) shown in orange. Dotted purple lines are referred to in discussions below 137

Figure 6.5 – Selection of post-failure specimens. a) and b) shows damage to soft phase coating between blocks, while c) shows that cracking was able to propagate through the stiff phase leading to an earlier failure compared to other geometries 138

Figure 6.6 – Comparison of representative stress-strain curves for the four geometries. This plot illustrates the increase in peak stress, strain at failure, and modulus of toughness of the osteomorphic specimen, as compared to the bricks-and-mortar

structure. The effect of the high peak load appears to be associated with interlocking, as it is the greatest for the “hourglass” and the “osteomorphic” cases – both involving interlocking 141

Figure 6.7 – Plot of modulus of toughness (as measured by the area under the stress-strain curve) vs. peak stress. Doubling of both modulus of toughness and peak stress achieved with the osteomorphic geometry is seen. Improvement of both characteristic properties due to the osteomorphic design is highlighted by the arrow. The shaded area highlights the improved mechanical properties due to the “combination” of hourglass and smooth honeycomb geometries 142

Figure 6.8 - Images of fracture sequence during experimental testing for a) brick-and-mortar, b) smooth honeycomb, c) hourglass, d) osteomorphic – hourglass side, e) osteomorphic – smooth honeycomb. The images represent the four characteristic stages of fracture i) initial state, ii) crack initiation, iii) crack propagation, iv) failure. Areas of stress delocalization are observed in all samples except c). Of particular note are these areas observed in the ii) stage of testing. Similarities in fracture paths is also observed in iv) for all samples except c)..... 144

Figure 6.9 – Overview of computational work: a) initial state of experimental specimen with crack initiation site highlighted in red, experimental crack initiation site of hourglass (b) and osteomorphic (c) specimens before brittle failure, FEA simulations showing the von Mises equivalent stress distribution at a crack initiation site for hourglass (d) and osteomorphic (e) specimens with central block highlighted in red, FEA simulations showing von Mises equivalent stress distribution for a central block at the crack tip for hourglass (f) and osteomorphic (g) geometries. These images illustrate the areas of stress concentration for the two geometries with interlocking features. The stress concentration in the “hourglass” block (f) extends through the entire depth of the specimen which results in its brittle failure. The 3D nature of the osteomorphic block (g) restricts the stress concentration to one side of the block, which reduces the likelihood of a crack propagation through the stiff phase..... 146

1. Introduction

1.1 Background and Motivation

Composites and hybrid materials [1] are increasingly playing an important role as structural materials in a wide range of fields due to their ability to combine the beneficial properties of their constituents. More importantly, they represent the possibility to achieve properties not possible using single, monolithic objects of the same materials, and this has driven research in materials and mechanical engineering in recent years, leading to significant advances in the development of new architected, hybrid materials. [2] The structures are often inspired by natural materials, which have been shown to be able to achieve exceptional mechanical properties and possess a multitude of functionalities. [3]

One family of these architected hybrid materials utilises a design principle known as *topological interlocking*. This concept is based upon the segmentation of a structure into discrete, identical elements which, by virtue of their shape and arrangement, are held in place in an interlocked manner in three-dimensions, without the need for connectors or binders. Topologically interlocked structures have been shown to possess superior mechanical properties not offered by monolithic counterparts including: improved energy dissipation [4], sound absorption [5] and tolerance to local failure [6]. There are interesting connections and similarities between topological interlocking and other research fields, in particular, to bio-inspired materials and structures [3, 7]. While not found in nature, topological interlocking has similarities with some of the geometries of naturally-occurring structures such as nacre [8] and suture joints [9], as well as design principles of energy absorption [10] based on tessellation and segmentation [11]. There remain many exciting areas of opportunity to exploit aspects of topological interlocking behaviour, integrated with bio-inspired materials design. In particular, multi-material structures combining hard and soft phases (as found in nacre), as well as hierarchical materials design [12], are all of interest. While there have been efforts to characterise the mechanical response of planar assemblies

of topologically interlocked blocks [13-15], there remain important areas in which knowledge is lacking, and in particular there is a need to characterise the relationship between multiple variables that characterise topological interlocking structures made from non-planar blocks and their properties.

1.2 Research Objectives

The thesis has two broad primary objectives:

- 1) to characterise a range of mechanical properties of topologically interlocked planar assemblies of non-planar blocks under concentrated point loading, and understand the effects of key component and system parameters on their performance;
- 2) to design, develop, fabricate and test a range of novel architected structures utilising the concepts of bioinspiration and topological interlocking.

A secondary objective is also realised in this work, which is to develop a greater understanding of the complex deformation mechanisms related to topological interlocking assemblies under concentrated point loading. This objective should inform future design of these structures, for greater control over the mechanical response, and when combined with Objective 1 provides a sound basis for further development and application of topological interlocking structures.

These objectives are achieved by using a combination of experimental and numerical tools. These include additive manufacturing, which was employed to fabricate a range of complex block geometries (including ones involving multiple materials) which allow mechanical testing. A numerical model based on finite element analysis (FEA) was developed to investigate the mechanical properties of topological interlocking assemblies. This parametric study was combined with an Artificial Neural Network (ANN) to establish the relationships between intrinsic material properties such as elastic modulus and coefficient of friction, and the extrinsic parameters, such as size of the assembly and applied boundary conditions.

1.3 Structure of Thesis

An overview of the work presented in this thesis, which is divided into seven chapters, is given here. The **current chapter** provides information on the background and motivation that represents the basis for the project, as well as outlining the objectives and structure of the work.

Chapter 2 is a critical summary of the multiple fields of research relevant for this thesis and sets the background for the current work. The topics covered include hybrid and architected materials, and the role of bioinspiration in driving new research in material and mechanical engineering. A broad analysis of topological interlocking is presented, including the efforts to characterise the mechanical response of this class of architected materials. The links of this work to bioinspired and hybrid materials are also outlined. Finally, some context for the tools used to study architected materials and applied in this work is provided, including various fabrication techniques, in particular additive manufacturing, as well as the computational and numerical tools.

Chapter 3 outlines, more specifically, the materials, techniques and methodologies used to undertake this current research.

In **Chapter 4**, a numerical finite element model is developed to investigate multiple variables known to affect the mechanical response of planar topological interlocking assemblies under a concentrated point loading. In particular, exploring the effect of the elastic modulus of the constituent material, the friction between blocks and the boundary conditions including fixed and pre-loaded lateral constraints of the global assembly, is the key focus. Chapter 4 also presents investigation of the effect of *size and scale* of the building blocks on non-planar topological interlocking planar assemblies. These results are combined using an Artificial Neural Network to highlight overall trends and to guide future development and design of these structures. The key outcomes include the characterisation of relationships between multiple variables, addressing specifically various mechanical properties for non-planar

blocks in planar assemblies. In particular, the elastic modulus of the building block material is shown to have the largest effect on the stiffness and peak force, the coefficient of friction displayed a clear positive trend with deflection to peak load and the effect of size and scale was numerically shown to agree with previous analytical and theoretical predictions for stiffness and peak load. The numerical characterisation of the effect of friction was extended to include the deflection to peak load and failure.

In **Chapter 5**, the concept of structural hierarchy is combined with topological interlocking to create hierarchically interlocked structures in three dimensions. This is introduced in the form of a secondary interlocking surface geometry. The role of non-planar block geometries in the mechanical response of topologically interlocked ensembles is also studied and the ability to modify and control the failure mechanisms, and hence the mechanical response, of topological interlocking planar assemblies by manipulating the block geometry is highlighted. The experimental results reported suggest that the hierarchical interlocking features cause a delay in the onset of slip, leading to an increase in the load bearing capacity. A greater understanding of the deformation mechanisms will also guide the design of topological interlocking in the future.

In **Chapter 6**, multi-material design concepts, in the form of composite and hybrid materials, are integrated with the topological interlocking paradigm to create novel three-dimensional structures. In the past, work in this field has primarily focussed on two-dimensional designs [9, 16]. The present study has extended these design principles into three dimensions with topological interlocking. The multi-material specimens were specially designed and fabricated via high resolution additive manufacturing and tested in two failure modes, using a combination of experimental and numerical techniques. Multi-material design and the concept of hierarchical interlocking (as introduced in Chapter 5) are combined and fabricated, experimentally displaying superior load bearing capacity. The added benefits of designing in three dimensions, particularly in the mechanical properties, are shown in this chapter. In particular, specifically-designed monolithic specimens exhibited a significant increase in stiffness and peak load bearing capacity, while maintaining high deflection to failure. These intricate, multi-material structures provide a promising avenue for future development of hybrid materials.

Finally, **Chapter 7** contains the conclusions of the thesis, as well as outlining recommendations for possible future work.

2. Literature Review

This thesis draws upon multiple fields of interrelated areas, and this review will introduce and assess these areas as they relate to the research undertaken here. In particular, the fields of topological interlocking, bio-inspired, hybrid and architected materials, as well as the tools and techniques used to study these areas, will be reviewed.

2.1 Hybrid Materials

Materials scientists and engineers strive to develop improved materials, as well as find new materials to extend or fill gaps in materials properties space [17]. Traditionally this has involved developing new polymer chemistries, metal alloys or new compositions for ceramics [1]. A more recent approach has been to combine two or more materials in specific configurations, to enable properties not offered by either alone [18], in an area known as hybrid materials [19]. This is a promising avenue of investigation, as it allows us to rethink the concept of materials design, and to have access to new design variables, such as shape, configuration and scale. In a similar concept, the term architected materials refers to a closely related class of materials with a specific focus on the geometry and topological make-up of the inner architecture of a material designed to influence its behaviour and properties [20]. For the most part, these two concepts can be considered the same, and will be used interchangeably in this work. Indeed, these materials could be viewed in some ways as the interface between materials science and mechanical engineering, with many possibilities offered by this multidisciplinary nature of this approach.

This approach enables combining materials to push the materials property space and create hybrid materials that draw from the best properties of their individual constituents, see Figure 2.1. The way shape and scale of the components are used becomes critical. Structures such as trusses, lattices, honeycomb structures and foams already do this to some degree, seeking to increase specific flexural stiffness and specific strength compared to monolithic materials, in this case using empty space as a component “material” [21].

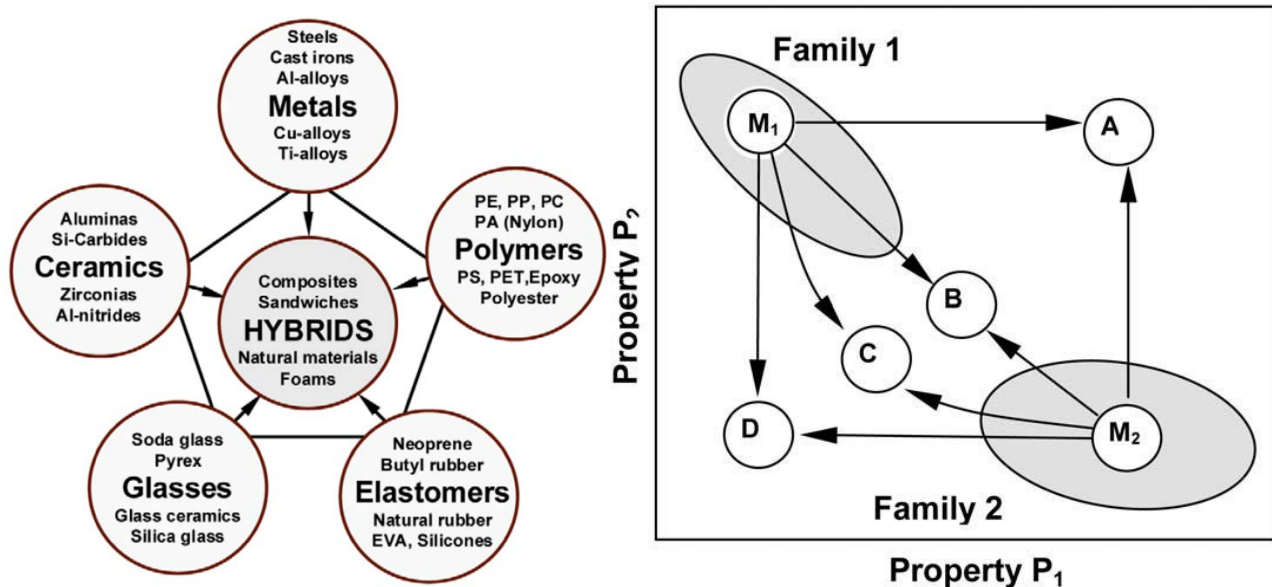


Figure 2.1 – Combining components and materials in multiple ways - with shape, scale and configuration becoming key design variables to fill material property space [1]

Segmentation and assembly of multi-component objects has been used much less often, but the principle can also be used to create structures which have vastly different properties. For example, electrical cable, wound and spun from metal wires, have stiffness vastly different from that of a monolithic cylinder made from the same material. Indeed, we can control the mechanical properties of the wire, not only by changing the metal itself, but by varying the diameter, number and coiling of the fibres, and hence, manipulate the properties of the architected material thus obtained. By extending this concept into three dimensions, similar benefits can be achieved. Indeed, segmenting a structure into smaller discrete elements can improve multiple properties, including damage tolerance and energy absorption capability, or toughness (amongst others), c.f. Figure 2.2. This ‘topological toughening’ is widely observed throughout Nature [12, 22-24]. Indeed, Fratzl et al. [11]

recently outlined and reviewed this phenomenon of tessellation in Nature and the efforts to design defect-tolerant, architected materials using these principles.

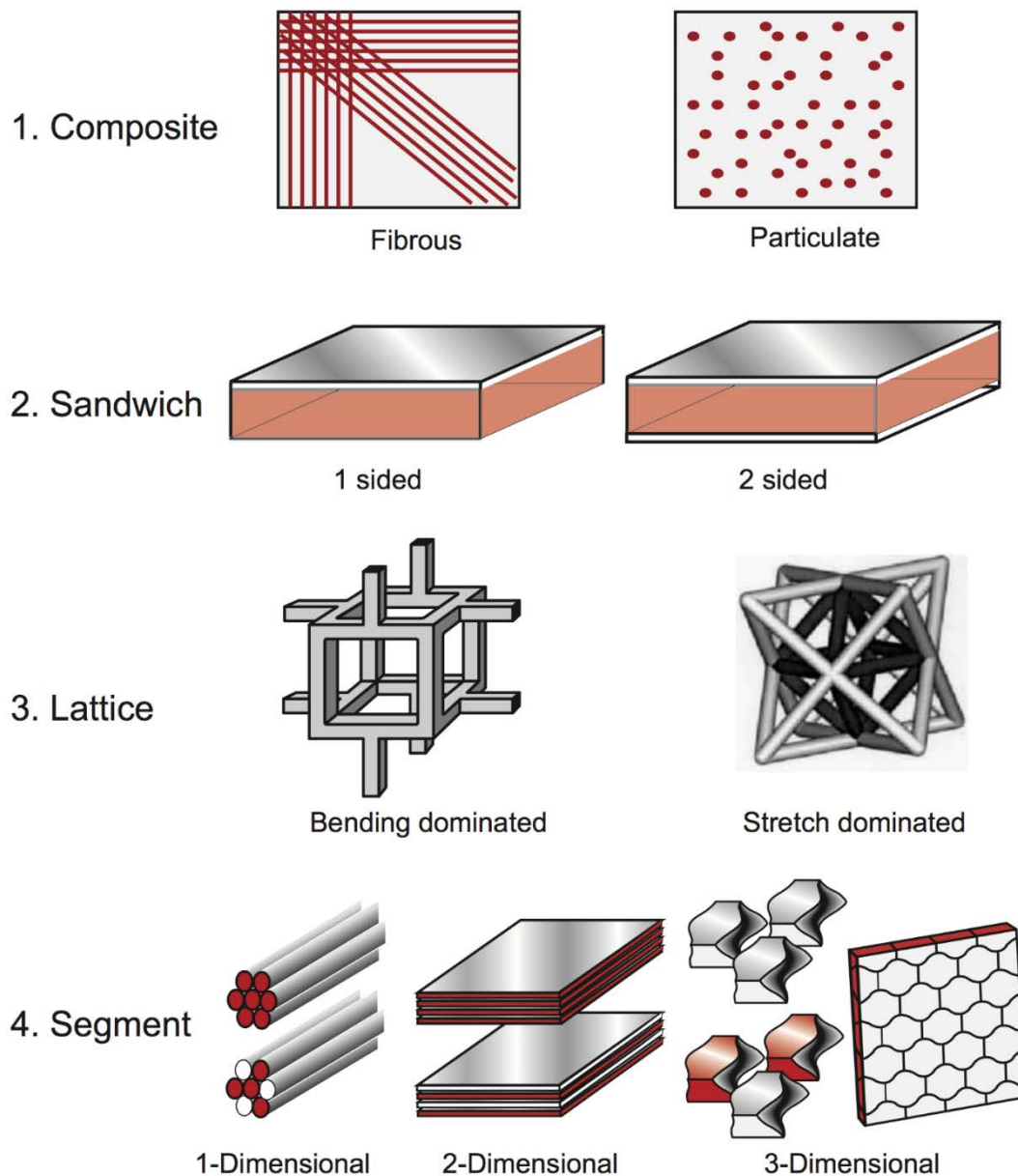


Figure 2.2 - Various families of hybrid or architected materials including segmentation in 1, 2 and 3 dimensions [25]

2.2 Bioinspired Materials

Many natural or biological structural materials are composites or hybrid structures [1, 2] with outstanding mechanical properties, which are surprisingly often achieved despite the presence of relatively weak constituents [3, 7, 10, 26]. The resultant materials are also remarkable with regard to the efficient use of available resources, made possible by the process of evolution. Indeed, many biological systems have mechanical properties that far exceed those of man-made materials [27] and have served as an inspiration for materials engineers in their quest for novel materials [28-35]. Some “classic” examples of structural natural materials include wood [36], bamboo [37], bone [38], and shells of some molluscs [39] which have complex internal architectures.

The key to the remarkable performance of these biological materials is the shape and spatial arrangement of their constituents across multiple lengths scales, also known as structural hierarchy [7]. This is particularly prevalent in various types of biological shells [40].

2.2.1 Nacre

One such example is nacre, the iridescent mother of pearl, found on the inner shell of some molluscs, which has attracted much interest from materials scientists due to its exceptional mechanical properties [8, 41, 42]. While nacre consists predominantly of aragonite, a highly brittle ceramic, it displays a unique combination of stiffness, strength, fracture toughness and energy absorption capabilities. At the core of this behaviour is the microarchitecture of nacre: a brick-and-mortar like structure made up of polygonal aragonite platelets forming a lamellar structure (95 wt%) with a soft, viscoelastic organic protein (5 wt%) binding the lamellae together [43], see Figure 2.3.

Despite the preponderance of aragonite in its structure, nacre is far tougher than monolithic aragonite [44], indicating that this behaviour is due to nacre’s composite nature and architecture, rather than the properties of the majority constituent. Over the last decade, various structural features were identified as contributors to the toughness of nacre,

including nano-asperities and the microscale waviness of the platelets, among others [8, 45-48]. It is clear from these studies that the spatial arrangement of the elements of the nacre structure is crucial for its outstanding mechanical properties. Under load, these structures generate progressive locking of slip between the adjacent platelets, causing hardening and toughening of the structure [47, 49, 50].

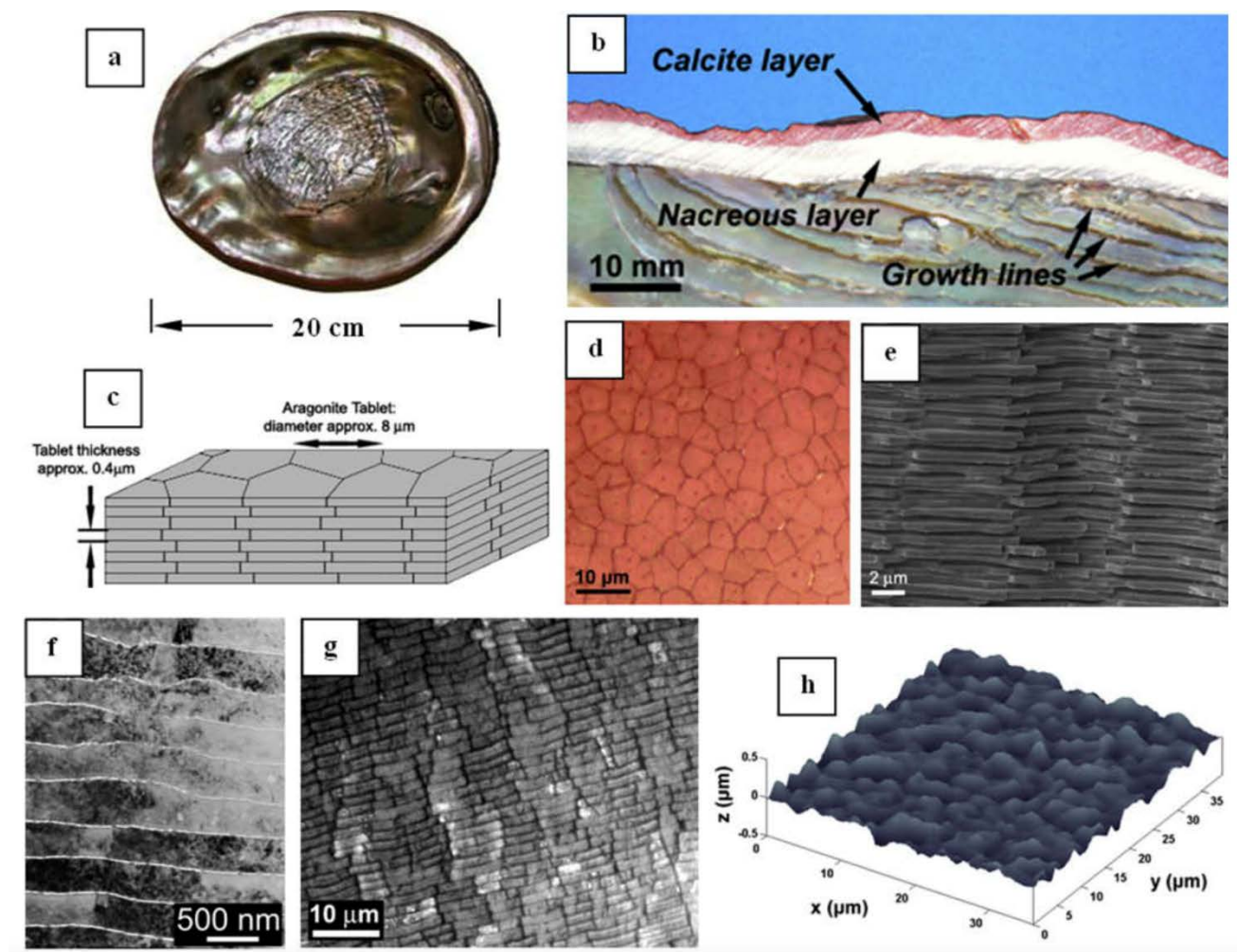


Figure 2.3 - Hierarchical structure of nacre [8]

Many examples of mimicking various aspects of the nacre structure (and that of other natural materials) in synthesising engineered materials have been reported [33, 41, 43, 51-56], many with encouraging results. Of particular note is the work by Barthelat et al. [57] who fabricated experimentally the “dovetail” features of nacre, attributed to progressive interlocking and highlighted the ability of this geometry to spread deformations over large volumes via stress delocalisation. Furthermore, additional mechanisms, including tablet

sliding and strain hardening, were also demonstrated and supported numerically, successfully duplicating these effects which have been identified in nacre. Similarly, Dimas et al. [16] fabricated a nacre-like structure using multi-material additive manufacturing. This work represented one of the first efforts at 3D printing of bioinspired, mechanically tough composites. These synthetic composites were fabricated and tested under Mode I tensile testing (see Figure 2.4) and shown to increase the toughness of the constituent materials by a factor of 20 as well as utilising similar deformation and fracture mechanisms to those identified in biological structural composites. Slesarenko et al. [58] extended this by studying the effect of tensile loading angles on these brick-and-mortar structures, and found the loading angle to play a significant role in the mechanical response, specifically, the improved toughness properties are only found in a narrow loading angle range. It is important to note in the above work, as well as others [59-61], that the focus was on investigating and modifying the nacre-inspired geometry in only two, rather than three, dimensions.

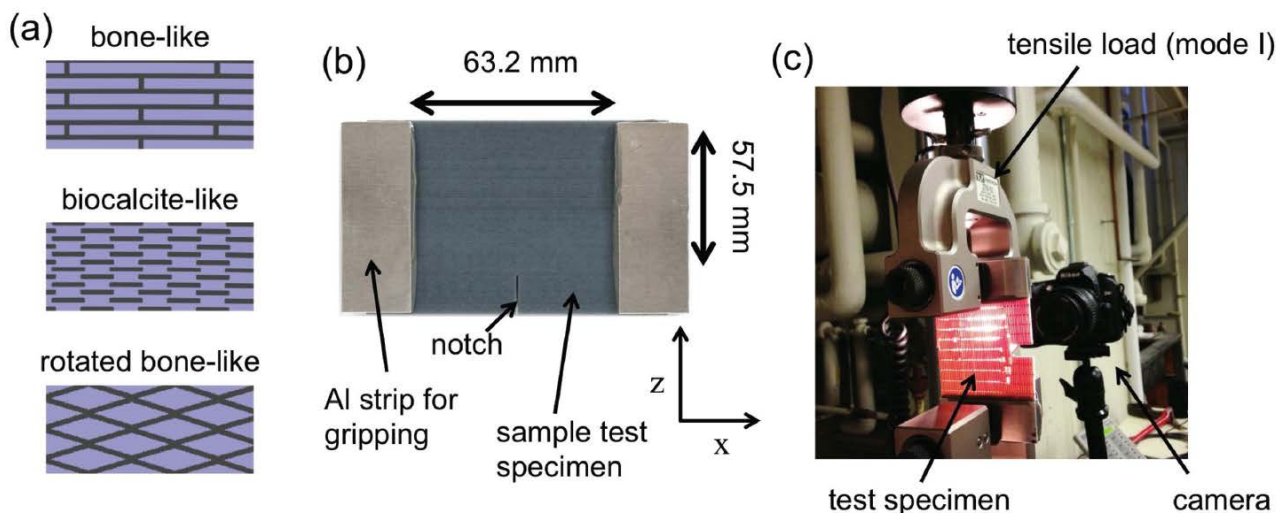


Figure 2.4 - Overview of printing and testing bio-inspired composites, after Dimas et al. [16]

2.2.2 Interlocking Suture Joints

Another fascinating group of biological systems are suture joints, found throughout Nature. They are generally comprised of stiff interdigitated sections joined by a compliant interfacial layer [62]. These joints have varying geometries, from simple curves to highly complex,

hierarchical waveforms, a selection of which are shown in Figure 2.5 [9]. These structures are of significant interest given their ability to provide a remarkable combination of properties, including flexibility, puncture resistance and rigidity [7]. Particular examples are found in turtle carapaces such as the red eared slider turtles [22, 63, 64] and leatherback turtle [65]. Much work has been undertaken to understand the design principles employed by these structures with the outlook for new architected materials, cf. Malik et al. [9], Li et al. [66-68] and Lin et al. [62, 69] These works focus on the two-dimensional aspects of interlocking, particularly saw tooth and rounded designs, optimising geometries for key mechanical properties, including stiffness, peak load, elongation to failure and energy absorption. Chen et al. [70] found the three-dimensional saw tooth interdigitated design of leatherback turtles extended and confirmed many of Li's results, particularly with regard to the optimum angle for tensile strength (30°) and shorter suture length ratios leading to increased flexibility. This work focussed on the interdigitated geometry on flat surfaces and did not include length scale hierarchy, though.

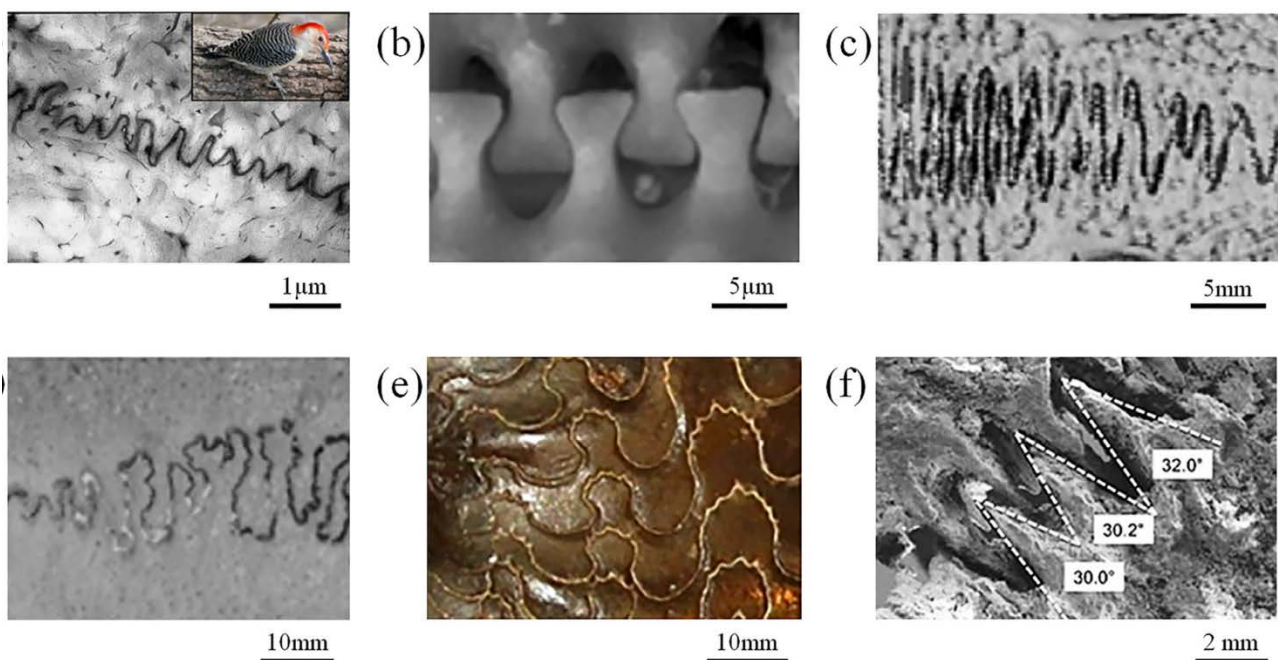


Figure 2.5 - A selection of suture joints found in Nature [9]

2.2.3 Hierarchical Structures

The complex hierarchical architecture these materials possess across multiple length scales has been identified as one of the primary reasons for the outstanding functionalities observed in Nature. [12]

The architecture of both nacre and turtle sutures combine segmentation into interlocked elements with a hierarchy of structural features at multiple length scales [12, 71]. A biomimetic approach adopting these concepts for use in engineering structures has driven scientists and engineers to develop new structural materials with growing success [24, 72]. Areas of particular interest include lattice structures [73, 74], spider silk [75] and smart actuators [76]. Indeed, structural hierarchy and interdigitated interlocking have been studied by Lin et al. [68] in two dimensions providing evidence that length scale hierarchy in a bio-inspired suture joint geometry gives rise to improved mechanical behaviour [62, 67, 77]. Niebel et al. [78] also used hierarchical surface roughening in the form of asperities to improve the ductility and fracture toughness of nacre-inspired, flat platelet structures. Mirzaeifar et al. [79] applied the concept of hierarchy to additively manufactured bio-inspired composites and found that this led to improved defect tolerance under Mode I fracture. Once again, this study focussed on two-dimensional design variables.

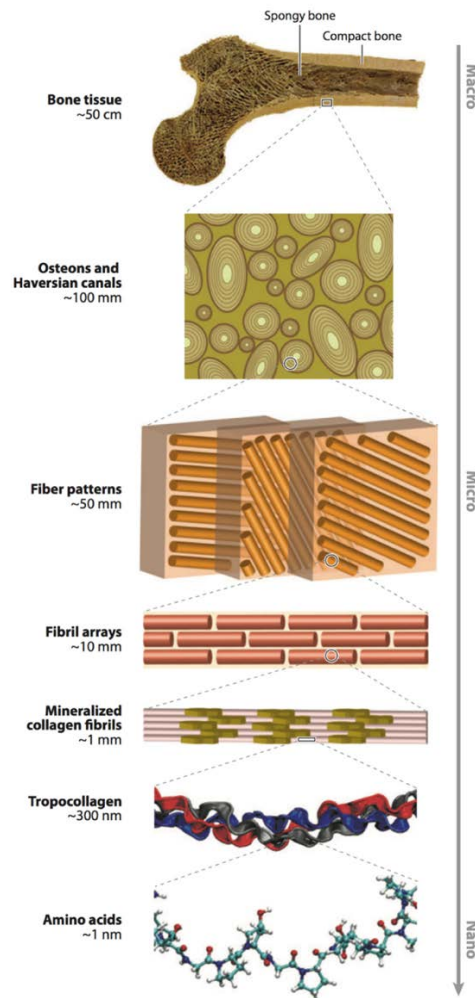


Figure 2.6 - Hierarchical structure of bone, leading to outstanding mechanical properties [80]

2.3 Topological Interlocking

2.3.1 Background

Segmentation and tessellation is a common design motif observed throughout biological systems [11, 23]. While not directly inspired by Nature, the field of *topological interlocking* [81] has emerged as a novel route to address challenges faced in materials science and engineering, due to its ability to combine useful mechanical and functional properties [1, 19]. Indeed, the similarities between the two materials design concepts are striking [22].

Topological interlocking is based on the segmentation of monolithic materials into specially-designed, discrete units which are identical and interlock in three dimensions to form an assembly [82]. In this way, each block is constrained by the geometry of its neighbouring blocks, providing the assembly a mechanism to have load-bearing structural integrity without the need for connectors or binders. A global constraint in the form of a frame, corner fasteners or tensioned wires is required to maintain the overall structure [83].

These systems have been found to possess a range of interesting and useful mechanical properties. Damage tolerance [84], deflection at failure [85], structural stability and energy absorption [86] are some of the key properties that are enhanced due to the inability for cracks to propagate across the boundaries of the discrete blocks. Recent work in which the puncture resistance of topological interlocking structures were compared to other, non-interlocking tessellated geometries were demonstrated and reported in [87].

The field of topological interlocking materials based on this concept was most clearly defined, in an engineering sense, by Dyskin et al. [82] and Estrin et al. [81], with its mathematical foundations presented in [88], and has advanced substantially in subsequent years. There are unexpected similarities of the principle of topological interlocking with earlier ideas in masonry dating back hundreds of years, including the design of Truchet and Abeille vaults, as discussed by Fallacara [89].



Figure 2.7 - Examples of Abeille (left) and Truchet (right) vaulted geometries [89]

The work by Glickman in the field of civil engineering [90] also predated the fully-fledged development of this concept in the materials engineering context. The design principle based on topological interlocking has subsequently been applied to problems ranging from sound absorption [5], sandwich panels [91], impact mechanics [92], adaptive structures [4, 93], bio-inspired tensegrity assemblies [14], multi-materials composites [94], and architectural design [89, 95, 96]. Indeed, the concept is material independent and has been applied to metals [86], ceramics [85, 97, 98], and polymers [99]. A recent article by Siegmund et al. [100] provides a useful summary of this field.

2.3.2 Platonic bodies

Various geometries of elementary building blocks that permit topological interlocking have been identified, cf., e.g. [81]. One particular family of such geometries are platonic bodies [83]. Structures of this kind, assembled from cubes or tetrahedra, have been well studied [88, 101-103].

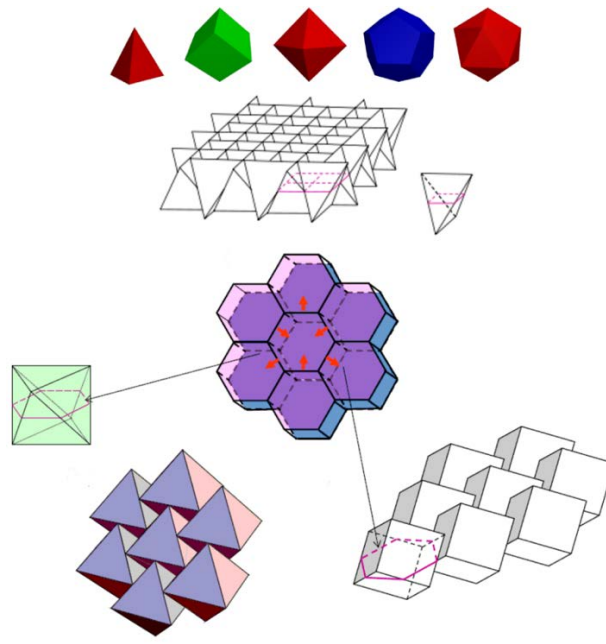


Figure 2.8 - A selection of platonic bodies capable of topological interlocking including tetrahedra and cube structures. Schematic of planar assembly orientations. Adapted from [15]

A recent example of a novel application of flat surfaced elements is their use in creating additively manufactured, bioinspired tensegrity structures (three-dimensional structures consisting of various sections under compression and tension) displaying mechanical responses different to the “traditional” topological interlocking assemblies with rigid frames [14]. This work is similar to that of responsive structures presented by Molotnikov et al. [93] (with non-planar blocks) who utilised wires made from a shape memory alloy for tensioning. Khandelwal et al. [4] also manufactured adaptive assemblies using similar techniques.

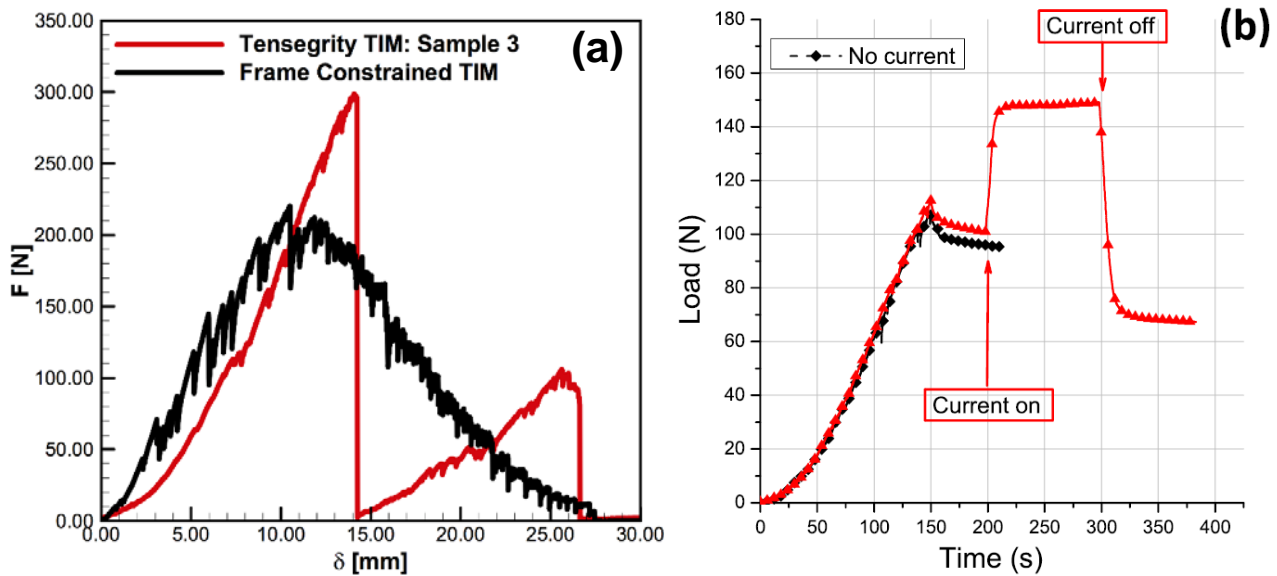


Figure 2.9 - Mechanical response of (a) bio-inspired tensegrity structure [14] and (b) responsive structures utilising a shape memory alloy as tensioning wires [93]

The deformation mechanics of assemblies of topologically interlocked blocks are also of keen interest. Estrin et al. [101] identified an interesting mechanical response of cubic blocks which display a “negative stiffness” effect [81], presumably due to transitions in their deformation behaviour from face-to-face contact to face-to-vertex contact between the blocks during loading and unloading.

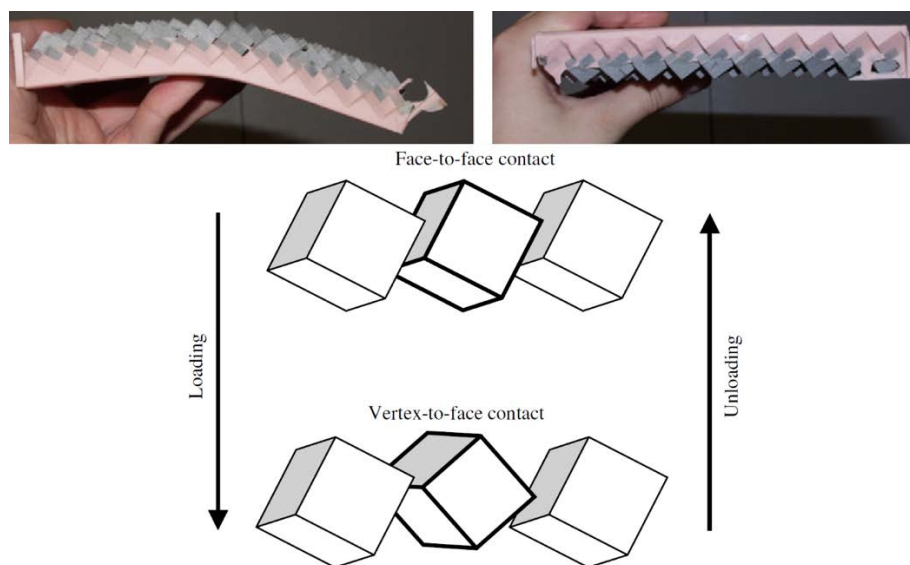


Figure 2.10 - "Negative stiffness" effect with associated deformation mechanism. Adapted from [101] and [81]

Khandelwal et al. [99, 104] and Mirkhalaf et al. [105] have also considered deformation mechanisms. The latter identified three primary sources of deformation and failure of planar assemblies under concentrated point loading: (i) tilt/bend of the assembly, (ii) slip or slide of the central block under load, and (iii) local irreversible, (plastic) deformation of the central block and those in its vicinity. However, there remains a lack of clarity in the understanding of these mechanisms, and thus modification and control of these mechanisms remains elusive.

2.3.3 Non-planar block geometries

Topologically interlockable blocks have been extended to include geometries with non-planar surfaces, in the form of *osteomorphic* blocks, so named due to their similarity to the shape of bone [5]. These blocks interlock due to their matching concavo-convex surfaces, which are defined by a set of mathematical equations [84]:

$$z_1 = \Delta h f(x) f(y) + h \quad (1)$$

$$z_2 = \Delta h f(x + a) f(y) - h \quad (2)$$

where the function f must meet certain periodicity conditions:

$$f(x) = f(-x)_{,SEP}^{[L]}$$

$$f(x) = f(x+2a)_{,SEP}^{[L]}$$

$$f(0) = 1_{,SEP}^{[L]}$$

$$f(a) = -1_{,SEP}^{[L]}$$

$$f'(0) = f'(a) = 0$$

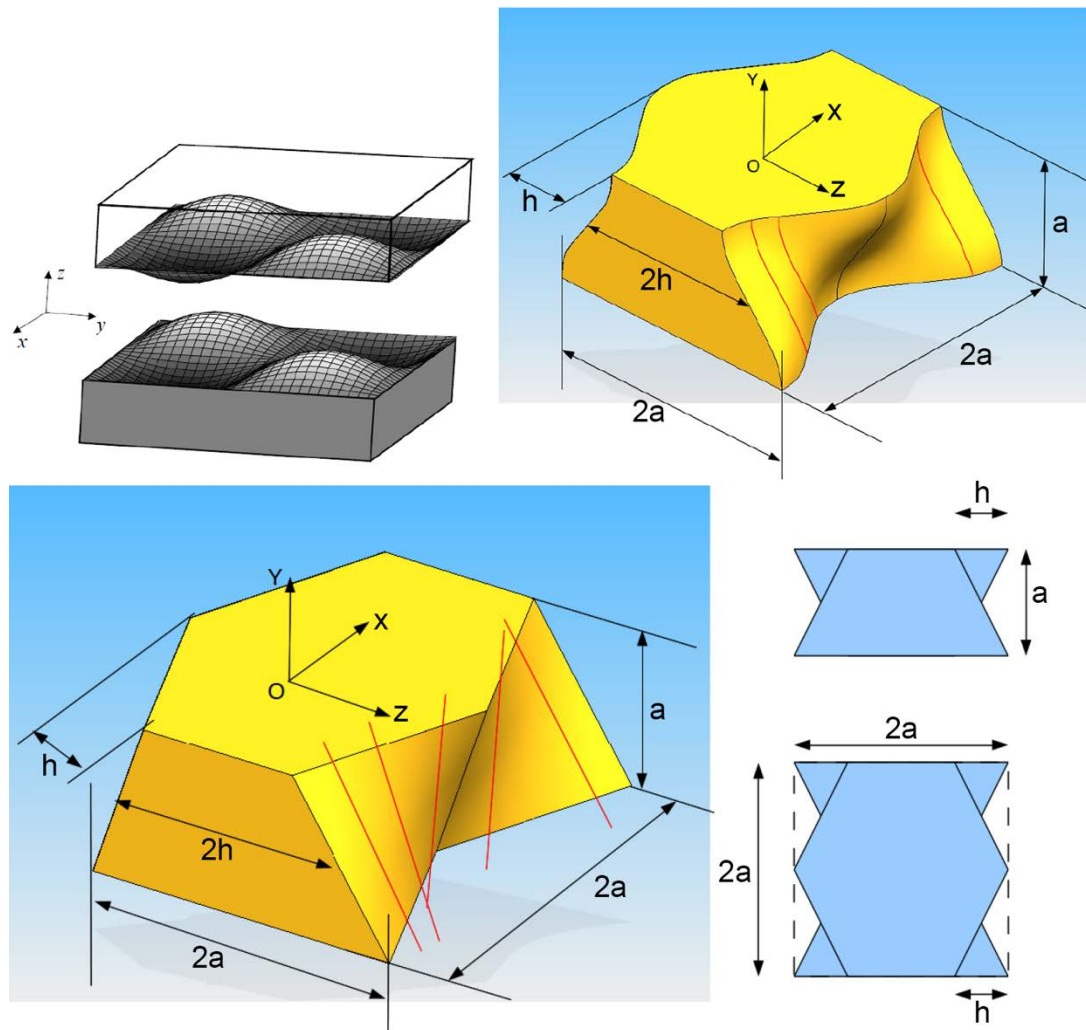


Figure 2.11 – Non-planar osteomorphic geometries with curved and flat contact surfaces. Adapted from [15]

Studies in the past have used different functions for these blocks, including fourth order polynomials [84], cosine functions [94], as well as "circular arc" and "straight edge" (triangle) [15, 98], all of them satisfying the above symmetry and periodicity conditions [5] required for interlocking to be possible. The effect of these will be discussed below in Section 2.3.6.

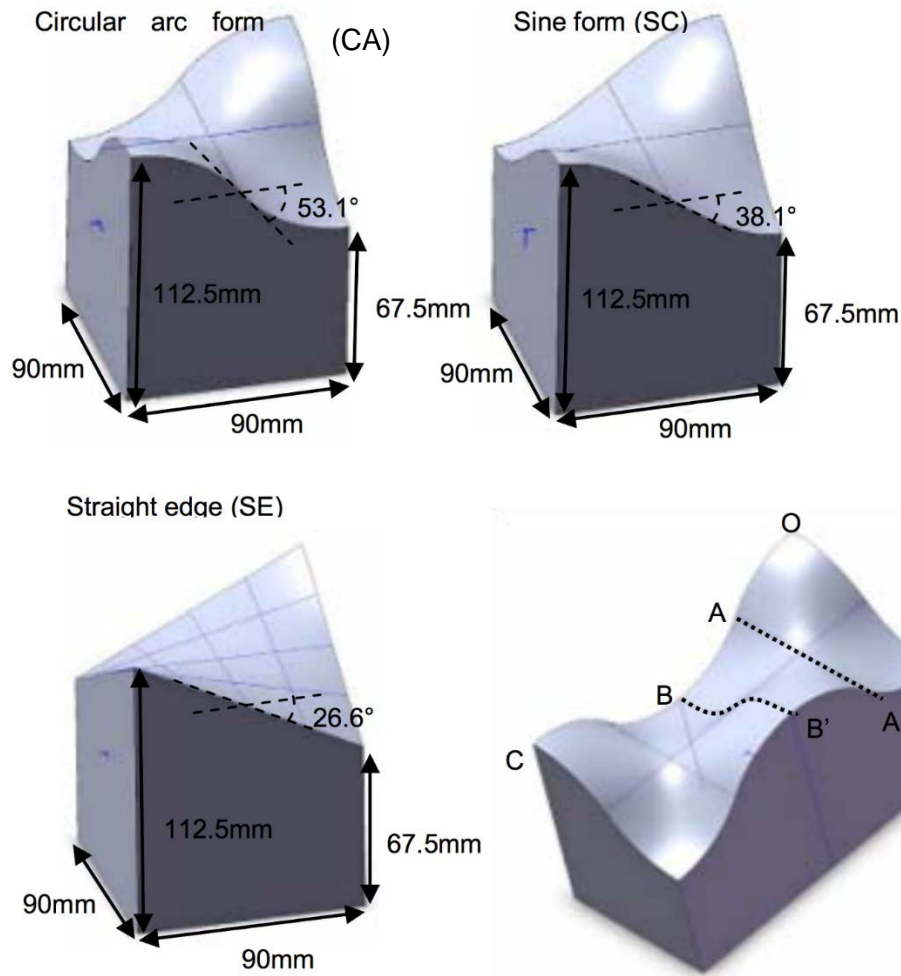


Figure 2.12 - Various osteomorphic geometries studied by Yong [98]

Multiple variables have been identified which affect the mechanical response of such topological interlocking assemblies, and a summary of previous work to characterise these effects is presented below.

2.3.4 Mechanical properties

Variables, such as friction, lateral load and elastic modulus have also been shown to affect topological interlocking plates under point loading. Dyskin et al. [84] demonstrated that for the same planar assembly of topologically interlocked blocks, a decrease in stiffness, peak load and toughness occurred when decreasing the lateral load of a constraining frame. This was only shown for two specific cases of non-planar blocks under point load and was not

extended to other structures. Molotnikov et al. [93] demonstrated a similar effect by experimentally modifying the torque applied to the lateral screw constraints (thus varying the lateral load on the frame) for four assemblies. Similarly, Yong's FE analysis showed that an increase in the coefficient of friction between blocks led to an increase in stiffness for osteomorphic assemblies [98].

Brugger et al. [106] demonstrated the effect of friction on the force-displacement curves of assemblies of cubes using DEM (cf. Figure 2.13), highlighting an increase in peak load with increasing friction. However, in these results when the coefficient of friction exceeds 0.4, no loss of load with increasing displacement is observed, which might be an artefact of the calculation.

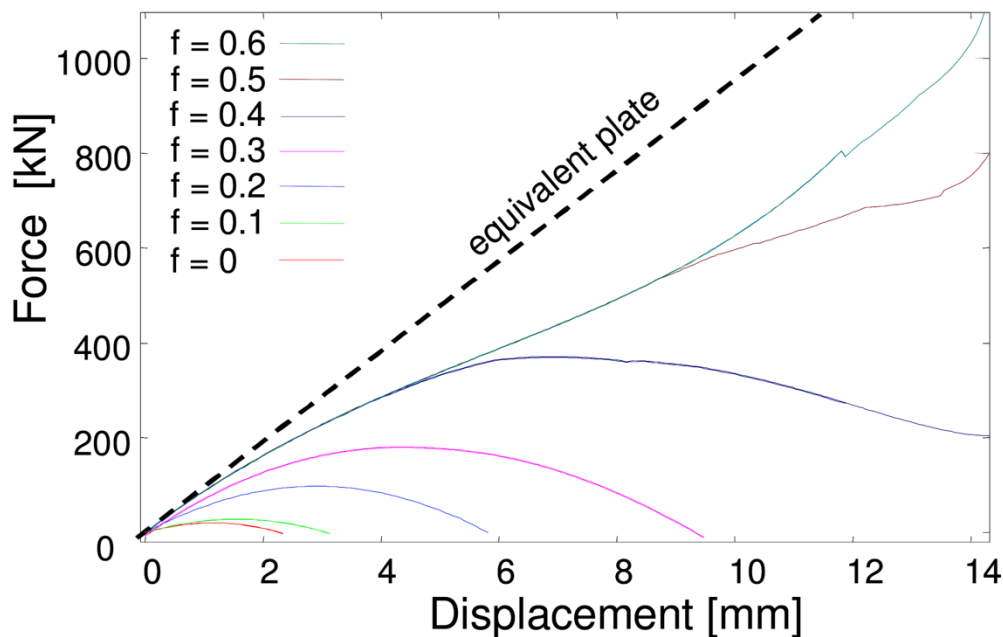


Figure 2.13 - Comparison of force-displacement curves for varying coefficient of friction values obtained via DEM [106]

Duguè et al. [15, 103] continued work done by Brugger et al. [106] in utilising a combination of DEM and FE (discussed below in Section 2.5), to study these effects further for both cube-shaped and osteomorphic blocks. In this work, Duguè demonstrated changes to mechanical point loading of planar assemblies in relation to elastic modulus, friction and lateral load. Increases in elastic modulus (3 – 390 GPa) were shown to increase peak load, stiffness and

toughness, while maintaining a constant deflection to failure for both osteomorphic and cubic structures.

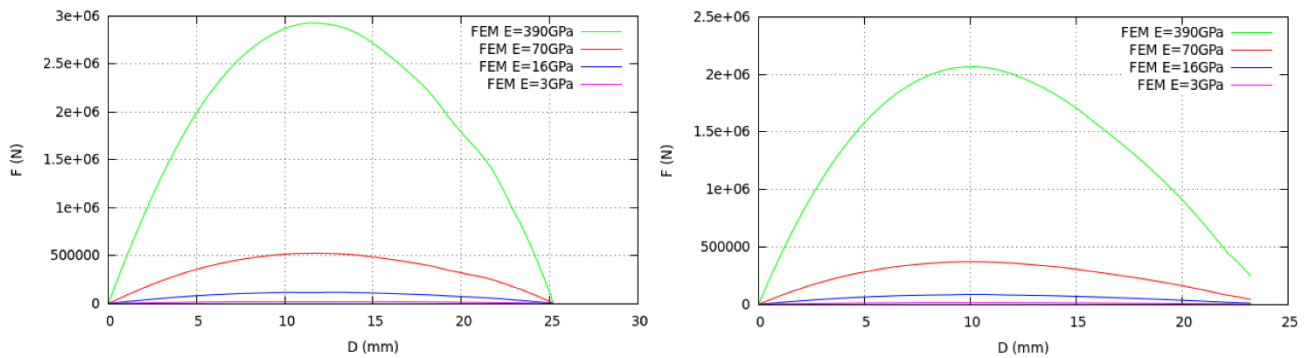


Figure 2.14 - FEM predictions of point indentation curves showing the effect of Young's modulus on cube-shaped (left) and osteomorphic (right) assemblies [15]

Friction was varied in the range of $\mu = 0 - 1$, and was shown to increase stiffness, peak load and toughness with increasing magnitude of the coefficient of friction.

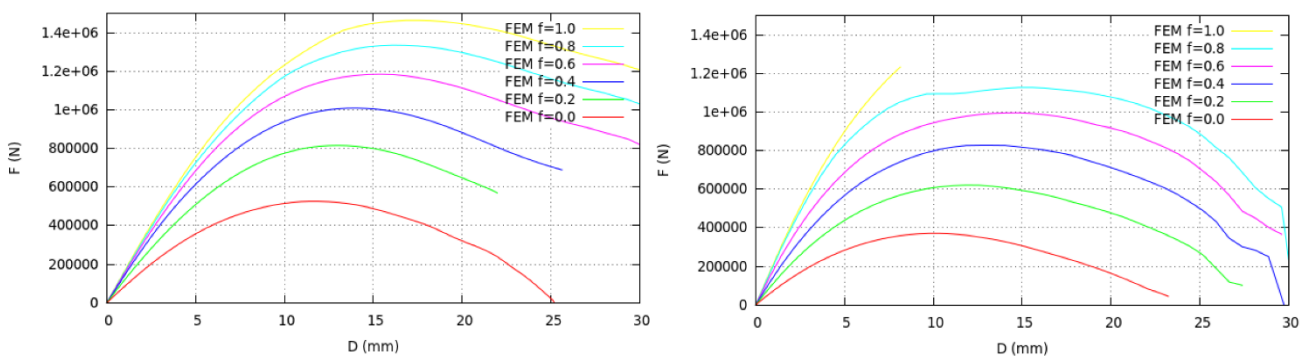


Figure 2.15 - FEM predictions of point indentation curves showing the effect of friction on cubic (left) and osteomorphic (right) assemblies [15]

Increasing lateral load was also found to increase the stiffness and peak load for cubic structures, however this trend was far less clear for osteomorphic blocks.

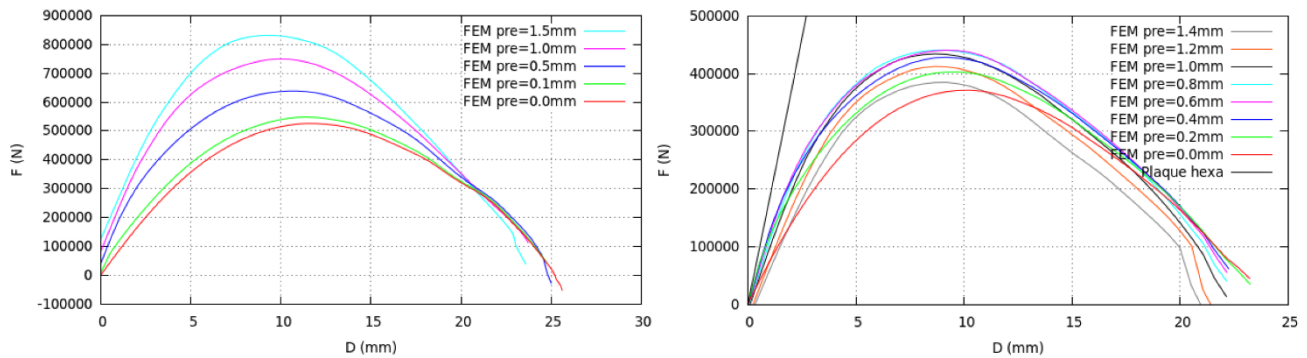


Figure 2.16 - FEM predictions of point indentation curves showing the effect of lateral load on cubic (left) and osteomorphic (right) assemblies [14]

Overall, this work was able to show the trends of these relationships, but did not attempt to quantify these into equations.

Schaare et al. [13, 86] conducted similar experimental and numerical (FE) studies using cube-shaped blocks. These included the effect of the intrinsic material properties (in particular, the elastic modulus, density and coefficient of friction), and extrinsic parameters, such as the lateral pre-load, on the peak load of planar assemblies under quasi-static point load. In this work, Schaare et al. found phenomenological exponential relations between the elastic modulus (in the range from 3 to 220 GPa) and the peak load and stiffness at specific lateral load (1.5kN) and coefficient of friction (0.3) values, as shown in Figure 2.17.

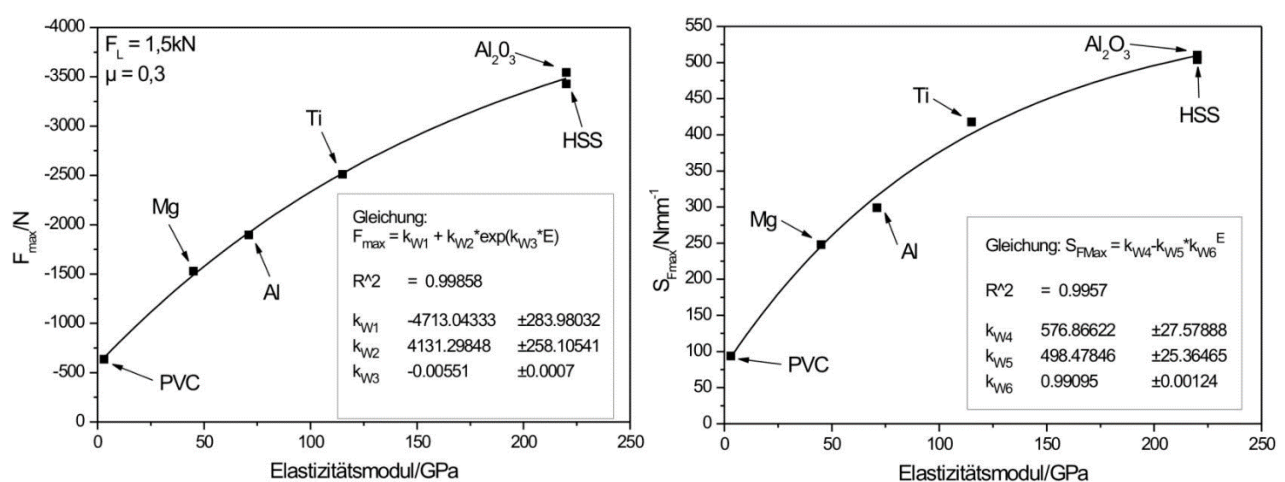


Figure 2.17 - Relationship between peak force, stiffness and elastic modulus as shown by Schaare [13]. The x-axis is given as Elastic Modulus in GPa

While the effect of the elastic modulus showed a clear trend, these studies also varied Poisson's ratio (0.25 – 0.35) and density (1.4 – 8.1 g/cm³), which were not accounted for in these equations, as their effect was deemed negligible. These equations were then used to study the relationship of peak load with: 1) lateral load (1 – 3 kN) and 2) friction ($\mu = 0 - 1$).

Furthermore, the effect of lateral load on peak load showed an increasing linear relationship between the two variables over a range of elastic modulus values.

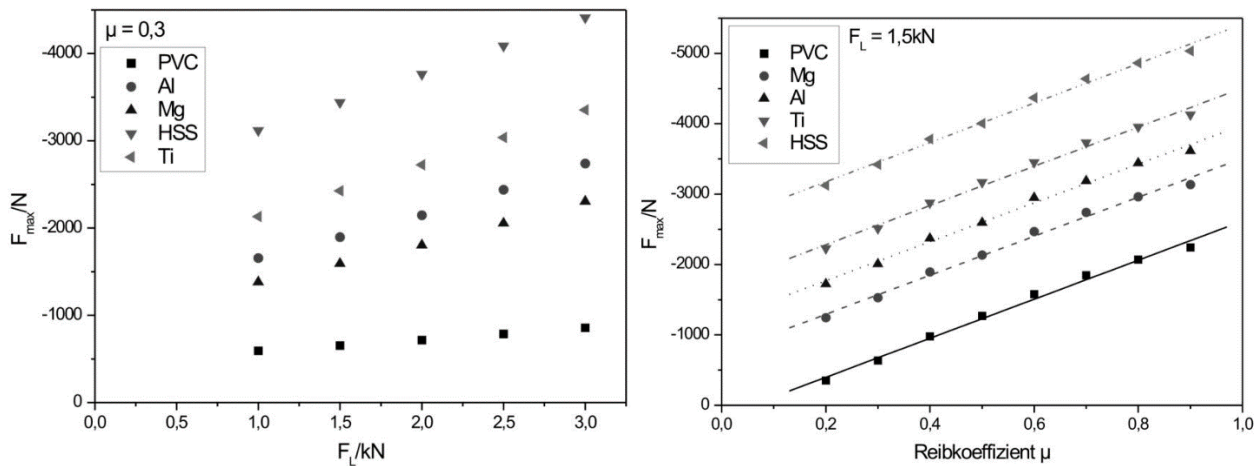


Figure 2.18 - Effect of lateral load, friction and elastic modulus on peak load F_{max} [13]. The x-axis (right plot) is given as coefficient of friction (μ)

This trend was characterised by the following equation:

$$F_{max} = k_1 + k_2 F_L \quad (3)$$

where F_{max} is the peak load, F_L is the lateral load and k_1 and k_2 are empirically fitted constants.

Using the above equation, an increasing linear relation for k_1 as a function of the elastic modulus was found, while k_2 exhibited an exponential dependence on E . These relations were substituted into Eq. (3) to express the effect of the lateral load and elastic modulus, cf. Figure 2.18.

A similar substitution was conducted for the coefficient of friction (μ). In this case, an exponential dependence was found for k_1 , while k_2 was found to be independent from the elastic modulus. However, Schaare et al. state that k_2 would likely be dependent on the lateral load, which is untested, however [13]. The k_2 value would also be governed by some of the effects discussed in Section 2.3.5.

While the study by Schaare [106] determined an empirically-derived formula for three of the above variables, the ability to relate them all to each other was lacking [13], which required a relationship between the peak load and stiffness and the lateral load and friction, in order to achieve a more robust general equation. This study focussed primarily on peak load, with little attention being given to stiffness.

Khandelwal et al. [99] developed a thrust-line model, based on the description of (typically compressive) load transfer between two points, which is well established for static masonry cases describing the quasi-static mechanical behaviour of tetrahedron-shaped blocks in a planar assembly. This work experimentally demonstrated a linear relationship between peak force, stiffness and work to failure against the density of tetrahedron-shaped blocks. The linear relationship was then found to also be relevant for properties of peak force and stiffness, as well as peak force and work to failure. The thrust-line model was shown to slightly over-predict and under-predict these two relationships, respectively. While this model was found to agree well with the mechanical response under point loading, and could be normalised to fit experimental data, it does not take into account friction, and therefore the slip between blocks within these assemblies – a defining process underlying the mechanical response of the assemblies.

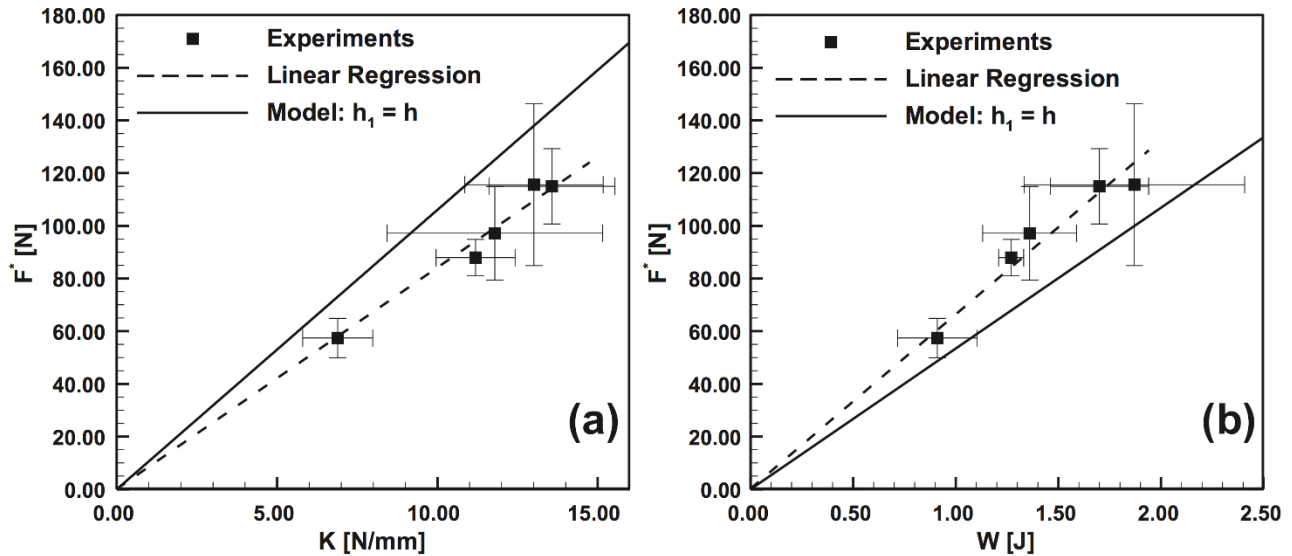


Figure 2.19 – Comparison of thrust-line model predictions with experimental results for force-stiffness and force-work relations with varying density of tetrahedral blocks in a planar assembly under point loading [99]

Khandelwal et al. [14] considered the effect of elastic modulus in their thrust-line model, primarily treating it as a constant factor which could be normalised out of the equations due to its linear relationship with stiffness, peak load and toughness. This approach was not investigated or validated further. Friction was also considered via FE, and the range was far larger than in the cited work by Schaare, from $\mu = 0.5 - 8$. An increase in stiffness up to $\mu = 2$ was found, after which stiffness remained constant up to $\mu = 8$. This is to be expected as achieving such high values of the coefficient of friction is not experimentally possible, and artificially high levels of μ essentially set the sticking condition in numerical simulations. Feng et al. [92] modelled planar assemblies of interlocked tetrahedra using FEA and found that stiffness, peak load and deflection at failure rose with increasing friction, cf. Figure 2.20. The study was conducted to determine the parameters of the simulations to fit experimental results, and the observed trends were not quantified.

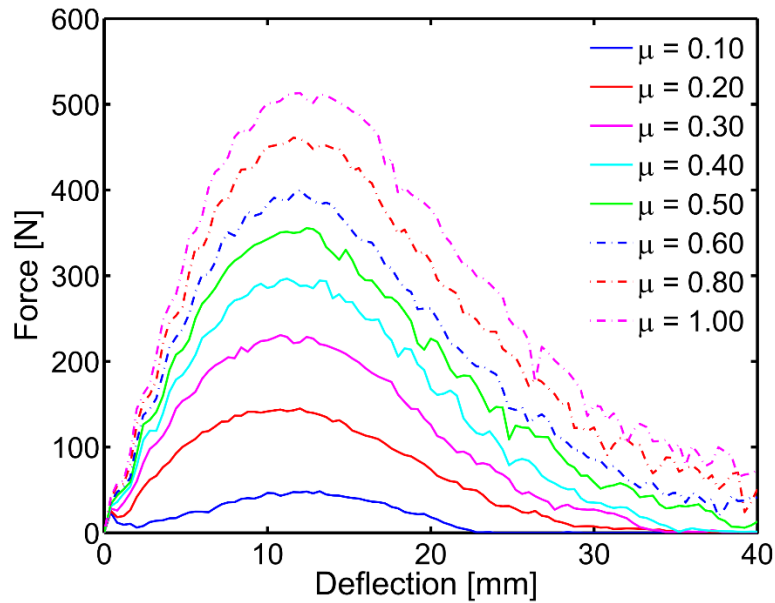


Figure 2.20 - FEM prediction of the effect of friction on the mechanical response of a planar assembly of tetrahedron-shaped blocks [92]

Autruffe et al. also considered friction when studying blocks manufactured from ice [107]. In their work, higher temperatures were associated with lower friction, given that a thin liquid film formed due to local melting would decrease the coefficient of friction. Using this technique, lower temperatures were able to furnish a higher stiffness of the assemblies, as shown in Figure 2.21.

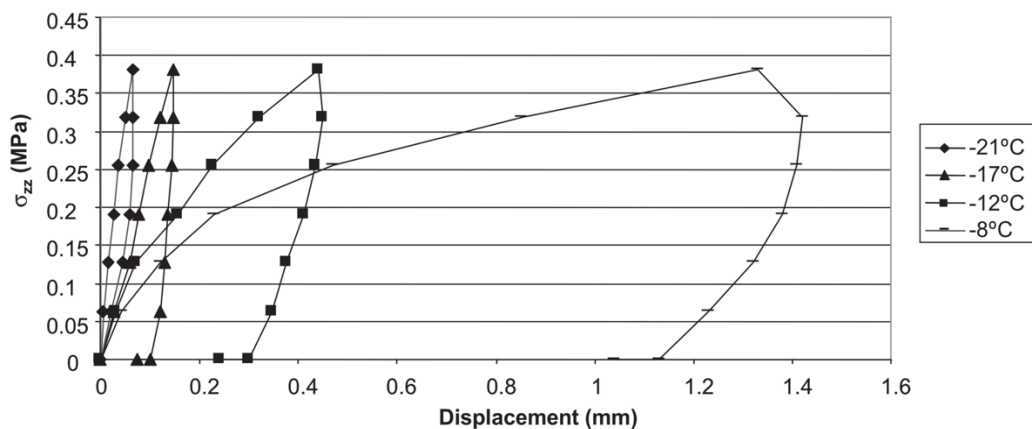


Figure 2.21 - Comparison of loading curves for planar assemblies of interlocking ice tetrahedra for different temperatures, with lower temperatures corresponding to higher values of the coefficient of friction [107]

Overall, friction, lateral load and elastic modulus have been identified as having an effect on the mechanical response, however any effort to characterise their effect has been limited in both scope and detail. Indeed, only basic trends have been outlined, with the most detailed and specific understanding coming from the thesis of Schaare [13] who quantified the effect of some of the variables in the form of diagrams, but did not link each of them together.

2.3.5 Size effects

The effect of size and scale have been identified as key variables in the mechanical response of topological interlocking planar assemblies, and efforts have been made to characterise this effect. Brugger et al. [108] presented initial numerical DEM observations comparing two specific topological interlocking plates (cf. Figure 2.22) and showed that decreasing the size of the blocks for a constant assembly size (and therefore increasing the number of blocks) resulted in a decrease in stiffness, peak load and toughness of the assemblies. However, no mathematical relations were developed to connect these variables. Instead, an explanation related to the number of contact surfaces was proposed, suggesting that the accumulation of relative local displacements leads to a more flexible overall assembly, similar to a chain with more links.

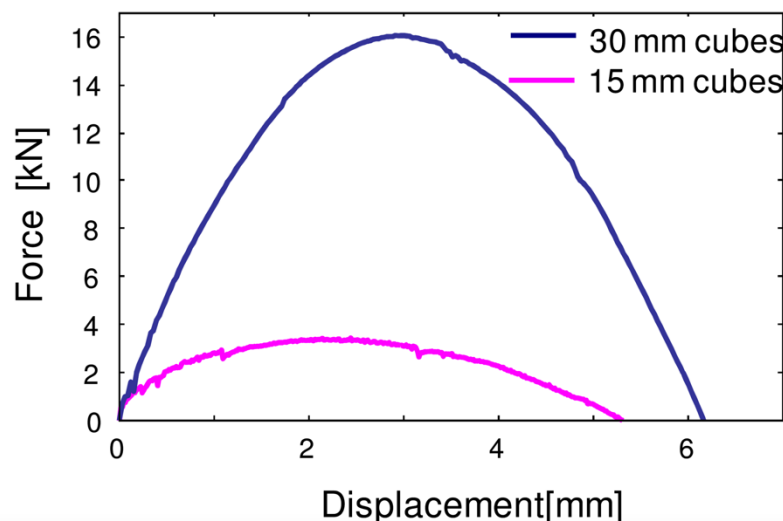


Figure 2.22 - Comparison of the effect of block size on load-displacement curves for assemblies of cube-shaped blocks for a fixed assembly size [106]

Duguè et al. [15, 103] extended this work using a combination of DEM and FE (discussed below in Section 2.5) to show a trend between two different size and scale cases for both osteomorphic and cube-shaped blocks. The first involved modifying the block size (with a constant number of blocks) and the second case varied the number of blocks (with a constant block size). In the first case considered, an increase in block size led to an increase in stiffness, peak load, toughness and deflection to failure.

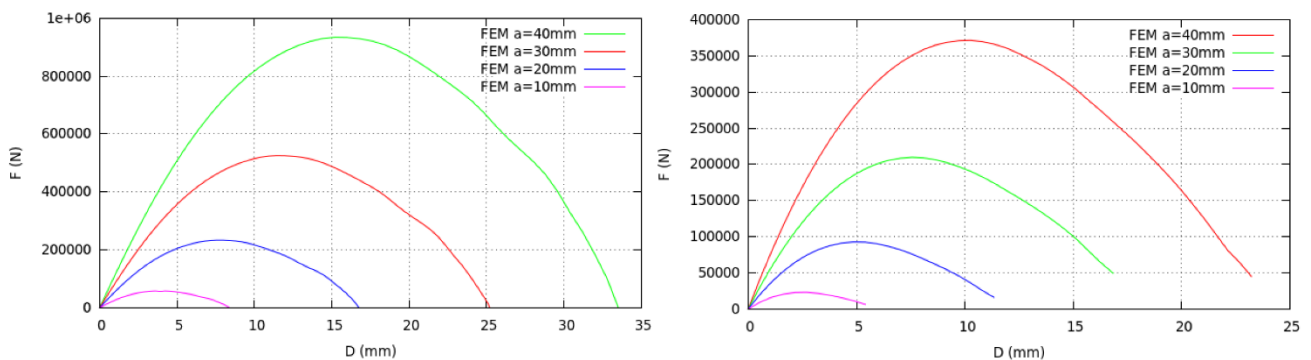


Figure 2.23 - FEM predictions of point indentation curves showing the effect of block size on cubic (left) and osteomorphic (right) assemblies [14]

In the second case, increasing the number of blocks (and therefore the assembly size), led to a decrease in peak load, stiffness and toughness, but an increase in deflection at failure. No quantification of these trends was put forward, only a direct comparison, which an explanation of the mechanisms agreeing with the earlier work of Brugger. [106, 108]

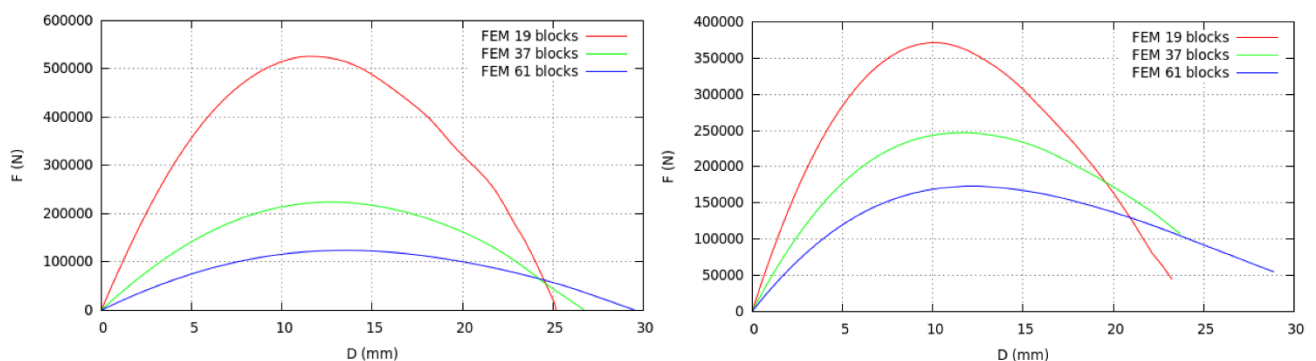


Figure 2.24 FEM predictions of point indentation curves showing the effect of assembly size on cubic (left) and osteomorphic (right) assemblies [14]

In addition to this, Khandelwal et al. used their thrust-line model (in conjunction with FE) to outline scaling laws for initial stiffness of planar assemblies of tetrahedra [104]. These laws relate the initial stiffness of tetrahedron-shaped blocks with various size parameters given ideal friction and fixed boundary conditions. They were found to be consistent with the predictions of the conventional plate theory [109]. Indeed, a power law relation was found to hold between three primary size parameters: 1) variable block size with constant assembly size, 2) variable assembly size with constant block size, and 3) variable block and assembly size with constant size ratio (block-to-assembly).

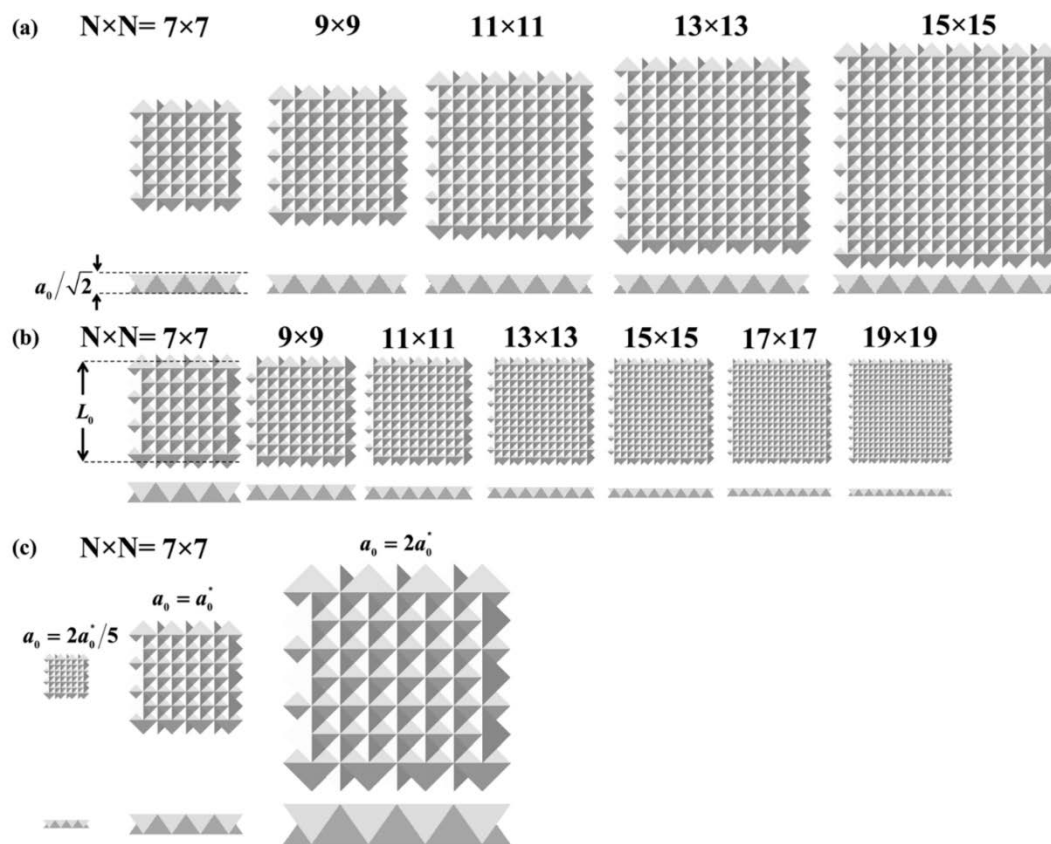


Figure 2.25 - Schematic overview of size and scale study conducted by Khandelwal et al. [104]

The results indicate that stiffness in Case 1 is proportional to the third power of the block size, in Case 2 it is inverse in the second power of the assembly size, and in Case 3 it is linear in the block size. Agreement with FE was good, although only three FE simulations were presented for Case 3. In Case 2 a regression of the numerical results returned a power

of -1.9, rather than the expected value of -2. Still, the results agree reasonably well with the analytical predictions for assemblies with a varying block size to assembly size ratio:

$$K \propto E \frac{a_0^3}{L_0^2} \quad (4)$$

as well as a constant size ratio:

$$K \propto E a_0 \quad (5)$$

where a_0 = block size and L_0 = assembly size.

The latter relation is of key importance, as it indicates a linear size dependence of stiffness for self-similar assemblies. Furthermore, the thrust-line model and the conventional plate theory present surprisingly similar relations despite vastly different underlying mechanics. Indeed, the plate theory [110] suggests that these relations exhibit the same size dependence as those given by Eq. (4) and (5).

In their thesis, Khandelwal extended this thrust-line model analytically to include peak force and total energy absorbed by linearising the initial stiffness model [14]. By defining the size ratio:

$$s = \frac{L_0}{a_0} \quad (6)$$

the expression for stiffness can be re-written as:

$$K \propto E \frac{a_0}{s^2} \quad (7)$$

Considering that peak force or load occurs at $F^* = K\delta^*$, where δ^* is the deflection at peak load and δ^* occurs only as a function of a_0 , the peak load is given as:

$$F^* \propto E \frac{a_0^2}{S^2} \quad (8)$$

Using Eq. (6), Eq. (8) can be written as:

$$F^* \propto E \frac{a_0^4}{L_0^2} \quad (9)$$

Finally, the total energy absorbed is approximated as $W = 1/2 F^* \delta_f$ where δ_f is the deflection at failure. Using the thrust-line model we obtain:

$$W \propto E \frac{a_0^3}{S^2} (2S + 1) \quad (10)$$

Khandelwal's study [14] considered the block size, assembly size and elastic modulus as control variables, but did not provide numerical or experimental validation of the expressions obtained for peak load or work of deformation. Indeed, Khandelwal concluded [14] that the size effect on strength and toughness can be reduced to the dependence of these quantities on the block size to assembly size ratio. By contrast, stiffness was observed to be dependent on the block size.

While the thrust-line model has been well proven in some cases, this extension of the model has yet to be validated, experimentally or numerically, particularly for block geometries other than tetrahedra, although according to Khandelwal these kinematic laws should still hold given an adaptation to the new configuration [14]. Khandelwal includes a parameter, α , which acts as a geometry factor and is constant for a given “family” or geometry of topological interlocking assemblies. Given the assumed conditions of hard contact (sticking, no slip) and fixed boundary conditions, it is essential that these factors be included in the model due to their significant effect on the mechanical response, as discussed in Section 2.3.4.

2.3.6 Geometry effects

Some work has been conducted to elucidate the effect of block geometry on the mechanical response of topological interlocking materials, however understanding is limited. Mirkhalaf et al. [105] used a laser cutting technique to impart impressive toughness to glass in two dimensions by carving three dimensional tetrahedral blocks with varying interlocking angles, into glass plates. These topological interlocking plates were tested under impact and quasi-static point loading. Quasi-static testing showed some limited differences in the mechanical response with varying tetrahedral angles. Under impact testing, a tetrahedral angle of 2.5° , infiltrated with Surlyn ionomer (a soft rubbery material), showed the best response. This multi-material approach, combining a stiff block phase with a soft, rubbery matrix was shown to be highly promising.

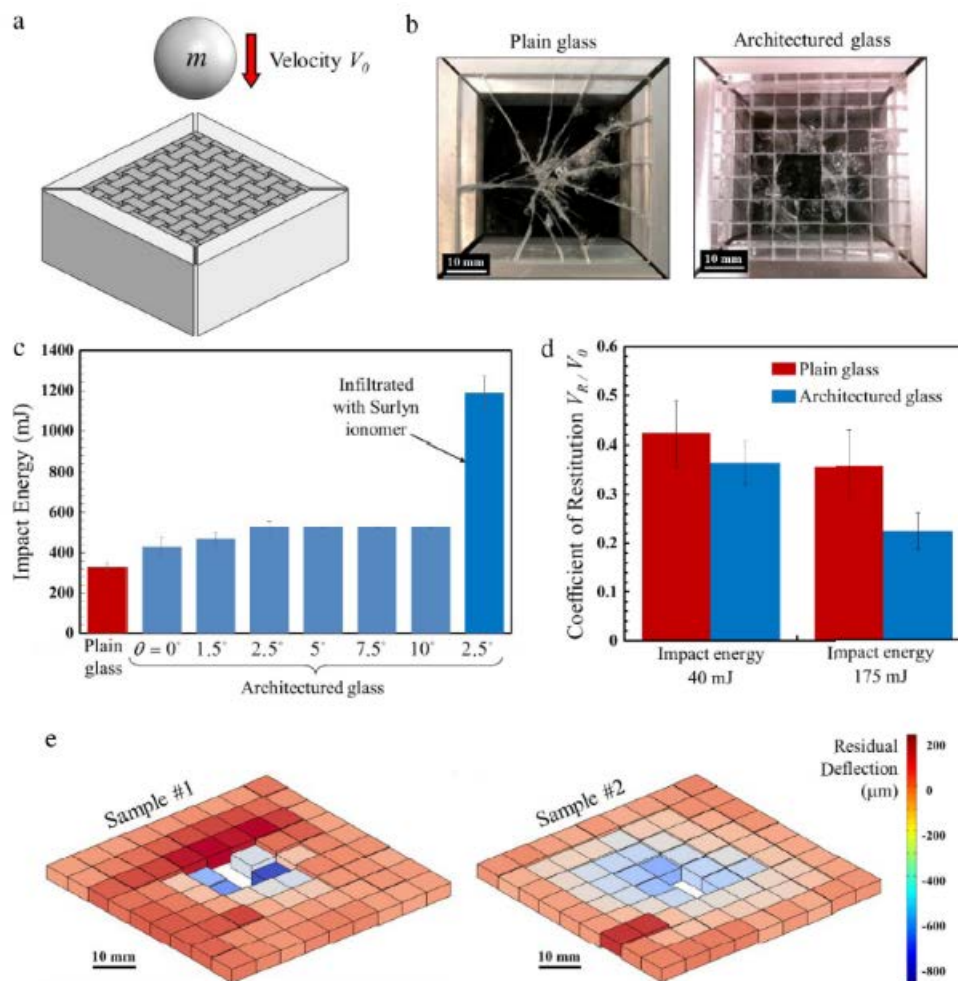


Figure 2.26 - Overview of impact testing conducted by Mirkhalaf et al. [105] showing impact energy of architected glass structures

In his thesis, Yong [98] presented various studies on non-planar blocks in the context of masonry bricks. This work included modifications to the amplitude ($\Delta h/(x,y)$) and curve function (as stated in Section 2.3.3) finding that indentation resistance increases with higher amplitudes and block geometry enabling a greater degree of interlocking.

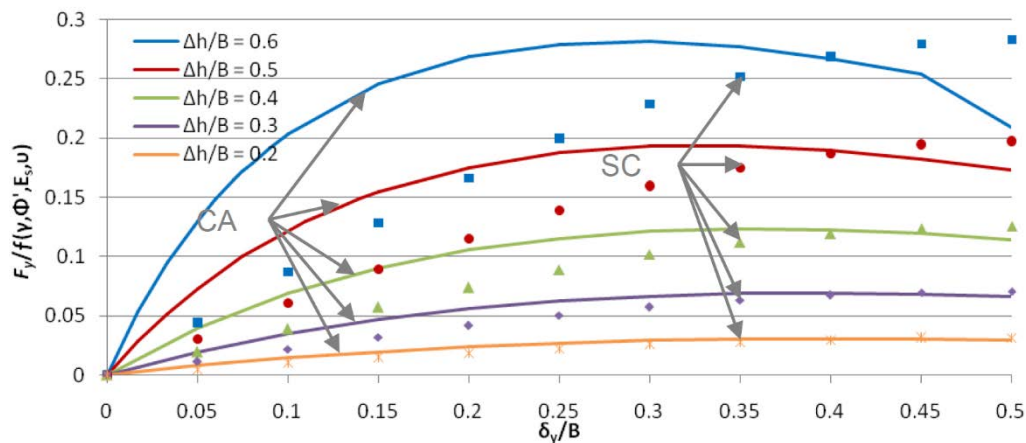


Figure 2.27 - Effect of amplitude and block geometry on the force-displacement curves for non-planar interlocked assemblies [98]. Refer to Figure 2.12 for abbreviations and geometries

Yong identifies the ability of the blocks to transfer load between blocks within the assembly as the primary factor that governs its mechanical response. However, the results reported in his thesis are mainly preliminary in nature, as they did not establish general relations between the measured characteristics and these variables. In addition, Yong numerically studied the effect of random asperities on the surface of osteomorphic blocks under compressive load. A decrease in load bearing capacity of the assembly when random asperities were introduced was demonstrated. Yong also attributes this to a decreased ability for neighbouring blocks to interact with another, due to a reduction of the surface area and a concomitant decrease in load transfer.

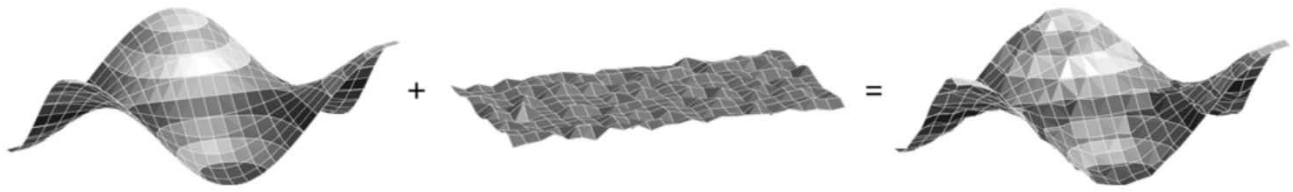


Figure 2.28 - Applying random surface roughness to FE simulation [98]

While Duguè et al. [15, 103] studied both cubic and osteomorphic blocks, only a basic comparison between the two geometries was presented. Differences in the deformation behaviour of the two geometries were highlighted for the case of cyclic loading, however the mechanical properties were not compared or contrasted.

Overall, the effect of geometry on the mechanical response of topological interlocking assemblies has not been investigated in-depth, particularly with regard to non-planar geometries. The latter were considered in the thesis of Yong [98], who provided preliminary data on the effect of the degree of interlocking on the load-displacement curves.

2.4 Fabrication

A number of methods have been used to create topological interlocking materials including casting [85], machining, [86, 102] and laser engraving [105]. In more recent times, additive manufacturing has emerged as a viable technique to fabricate topological interlocking materials [99]. In particular, efforts to create multi-material structures, such as the glass-ionomer hybrid created by Mirkhalaf et al. [105], have led others to additive manufacturing as a route with more design freedom. A recent article [100] has provided a comprehensive overview of the techniques suitable for manufacturing of topological interlocking materials. The established and emerging techniques of additive manufacturing are described below in some detail.

2.4.1 Additive Manufacturing

Additive manufacturing (AM) refers to a group of technologies that are able to create physical parts or systems from digital three-dimensional Computer-Aided Design (3D CAD) data and is commonly referred to as 3D Printing. The parts are generally built up by adding thin layers of material upon one another until the full (usually) three-dimensional part is realised. There are various techniques that fall under the AM umbrella, including extrusion-based methods, powder bed fusion processes and directed energy deposition. These techniques are capable of printing most materials, including metal and ceramic components. Two of the primary processes for polymeric AM is extrusion-based technology and polymer jetting.

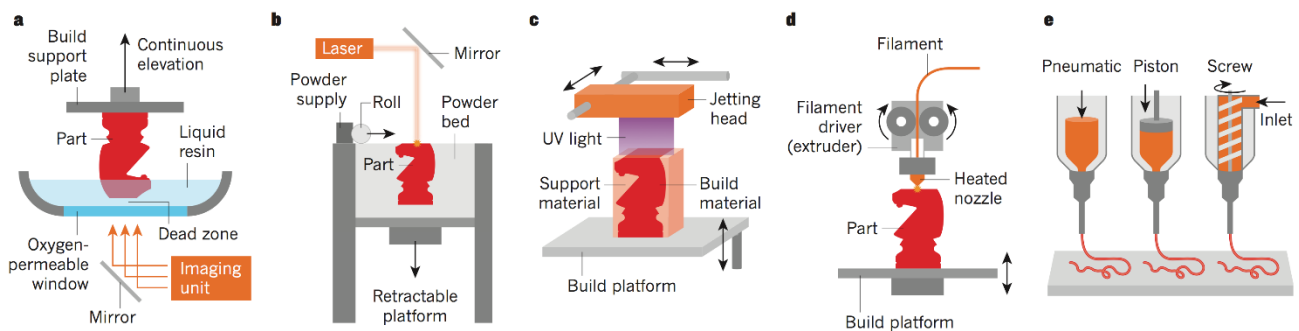


Figure 2.29 - A selection of printing processes - a) stereolithography, b) selective laser sintering, c) polymer jetting, d) and e) extrusion based techniques [111]

Extrusion based technology, in particular the Fusion Deposition Method (FDM), is the most widely used method due to the relative ease and low cost of the process. This process essentially consists in controlled extrusion, which involves heating a polymer (usually in a fibre form which is being fed through a heated nozzle) to a molten state, before depositing the material layer by layer. There are variations of this process, with different materials, pressures and temperatures being used, however the basic principle is the same [112]. Indeed, this process has been used to create novel, bioinspired multi-material composites [113] by using magnets to orientate alumina platelets in a polymer matrix during the printing process. Compton et al. [114] used an epoxy-nanoclay composite with highly aligned fibres in a novel extrusion-based method to create lightweight cellular materials with an impressive combination of stiffness and strength.

Polymer jetting is an alternative process that uses small nozzles to dispense liquid photopolymerisable monomer from a print head analogous to two-dimensional inkjet printing. This material is then cured by ultraviolet (UV) light using a source situated on-board the printing head, which immediately causes the liquid resin to react and solidify, Fig. 4 [115]. This technique tends to have superior print resolution, build quality and mechanical properties over the FDM techniques.

A number of companies utilise the polymer jetting technique, one of which is Stratasys, who have termed this process “PolyJet” technology, Fig. 2.30. This particular technology employs a number of proprietary polymer blends containing acrylic monomers, acrylates and photoinitiators and is capable of multi-material printing which can print stiff and flexible phases within a single build.

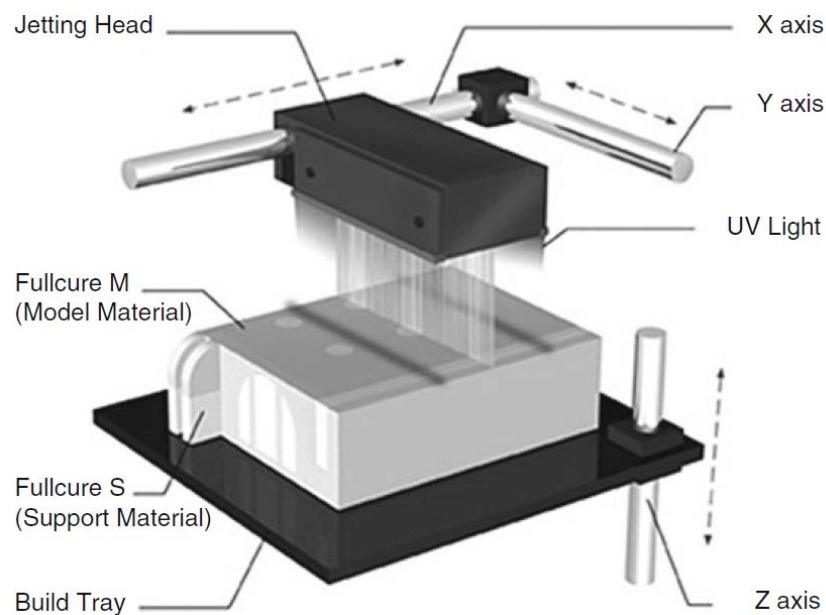


Fig. 2.30 - PolyJet printing process [112]

This system is particularly attractive due to its ability to print at high resolution, with a layer thickness of 16 – 30 μm , and is capable of printing parts with sub-millimetre features. Significantly, the PolyJet technology is suitable for combining rigid and rubbery polymers *in situ*, allowing for control of mechanical properties by mixing these polymers in various proportions.

This technology grants additional design freedom when considering engineered hybrid materials, which has been shown to be highly effective in a number of studies, in particular with bio-inspired materials [116]. Ongoing work has shown the ability to create 3D periodic composites with tailored mechanical properties [117], produce biomimetic shark skin [118], topology optimized compliant multi-material structures [119], and mechanisms for novel load transfer applications [120, 121], as well as making use of thermal properties for '4D Printing' [122]. These dynamic '4D' parts are particularly attractive, as thermal changes allow for responsive structures to be fabricated. Indeed, this technology has been used to create bio-inspired structural hybrid materials, such as suture interfaces found in molluscs [62], and also study the deformation and fracture mechanics of materials mimicking nacre [16, 61] and bone [123]. In particular, Dimas et al. [16] demonstrated the ability to print high resolution, multi-material components with an impressive combination of stiffness, strength and toughness. The geometry employed, inspired by Nature's hard and soft microarchitectures, was limited to a two-dimensional study of various designs.

The ability to create 3D CAD models using available software (such as SolidWorks and Rhinoceros) enables the process from conceptualisation to design and physical modelling to be streamlined. This process also allows for the 3D source data to be utilised in numerical simulations as a further means to better understand the mechanical behaviour of a prototype physical structure.

2.5 Computational Techniques

A useful tool for engineers and scientists to investigate and better understand physical systems is computational simulation. The selection of the computational tool depends on the time scale and the length scale of the experiment. While FE techniques are applicable for simulations at continuum level, a myriad of highly advanced techniques and methods to model a broad range of systems at multiple length scales including Direct Fourier Transform (DFT) and Molecular Dynamics (MD), cf. Figure 2.31, have emerged. Indeed, Sen et al. [124, 125] used a two-dimensional meso-scale model, inspired by atomistic approaches, to

simulate the mechanical behaviour, including the fracture mechanics, of various geometries of simplified structural bio-composites.

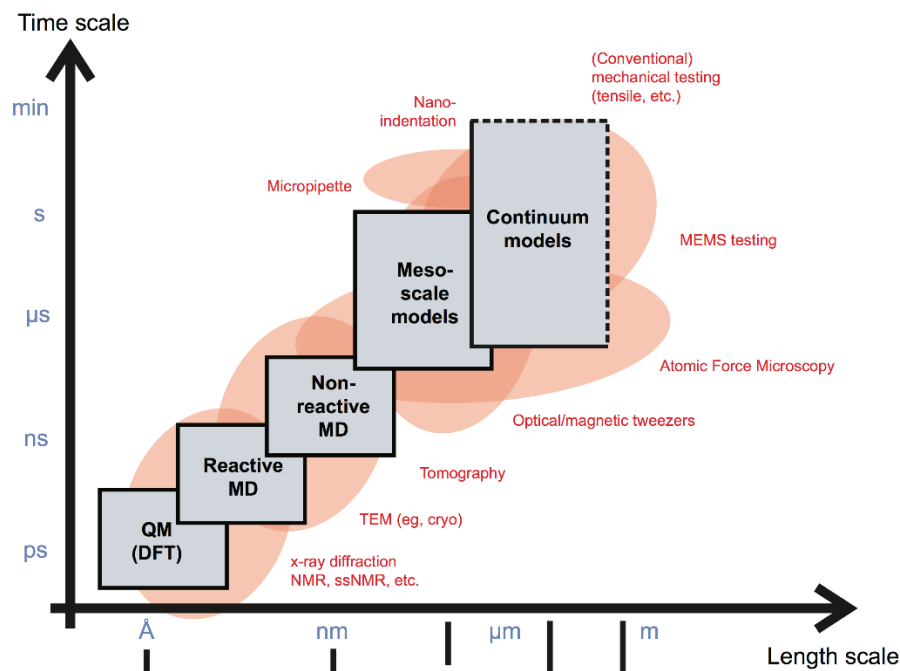


Figure 2.31 – Various modelling techniques ranging in size and time scales with comparative experimental techniques [126]

When dealing with the macroscale systems, two widely-used techniques are Discrete Element Method (DEM) and Finite Element Method (FEM).

The DEM is generally applied to model discontinuous materials at multiple length scales, usually achieved by assigning a body a central point of mass, a base point and six degrees of freedom (three translational and three rotational ones). In addition, geometries can be assigned to each point as polyhedral faces. This allows the geometries to interact via a number of forces including friction, gravity and adhesion [127]. FE is based upon subdividing or discretising a continuous structure into a network of smaller elements whereby calculations are performed for each element from which the outputs can be analysed and aggregated. The nodes of each element are generally calculated for displacement, force, stiffness and load, which makes the technique useful for representing complex geometries and capturing the effects of loading conditions, including complex ones [128].

Both of the above techniques have been used to simulate topologically interlocked structures. Brugger et al. [106, 108] and Dugué et al. [15, 103] used a combined DEM and FE approach to model assemblies of cubic and osteomorphic blocks. In this technique, the contact laws are determined via FEA of relative movement of simple bodies in contact with one another. These contact laws are then implemented as local rules for neighbouring discrete elements within a full assembly.

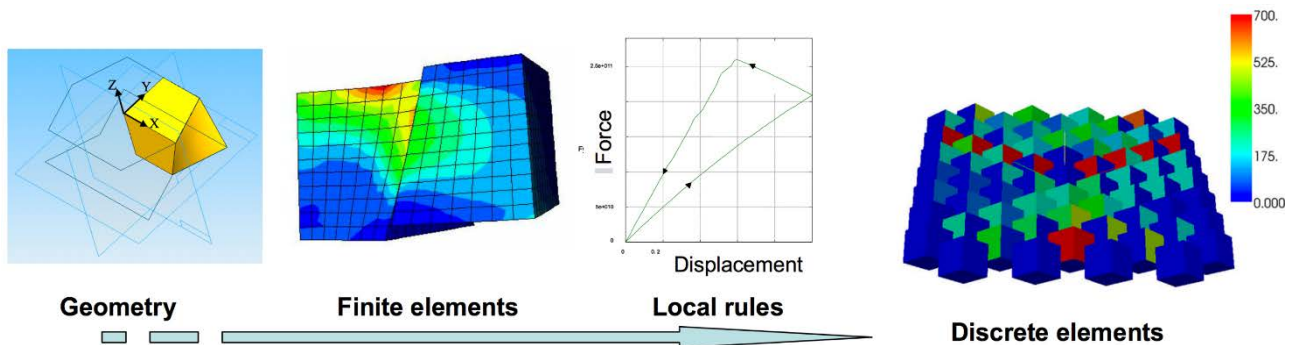


Figure 2.32 – Overview of combined DEM-FEM employed by Brugger et al. and Dugué et al. [108]

This saves significant computation time as well as producing reasonable agreement in force vs. deflection curves between the two simulation methods. Figure 2.33 shows these two methods produce force-deflection curves with similar peak loads, yet are different with regard to stiffness and deflection at failure.

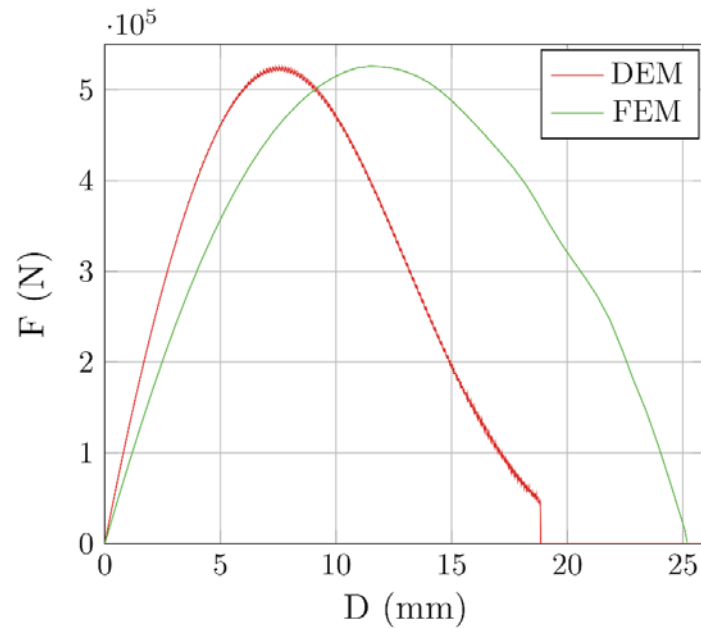


Figure 2.33 - Comparison of DEM v FEM for assembly of cube-shaped blocks [103]

Schaare et al. used FE [86, 102] to model similar structures. Indeed, FE has been used extensively in this area to model a range of responses [96, 98, 99], in particular, by Feng et al. [92] who utilised FE to model the impact mechanics of planar assemblies of interlocked tetrahedra. In this case, Feng et al. used fixed boundary conditions and fitted two parameters, viz. the coefficient of friction and contact stiffness, to match the experimental results.

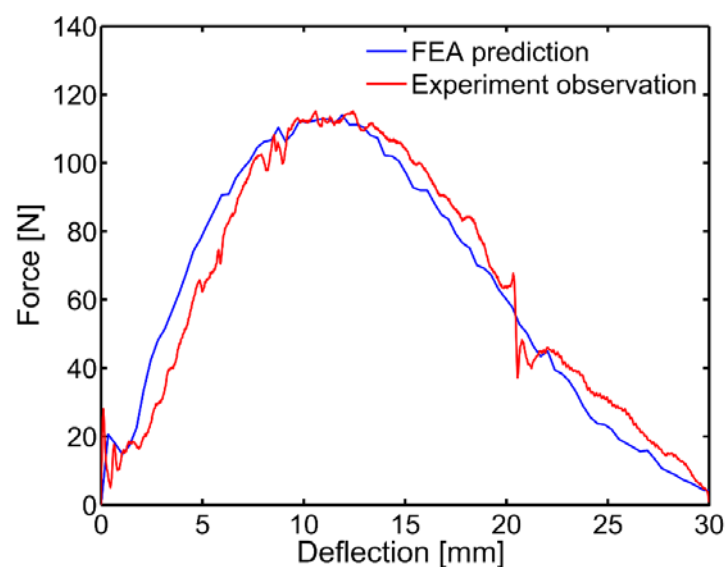


Figure 2.34 - FE and experimental curves for a planar assembly of interlocked tetrahedra [92]

While the two techniques are powerful, FE is more adept at modelling complex geometries (such as the osteomorphic shape), multi-material continuum systems, large deformations and plasticity, while DEM can be limited in modelling some these aspects without significant calibration.

One of the most widely used FE software packages is ABAQUS, which is a commercial software distributed by Dassault Systèmes under the Simulia brand. This is a state-of-the-art software package capable of high end nonlinear analysis that includes plasticity (including large deformations, material nonlinearity and contact problems) as well as integrating with multi-physics systems in describing their mechanical and thermal behaviour.

Finally, in considering complex systems with multiple variables it is often difficult to gauge their relative effect, particularly if there are multiple output properties to consider. One technique, which provides a potential route to address this, is known as Artificial Neural Networks (ANN) [129]. This method has become a powerful computational technique due to its ability to mimic the pattern of the brain. This is achieved by connecting multiple input variables (or nodes) with multiple outputs through a “hidden” layer of nodes, an example of which is shown in Figure 2.35. This structure can be made far more complex, with a greater number of nodes and hidden layers to address more difficult problem sets.

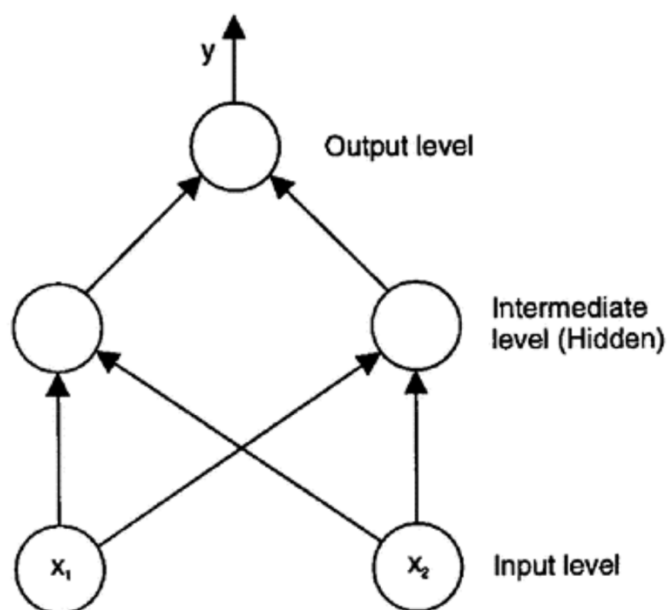


Figure 2.35 - Basic example of an ANN structure with two inputs, one hidden layer (with two nodes) and one output [129]

This system is able to detect patterns based on “supervised learning” through training via data of inputs and the expected outputs. The connections between the nodes are assigned weights which are determined by an error minimisation function between expected and predicted values. While this model has no physical or mechanistic basis, it is useful in determining patterns and relative influence between inputs and outputs for complex multi-variable problem sets. The use of ANN in the present PhD project – the first ever in the context of topological interlocking materials - will be discussed further in Sections 3.6 and 4.4.4.

2.6 Summary

The above literature review provides a summary of the current state of research, primarily in the fields of topological interlocking, bio-inspired, hybrid and architected materials, as well as the tools used to investigate these areas. Despite the breadth of research covered, the review tries to highlight the pertinent and specific features of the field and their relation to the body of work presented below. It can be seen that while efforts have been made to

characterise various parameters of topological interlocking assemblies, there remains much work to be done to establish robust and reliable relations between the mechanical properties and material parameters as well as the extrinsic characteristics, including the coefficient of friction, lateral load, block dimensions and the size of the assembly. Furthermore, while a biomimetic approach has been successful in design of structural composites, most of the work has focused on two-dimensional design. Pursuing a three-dimensional route is thus of much interest. Combining the concepts of bioinspiration and topological interlocking is similarly of interest, as limited work has been devoted to this combined approach thus far, particularly, with three-dimensional, hierarchical interlocking. We endeavor to present the outcomes of research into such a combined approach in the following sections of the thesis.

3. Methodology

3.1 CAD Design

A range of designs were employed for both the computational and experimental work. In order to facilitate these complex designs, a number of computational softwares were used. The majority of design work was conducted using SolidWorks, distributed by Dassault Systèmes. The design of the osteomorphic blocks was created using a parametric model, where the dimensions are controlled by easily adjusted variables which gives the ability to adapt the block quickly in various ratios for different assemblies, sizes and testing set ups. The osteomorphic geometry was achieved by defining the edge curves of one quarter of the curved surface via mathematical equations. The edges are then filled with a surface and extruded to create a quarter block. Simple mirroring operations can be used to achieve the desired half or full block.

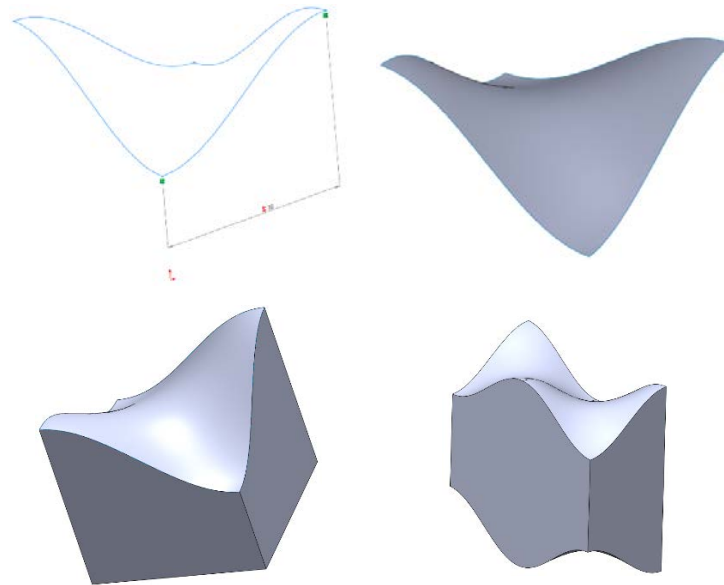


Figure 3.1 - Design of osteomorphic block showing progression from function generated edge curves, surface, quarter block and full osteomorphic solid geometry

The osteomorphic blocks are given by a set of mathematical equations, as outlined in Section 2.3.3, with the key interlocking surface defined as;

$$z_1 = \Delta h f(x) f(y) + h \quad (3.1)$$

where the function f meets certain periodicity conditions and Δh and h control the degree of interlocking. The need to modify the geometry of the block, such as in Chapter 5, was critical to the design, and as such the model created in SolidWorks was created to facilitate these modifications, by replacing the critical function f , with the necessary, defining equations for the straight, triangle geometry and square wave geometry, see Figure 2.11 Figure 5.2

Half blocks could also be easily integrated into the design as the outer blocks in the assembly. Assemblies were then produced by a simple linear patterning operation. The assemblies were designed as flat plates to facilitate point indentation testing as well as easily modified for mode I tensile testing of multi-material structures.

Solidworks also allowed a design of multi-material samples used in Chapter 6. This is achieved by modifying osteomorphic functions to generate the stiff block. Linear patterning was used to generate the plate assembly, with a small offset distance between each block defining the geometry of the soft phase. Additionally, an offsetting function was used to achieve the individual multi-material blocks with the soft coating surface, with more details provided in Chapter 6.

3.2 Fabrication

The fabrication of the experimental test specimens was conducted using additive manufacturing, with the primary machine being an Objet Connex500 multi-material 3D printer manufactured by Stratasys, Ltd. This machine employs polymer jetting technology which uses small nozzles to dispense proprietary, acrylate-based, liquid photopolymerisable monomer from a print head, analogous to two-dimensional inkjet printing. This material is then cured by ultraviolet (UV) light using a source situated on-board of the printing head, which immediately causes the liquid resin to react and solidify in a layer-by-layer fashion. The material is forced through the printing unit, which contains eight printing heads, each containing 96 nozzles with 50 μm diameter. The nozzle size controls the accessible length scale of the 3D printer and plays a determinant role in the scale of the assemblies.

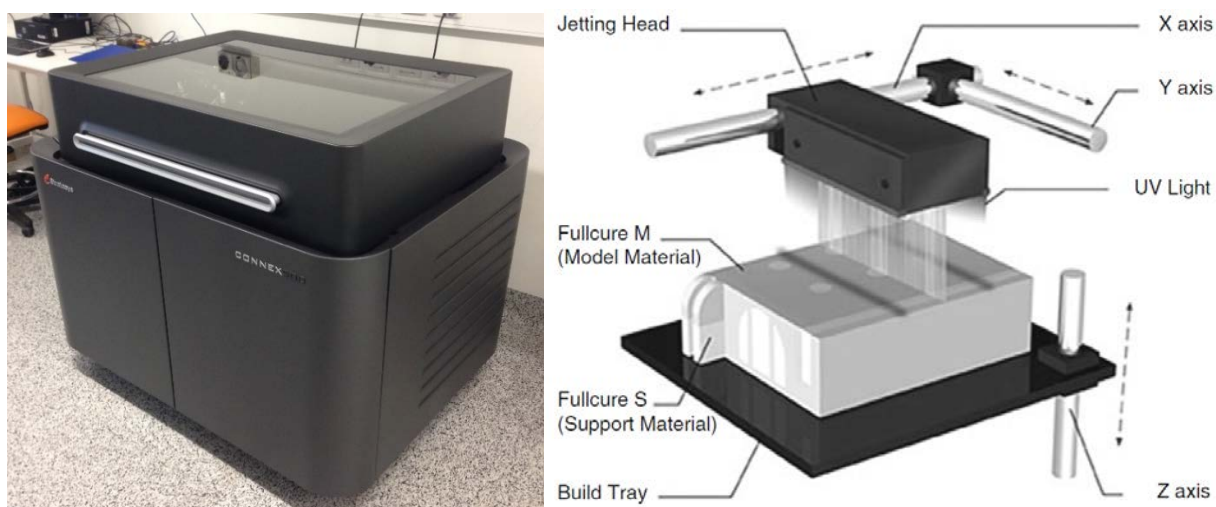


Figure 3.2 - a) Connex500 used for fabrication of experimental specimens. b) Schematic of polymer jetting process used by Connex500 [112]

Significantly, this technology is capable of combining rigid and rubbery polymers *in situ*, allowing for control of mechanical properties by mixing these polymers in various proportions. Two polymers in particular, VeroWhitePlus (VW+) and TangoBlackPlus (TB+), represent the two ends of the polymer spectrum and act as the two primary base materials for this work. VW+ is a white, stiff/rigid polymer and TB+ is a black, soft rubber-like polymer. By using this technology, it is possible to manufacture parts composed of two very different base materials with near perfect interfaces, as well as combining the two in different ratios to create 12 “Digital Materials” (DMs). The widely differing values of the elastic modulus between these two materials makes them convenient candidates for synthesis of nacre-like composites amongst other things. Indeed, these materials and the device used to print them has been employed in a number of studies [16, 79, 119, 121, 130] of the mechanical response of architected materials [117] due to its ability to print complex, high-resolution specimens. Furthermore, the polymer jetting technique and the subsequent high resolution of the Connex500, reduces the amount of anisotropy observed in these 3D printed materials, when compared to other 3D printing techniques, such as Fused Deposition Modelling (FDM). [111]

3.3 Materials

A number of key properties were characterised for these base polymeric materials. In each case, specimens were specifically designed and manufactured as necessary for the undertaken testing. The aim for this testing was to achieve a basic characterisation of the constituent material as well as act as input for numerical simulations, specifically the elastic modulus.

3.3.1 Hardness

Hardness testing involved the use of a type A Shore Durometer indentation on TB+ and 6 of the softer DMs in accordance with ASTM D2240. These values were then converted to give an approximation for Elastic Modulus (MPa) given by the following equation [131];

$$E = \frac{0.0981 (56 + 7.62336 S)}{0.137505 (254 - 2.54 S)} \quad (3.2)$$

where E is the Elastic Modulus in MPa and S is type A Shore hardness.

Table 3.1 shows the average type A Shore hardness values for TB+ and the six rubber-like DMs. Young's modulus approximations are also shown, which are based upon the hardness values as calculated using Equation 3.1. The hardness results agree well with the supplier values, as given by the last two numbers in the material name, while the value of Young's modulus shows reasonable agreement with data obtained from tensile testing.

Table 3.1 - Shore hardness type A values with Young's modulus approximations. Note the last two numbers of the material code refers to the supplier value for Shore Hardness (Type A).

Material	Shore Hardness (Type A)	Young's Modulus (MPa)
9895	88	17.22
9885	81	10.08
9870	71	5.85
9860	61	3.80
9850	49	2.39
9840	41	1.77
TB+	30	1.15

3.3.2 Mechanical Properties

Tensile testing of VW+, TB+ and 6 DMs was conducted in accordance with ASTM D638 for tensile testing of polymeric samples. All testing was conducted under quasi-static loading using an Instron 4505 Universal Testing Machine with a 5 kN static load cell. Tensile properties were established for VW+, TB+ and six DMs. The key mechanical property was

the elastic modulus, Figure 3.3, however the yield strength ($\sigma_y = 33.3 \pm 0.5$ MPa) and the hardening and plastic behaviour were also important for simulations involving VW+, Figure 3.4.

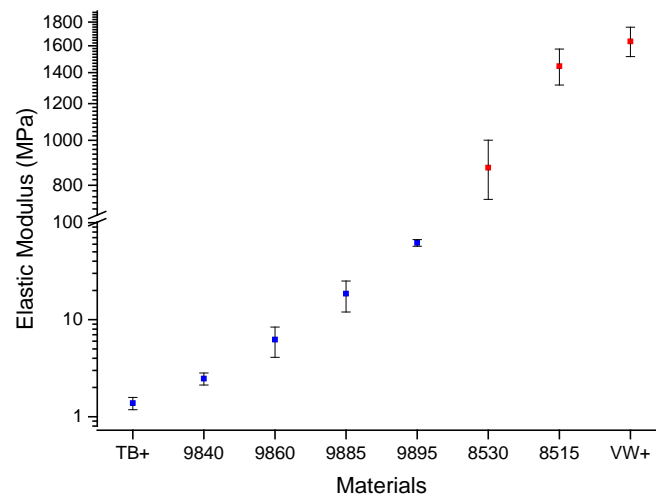


Figure 3.3 - Plot of elastic modulus obtained from tensile testing of the various printed materials. Rubber-like samples shown in blue, rigid shown in red

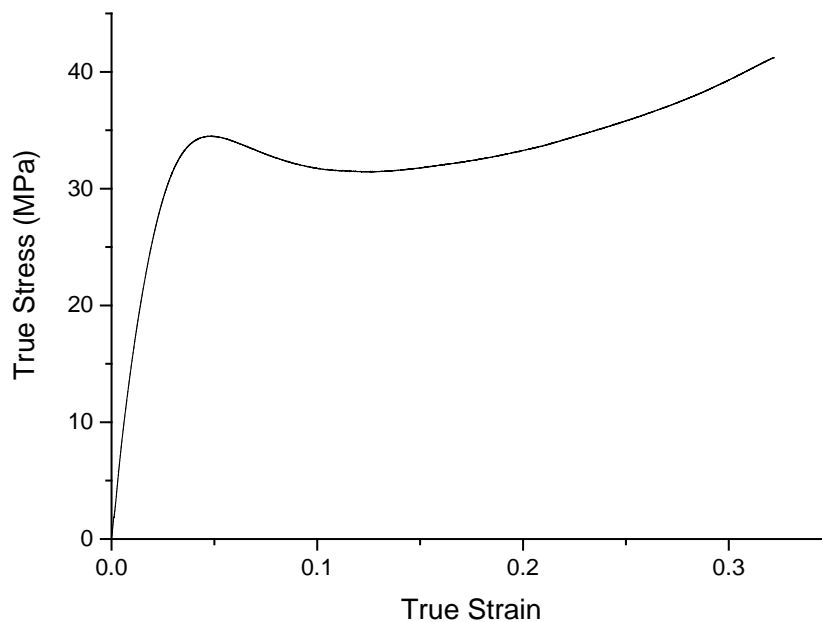


Figure 3.4 - Representative true stress-strain curve of VW+ under uniaxial tension

3.3.3 Thermal Properties

DMTA was utilised to assess the glass transition temperature (T_g) of VW+ and TB+ to assess any potential to create interesting structures based upon temperature changes. Using a Perkin Elmer DMA 8000, samples ($17.5 \times 9.5 \times 2 \text{ mm}^3$) were printed and tested between -70 to 180°C at a ramp rate of 3°C/min using dual cantilever bending deformation. The values for T_g (°C) measured using DMTA for VW+ and TB+ were 73.07 ± 1.62 and 10.55 ± 0.49 , respectively, Figure 3.5. It can be expected that the T_g values for 12 DMs will fall into a range between these two values.

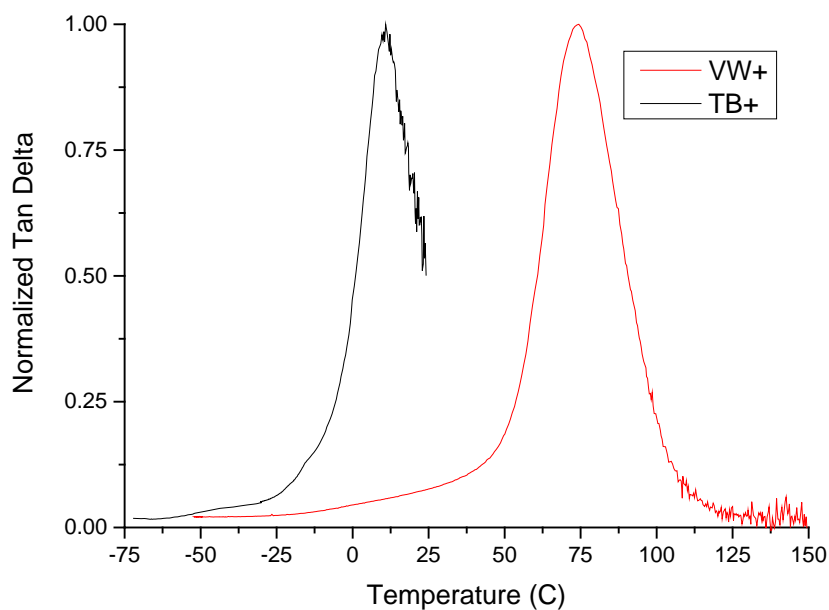


Figure 3.5 - Normalized tan delta plots for TB+ and VW+ highlighting difference in T_g

3.4 Mechanical Testing

There were two primary methods for mechanical testing used in this work. The first involved quasi-static, concentrated out-of-plane loading to cause failure of the various plate assemblies, designed to highlight the load bearing capacity in the normal direction of these assemblies. The examples of such potential applications include body armour, impact road barriers and semi-permanent constructions. The second method of mechanical testing was single edged notched tensile (Mode I) to demonstrate the fracture resistance of multi-material structures, in potential applications where fracture resistance and high tensile strength are key objectives, such as structural aerospace composites.

3.4.1 Out-of-plane point loading

Point loading was applied perpendicular to the plate via a rounded steel indenter 7mm in diameter attached to a 5kN static load cell in an Instron 4505 testing machine at a constant deformation rate of 4mm/min.

The plate was held in a c'-shaped steel frame with adjustable screw-driven boundaries to apply variable lateral pre-load to the plates as measured with a Mark-10 MR02-500 force sensor, as shown in Figure 3.6 a).

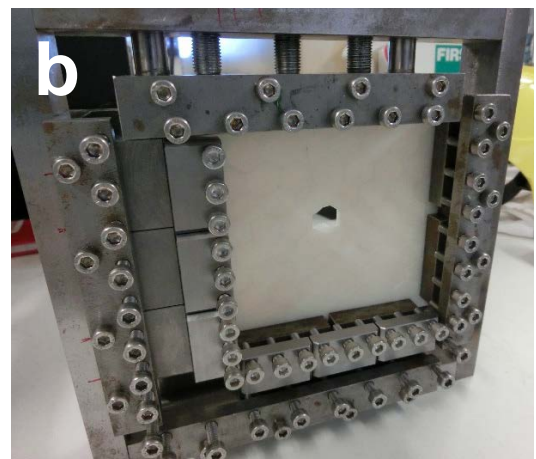


Figure 3.6 – a) Mechanical test set-up for osteomorphic assembly, with indenter and force sensors shown. Indenter moves down through the assembly to apply a concentrated point

load to the centre of the assembly, b) Post-failure specimen with steel inserts shown for variable sized assemblies

The reference assembly contained blocks with dimensions of 20 x 20 x 10 mm³ and a plate assembly span of 160 x 150 mm². Variable assembly and block sizes were accommodated by manufacturing steel inserts of varying dimensions to allow for smaller blocks and spans, as shown in Figure 3.6 b). Solid plates of the base material were also tested in this configuration and are presented within the respective results chapters.

3.4.2 *Mode I tensile*

Mode I tensile testing was conducted in Chapter 6. These single and multi-material samples were monolithic, continuous hybrid specimens in the form of flat panels which were printed with the soft phase comprising approximately 13.5% by volume, with an in-plane thickness of 250 µm. The dimensions of the samples were 64.75 mm x 58.5 mm and 3.125 mm in thickness. The specimens were fabricated with 10 blocks along the tensile direction and 24 blocks across.



Figure 3.7 – Image of basic mechanical testing set up for Mode I single edge notched tensile testing. Grips are shown in black at the top and bottom of the image, moving up and down, respectively, to impart a tensile load on the hybrid samples

The samples were printed with notches (9.745 mm by 0.79 mm), without the need for additional cutting prior to testing. Failure of the samples always occurred at the notch tip, which indicated that the printed notches were sufficiently sharp. The specimens were loaded in an Instron 4505 testing machine with a 20 kN static load cell. The samples were printed with specifically designed “knurled” VW+ sections at either end of the architected sample region. The size and shape of these knurled sections were intended to minimise slippage with the machine’s grips when applying the tensile load. Testing was conducted with 3 mm/min displacement rate. It is important to note that these testing conditions did not follow any established standard. While the apparatus was designed to impart uniaxial tensile forces to the specimens, as the crack propagated, non-uniformity of load occurred, leading to an induced torque when the force was applied to the uncracked region of a specimen.

3.5 Numerical Modelling

FEA was undertaken to investigate the mechanical behaviour of the assemblies and to gain an insight into the mechanisms involved for both the out-of-plane concentrated point loading and the mode I tensile testing. A detailed description of the model is given in Sections 4.3, 5.2 and 6.2. A general overview introducing the essential aspects of modelling to be considered in the aforementioned sections is provided below.

The implemented model of the two testing modes was very similar (ie. variables and parameters) with any minor differences noted in Chapter 6. The workflow enabled to achieve this involved importing CAD models from SolidWorks into ABAQUS/CAE and finite element models were created. This set up was modified the hierarchical interlocking study undertaken in Chapter 5, due to the highly complex geometry. In this case, the CAD models were exported from Rhinoceros 3D into HyperMesh (part of the HyperWorks suite, Altair Engineering, Inc.). Computational work was undertaken utilising commercial ABAQUS/Explicit v6.14 Finite Element Analysis (FEA) software. The Explicit solver was employed due to its ability to deliver a convergent solution for highly nonlinear systems with many complex surface interactions under transient loads. The specific details of the simulations, such as the mesh selection, convergence studies, material model, friction etc., are provided in Sections 4.3, 5.2 and **Error! Reference source not found..**

3.6 Artificial Neural Network

Neural network modelling in Chapter 4 was implemented utilising commercially-available JMP statistical software (part of SAS). Two neural networks were developed with one hidden layer as part of the structure. The number of hidden nodes was varied and the number which maximised the R^2 value selected. This was found to occur when the number of hidden nodes was equal to the number of input nodes. A simple holdback method was used to train and validate the model, whereby two thirds of the data is selected at random to train the model and the final third is used to validate the accuracy of the model. The size of each dataset (training and validation) was varied and until the optimized R^2 value for all datasets was reached. The input data from ABAQUS was fed into the hidden nodes, containing a sigmoid

function, in this case, hyperbolic tanh function. The outcome of these functions at each hidden node was then weighted and summed to determine the output.

3.7 Summary

The methodology for the research in this thesis has been provided in this chapter, outlining the materials, process and methods, both experimental and computational, utilised within the body of work. This includes the material properties, mechanical testing, FE implementation and neural network techniques used across all the results chapter.

4. Characterisation of the mechanical behaviour of non-planar topological interlocking blocks within planar assemblies

4.1 Introduction

The concept of topological interlocking materials [81] has emerged as a promising class of architected or hybrid material [132] to meet unique materials design challenges. One of the obstacles facing the utilisation of topological interlocking assemblies is understanding, controlling and predicting the mechanical response of assemblies with varying parameters. When applying topological interlocking materials to a desired application, certain design variables may be constrained (such as the size or constituent material), and modifications to other parameters are required to meet the objective specifications. Indeed, understanding how the mechanical response changes with variables such as elastic modulus, friction and boundary loading conditions has already been the focus of some research in related systems [13]. Further parameters, such as size and scale have also been identified elsewhere as critical variables which effect the mechanical performance of topological interlocking assemblies [14, 15]. However, the development of broad, quantitative relationships between these variables is still lacking. Such trends are critical in developing and designing topological interlocking assemblies for application in the future.

This chapter presents computational and experimental results outlining the behaviour of non-planar topological interlocking blocks in planar assemblies, when a concentrated out-of-plane point loading is applied. This work will investigate multiple variables known to affect the mechanical response of these assemblies and look to combine these trends to understand behaviour and guide future development and design of these structures. In

particular, exploring the effect of the elastic modulus of the constituent material, the friction between blocks and the boundary conditions including fixed and pre-loaded lateral constraints of the global assembly, will all be investigated. Further work will also be presented investigating the effect of size and scale on non-planar topological interlocking planar assemblies. In particular, variations in the size of individual blocks (t) and overall assembly size (s), as well as scale (that is, assemblies with a constant ratio of block size to assembly size (s/t)), will be studied.

The results and analysis of this chapter are set out in the following manner. Firstly, the development and validation of the finite element model is presented. Following this, each of the three assembly variables: 1) elastic modulus, 2) friction and 3) boundary conditions are presented, analysed, and compared and contrasted with previous work [13-15] to determine relationships and trends relating these variables to the mechanical behaviour of the topological interlocking assemblies. Subsequently, the results of the effects of each of the size and scale variables will be presented as follows: a) of the effect of variable block size (t) where assembly size (s) is constant; b) of the effect of variable assembly size (s) where block size (t) is constant; c) of the effect of scale or variable s and t where s/t is constant.

The properties used to compare the overall load-deflection response will include, the stiffness (K), peak force (F_P), deflection to peak load (δ_P) and failure (δ_f). A final results section combines these variables using an Artificial Neural Network (ANN) to establish overall relationships governing the mechanical response of topological interlocking planar assemblies under point loading. Analysis and discussion of the mechanisms will follow.

4.2 Study Design and Setup

The primary tools used to develop the modelling results was finite element analysis, as described in Chapter 3. These results are compared with experimental outcomes from testing additively manufactured assemblies. The aim of the experimental testing was two-fold: firstly, to validate the reference assembly as described below, and secondly, to

demonstrate reasonable *qualitative* agreement between the simulation and experimental results.

The goal of the modelling was to enable a broader representation of the topological interlocking effect, and as such was slightly simplified when compared to the experimental results. For instance, the simulations do not account for certain effects, such as damage or plasticity. These effects would make it more difficult to decouple the effects of the variables being investigated and will also increase significantly the computation time. The aim of this work is to develop a broader guide to the design of topological interlocking assemblies beyond the applied example of the experiments, while still capturing the key mechanics and providing reasonable quantitative representation.

As a result, this provides a valuable insight into the mechanisms of these structures under loading. Indeed, the range of variables was chosen to determine the effects of a broad range of these parameters, even if their values in proximity of the upper and lower limits of these ranges are not allowed physically (e.g. a 10kN lateral force would damage or deform the assemblies made from a material with $E = 1.7$ GPa; or a coefficient of friction greater than 1 etc.). However, looking at the effects of setting values to these limits is useful for a number of reasons as it helps to highlight the extreme effect these parameters may have on the mechanical response of these assemblies.

The reference assembly properties are outlined in Chapter 3, but the key input parameters across all the studies given here are:

Table 4.1 – Reference assembly numerical input parameters

Input Parameter	Reference Value
Elastic modulus (E)	1.7 GPa
Lateral pre-load (F_L)	1 kN
Coefficient of friction (μ)	0.3
Block size (thickness)	20 x 20 x 10 mm (thickness (t) = 10 mm)
Assembly size (span)	160 x 150 mm (span (s) = 150 mm)

Characterisation of the mechanical behaviour of non-planar topological interlocking blocks within planar assemblies

The three “assembly” variables (elastic modulus, lateral pre-load and coefficient of friction) are each varied independently, with the reference assembly being common across all ranges. Numerical modifications to the elastic modulus and friction were applied by varying the single material and interaction variables, as shown in Figure 4.1 and described further in Chapter 3.

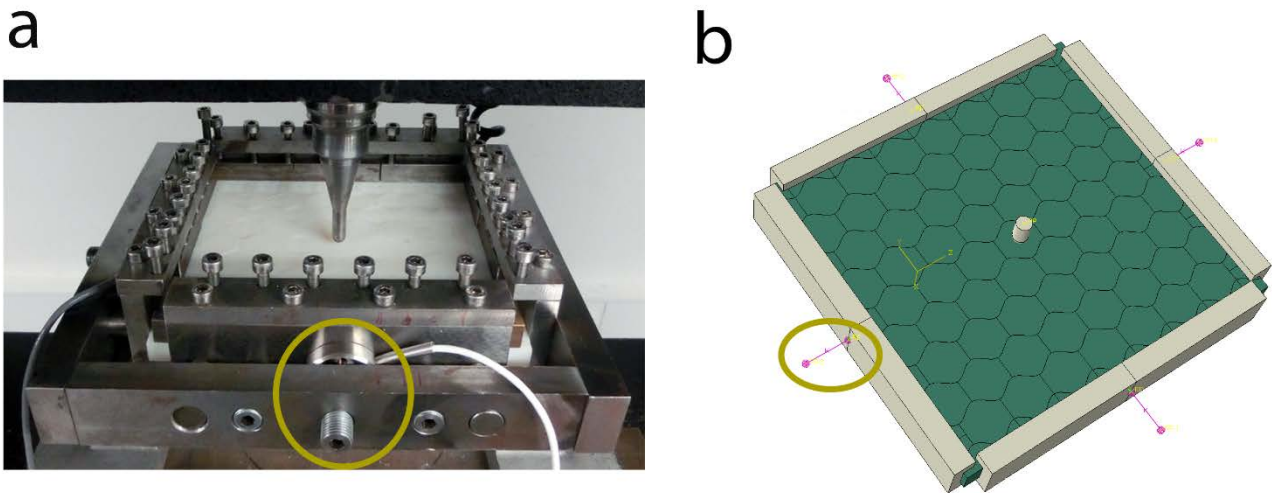


Figure 4.1 - Schematic of assembly studies in Chapter 4, a) experimental and b) computational. – 1) elastic modulus: a) modified material, b) changes to elastic modulus of green bodies 2) boundary condition: a) lateral pre-load controlled by screws, measured by force sensors, b) modified spring constants highlighted in pink 3) friction: b) modified penalty coefficient of friction between blocks

The test matrix of assembly systems to study is shown in Figure 4.2. A range of five assemblies were chosen for each study, with a 50% increase in size from the lowest to the highest bounds. For instance, the thickness was varied from $t = 8\text{mm}$ to $t = 12\text{mm}$ and the span was varied from $s = 120\text{mm}$ to $s = 180\text{mm}$ (see Figure 4.2). The reference assembly is shown in the red box in Figure 4.2 with the three various size case studies shown in a, b and c.

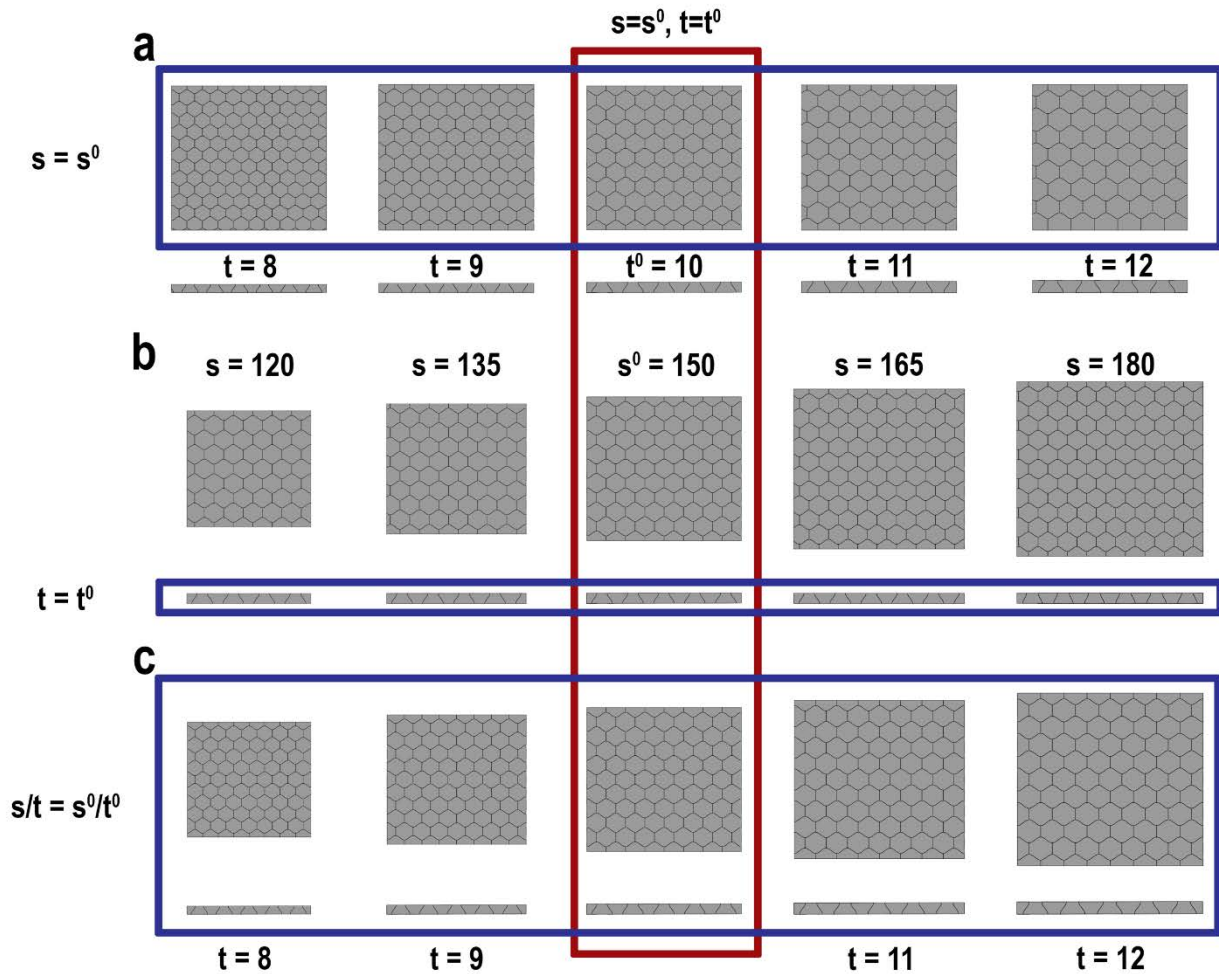


Figure 4.2 - Schematic of size and scale studies in chapter 4, a) variable block size (t) with constant assembly size (s), b) variable assembly size (s) with constant block size (t), c) variable block size (t) and assembly size (s) with constant size ratio (s/t). The red box indicates the constant reference assembly. t is given as the block thickness and s defines the length or span of the assembly. Values are given in mm

In order to compare the effects of multiple parameters being varied, an Artificial Neural Network (ANN) approach was employed. This technique provides a useful, graphical way to compare and visualise multiple inputs and outputs. Further details regarding this model is given in Sections 2.5, 3.6 and 4.4.4.

4.3 Finite Element Model Development and Validation

The general approach to modelling the mechanical assemblies is outlined in Chapter 3, however more specific details applicable to this work are provided below.

4.3.1 *Software Environment*

The assemblies modelled posed a challenge as they have translational and rotational degrees of freedom, as well as multiple complex interfaces with changing contact conditions. In this work, ABAQUS/Explicit software is selected due to availability of a general contact algorithm, implemented as a penalty method (a stiffness-based approach), allowing for an automatic determination of contact surfaces and as such constitutes an ideal tool for this analysis.

4.3.2 *Quasi-static Modelling*

The assemblies were assumed to be under quasi-static loading conditions. For the out-of-plane concentrated point testing, loading was simulated by displacing the indenter considered as a rigid body and force measurements were taken as reaction forces from the top node of the indenter and central side nodes of the frames. The point indenter and the frame were modelled as rigid bodies to which external loads were applied. Spring elements were introduced to model the compliance external frame (Section 4.3.6), while for the point indenter, a smooth step displacement (Figure 4.3) was applied to the top of the indenter. A smooth step was selected to minimise any inertial effects related to the explicit nature of the solver.

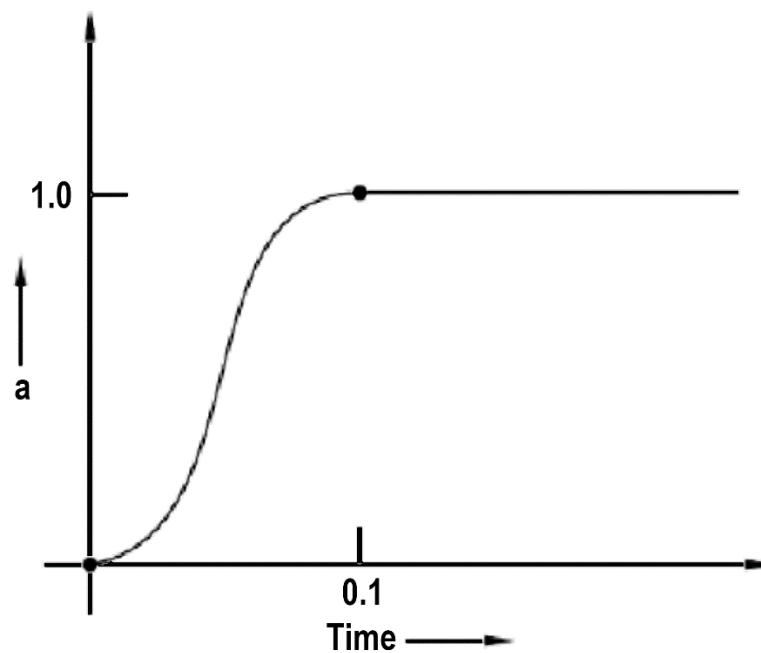


Figure 4.3 – An example of a smooth step amplitude used for applying displacement in the model. The numbers given here are indicative only [133]

Since ABAQUS/Explicit is designed for solution of dynamic process, a careful selection of the time increment and the total time of the simulation is required. In order to obtain a valid solution in the quasi-static simulations, the time step was reduced artificially. The problem with this approach was that if the simulation speed is increased too much, inertial forces may falsify the predicted response. To evaluate this effect, the time step was incrementally reduced until the results began to diverge and become unrepresentative. The time step chosen was thus the smallest time step prior to divergence. The ratio of the kinetic energy to the internal energy for the shortest time increment providing accurate results was then calculated to ascertain that the kinetic energy was sufficiently small, as defined by ABAQUS as less than 1% of the internal energy [133]. The ratio of kinetic to internal energy vs time is plotted in Figure 4.4, demonstrating this ratio is below 1% for the duration of the simulation. A loading time of 0.1 seconds in the simulations was found to be adequate. The final displacement of the indenter was set at 25 mm (corresponding to experimental results) which set the rate of loading.

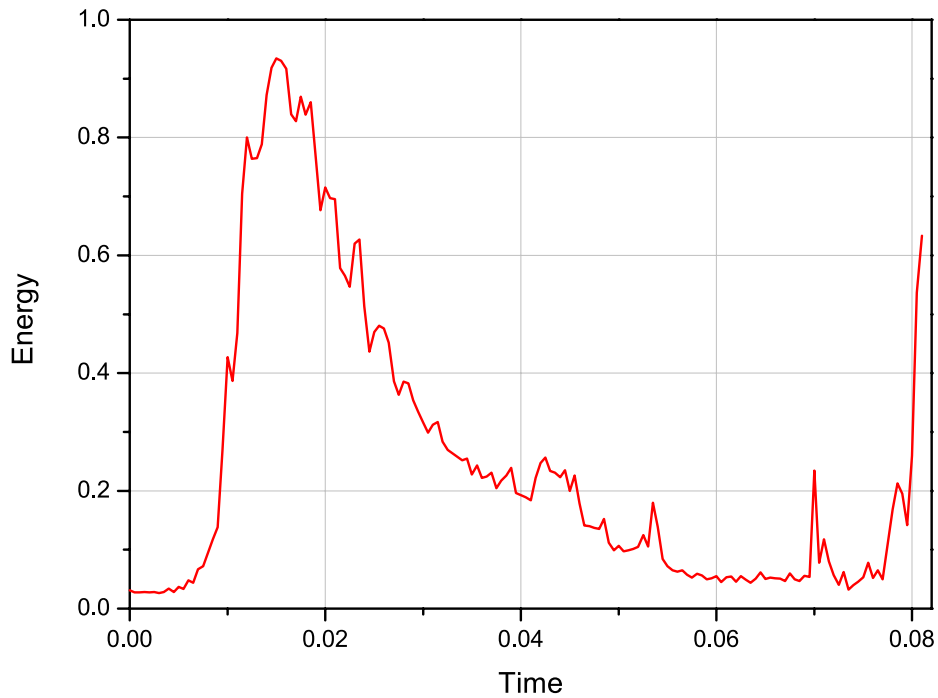


Figure 4.4 – Plot of the ratio of kinetic energy to internal energy vs time. Note that block removal occur at time = 0.082. Ratio is less than 1% throughout time period

4.3.3 Material Properties

The reference assembly was defined as an isotropic linear elastic material with values for Young's modulus ($E = 1700$ MPa), Poisson's ratio ($\nu = 0.39$), and density ($\rho = 1.17$ g/cm³). These values are taken from a combination of the VW+ material supplier (Stratasys Ltd.), experimental results (Section 3.3) and from previous literature [117].

4.3.4 Interaction

The contact between interlocking blocks is modelled using a general contact algorithm which utilised a penalty method (a stiffness-based approach). The main input parameter for this model is a tangential friction coefficient of μ . This value was determined experimentally using

a Nanovea Tribometer T50 by rotative wear friction, involving a small ball on substrate, both of which were VW+. A range of testing parameters were used to gain an average value. These parameters included a load of 1-2 N, a radius of 6-12 mm, a speed of 1000 – 1400 mm/min and a sliding distance of 10 – 30 m. A value of $\mu = 0.3 \pm 0.01$ was found to be representative for the initial value for the coefficient of friction.

4.3.5 *Mesh*

Convergence studies were carried out for mesh sizing to determine the necessary element size. Sufficient mesh density was necessary to accurately represent the stresses throughout the block and to represent the shape of the block with adequate resolution. $20 \times 20 \times 10 \text{ mm}^3$ blocks with 1280, 2800, 4032, 8064 and 12082 quad elements per osteomorphic block were tested for convergence of the load-displacement curves for the reference assembly. It was determined that the results converged for a mesh with 2800 elements. However, 4032 quad elements per osteomorphic block were selected, as within this work, blocks of varying size and geometry were to be used (including smaller blocks). The C3D8R quad element was selected in ABAQUS which is a reduced integration element utilising a linear stress field. It was selected to reduce computation time, with some reduction in accuracy, which is offset by the increased number of elements. The mesh size was kept consistent across these variations and as such, a larger number of elements were selected to ensure a representative result across all block types.

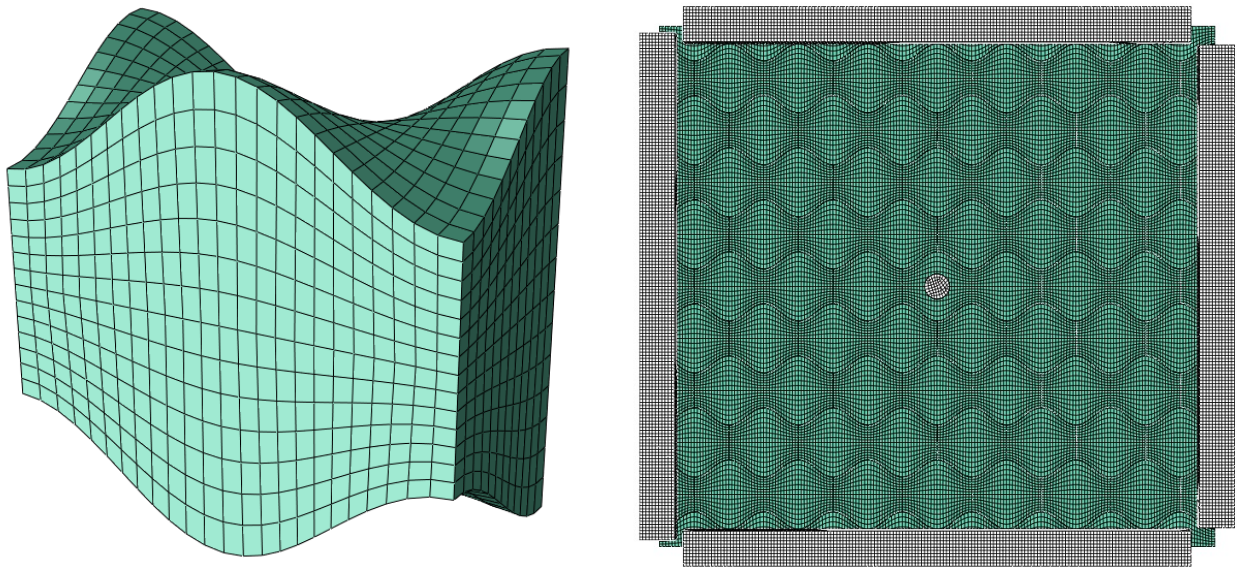


Figure 4.5 – Uniform quad meshing utilised in ABAQUS for reference osteomorphic assembly

4.3.6 Boundary Conditions

The frame and indenter were modelled as rigid bodies with rigid elements provided by ABAQUS. However, the need to accurately model the pre-load of the reference assembly ($F_L = 1\text{kN}$) and associated elastic compliance of the steel frame and screws is not captured by a simple rigid body feature. This was achieved through the use of a single spring element attached to the centre of each of the rigid frame bodies, Figure 4.6.

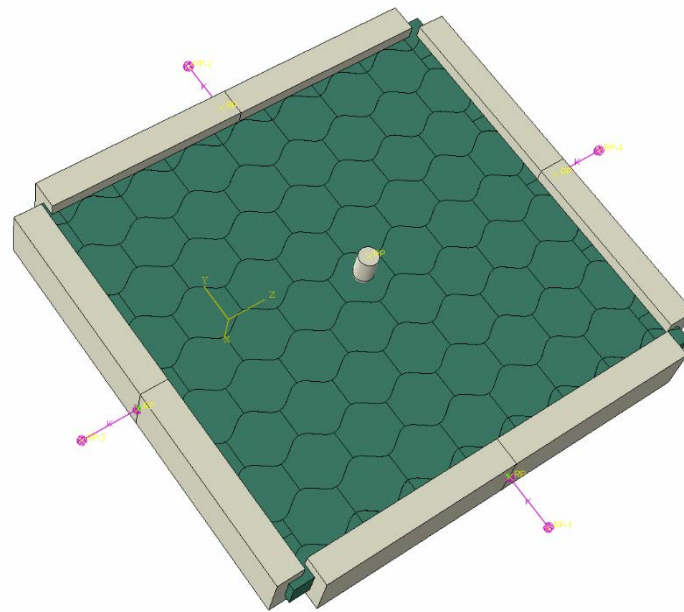


Figure 4.6 - Simulation set up showing a planar block assembly, indenter, frame and idealised elastic springs

The primary fitting parameters were related to the boundary conditions of the assembly. A single spring attached to the centre of each of the rigid frame bodies (Figure 4.1b) was used to model the assembly pre-load and associated elastic compliance of the steel frame and screws (Figure 4.1a).

The spring resisted normal displacement of each edge of the boundary that was the only degree of freedom permitted by the boundary constraints. The lateral pre-load of the experimental set-up was reproduced by displacing the outer spring nodes, therefore the associated parameters, spring stiffness (κ) and spring displacement (δ_s), were treated as fitting parameters, the only ones within the model. These parameters thus become crucial in determining the mechanical response of the assembly.

A similar method whereby the spring element was displaced to apply lateral pre-load has been previously reported by Schaare et al. [86]. However, a slight modification to his method was necessary, due to a definition requirement by a newer version of the ABAQUS software used in this work, to define an inertia for rigid bodies within the explicit solver environment. As such a convergence study, determined a sufficiently small inertia which would not affect

the impact of the spring force applied to the assembly. This was found to occur at 10^{-3} (value relative to density), as shown in Figure 4.7.

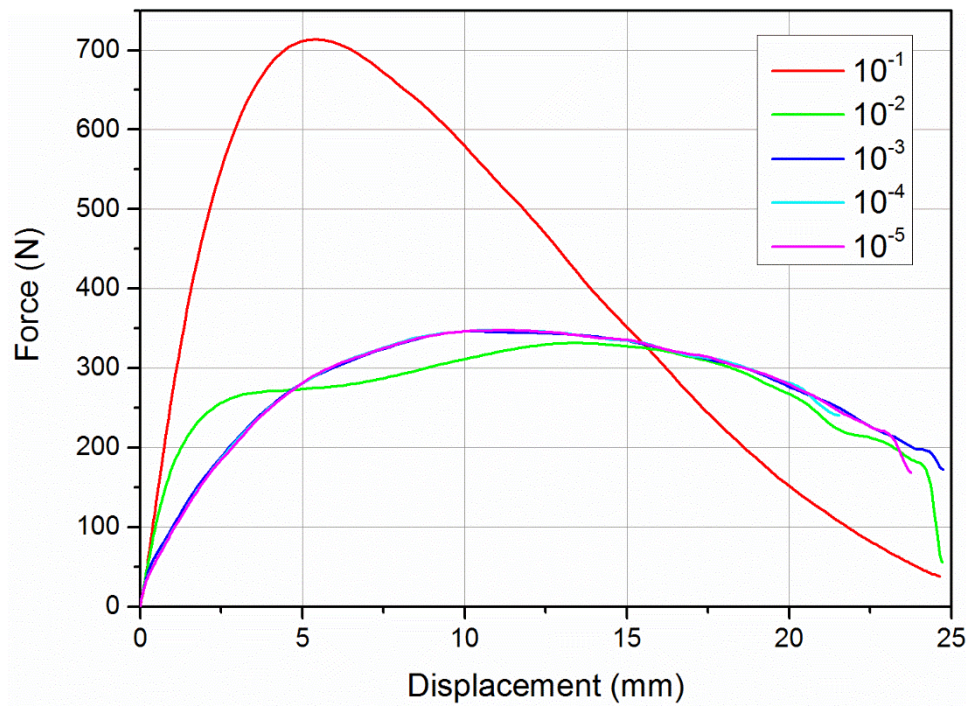


Figure 4.7 - Plot of force (N) v displacement (mm) as a function frame inertia for the reference assembly. Inertia values are relative to the material density

The only fitting parameters remaining were the spring stiffness and spring displacement, as such a study to determine the best fit for the reference assembly was conducted. This was achieved by varying both parameters independently through a range from 0.1N to 100kN and 0.001 mm to 10 mm. The best fit was found for a spring stiffness of 2kN/mm and spring displacement of 0.05 mm. These comparison results are shown in Figure 4.8.

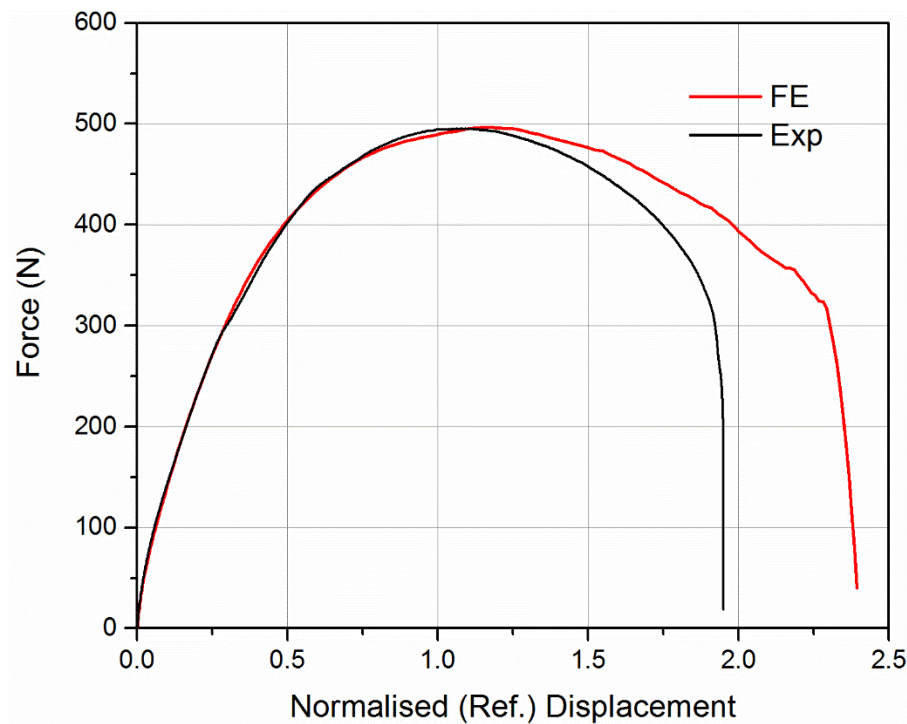


Figure 4.8 - Comparison of force(N) v displacement (mm) curves for experimental and simulation of the reference assembly

The fit is excellent up to the maximum load and then deviates due to the absence of the damage and plasticity models in the simulations. Plasticity and damage of the material of the blocks were not included in this simulation, however this is observed in experimental samples, Figure 4.9. It is therefore expected that the simulation results may diverge and over-predict the experimental results (Figure 4.8) when approaching the final failure of the assembly or upon complete block removal.

4.3.7 Validation

Primary fitting parameters used for fitting the experimental results are related to spring stiffness (κ) and spring displacement (δ_s). Once these parameters were obtained for the reference assembly, the parameters were used for all subsequent simulations.

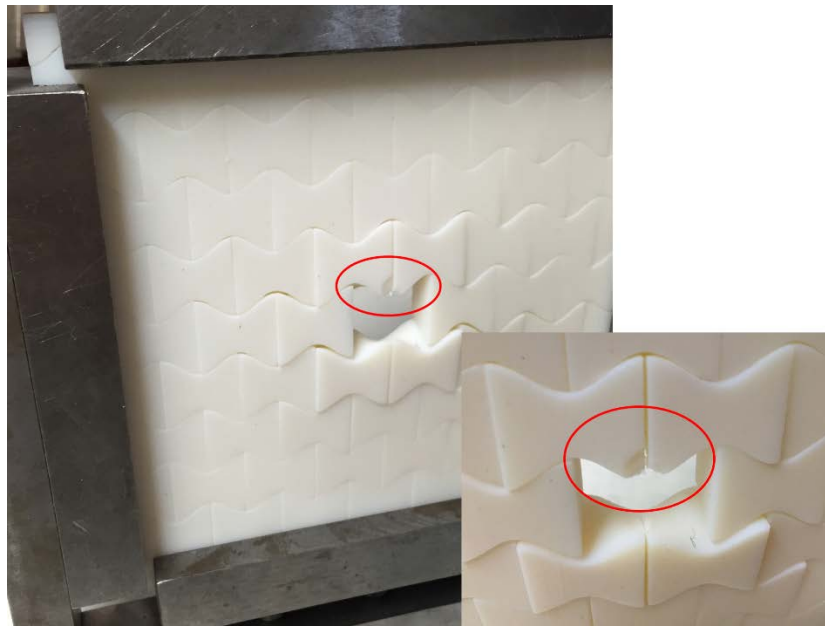


Figure 4.9 - Example of post-failure damage observed for mechanical testing of reference assembly

The validity of the proposed model was examined by simulating the assemblies with different mechanical properties (E) and varying the applied boundary conditions (κ). The results are shown in Figure 4.10. Good agreement between numerical and experimental results is observed. For instance, it can be seen that our model predicts well the behaviour of the assembly with decreased pre-load $F_L=0.5$. Modifications to the lateral load were implemented by linearly varying the spring stiffness constant (e.g. if the experimental lateral load was decreased by 50%, the spring stiffness constant also decreased by 50%). All other variables were kept constant. However, some deviation from experimental findings is observed and discussed further within the results section of this chapter.

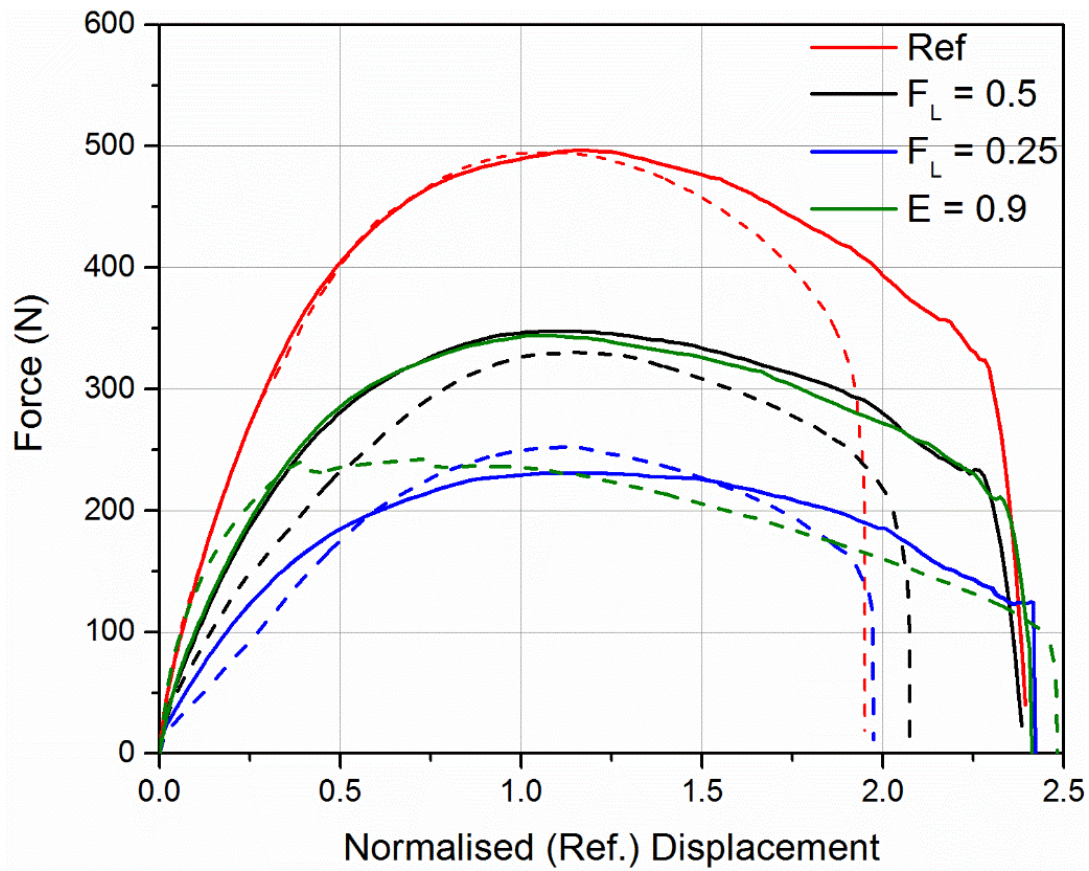


Figure 4.10 - FE validation of assembly variables. Experimental results shown with dashed lines. F_L denotes the value of the applied lateral load in N

Further validation was conducted by varying various size parameters, while keeping all other assembly variables constant. These results are shown in Figure 4.11. Once again, reasonable agreement is demonstrated, with further discussion presented below in this chapter.

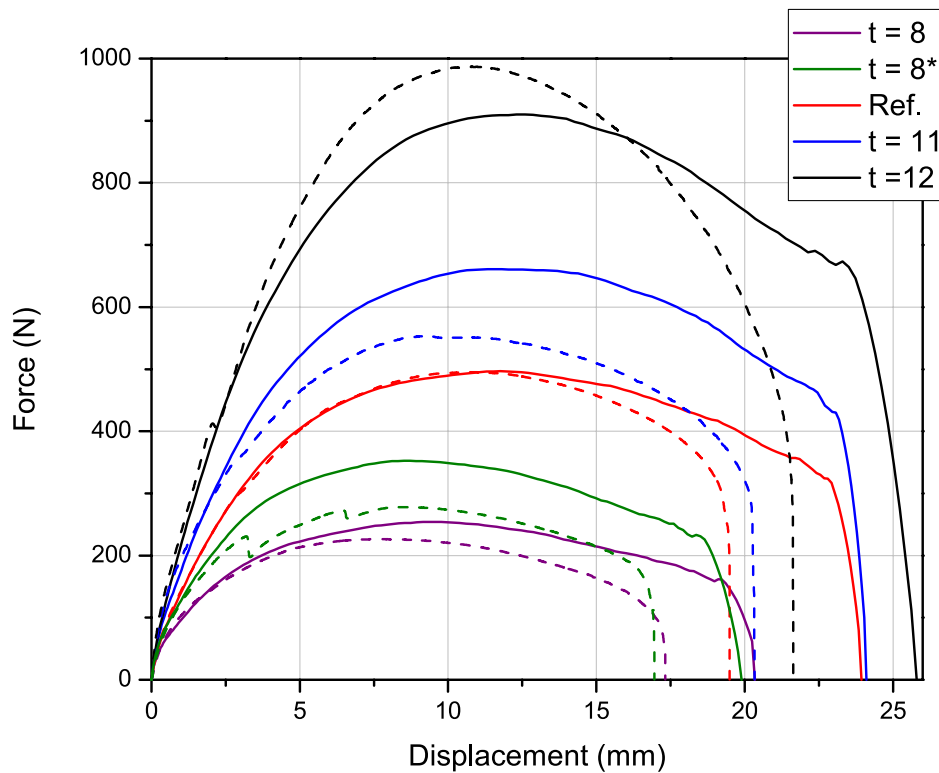


Figure 4.11 - FE validation of size parameters. Experimental results shown with dashed lines. t represents the thickness of a sample in mm

The observed agreement in results obtained in Chapter 5, with changes to geometry, provided further validation to this method.

4.4 Results

4.4.1 Assembly Parameters

4.4.1.1 Elastic Modulus

The first property investigated was the effect of elastic modulus of the blocks on the mechanical response. Figure 4.12 shows a plot of force vs normalised displacement for a

range of elastic moduli (0.9 – 200 GPa) where $\mu = 0.3$ and $F_L = 1\text{ kN}$. Increases in stiffness (K) and peak force (F_P) can be observed with increasing modulus, agreeing well with previous observations [13, 15] for different geometries. There is no noticeable change in δ_P and δ_f with elastic modulus. A reasonable agreement is observed with experimental results, with the low modulus (0.9GPa) specimen showing strong correspondence to approximately 0.35 normalised displacement, when divergence from the numerical results occurs. This is due to large plasticity effects of the softer experimental material, which leads to a decreased F_P , when compared to the idealised numerical results. As noted earlier, failure was observed to occur at lower normalised displacement (1.9 normalised displacement) in the experimental results of the reference assembly due to small amounts of damage (Figure 4.9). Overall, the shape of the curves remain similar as a function of elastic moduli, as indicated by the similarity of δ_P and δ_f .

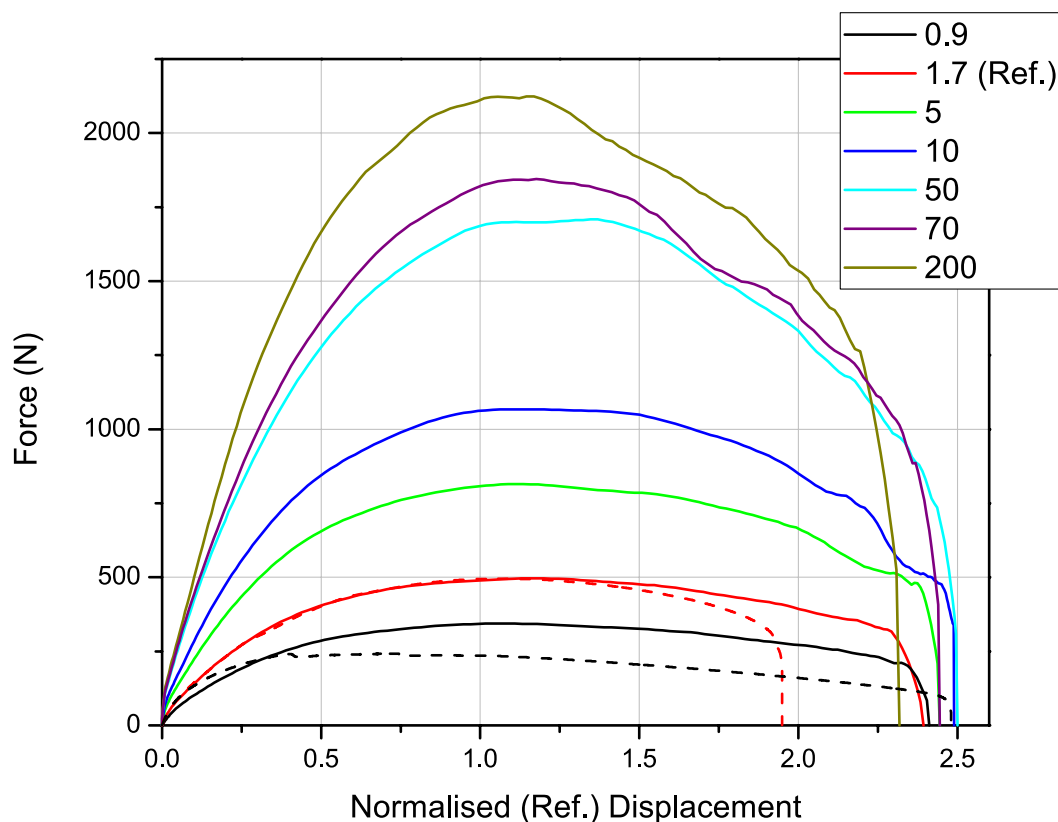


Figure 4.12 - Plot of force (N) vs displacement (normalised to reference t) for various elastic moduli (0.9 – 200 GPa) when $F_L = 1\text{ kN}$ and $\mu = 0.3$. Experimental results are shown with dotted lines

Characterisation of the mechanical behaviour of non-planar topological interlocking blocks within planar assemblies

These mechanical properties are plotted in Figure 4.13 against elastic modulus. Both K and F_P appear to follow a similar linear, logarithmic relationships with elastic modulus. These trends are strong ($R^2 = 0.994$) and is similar to the relationship described by Schaare [13] for cubic blocks, although a negative exponential and power law equation was used to fit that data. The deflection values, which are plotted as raw data (ie. mm), appear to be reasonably constant, with no clear trend in these values with elastic modulus. This is to be expected given that E is a property of the constituent material, with no changes to size or thickness.

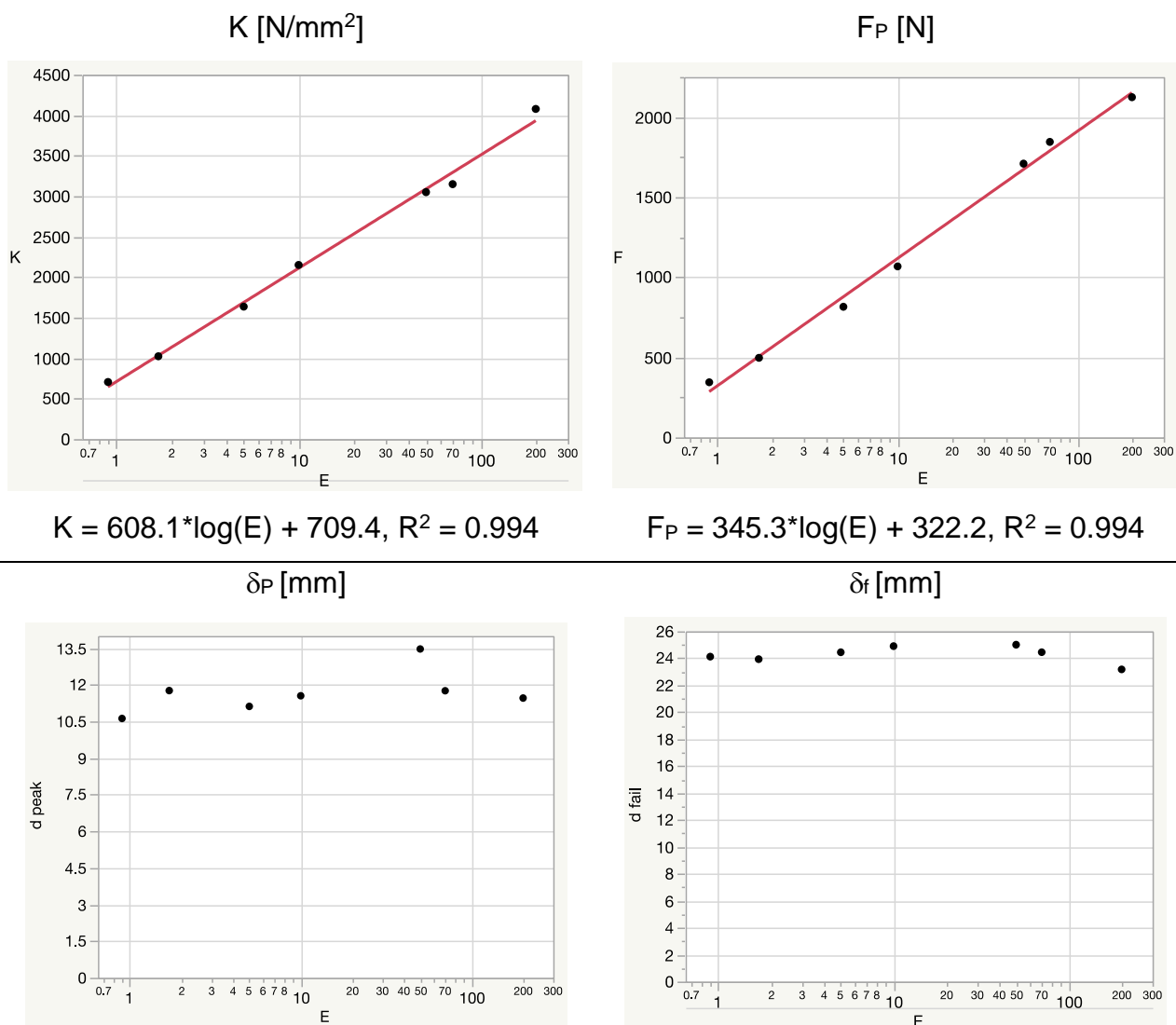


Figure 4.13 – Plots of mechanical properties for various moduli (GPa), including K (N/mm²), F_P (N), δ_P (mm), and δ_f (mm). $F_L = 1\text{ kN}$ and $\mu = 0.3$. A strong logarithmic trend is observed

for K and F_P , while no trend is observed for the two deflection values. E axis plotted on logarithmic scale

4.4.1.2 *Boundary Conditions*

The second property analysed was related to the boundary conditions of the planar assembly. The lateral force (F_L) was numerically-modified through a range of values (0.1 – 10 kN) and the resultant force-displacement curves were recorded in Figure 4.14 for assemblies where $E = 1.7\text{GPa}$ and $\mu = 0.3$. As with the results for elastic modulus, a clear increase in K and F_P with increasing F_L was observed. A fixed boundary condition specimen is also included in Figure 4.14, which shows a F_P approximately 20% larger than the system with a 10kN lateral load. At low normalised displacements (ie. $\delta < 0.2$), the fixed boundary condition has a lower load bearing capacity than the 10kN specimen, although for higher deformations the fixed sample has a higher response to loading. The fixed sample also shows a greater deflection to failure than the pre-loaded specimens.

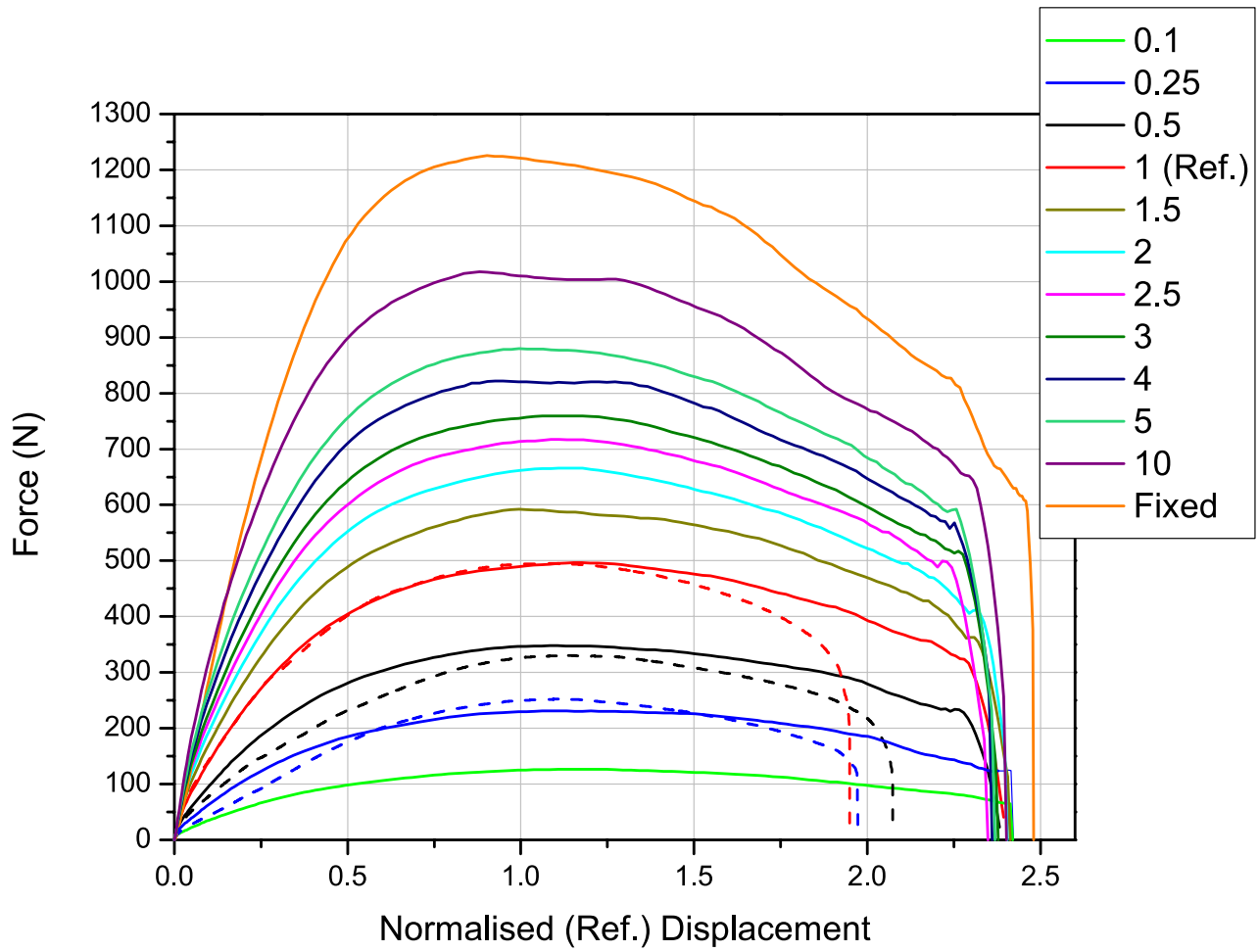


Figure 4.14 – Plot of force vs displacement (normalised to reference t) for various lateral forces (0.1 – 10 kN) when $E = 1.7$ GPa and $\mu = 0.3$. Experimental results shown with dotted lines

Mechanical properties were plotted for F_L between 0.1 – 10 kN. A strong positive relationship was found for both K and F_P (as shown, plotted on a logarithmic scale). A curve for both has been fit to describe the relationship showing a strong correlation between F_L , K and F_P . Schaare [13] found a similarly strong correlation for cubic structures and F_P investigated between 1 and 3 kN, however it was determined to be a linear relationship, likely due to the smaller variable range. In this study, a larger range reveals a deviation from a linear relationship at the lower and upper bounds indicating a non-linear relationship. Deflection to failure appears to be constant, while deflection to peak load shows a weak negative relationship with lateral force.

Characterisation of the mechanical behaviour of non-planar topological interlocking blocks within planar assemblies

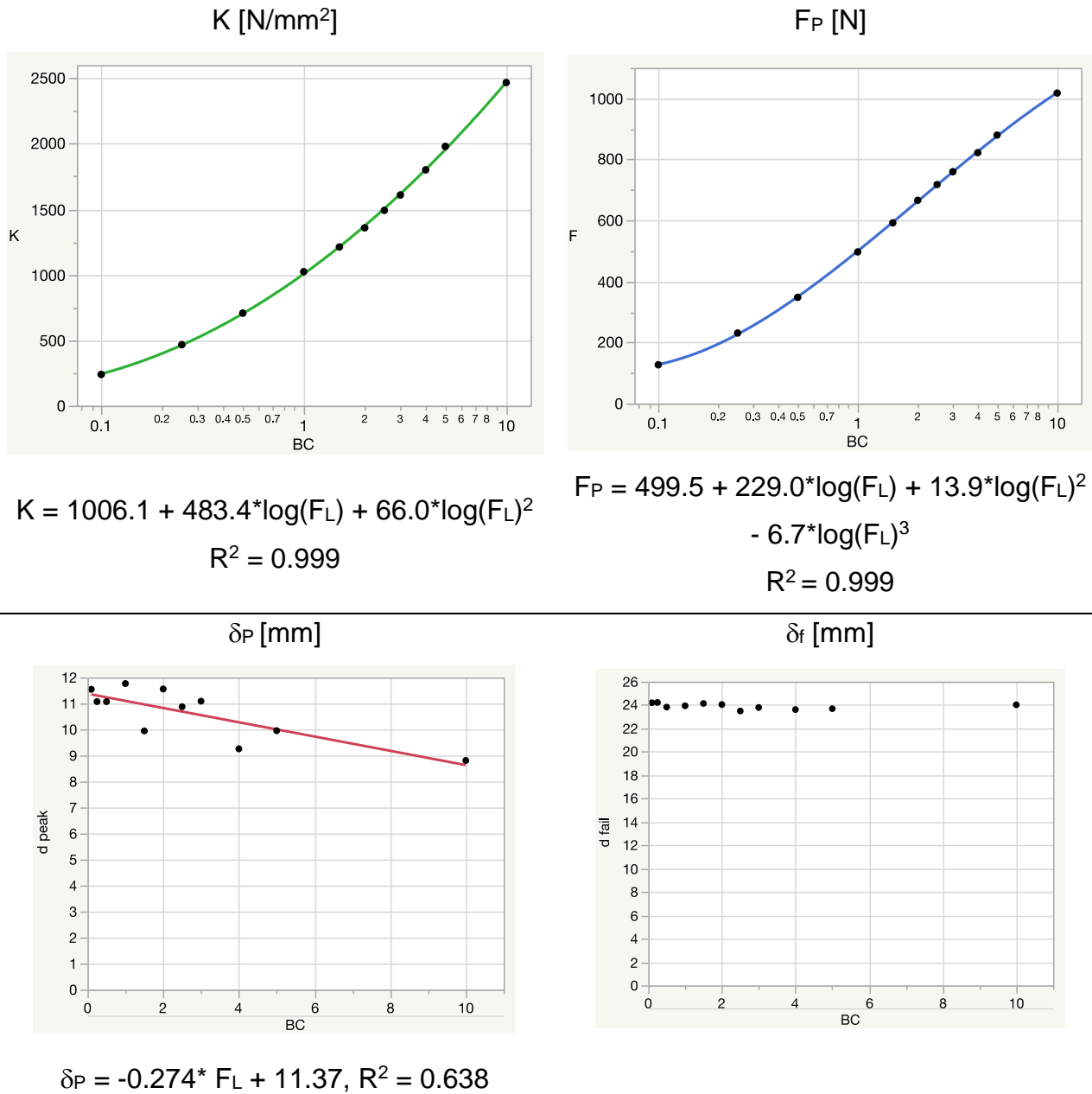


Figure 4.15 - Plots of mechanical properties for various lateral forces, including K (N/mm²), F_P (N), δ_P (mm) and δ_f (mm). $E = 1.7$ GPa and $\mu = 0.3$. A strong, positive logarithmic trend is observed for K and F_P , while the deflection values show a weak negative trend between lateral force and deflection to peak force and failure

4.4.1.3 Friction

The third variable investigated was the coefficient of friction. The force-displacement curves for a range of coefficients from 0.01 to a solid plate are shown in Figure 4.16. This plot shows the effect of friction through a very broad range of coefficients, including coefficients greater than those which can be physically achieved. Such high coefficients of friction simulations act as a point of reference for previous work by Khandelwal et al. [104] who used very high values to simplify his numerical model (remove the effect of friction) and validate their analytical model. Furthermore, these high values indicate the “common sense” validity of the simulations, as after the “elastic region” of the load-deflection curve (approximately 0 – 0.5 normalised displacement) the simulations breakdown and become physically non-representative due to their not allowing the blocks to slip. This is shown in simulations $\mu = 2 - 100$. Furthermore, the experimental and numerical results for a solid plate are also included in this plot, shown in black. These are a point of reference for the topological interlocking results to provide context. Further results, related to the solid, monolithic plate are discussed in Section 4.5

These results show that K and F_P increase with increasing μ , which agrees well with previous studies for a range of different materials and geometries [13, 15, 92, 98]. Additionally, these results also show that negligible changes in δ_f are observed outside of very low or very high friction values. Instead, the greatest change is observed in δ_P , where a clear increase is observed with increasing coefficient of friction. This broadly agrees with findings by Dugué [15] who studied cubic and modified osteomorphic blocks, but directly contradicts Feng et al. [92] who found the opposite to be true (ie. constant δ_P , increasing δ_f) for tetrahedral blocks under impact loading. This contradiction could be due to a number of differences in the studies, including loading method, boundary conditions or block geometry. Indeed, the potential for variations in block geometry to play a role in surface interaction is a conjecture which is investigated in Chapter 5.

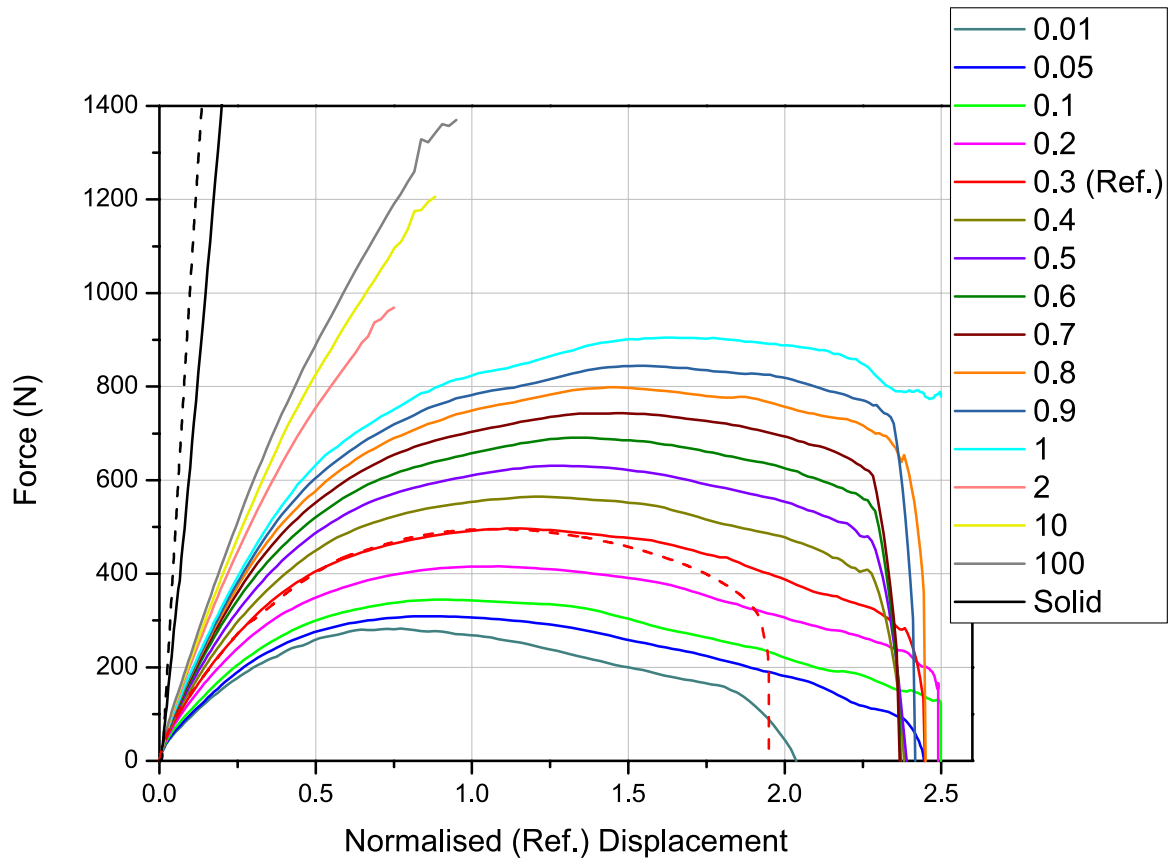


Figure 4.16 - Plot of force (N) vs displacement (normalised to reference t) for various coefficient of friction ($\mu = 0.01 - 100$), when $E = 1.7 \text{ GPa}$ and $F_L = 1 \text{ kN}$. Experimental results shown with dotted lines

The above discussion points are highlighted in Figure 4.17. Strong, positive, approximately linear trends are apparent for K , F_P and δ_P , while δ_f appears constant for values displayed up to $\mu = 2$. Trend lines have not been fitted in order to highlight the slight variations associated with the upper and lower bounds of the friction range. The F_P trend shows good agreement in the low range with studies by Schaare for cubic blocks [13], however divergence from a simple linear trend is clear in these results when the range is expanded outside of $\mu = 0.2 - 0.9$ range studied by Schaare. The strong increase in δ_P is also clear in the figure below. This change to the shape of the load-deflection curves results in a decreased softening region and a more sudden failure. Overall, the increase to stiffness, peak load and deflection to failure, as a consequence of the decreased ability for individual blocks to slide past one another, provides an interesting avenue to control the mechanical

Characterisation of the mechanical behaviour of non-planar topological interlocking blocks within planar assemblies

behaviour associated with topological interlocking – a topic investigated in greater detail in Chapter 5.

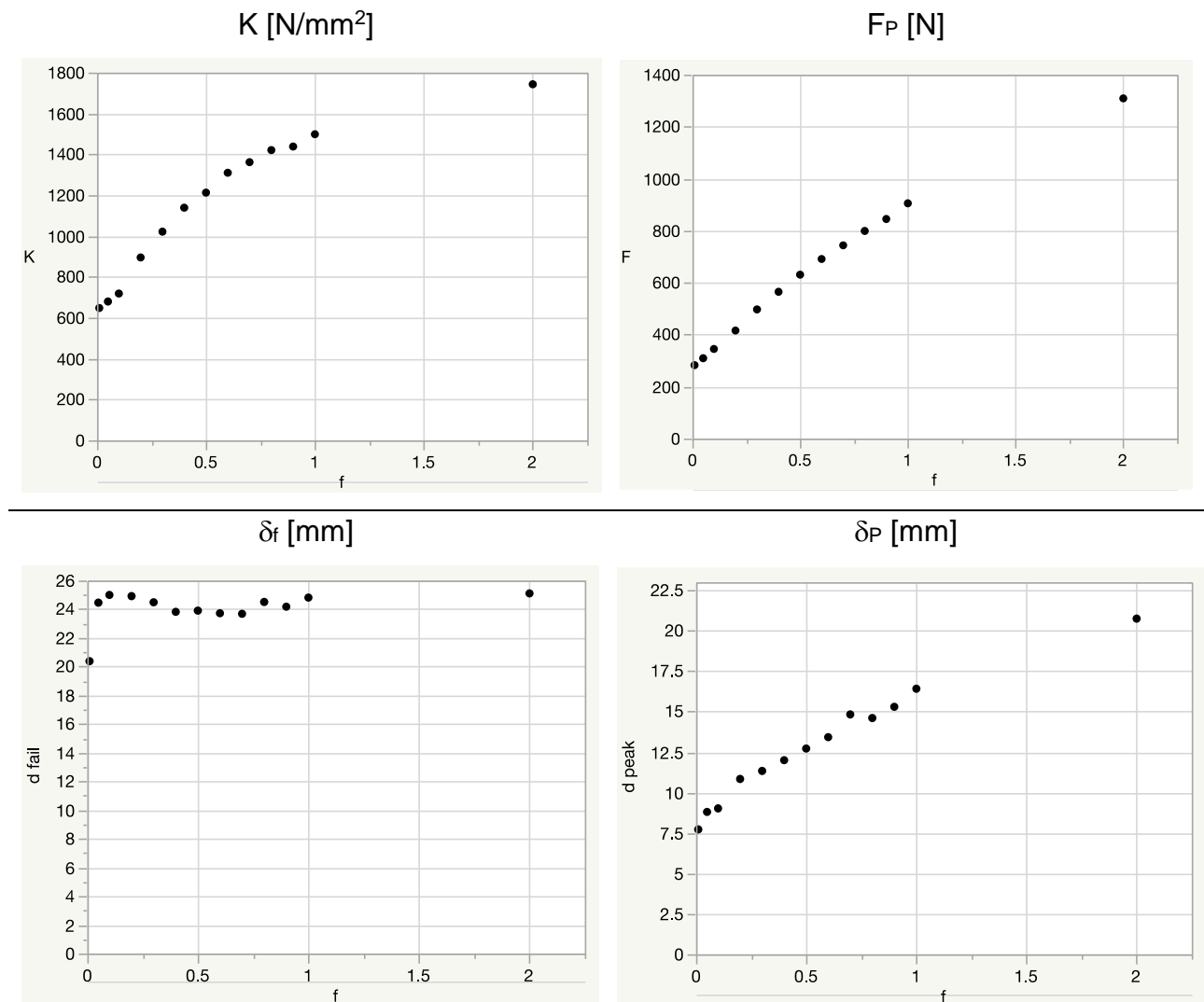


Figure 4.17 - Plots of mechanical properties for various coefficients of friction, including K (N/mm²), F_P (N), δ_f (mm) and δ_P (mm). $F_L = 1$ kN and $E = 1.7$ GPa. Strong, broadly linear, positive trends are observed for K , F_P and δ_P , while δ_f appears to be approximately constant

4.4.2 Size Parameters

4.4.2.1 Variable block size and constant assembly size

The first parameter studied was block size (t), whilst maintaining a constant assembly size (s) (Figure 4.2a). Figure 4.18 shows a plot of force vs displacement for a range of t (block thickness) values from 8 to 12 mm. A clear increase in K , F_P , δ_P and δ_f can be observed with increasing values of t . The increase in δ_f is of particular note, as this effect was not observed with changes to the assembly parameters. The experimental results are shown by the dotted lines, with good agreement observed for computational results, particularly with K . Delayed failure is observed for all simulation results which, as noted earlier, is most likely due to small amounts of damage observed in the experimental samples, as well as slight asymmetry observed during the final stages of deformation before block removal. Numerical instabilities are observed immediately before failure in the computational results, related to block removal, as discussed below in Section 4.5.

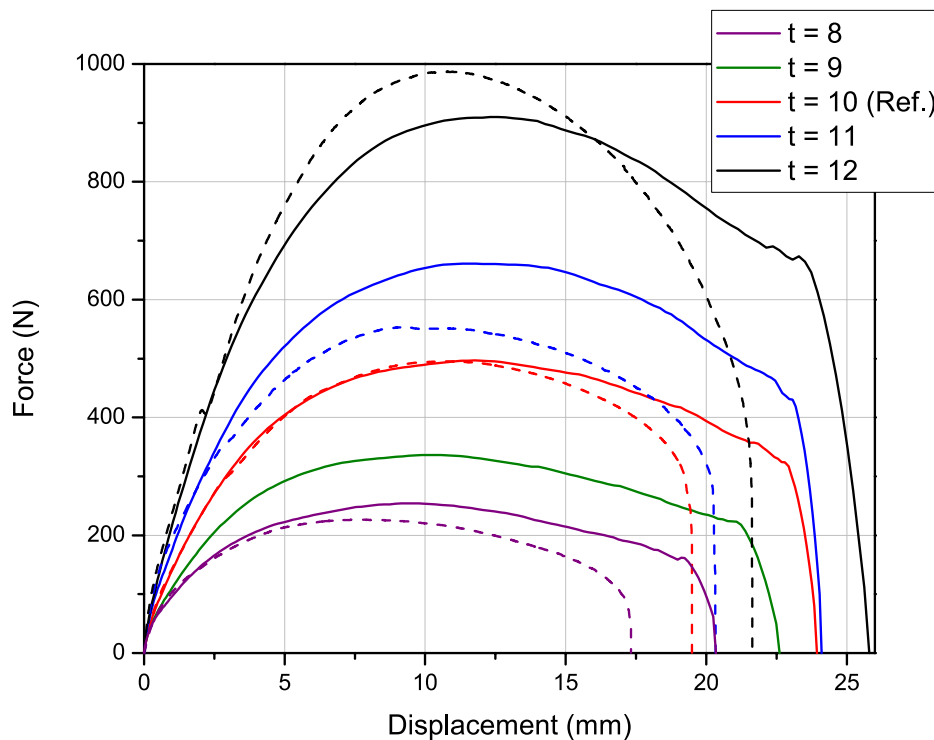


Figure 4.18 – Plot of force (N) vs displacement with varying t (mm) and constant s (mm).
Experimental results shown with dotted lines

Figure 4.19 shows that the mechanical properties plotted against thickness. K and F_P both follow a strong, positive power law behaviour. The result for K , with a power law exponent of 2.8, agrees reasonably well with the previously reported analytical model (third-degree power law) proposed by Khandelwal et al. [104], despite differences in geometry, surface relationships and boundary conditions. Peak force ($t^{3.3}$) also shows reasonable agreement with the theoretical model based on an extension of the thrust-line analysis suggested in [14] with a fourth-degree power law. This potentially implies that variations of stiffness and force with the inherent size or thickness of a topological interlocking plate occur independently of factors such as friction, geometry, material properties and boundary conditions, given that all these variables have been modified between this study and those previously reported in [14]. δ_P and δ_f also show an increasing trend with t . This trend is smaller ($t^{0.667}$ and $t^{0.5}$, respectively), however does indicate that changes to the deflection values occur with modifications to the block size.

Characterisation of the mechanical behaviour of non-planar topological interlocking blocks within planar assemblies

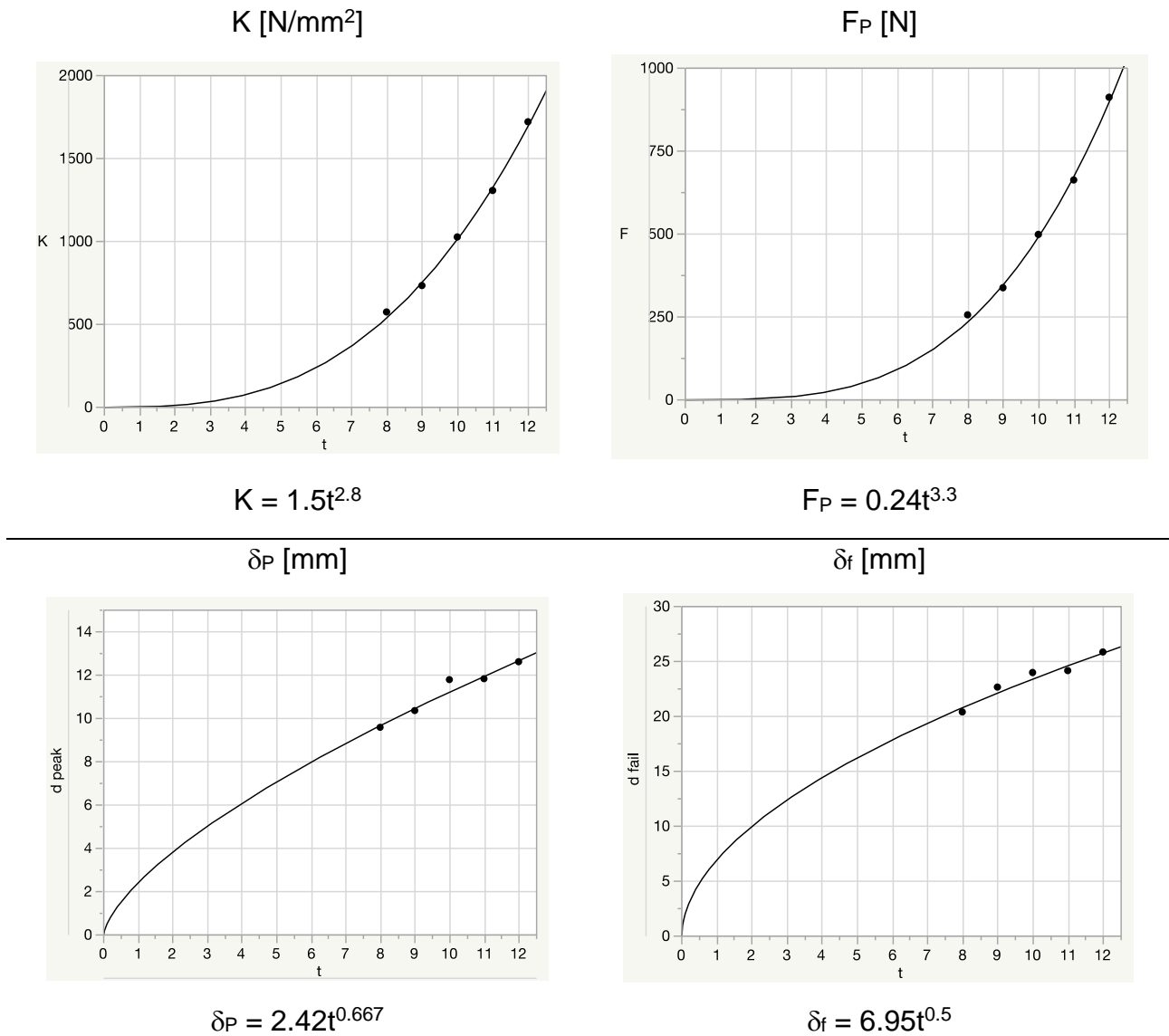


Figure 4.19 - Plots of mechanical properties for varying t (mm) and constant s (mm), including K (N/mm²), F_P (N), δ_P (mm) and δ_f (mm). Strong, positive power law relationships were observed for K and F_P . δ_f and δ_P show a positive, weaker trend with t

4.4.2.2 Variable assembly size and constant block size

The second set of parameters considered (Figure 4.2b) are the variables of assembly size (s) with constant block size (t), the results of which are shown in Figure 4.20. This plot shows the force vs displacement curves for different assembly spans. A clear trend is observed

where K and F_P decreases with increasing assembly size. Additionally, an increase in δ_f is observed with increasing assembly size.

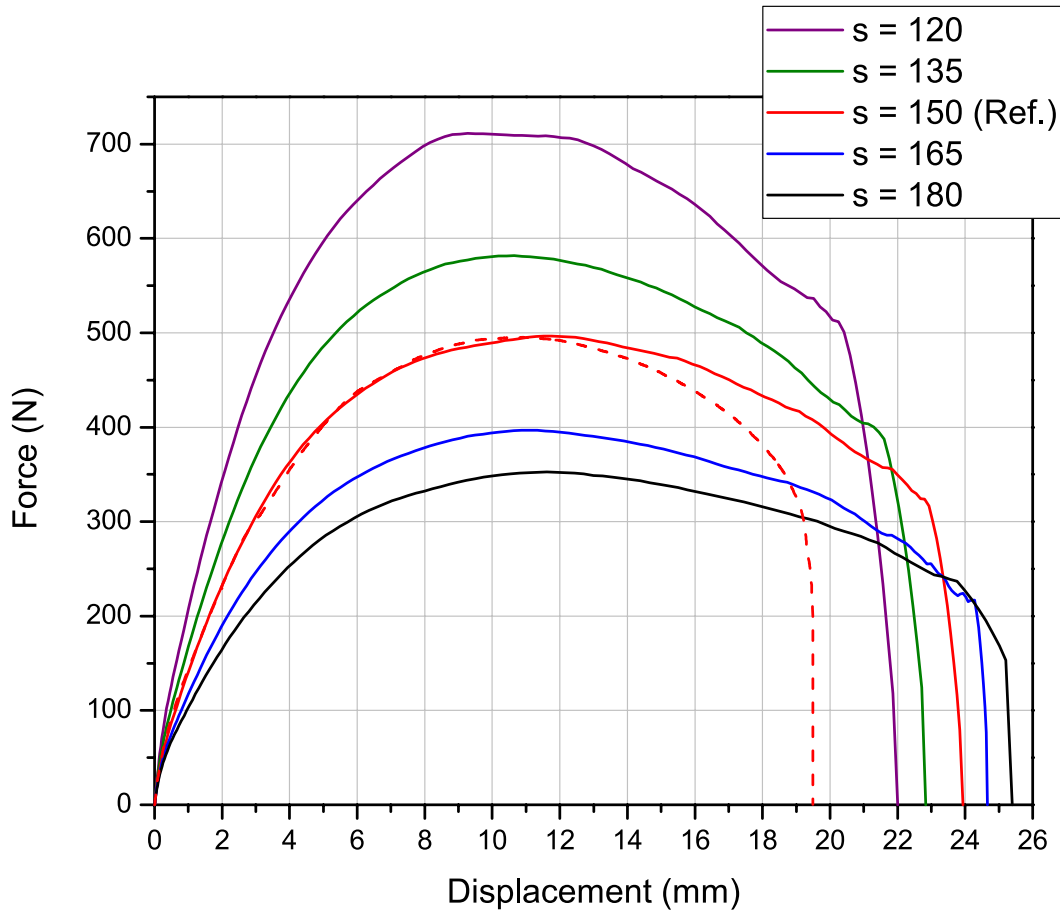


Figure 4.20 - Plot of force (N) vs displacement (mm) with varying s (mm) and constant t (mm). Experimental results shown with dotted lines

Mechanical properties have been plotted against s , shown in Figure 4.21. A negative, second-degree power law is fitted to K , which shows exceptional agreement with the analytical model in Khandelwal et al. [104]. The relationship of s with F_P has an exponent of -1.75 which approaches the theoretical value of 2 predicted in [14]. These results, taken with those from the previous section, indicate that the model proposed by Khandelwal et al. [99, 104], based on thrust-line analysis, which was presented using tetrahedral blocks, can be extended to other topological interlocking plate systems. δ_f shows an increasing trend, while δ_P displays a weaker increasing trend, which once again enables control of deflection properties, as in Section 4.4.2.1

Characterisation of the mechanical behaviour of non-planar topological interlocking blocks within planar assemblies

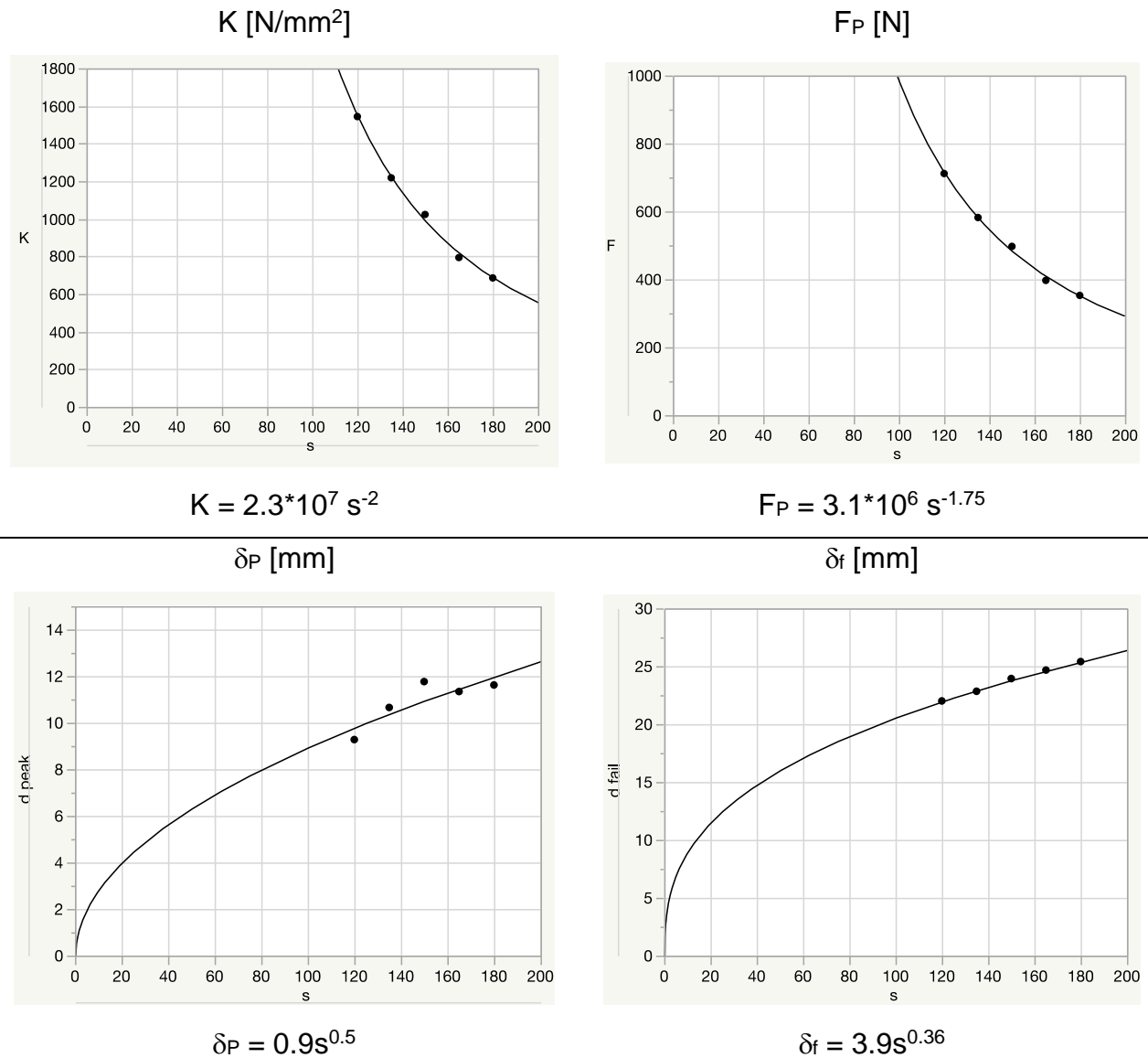


Figure 4.21 - Plots of mechanical properties for varying s (mm) and constant t (mm), including K (N/mm²), F_P (N), δ_P (mm) and δ_f (mm). K shows a negative second-degree power law trend with F_P displaying a similar trend. δ_f and δ_P show a positive, weaker relationship with s

4.4.2.3 Variable block size and assembly size with constant size ratio

The third variable studied was scale, (Figure 4.2c) which is characterised by increasing both the block size (t) and assembly size (s), with the ratio between the two being constant (s/t). Figure 4.22 shows the force vs displacement curves for five assemblies of varying scale. K appears approximately constant over the range studied. The experimental result for $t = 8\text{mm}$ shows a lower than predicted F_P , however two large, sudden drops in load are observed at approximately $\delta = 3\text{ mm}$ and $\delta = 6.5\text{ mm}$. This effect is investigated in greater detail in Chapter 5, with the expected cause due to slip of the central block relative to the neighbouring block. This has the overall effect of decreasing F_P , below the ideal, computationally-predicted value.

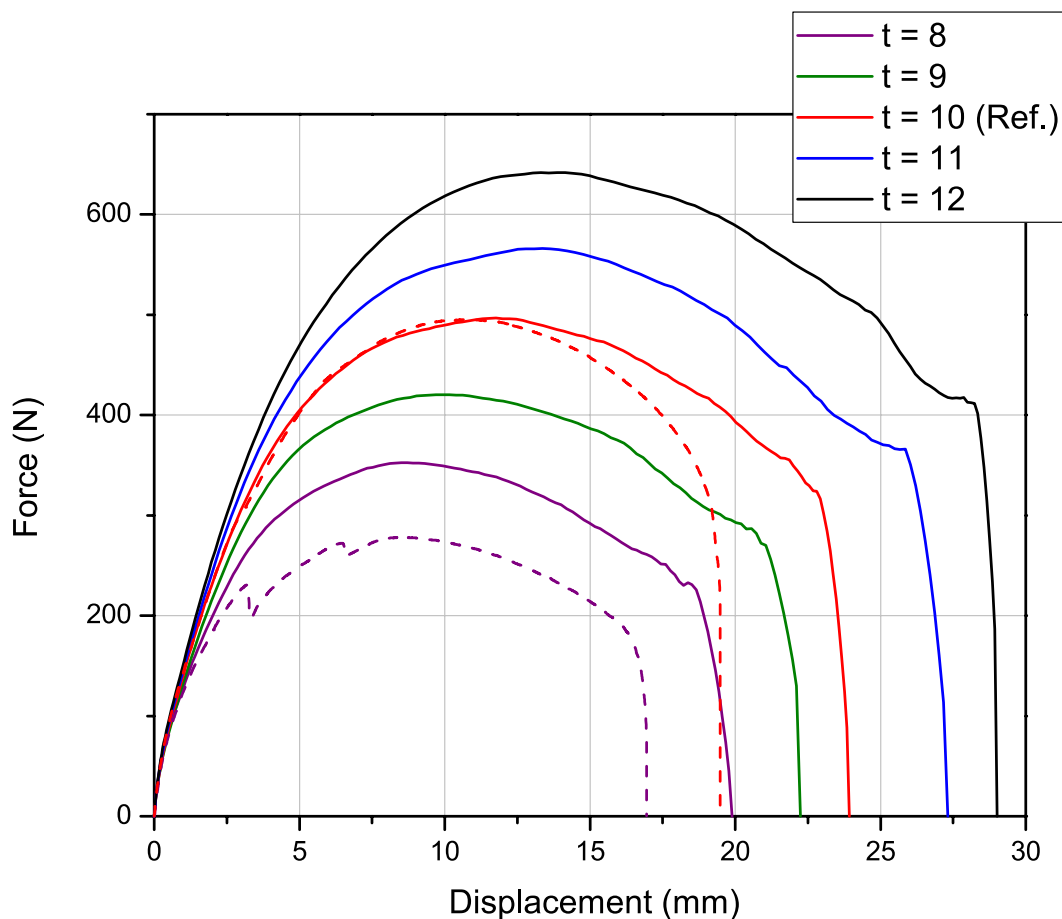


Figure 4.22 - Plot of force (N) vs displacement (mm) with varying s (mm) and t (mm), with constant s/t . Experimental results shown as dotted lines

The above results show that these curves appear to approximately “scale” as well. In other words, the F_P , δ_P and δ_f appear scale approximately linearly with “scale”, defined here as the block thickness (although assembly span could also be used). Indeed, this effect is better observed when the curves are normalised to a reference thickness, $t = 10$ mm, as shown in Figure 4.23. This figure highlights the scaling effect, with δ_P and δ_f appearing approximately constant. The change in F_P also becomes much smaller.

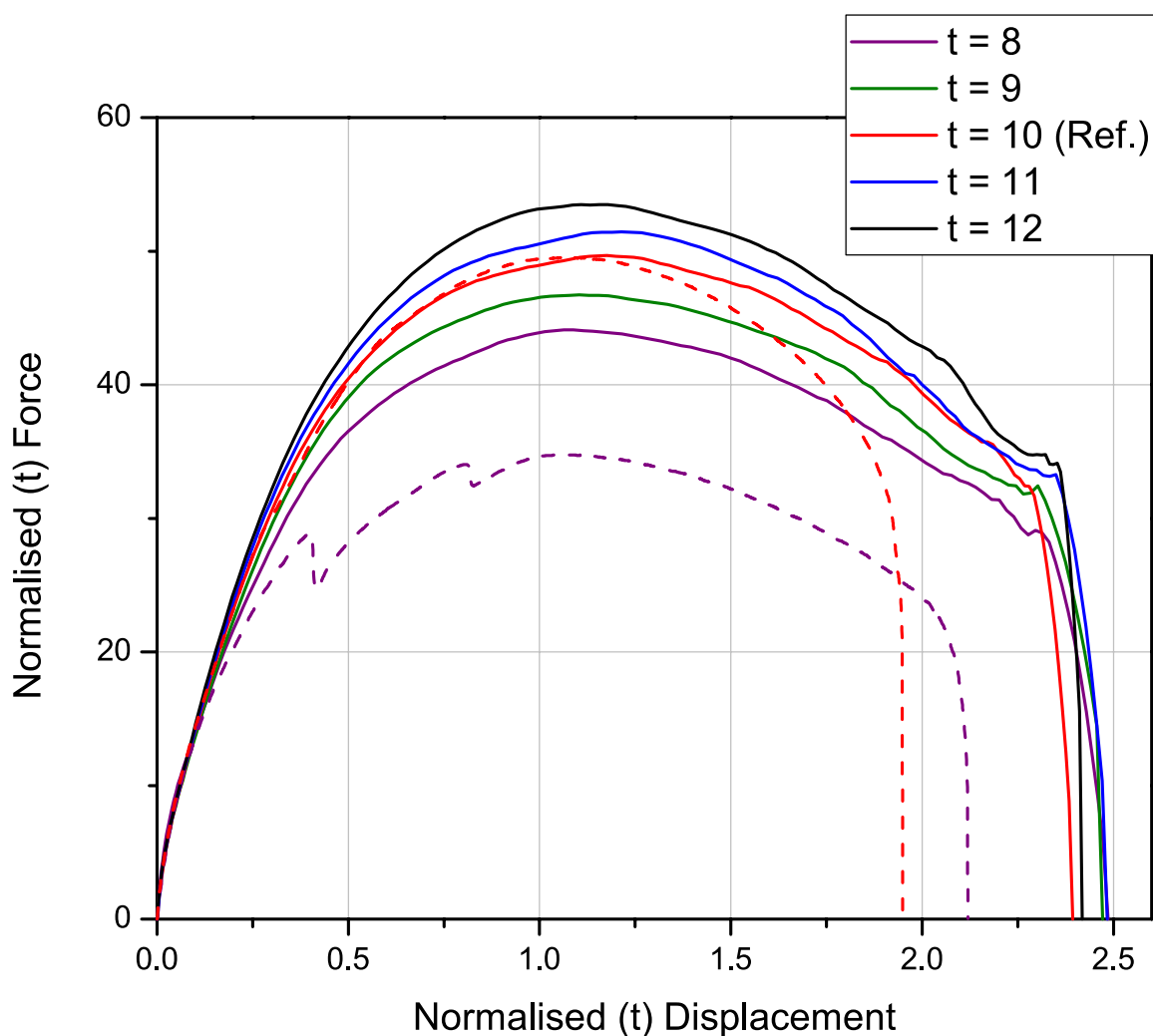


Figure 4.23 - Plot of normalised (t) force vs normalised (t) displacement with varying s (mm) and t (mm), with constant s/t . Experimental results shown with dotted lines

Characterisation of the mechanical behaviour of non-planar topological interlocking blocks within planar assemblies

Once again, these properties are plotted and a power law fitted, in Figure 4.24. Unlike the trends observed in the previous two sections, these trends are reasonably close to the power of 1, indicating a linear relationship. δ_f in particular, shows a strong linear trend.

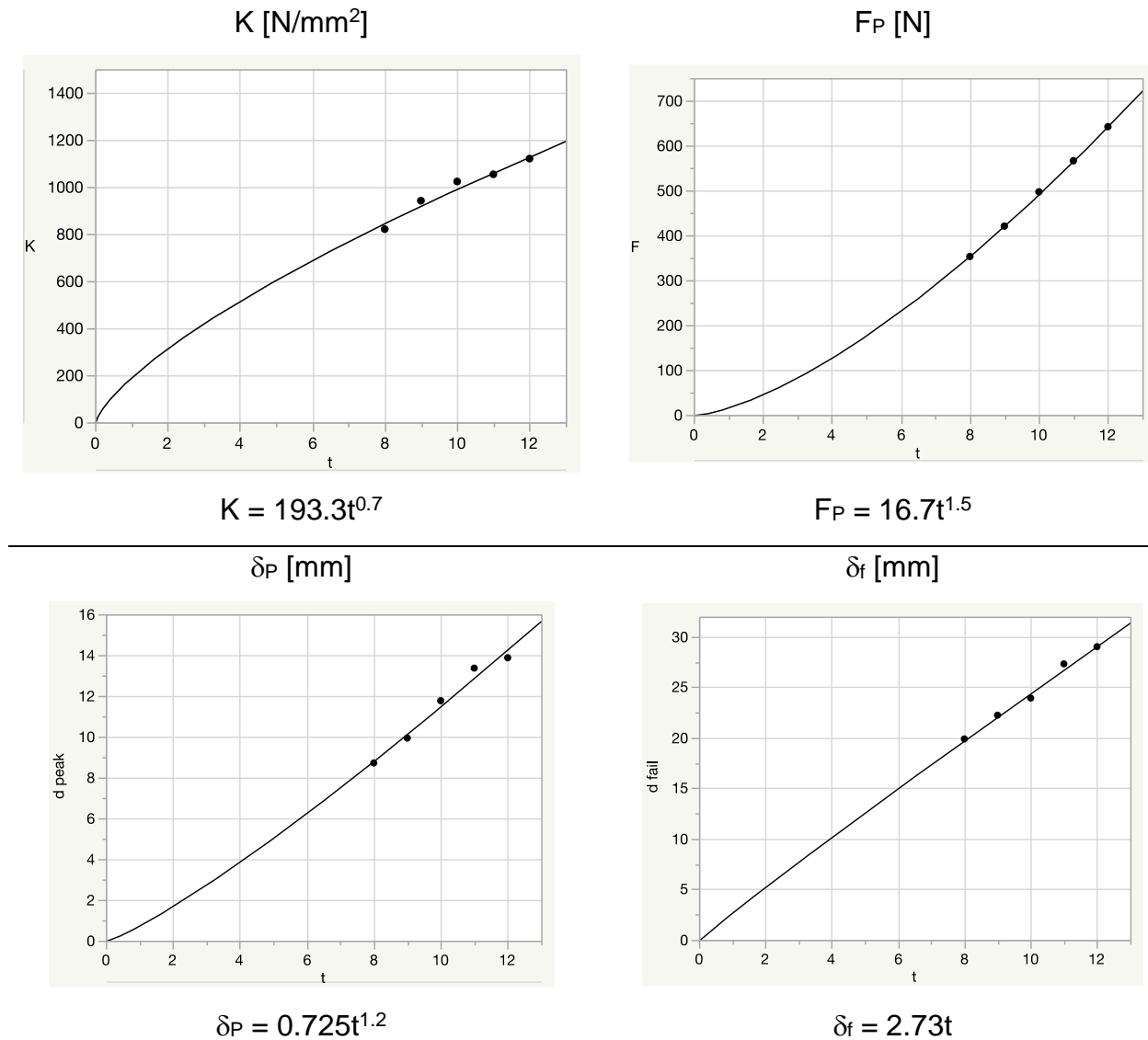


Figure 4.24 - Plots of mechanical properties for varying s (mm) and t (mm), with constant s/t ratio, including K (N/mm²), F_P (N), δ_P (mm) and δ_f (mm). K , F_P , δ_f and δ_P show a weaker positive power law trend with t (or s)

4.4.3 Discussion

The three size case studies investigated, and the resultant power law trends presented above, show good agreement with the power laws which were previously reported by Khandelwal [15], in particular the stiffness and peak force trends of tetrahedral blocks as described analytically by Khandelwal et al. [104]. This is quite remarkable given the large differences in the topological interlocking systems considered. This previously reported theoretical model considered a more idealised theoretical system (with no friction, rigid boundary conditions and tetrahedral blocks). While there is some discrepancy between these results and the previously reported thrust-line model [104] (and its theoretical extension to include peak force and work [14]), the similarity in trends is noteworthy. Indeed, these results not only validate the proposed models with numerical evidence, but they extend these models to include data on the shape of the force-displacement curves in the form of deflection to failure and peak load, which has not been previously reported [14, 104]. Furthermore, the changes in this model, such as friction, lateral load and non-planar geometry, provide a strong indication that the size and scale trends described here would apply to range of assemblies, with varying characteristics, for example with different geometries or friction properties.

Qualitatively, the results related to size and scale also broadly agree with those presented by Duguè [15], showing similar trends to the load-displacement curves for osteomorphic and cubic blocks, particularly related to the increase K and F_P . Duguè did not quantify these trends, and therefore we report these relationships specifically for osteomorphic geometry for the first time.

The trends presented in the three size case studies related to deflection to failure show that, unlike the results for the assembly parameters, it is possible to modify this property based on the size and scale of the assembly design. The deflection to peak load also shows a strong dependency on size. However, there is a clear difference between this dependency and, for example, friction where a different relationship is observed (c.f. Figure 4.25). When considering the variation of size, both deflection to peak load and deflection to failure scale similarly to each other. Conversely, with an increasing friction the deflection to peak load

approaches the deflection to failure. This effect is shown in Figure 4.25 and has the potential to be exploited in the design of topological interlocking assemblies as it provides an avenue to modify the deformation behaviour of the assembly. This is explored further in Chapter 5.

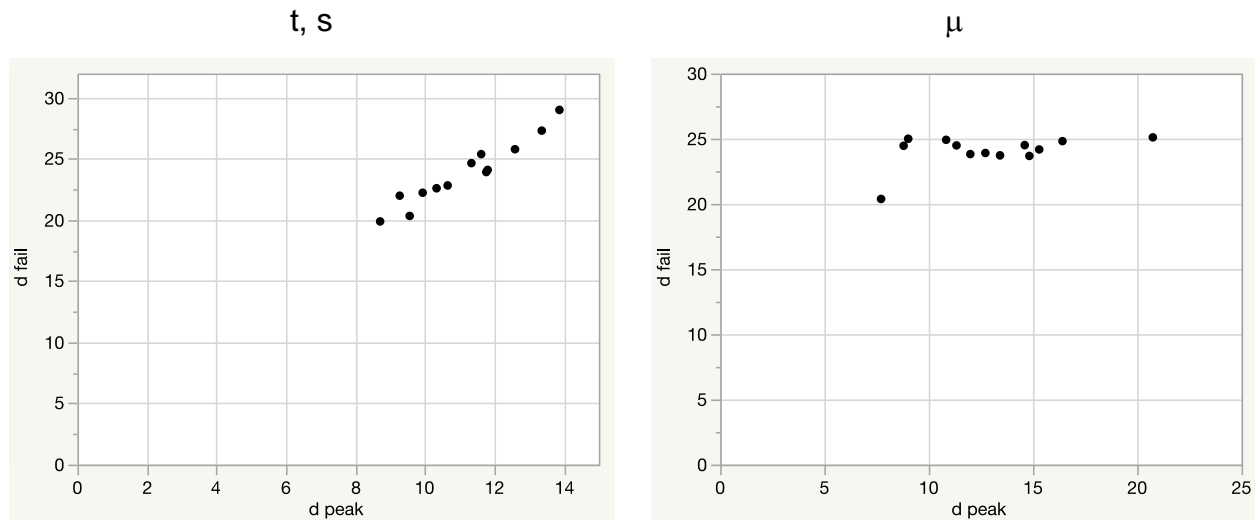


Figure 4.25 - Plot of δ_f (mm) vs δ_P (mm) for the three size case studies presented in this chapter as well as for μ . A clear positive trend is observed between the two properties when related to size, while δ_P approaches δ_f with variable friction

A further trend observed across all the parameters studied, is the relationship between K and F_P , as highlighted in Figure 4.26. This figure shows the strong linear correlation between these two mechanical properties. Deviation from this trend is observed at the upper bounds of both lateral load and friction (in either direction). However, as previously noted, these upper bounds represent unrealistic physical systems. The plot does, however, provide a useful guide to predict peak load or stiffness, if only one value is known, for topologically interlocked assemblies using osteomorphic blocks.

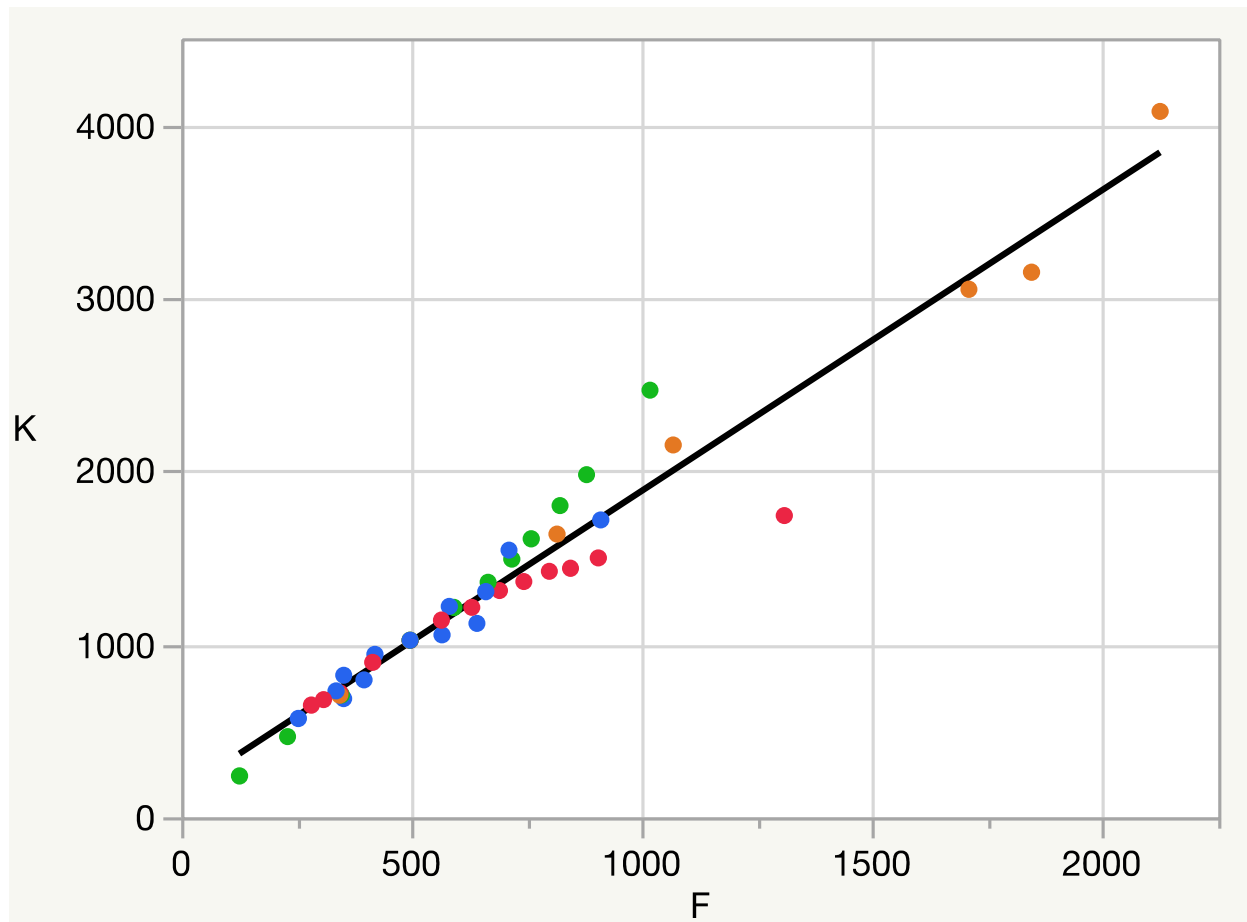


Figure 4.26 – Plot of K (N/mm²) vs F (N) for all variables. Linear relationship fitted between the two properties. Trend line given as: $K = 1.74F + 147$, $R^2 = 0.947$. E = orange, μ = red, F_L = green, size = blue

4.4.4 Artificial Neural Network Model

In order to assess the above variables in relation to one another in a meaningful way, an Artificial Neural Network (ANN) was employed to interpret the five input variables (elastic modulus, lateral load, coefficient of friction, block size and assembly size). More detail regarding the ANN model utilised can be found in Sections 2.5 and 3.6. A simple diagram of the ANN structure shown in Figure 4.27, which has a single hidden layer with five nodes (equal to the number of input nodes).

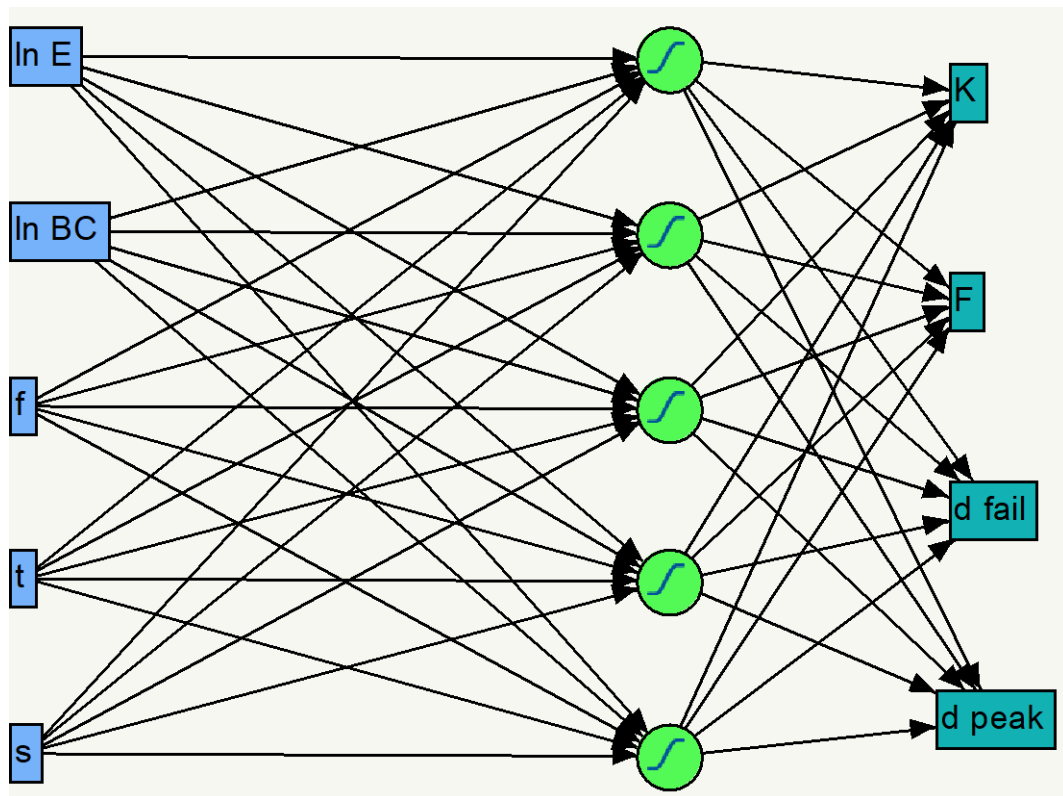
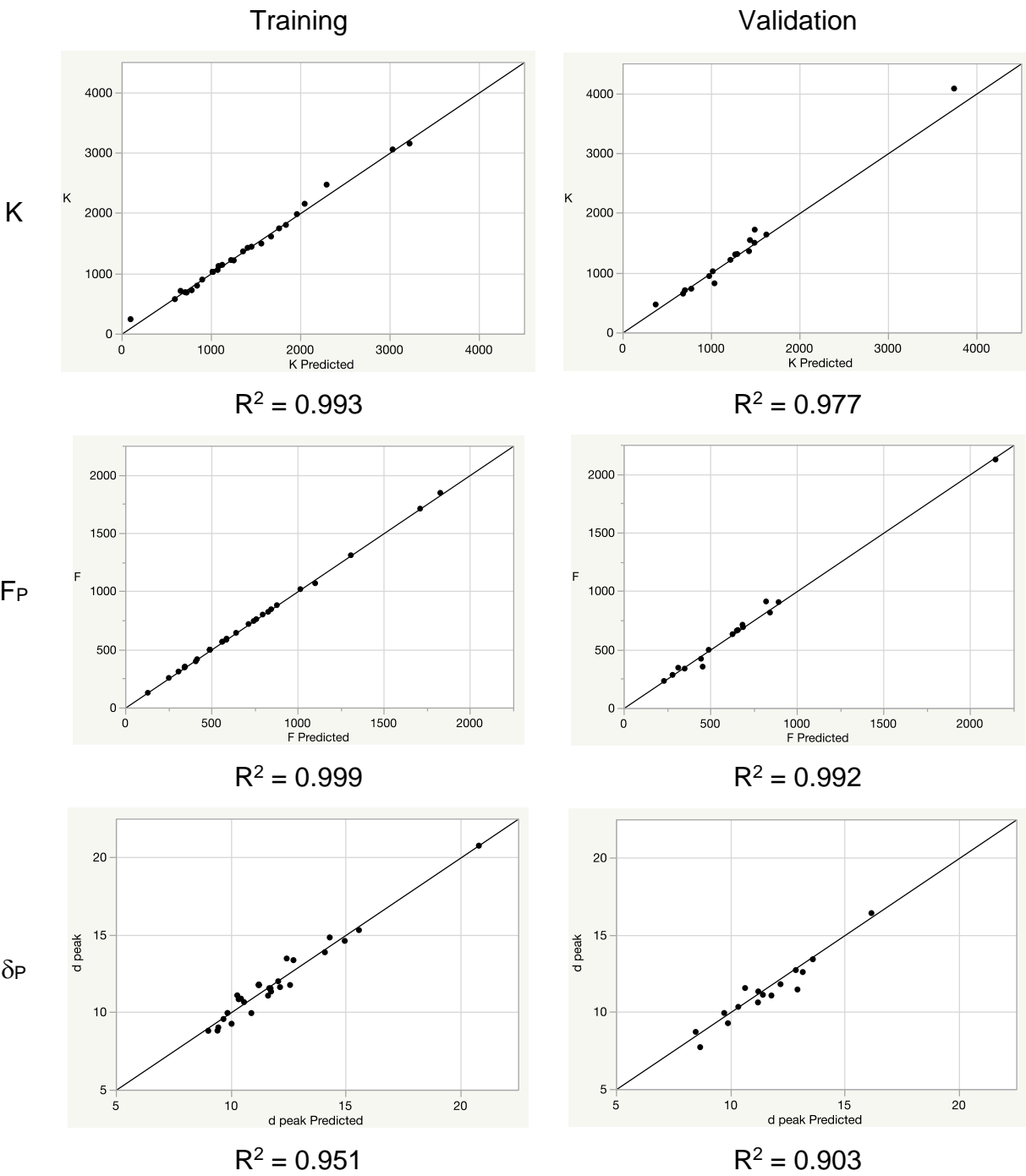


Figure 4.27 - Diagram of ANN structure. The five input parameters are shown on the left with elastic modulus (E) and lateral load (BC) adapted to a logarithmic scale, as the values are not well distributed on a linear scale. A single layer with five hidden nodes utilising tanh functions are shown in the centre. Predicted output variables (stiffness, peak force deflection to failure and deflection to peak load) are shown on the right

A random holdback technique with a two thirds training fraction, was employed. The variables of elastic modulus and lateral force were adapted to a logarithmic scale as the values were not well distributed on a linear scale and to allow for a more gradual change in values.

The fit of the ANN was assessed by plotting the actual output values against the predicted values for both the training and validation sets, as shown in Figure 4.28. The strong correlations (greater than $R^2 = 0.903$) are observed K , F_P and δ_P , between the actual and predicted values show that the model is a good fit, which follows expectations, due to the clear trends observed previously for individual manipulation of variables. δ_f shows a weaker, but still significant correlation, also consistent with the weaker trends observed earlier.

Characterisation of the mechanical behaviour of non-planar topological interlocking blocks
within planar assemblies



Characterisation of the mechanical behaviour of non-planar topological interlocking blocks within planar assemblies

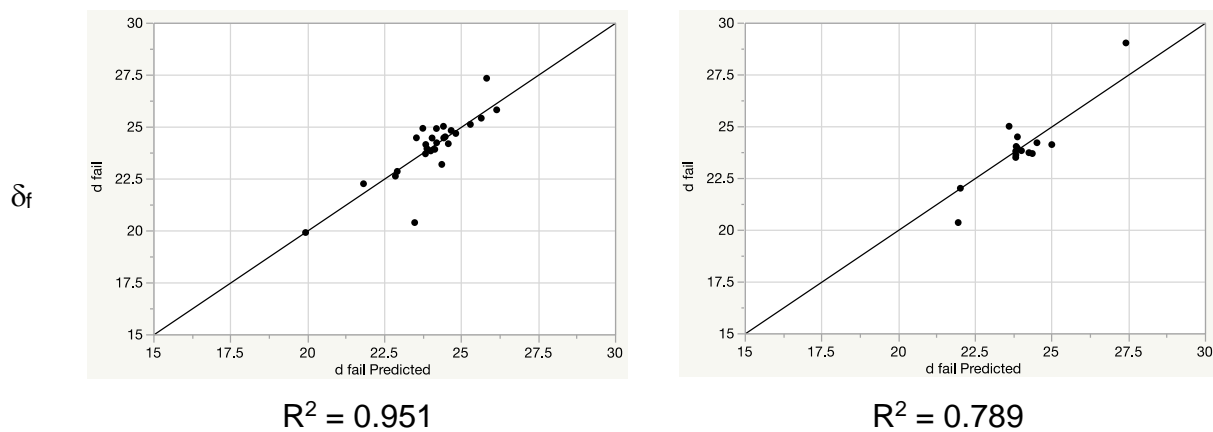


Figure 4.28 - Plots of actual ν ANN predicted values for training and validation sets across four outputs

The key results of the ANN, predicted contour plots, are shown in Figure 4.29. These results show the relative effect of each parameter on the four output properties - the larger the slope, the greater the relative impact on the output. For example, the effect of friction on the deflection to peak force is clearly much larger than the effects of modulus or lateral force, as indicated by the much higher slope in the middle bottom curve. Furthermore, it can be seen that elastic modulus has the greatest influence on the stiffness and peak force, while lateral load and friction also have significant effects.

The effect of t and s is still highly significant, similar in magnitude to friction and lateral force for K and only slightly less significant for F_P . Importantly, s is the only variable studied which has a negative association with K and F_P .

The δ_f relationships show that t , followed by s , have the largest impact on this value, while the three other variables display a negligible effect, remaining largely independent of deflection to failure. This insight is critical in the design of topological interlocking assemblies, with size variable providing us with the greatest ability to control the deflection to failure of this class of assemblies. δ_P shows the strong dependency on μ , with t and s displaying a strong significance to this property, certainly greater than E and F_L .

Characterisation of the mechanical behaviour of non-planar topological interlocking blocks within planar assemblies

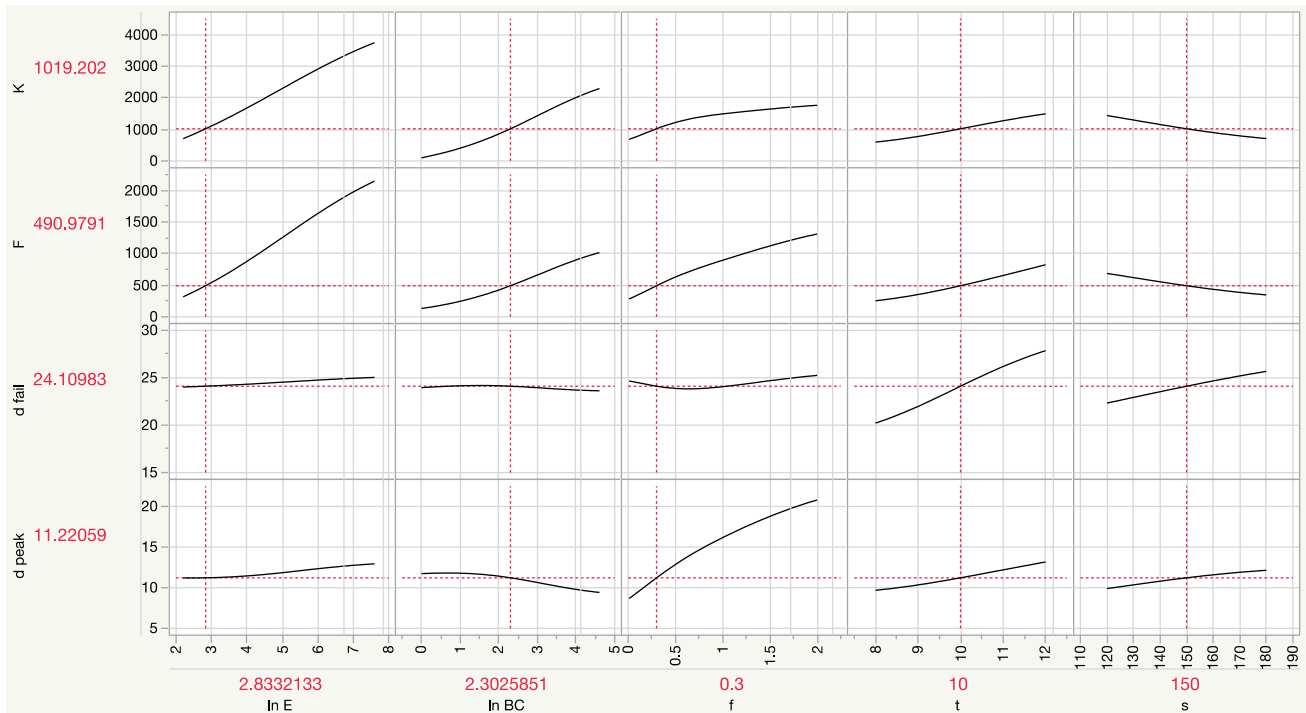


Figure 4.29 - Predicted contour plots for four outputs with the five corresponding variables. These plots show the predicted values (y-axis) of the reference assembly input variables (x-axis). The shape of each contour represents the relative effect of each input on the corresponding output

One important note on Figure 4.29 – while E , F_L and μ represent a large range of values for each variable, the size variables, t and s , are limited in the overall sense. That is, the range of possible sizes is much greater than those investigated in this study, while the other variables have been tested to their feasible limits. A consequence of this is that the relative effect of the size variable appears smaller than the potential impact of these variables i.e. size will affect the mechanical properties to a greater extent than those represented in Figure 4.29. However, given the strong relationships shown earlier in this chapter, which are supported by previous literature [14], it is reasonable to extrapolate these trends to higher and lower bounds.

It is also worth noting the similarity in the shapes of the curves in Figure 4.29 when compared to their respective counterparts in the earlier sections of this chapter. For example, the small negative relationships between δ_P and F_L , and the declining positive trends for μ across the

three outputs can be seen, and is a good indication of the validity of this neural network model. These plots, and the ANN more broadly, enable the estimation of output values for each of the given the inputs, with the ability to modify these inputs and estimate their effects on the outputs directly.

Figure 4.29 also highlights the predicted output values for the reference assembly variables as shown by the values across each axis. The ANN predicted output variables are given as $K = 1019 \text{ N/mm}$, $F_P = 491 \text{ N}$, $\delta_P = 11.2 \text{ mm}$ and $\delta_f = 24.1 \text{ mm}$. These results show good agreement with the actual values of the reference assembly ($K = 1023 \text{ N/mm}$, $F_P = 497 \text{ N}$, $\delta_P = 11.8 \text{ mm}$ and $\delta_f = 23.9 \text{ mm}$).

Given the large number of variables, it is difficult to visualise all of these simultaneously. However, one further method to visualise the ANN is shown in Figure 4.30, with a table of surface plots for various combinations of properties. These plots show the fitted model as a coloured surface, with the actual data points plotted as black dots. These surfaces highlight the fit of the model to the data as well as contextualise the results more broadly. A selection of surface plots are shown, which include:

- K vs $\ln(E)$ and $\ln(F_L)$
- F vs $\ln(E)$ and μ
- δ_P vs μ and t
- δ_f vs t and s

Each of these surface plots highlight the two variables which have with the largest impact on each of the output properties shown. When designing topologically interlocking assemblies, these surface plots provide a guide to which variables which can be modified to provide the greatest impact on the desired property

Characterisation of the mechanical behaviour of non-planar topological interlocking blocks
within planar assemblies

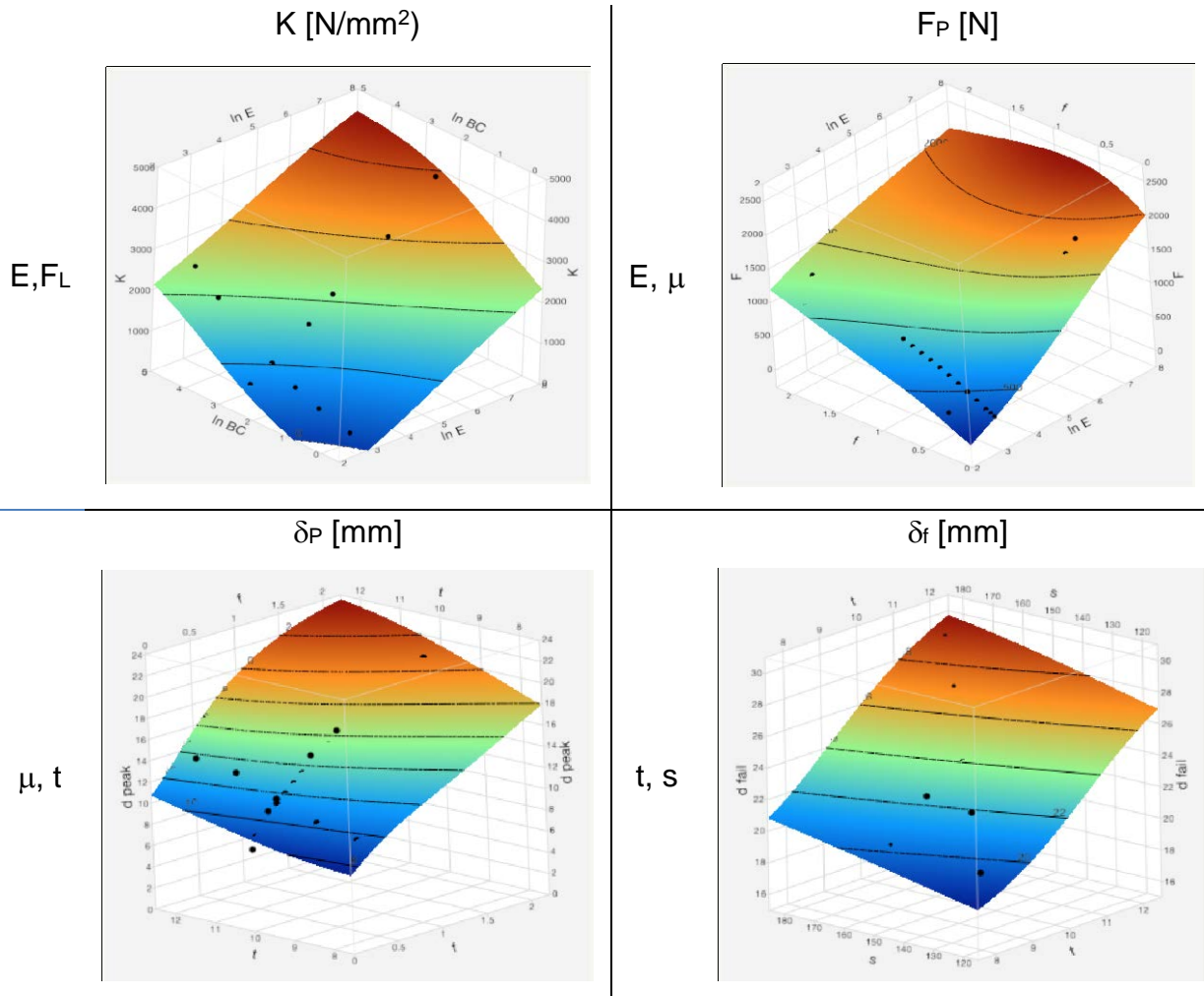


Figure 4.30 - Surface plots of selected variables with largest impact on outputs. Scale for colour gradients are not uniform across plots

The ANN also provides a quantitative output in the form of equations. A set of equations are provided (Eqns. 4.1 - 4.4) which predict the four output variables, by weighting the five hidden tanh functions (Eqns. 4.5 – 4.9).

$$K = 1327.7H_1 + 227.11H_2 - 29.299H_3 - 1290.9H_4 - 1227.4H_5 + 487.67 \quad (4.1)$$

$$F_p = 423.67H_1 + 222.58H_2 - 434.85H_3 - 709.76H_4 - 509.12H_5 + 227.65 \quad (4.2)$$

$$\delta_f = 0.97899H_1 - 6.9388H_2 - 4.3042H_3 + 1.9394H_4 - 0.57419H_5 + 26.06 \quad (4.3)$$

$$\delta_P = -5.0799H_1 - 1.0196H_2 - 6.5907H_3 + 3.2206H_4 - 6.9134H_5 + 8.8196 \quad (4.4)$$

where;

$$H_1 = \tanh\left(\frac{1}{2}(0.674 \ln(E) + 0.855 \ln(F_L) + 0.394\mu + 0.613t - 0.0336s - 6.37)\right) \quad (4.5)$$

$$H_2 = \tanh\left(\frac{1}{2}(0.379 \ln(E) + 0.280 \ln(F_L) + 0.665\mu - 0.0789t - 0.0264s + 2.76)\right) \quad (4.6)$$

$$H_3 = \tanh\left(\frac{1}{2}(-0.549 \ln(E) - 0.188 \ln(F_L) - 1.20\mu - 0.445t + 0.00281s + 6.90)\right) \quad (4.7)$$

$$H_4 = \tanh\left(\frac{1}{2}(-0.267 \ln(E) + 0.108 \ln(F_L) + 0.410\mu + 0.0747t - 0.00963s - 0.189)\right) \quad (4.8)$$

$$H_5 = \tanh\left(\frac{1}{2}(-0.258 \ln(E) - 0.245 \ln(F_L) - 2.08\mu - 0.0968t + 0.00171s + 1.68)\right) \quad (4.9)$$

These statistical equations enable the prediction of the four key mechanical properties investigations, given the five input variables across a broad range of values but does not explain the physical origin of these trends. It should be noted that these equations will only be valid within the bounds of the input data. However, given the actual data covers a broad range of variables, these equations will cover the conceivable range of physically-allowed topological interlocking planar assemblies with osteomorphic blocks. Furthermore, the effects of plasticity, fracture toughness and damage are not considered in these equations, leading to an idealised system prediction. As noted earlier in the chapter, given the broad range of variables investigated, some combinations of properties are not physically allowed.

4.5 Discussion

The finite element simulations provided the basis for the majority of the results for this chapter and as part of these results, stress distributions of the assemblies, were also generated. Figure 4.31 shows a progression of the von Mises stress distribution on the top surface (A) of the reference assembly during out-of-plane concentrated point loading.

In Part A of the figure, the initial point loading on the central block (1) concentrated in the middle of the central block, can be observed. This load is quickly transferred and spread to

the directly neighbouring “ring” osteomorphic blocks (2), mainly via curved interacting surfaces. This resultant stress delocalisation appears to occur via the compressive load between blocks, an observation supported by the stress distribution on the bottom surface of the plate (c.f. B4). This compressive load transfer mechanism has been previously noted by a number of studies [14, 83, 99, 134, 135], however visualisation of this effect to date was missing, due to, in part, the computational expense.

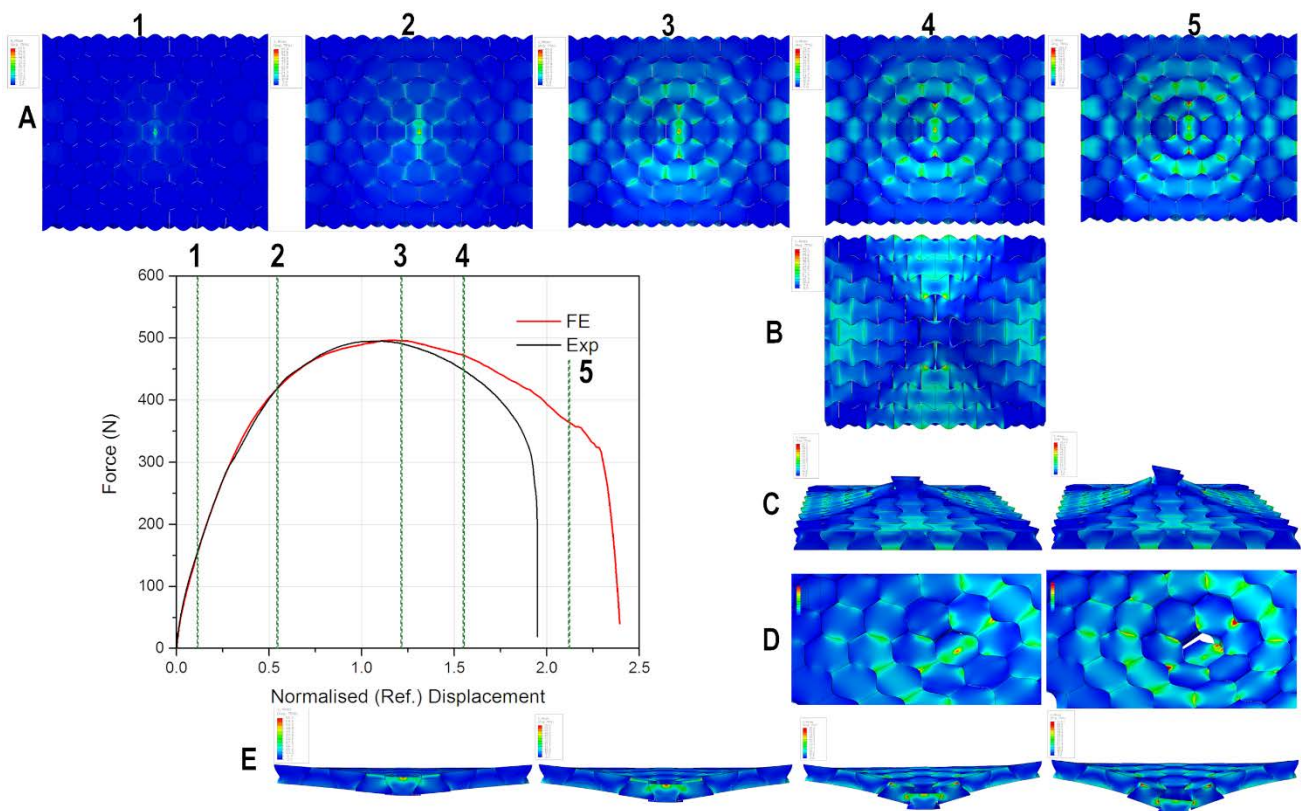


Figure 4.31 – Multiple views of the progression of the von Mises stress distribution for the reference assembly during point loading. “Rings” of stress concentration are observed on the top of the assembly in A. A “X” pattern is observed on the back of the plate in B. C-E) Various angles highlighting deformation mechanisms of the assembly. Scale for all images ranges from 0 (Blue) to 65 (Red) MPa. Max range exceeded in (4) and (5) in confined regions. Values above 65 MPa not shown in red, as they are considered unrepresentative due to the exclusion of plasticity or damage in the simulations.

Continuing in the progression of top stress distributions in Figure 4.31, it can be seen that at peak load in (3A), the stress is concentrated into a series of circles or “rings” emanating around the central block. The “rings” follow a path around the central block, with each adjacent block moving outwards from the centre forming a new “ring”. The magnitude of the stress associated with the “rings” decreases the further away they are from the central block. At the interface between each block the largest stress concentrations are observed, as the compressive load is transferred between blocks. The stress distribution pattern is maintained as displacement continues, as seen in 4A and 5A (Figure 4.31). While the stress within the assembly continues to increase, the pattern is unchanged, appearing as though the ability for the assembly to delocalise the stress concentration has reached plateaued. The correlation between the peak load and the stress distribution is indicative of a shift in deformation mechanisms – something that is investigated in more detail in Chapter 5. The stress distribution can be seen to delocalise from the central block out through the plate during the initial displacement region. Once the load-displacement curve reaches a maximum, the delocalisation of stress also reaches a “plateau” and the pattern remains constant during the softening region of the load-displacement curve.

Additionally, two distinct deformation mechanisms can be observed taking place during loading in the finite element simulations in Figure 4.31. The first is the “tilting”/“bending” of the entire assembly, centred around the loading point, best visualised in 2 and 3E. The second is the slip of the central block relative to the neighbouring block, which can be seen in images 4 and 5 of Figure 4.31. These mechanisms do occur together during the deformation process, however the slip mechanism is more prevalent in the later stages of the load-displacement curve, after the peak load is reached and within the softening region. Tilting/bending appears to dominate more in the initial stages of loading, before peak loading (2E). The manipulation and control of these mechanism is a focus of Chapter 5.

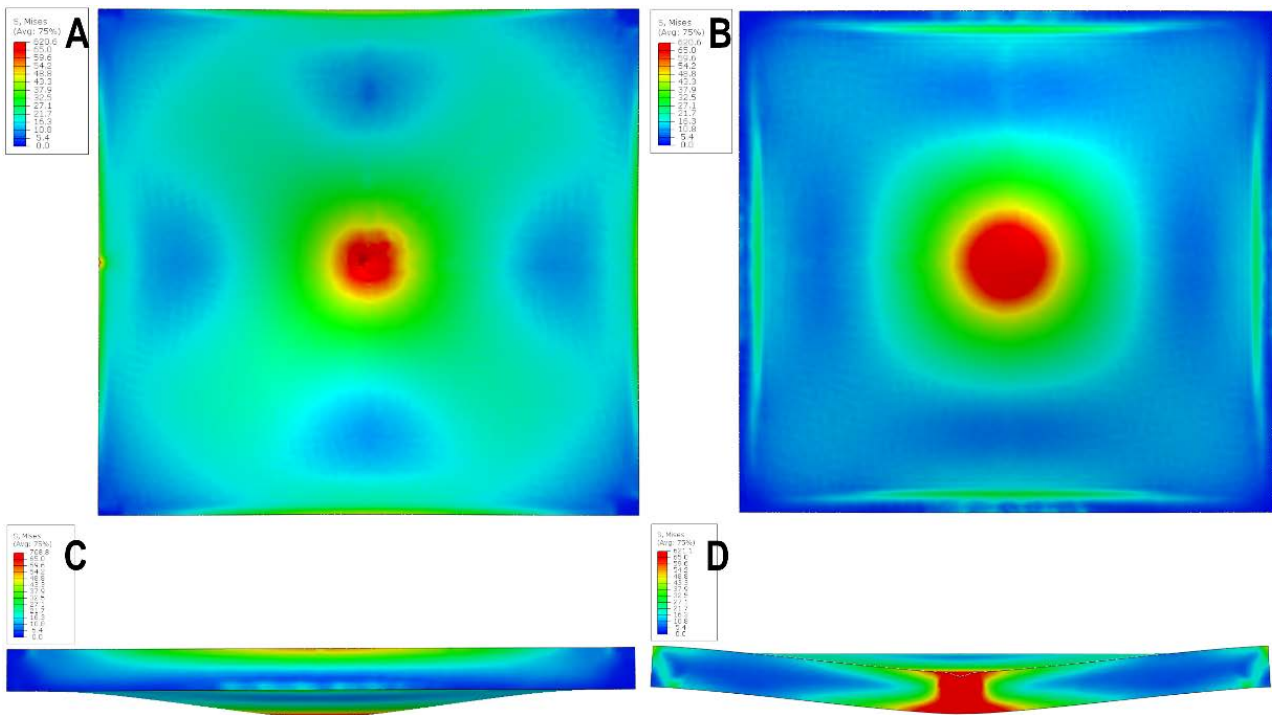


Figure 4.32 – Von Mises stress distribution of a solid plate at representative displacement of 7 mm. A) top, B) bottom, C) side and D) cross section of solid plate. Scale for all images ranges from 0 (Blue) to 65 (Red) MPa. Values above max are shown in red

The stress distribution for a solid plate is also shown in Figure 4.32. This figure shows a distinct “X” pattern formed on the top surface (A), centred around the point load. This is quite distinct from the multiple ring pattern formed in the topological interlocking assembly (Figure 4.31). This is due to the solid plate experiencing far more tensile stress, particularly remote from the concentrated loading area, as observed on the bottom surface (B). The simulated plate does undergo deflection, as seen in C and D of Figure 4.32, however due to the lack of plasticity and damage, is not wholly representative, particularly quantitatively. Despite this, the qualitative information presented above is useful as it highlights the vastly different stress distribution experienced by topological interlocking plates, when compared to monolithic counterparts.

Experimental results showed good qualitative agreement with the computational results. Figure 4.33 shows the reference assembly (a-d) post-failure, which show the single central block being removed from the surrounding assembly. Some tilting/bending of the assembly

can be observed in a), while some residual deflection of the central blocks remain after failure (c and d). As mentioned previously, small amounts of damage are observed on the corner of the blocks directly adjacent of the central blocks, with their corners cracked off (b and c), which was also noted in Chapter 3. Solid plate samples are also shown in Figure 4.33 (e and f). These demonstrate the catastrophic failure of the specimens, with a central circle punched through the middle of the plate. The failure pattern, which is similar to a ballistic damage profile, spreads from the central block, across the back of the plate (opposite side to loading). A large portion of the plate has been removed, with cracks extending out in a similar “X” shape pattern towards the corners, as observed in the simulation stress distribution in Figure 4.32. The plates retained no structural integrity after testing, and fall into multiple pieces once removed from the constraining frame.

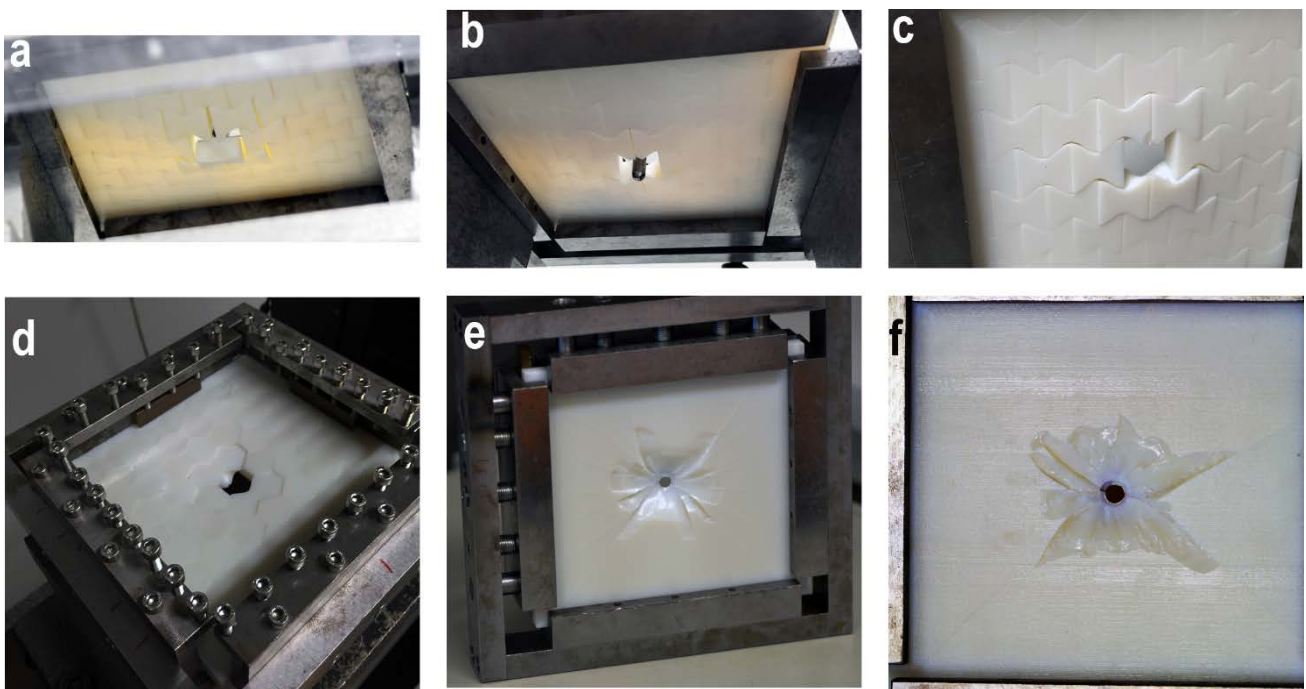


Figure 4.33 – Various experimental specimens post-failure. a) – d) reference assembly, e) and f) solid plate

Finally, in both the simulation and experimental results, an asymmetry in the removal of the central block can be observed. That is, towards the final stages of loading and immediately before failure, tilt of the central block relative to the assembly (c.f. Figure 4.31 5C and Figure

4.33 a) can be observed. That is, one side of central block leans or tilts towards the final stages of deformation and the block is removed at an angle. This central block tilt before failure leads to one edge of the block transferring the majority of the load through a smaller area, acting to concentrate the stress. It is suggested here, that this is the primary reason the experimental results have a lower displacement when compared to the computational results (as damage is not included in these). Indeed, this effect is manifest in the perfectly symmetrical computational work, by instabilities towards the final stages of deformation. The small deviations immediately before failure on the load-displacement curve, often appear as the block “shakes” or “rocks” in the simulation, something not observed in the experimental work. The design of geometries which avoid this behaviour could lead to improved mechanical performance of topological interlocking assemblies.

4.6 Conclusions

The desire to develop and use topological interlocking assemblies has led to the need to understand how key variables affect the mechanical properties of these structures. In this chapter, numerical results, supported by experimental data were presented showing the effect of number of variables on the mechanical response of non-planar topological interlocking blocks within planar assemblies. These variables included elastic modulus, lateral force, coefficient of friction as well as size and scale which were investigated numerically and experimentally. An artificial neural network was employed to link the multiple variables, as a means to compare and contrast the multiple inputs and outputs. The results showed that elastic modulus has the greatest effect on the stiffness and peak force, however the friction and lateral load also play significant roles. Specifically, all three showed a clear positive trend in relation to peak force and stiffness. Deflection to peak load and failure, measures of the shape of the load-displacement curves, were shown to be generally independent of the three assembly variables. The only exceptions to this were the coefficient of friction which showed a clear positive trend with deflection to peak load. Consequently, assemblies with increased friction showed a smaller softening region before a more sudden failure, with an overall increase in the stiffness and peak load.

The effects of variable block size and assembly size were numerically shown to affect the stiffness and peak force with a power law dependency, similar to those described analytically and theoretically, despite largely different assembly characteristics. These relationships were extended to include the effects of deflection to peak load and deflection to failure, the first time such quantifiable characterisation has been presented, enabling a route to design assemblies with controlled values of deflection. Evidence was presented highlighting the strong correlation between stiffness and peak force for this class of architected materials. In particular, the negative correlation between assembly size, peak force and stiffness was of note, as was the ability of size to strongly influence the deflection to failure.

This chapter has provided an insight and significant evidence into the effects of a number of variables, which can be utilised in the design of topologically interlocked planar assemblies under concentrated point loading with a controlled, predictable mechanical response. The results will act as a strong guide in the future design and development of these structures.

5. Deformation mechanics of non-planar topologically interlocked assemblies with structural hierarchy and varying geometry

5.1 Introduction

In the previous chapter, the effect of various properties of the blocks on the out of plane mechanical response of the topological interlocking plates was investigated. Specifically, the geometry was kept constant as the osteomorphic form, while the size, material, boundary conditions and surface interaction properties were varied.

The working hypothesis of this chapter is that the geometry also plays a critical role in the mechanics of topological interlocking assemblies, particularly in relation to the interaction of the interlocking surfaces. In order to investigate this, a number of strategies were used. Initially, a secondary interlocking surface feature was introduced to the osteomorphic geometry, one order of magnitude smaller than that of the block, leading to what we label as “hierarchical interlocking”. This concept is taken from Nature, where structural hierarchy has been observed in many systems [12, 39, 50], and having been since created synthetically in multiple studies [41, 55, 62, 69, 74]. Such structural hierarchy was anticipated to improve the peak load bearing capacity of the assembly, as such bio-inspired approaches have shown promising results in other systems [22, 63]. Indeed, the topological interlocking design is analogous to the red slider and leatherback turtle carapaces, which are known for their fascinating architecture and combination of mechanical properties [62, 67, 77] In these shells, interdigitated features provide the ability to reconcile the conflicting properties of flexibility and rigidity, providing the one or the other as required, as noted in Chapter 2.

In this work we apply the idea of hierarchical structure to topologically interlocked assemblies and study the behaviour of such assemblies under point indentation load. A specific script in the Rhinoceros CAD package was developed, which allows an *ad hoc* creation of hierarchical features on any surfaces of the interlocked blocks, see Figure 5.1 and Figure 5.2. The deformation mechanics of these structures were revealed using finite element analysis (and validated through experimental work), which provided us with an insight into different mechanisms of interaction of the surfaces such as tilt/bend, slip, and plastic deformation.

A particular focus of this study was to evaluate the effect of a secondary profile introduced on the interlocking contact surfaces of osteomorphic blocks, and to understand the link between the elementary deformation mechanics of the blocks within an assembly and the mechanical response of the latter in terms of the load vs. displacement curves. Using the obtained knowledge from these geometries, two new interlocking block geometries were derived from the original design of the osteomorphic blocks. These geometries are specifically designed to alter the deformation mechanisms under point loading, and are shown to directly result in changes to the mechanical response of the assemblies under point loading. Indeed, we demonstrate that we are able to control these behaviours for tailored mechanical responses of topological interlocking assemblies for specific applications through block geometry design.

5.2 Methods

5.2.1 *Design of structures*

In this study, a well-established, osteomorphic block design, which was used in Chapter 4, with the curvature of the contact surfaces of the blocks defined by substituting the $f(x,y)$ term with a cosine function (Figure 5.2) [84, 98, 135] and Δh and h set to 2.5 mm and 7.5 mm, respectively. As previously noted [84], these non-planar, curved surfaces lead to a large (as

compared to basic polyhedra), contact surface area between block, as well as minimising stress concentrations within a block.

This work also involved two major transformations of the basic osteomorphic block, which is considered as a reference block:

- modifications to the surface to enable hierarchical interlocking, and
- changes to the geometry of the block itself.

In order to achieve the additional complexity of the hierarchical interlocking, a custom script was created using the Grasshopper plugin for the Rhinoceros 3D 5.0 (Robert McNeel & Associates) CAD package. This script creates a fully parametrised design of these complex geometries, which allowed significant freedom over the scale of various features.

Initially, the same process as that used in Chapter 4, was utilised to generate the osteomorphic surface from function defined edge curves. This surface was then divided into a gridded mesh, with alternating squares defined into 2 sets. Point entities were defined, offset from the centre of each square, above and below for each set. The grid and points were then used to generate a surface with an array pyramids with alternating directions. These surfaces were extruded and mirrored in a similar process to those used in Solidworks to define the full hierarchical block. Each variable could be modified to allow for the pyramidal surface features to be implemented at various heights and widths, see Figure 5.1.

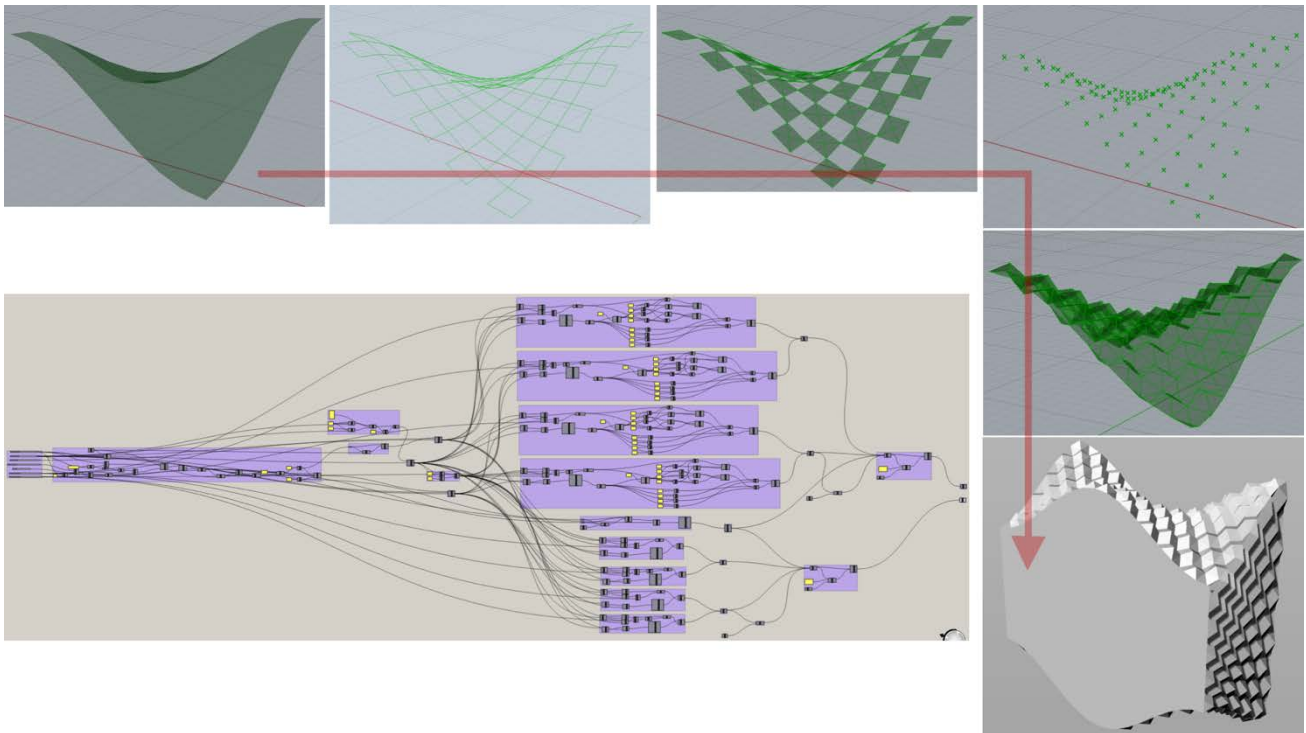


Figure 5.1 - Schematic view of Grasshopper script in Rhinoceros 3D to generate hierarchical interlocking blocks in Chapter 5. Progression from the same curved surface to gridded mesh, checker board pattern and point generation, allowing implementation of pyramidal surfaces features on solid block geometry

The surface modification to add an additional degree of interlocking at a length scale one order of magnitude lower than interlocking at the scale of the blocks themselves, whereby the reference block size has a centimetre length scale, while the secondary surface features introduced here are at a millimetre length scale. As noted earlier, these surface modifications are inspired by the suture joints of red-eared slider [22] and leatherback [70] turtle carapaces. In this work, we modify the primary interlocking surfaces by establishing a periodic pattern of pyramids with 1 mm x 1 mm base and 0.5 mm height, see Figure 5.2e, f and g. In this pattern, outward and inward facing pyramids alternate. Due to this secondary surface feature, the matching faces of the neighbouring blocks will interlock at a new length scale, in addition to being interlocked at the scale of the entire block itself. Indeed, this design also increases the number of interacting surfaces by a factor of approximately 500 and the overall surface area by approximately 20%. Importantly, the size scale at which this feature occurs - an order of magnitude smaller than the block size - is still sufficient to observe

geometrical interlocking, as opposed to the inherent surface roughness at the level of random, irregular asperities. This addition of a secondary interlocking pattern at the surface of the blocks to the primary interlocking of the blocks themselves will thus be referred to as “hierarchical” interlocking.

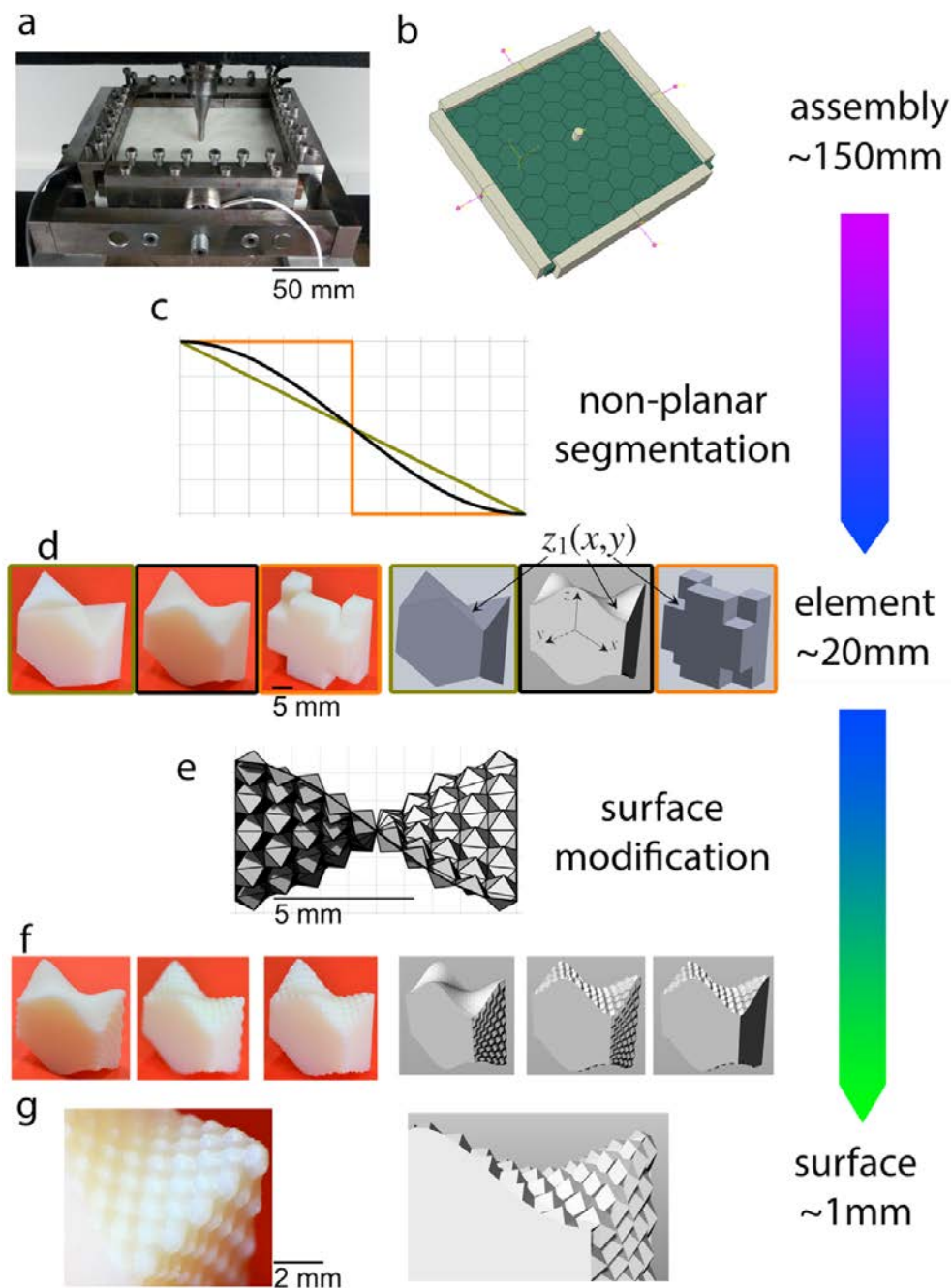


Figure 5.2 – Overview of the hierarchical approach to block geometries and piece-wise planar block assemblies used – a) experimental setup showing assembled osteomorphic blocks, indenter, screw-driven frame and lateral force sensors. b) Computational setup with

the same dimensions as the experimental one (160 mm x 150 mm) and the block size of 20 mm x 20 mm x 10 mm. (c) Two-dimensional representation of shapes used for non-planar interlocking curves for block geometries, orange: square, black: osteomorphic, dark yellow: triangle. (d) As-fabricated and designed individual blocks with various geometries. (e) Representation of pyramidal surface modifications to an osteomorphic block. (f) As-fabricated and designed individual blocks, with various hierarchically interlocked surfaces. (g) Pyramidal profile design, individual pyramids approx. 1 – 2 mm in size

The second variation involves a change in the block geometry. The cosine osteomorphic block was again used as a reference, while two contrasting surface geometries were developed to compare the deformation mechanics of the assemblies based on such blocks. While previous reports focused on some changes to the surface curvature [98], or changes to tetrahedron-shaped blocks [105], here we present a triangle curve and a square curve as more extreme examples of interlockable blocks with piece-wise planar surface geometries, cf. Figure 5.2d. These curves follow the same mathematical formulation as the original osteomorphic blocks, except with the cosine function being replaced by a triangular wave function and a square wave function. A geometry similar to the triangle one has been previously reported [98, 103], and the building block of this kind will be referred to as a “triangular block”. A contrasting geometry is represented by the square curve, Figure 5.2d. It will be denoted as the H+ block due to the letter “H” shape apparent when viewed from one of its sides, and the “plus” sign visible from the opposite side. We hypothesise that this block will completely suppress the ability for the blocks to slide or slip past each other, which is useful for analysing the effect of slippage on the mechanical performance of topological interlocking assemblies. In contrast, the triangle blocks are expected to allow for more slip than the cosine osteomorphic blocks, due to their piece-wise flat surfaces. Indeed, the straight triangle blocks bear a resemblance to tetrahedron-shaped blocks, and it could be anticipated that the mechanical performance of an assembly of triangle blocks would be similar to that of tetrahedra. This provides a convenient way of comparing the different geometries, while maintaining similar size parameters of the blocks. Below, we look into the key mechanics underlying the mechanical response of this class of architected materials with the aim to provide some guidelines for future design of topological interlocking materials.

5.2.2 *Experimental*

The specimens were fabricated using the same technique as Chapter 4, with the same dimensions and mechanical test set up employed, i.e. assembly size = 160 x 150 x 10 mm, block size = 20 x 20 x 10 mm, lateral load = 1kN etc.

5.2.3 *Computational*

Finite Element Analysis (FEA) was utilised to study the behaviour of interlocked structures under point loading and is essential for understanding the interaction of adjacent blocks, as well as the combined behaviour of the assembly. The setup of the model was the same as that employed in Chapter 4, however, the additional complexity of the geometry led to significant challenges in the meshing of the assembly. In order to model the highly complex hierarchical interlocking blocks, a multi-stage process was utilised. This involved importing the geometry from Rhinoceros 3D (described below) and generating an appropriate mesh using HyperMesh (part of the HyperWorks suite, Altair Engineering, Inc.) of approx. 19500 variable tetra mesh elements (approx. five times greater than the reference block) for the central block and 14200 elements (approx. four times greater) for the blocks directly neighbouring the central block. While the number of elements is large, this still represented quite a coarse meshing regime – approximately one element for each pyramidal surface feature (as shown in Figure 5.3. Admittedly, this meshing regime is not ideal to capture some of the deformation mechanisms, such as plasticity – the overall geometrical effects, which were of interest, could be observed, as discussed further within this chapter. This mesh was then imported into the ABAQUS model as described above, with the central 7 blocks replaced with the hierarchical interlocking variably meshed blocks. The remainder of the assembly towards the edges, was identical to the previous model used for the reference assembly in Chapter 4.

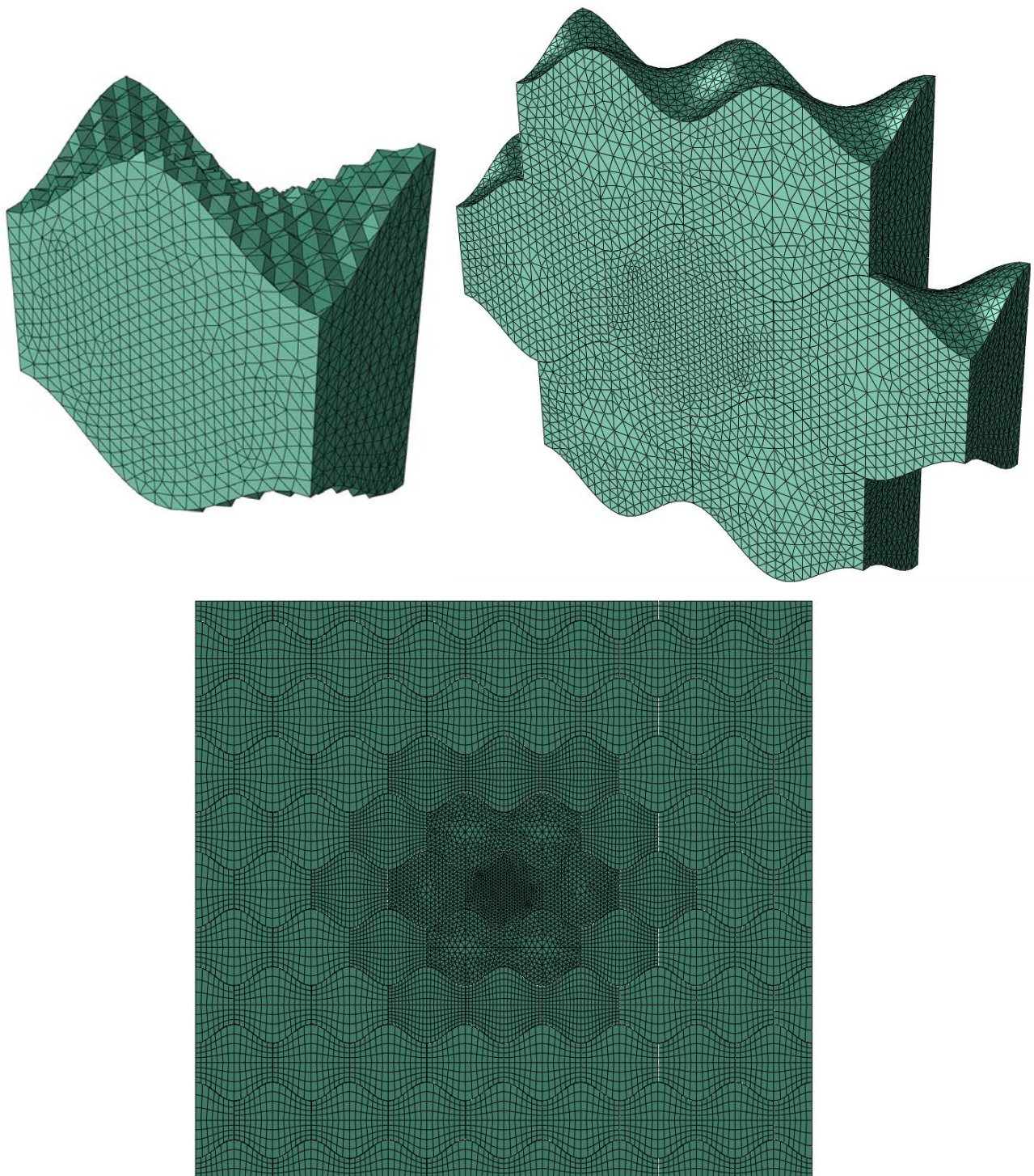


Figure 5.3 – Variable tetra meshing utilised in Hypermesh for central blocks. The same quad meshing regime, from Chapter 4 was used for the outer assembly blocks

This approach was chosen as it allows the modelling of the deformation behaviour of the hierarchical interlocking blocks in an assembly. Reducing the number of blocks modelled

with hierarchical features to the seven central blocks, was motivated by the fact that the experimentally observed deformation was concentrated on these blocks. Furthermore, this approach allowed a substantial reduction in the required number of finite elements for this simulation and therefore lower the computation time.

5.3 Results

5.3.1 Hierarchically interlocking assemblies

In order to study the effect of hierarchical interlocking, the pyramidal surface modification was applied to different surfaces of the osteomorphic block – either the curved interlocking surfaces or the planar side surfaces, or both, as shown in Figure 5.2. The specimens were additively manufactured, assembled into plates and mechanically tested under point loading, as described in Chapter 3. The set-up of the tested specimens was identical to that of the reference assembly used in Chapter 4, with the geometry, the only modification.

The load-displacement curves (with load normalised to the peak load of the reference assembly and displacement normalised to the block thickness) of these hierarchically interlocked assemblies are summarised in Figure 5.4, which reveals an interesting trend.

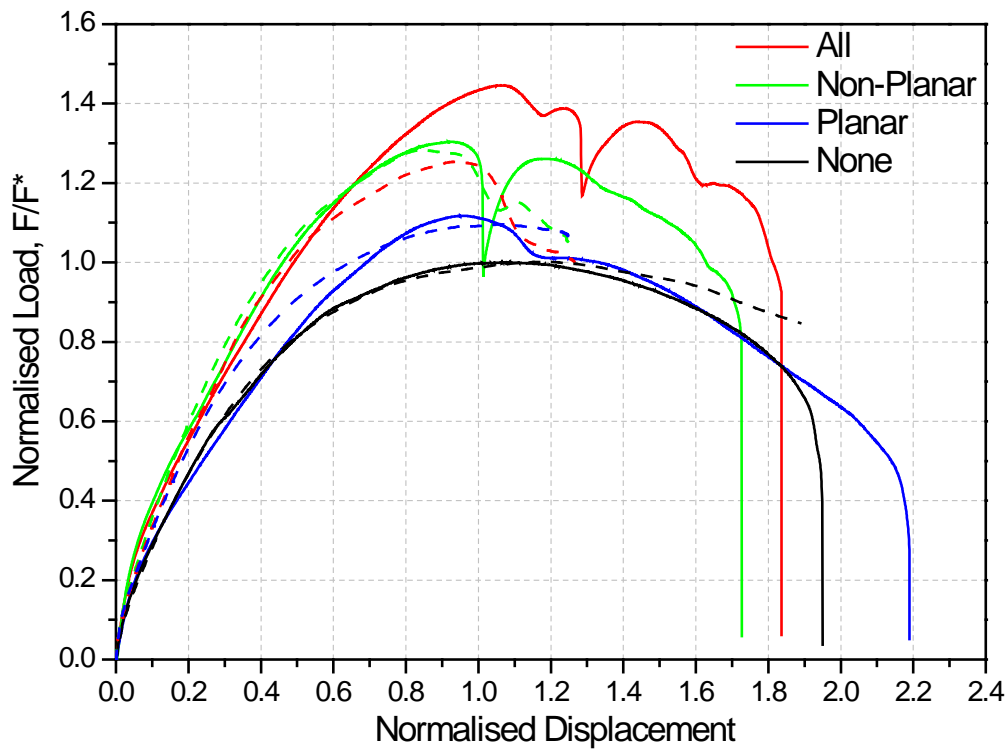


Figure 5.4 - Load-displacement curves for hierarchically interlocked assemblies. Load F is normalised with respect to the peak load F^* for the assembly of reference osteomorphic blocks, while displacement is normalised with respect to the plate thickness. The solid lines represent experimental results and the dashed lines represent computational results, which are presented up to the displacements at which a divergence from the experimental results occurs. Experimental testing was conducted in triplicate as a minimum

It can be seen that the additional degree of interlocking, whilst maintaining a reasonably similar initial stiffness of the assemblies due to the secondary surface profile, led to an increase in the peak load in all cases. The smallest increase in peak load was found when only planar side surfaces were modified by secondary patterning, and it was greater when the non-planar interlocking surfaces were patterned. The greatest effect was observed when all surfaces were patterned. The occurrence of sharp load drops around or after the peak load appears to coincide with a sudden slip of the central loaded block, relative to the neighbouring blocks, due to the surface pyramids sliding past one another. This "softening" of the assembly tends to follow these sudden decreases in load, ending in failure. A smaller

irregularity, possibly due to slip of the block under load as well, is observed in the reference sample at lower deformations (normalised displacement of about 5.3).

The above idea that the precipitous load drops are the result of slip of the central block relative to the rest of the assembly suggests that the peak load can be increased by inhibiting the onset of slippage. Slip also leads to a decrease in the deflection at failure, cf. Figure 5.4. This minor decrease is most likely related to breakage of the surface pyramids at the edge of the central block, followed by slip of the central block as a whole. Another contributing mechanism is the "tilt/bend" of the entire assembly as point loading occurs. These two effects are not mutually exclusive and occur in parallel, as discussed by Mirkhalaf et al. [105], and were also observed for the reference osteomorphic assembly. However, it is likely that tilt/bend can be more closely related to the ascending, 'elastic' portion of the curve, while slip of one or more blocks signifies the onset of the irreversible, 'plastic' deformation.

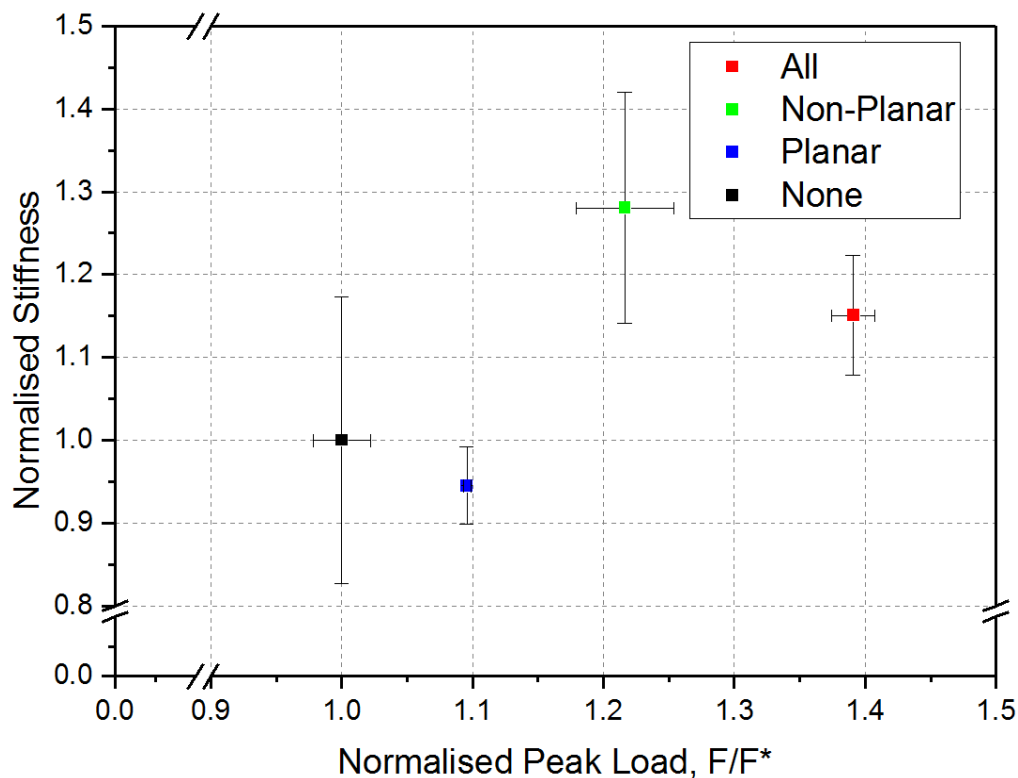


Figure 5.5 – Experimental peak load vs. stiffness for assemblies with hierarchal interlocking, normalised with respect to the peak load and stiffness of a reference assembly of osteomorphic blocks. The error bars indicate the scatter in the data. Peak load error bar for the case referred to as “planar” are small and are contained within the symbol. Stiffness is

taken as the tangent at 0.01 normalised displacement. Experimental testing was conducted in triplicate as a minimum

Initial observation of the results seems to indicate that the surface patterning producing an extra level of interlocking simply gives rise to increased friction. There are a few important differences between the hierarchical interlocking and friction. Conventional friction is generally associated with surface roughness, primarily due to random, irregular asperities at the nanometre to micrometre length scale. Discontinuous sliding referred to as stick-slip can occur when in a certain range of sliding velocities, the coefficient of friction is a decreasing function of the velocity. This may be a result of a negative rate sensitivity of the asperity shearing or breakage. [136] The interdigitated pyramidal features imposed in this work are regular, ordered and designed to interlock at a millimetre length scale. Indeed, here we propose that the large spasmodic drops in load observed in Figure 5.4, are not due to frictional stick-slip, but are rather associated with the pyramids on the mating surfaces sliding past one another in a collective process. This conjecture is supported by the fact that almost no visible damage or shearing of the surface pyramids was observed at the completion of the tests.

Comparison of Figure 5.4 and Figure 4.12 (which shows the effect of friction on the mechanical response of the assembly to out-of-plane loading) reveals a clear difference in the effects of hierarchical interlocking, when compared to friction. Increased friction leads to a similar increase in both stiffness, peak load and displacement to peak load (Figure 4.13), while hierarchical interlocking shows increases to peak load, a small increase in stiffness and negligible changes in the displacement to peak load. Additionally, sharp decreases in load are observed in hierarchically interlocked specimens which are not observed with varying friction.

Yong [98] noted in a numerical FE study of osteomorphic blocks, that when random surface asperities were introduced, a reduction in peak load bearing capacity was observed when compared to those assemblies with smooth interacting surfaces. Yong [98] attributed this result to a reduction in surface contact area, due to the random nature of these asperities. Our current view is that the observed results stem from a combination of an increase in the

contact area between the blocks (due to their well-ordered design) and the extra resistance to sliding due to a large number of pairs of pyramids on the mating surfaces engaged in interactions at a multitude of angles.

The behaviour of assemblies with the four geometries considered was simulated using FEA to gain a better understanding of the response of the structures to the point loading, as well as the interaction of adjacent blocks. Figure 5.4 shows a good qualitative and quantitative agreement with experimental results. Initial stiffness is well matched for all samples, excluding the example of planar geometry which slightly over-predicts stiffness. The magnitude and location of the peak loads are also in good agreement. The complex geometry of the full hierarchical specimen (designated 'All') resulted in computational difficulties, most likely related to meshing artefacts at the edges of the two joining pyramidal surfaces (curved and flat), leading to a slightly lower-strain divergence from experimental results. Interestingly, the model does predict a significant drop in peak loads around 1.0 normalised displacement in both 'All' and 'Non-Planar' samples with good accuracy, capturing the effect of neighbouring surface pyramids sliding over one another.

The assemblies were inspected visually and simulated numerically, by finite element analysis (FEA), with particular emphasis on the behaviour of the central blocks during deformation. The amount of slip (the relative displacement of the central block to its directly neighbouring blocks) is shown as a function of normalised displacement in Figure 5.6a. This provides a quantifiable measurement of the contribution of slip to the overall displacement of the assembly, with the other contributions being assembly tilt/bend and plastic deformation. Figure 5.6a shows the normalised slip for the various geometries (including those discussed in the section below) against the overall normalised displacement. This plot demonstrates that geometries which have higher load bearing capacity slip less than those with a lower load bearing capacity. Indeed, if we take the point at normalised displacement of 1.0, it can be seen that the reference assembly exhibits approximately 0.23 slip, the planar one 0.12, and the non-planar one 0.04, while the 'All' assembly experienced less than 0.03 slip. The difference between these values and the magnitude of total normalised displacement (1.0) is the contribution of tilt/bend and/or plastic deformation to the overall displacement. These values show a clear correlation between load and slip. Indeed, a

significant increase in slip is observed between 1.0 and 1.2 normalised displacement, which corresponds well with the decrease of load observed in the curves presented in Figure 5.4. The different slip characteristics of the assemblies considered were evaluated by FEA at 1.0 normalised displacement. They are visualised in Figure 5.6b. A large displacement of the central block of the reference geometry and a negligible displacement for the 'All' geometry can both be seen. The simulation results for non-planar and planar block assemblies display the effect of the surface modifications well, the planar hierarchically interlocked surface interaction showing minimal slip and the curved concavo-convex surface exhibiting the ability to slip.

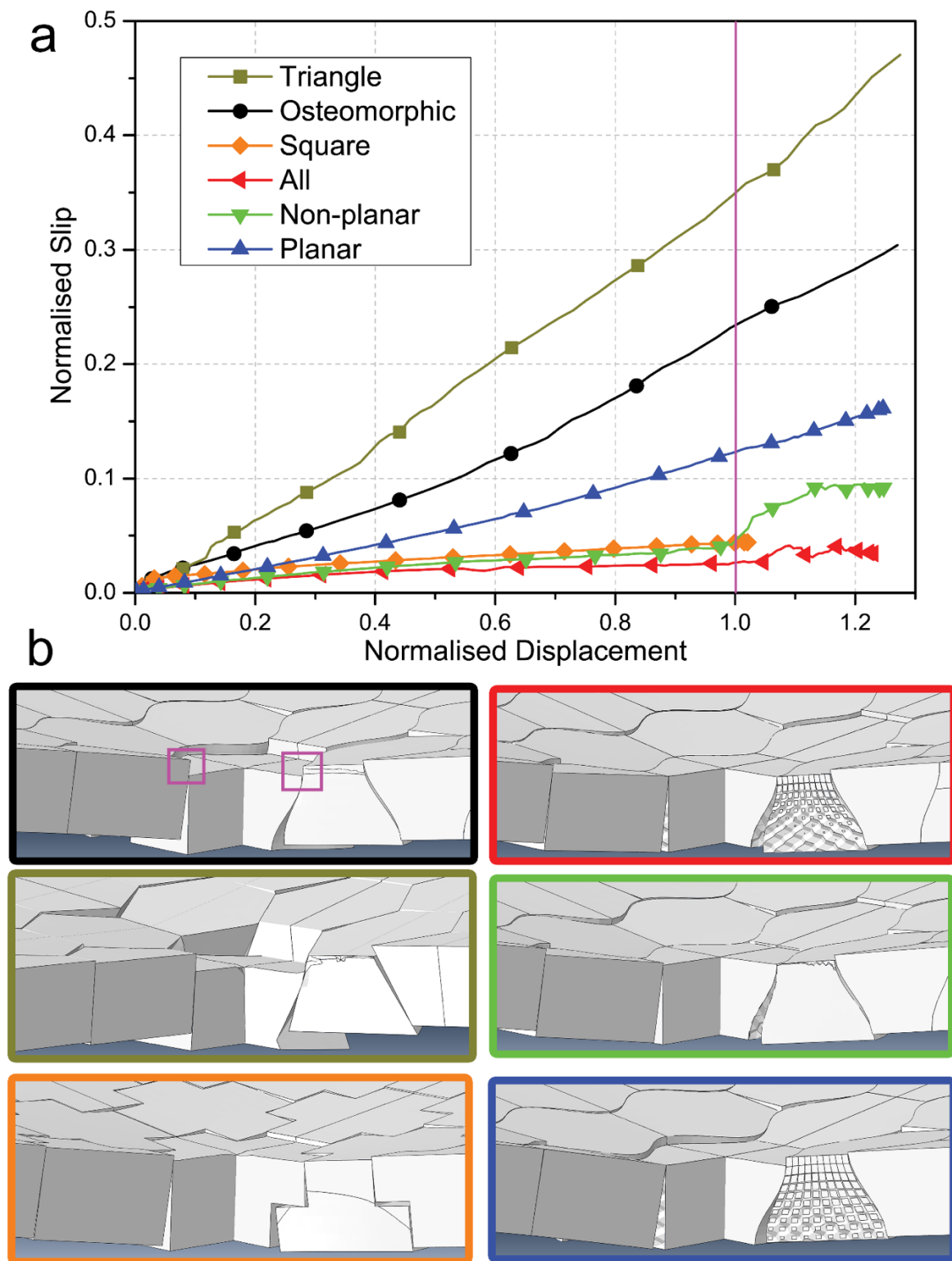


Figure 5.6 – Displacement of central block relative to neighbouring blocks as measured by average distance of two edges shown in purple squares: a) plotted as a function of normalised displacement, b) images of computational output for central block at 1.0

normalised displacement (as shown by the purple line in Figure 5.6a). Colour borders correspond to curve colours in Figure 5.6b. Displacements have been normalised in the same way as in Figures 5.2 and 5.5

5.3.2 Modified geometries to adjust slip characteristics

A comparison between the load vs. displacement curves of three primary shapes - smooth (cosine), straight triangular, and square (H+) blocks is shown in Figure 5.7 a. Once again, the results of cosine-generated osteomorphic block assembly are included as a reference. One of the primary effects observed in Figure 5.7a is the shape of the curves for the H+ blocks (4.99 mm and 4.95 mm in size), which is distinctly different to those for the reference assembly and the assembly of the straight triangular blocks. It is clear that the H+ blocks show no 'deformation softening', the load increasing continuously until brittle failure, which then occurs suddenly. By contrast, for the assembly of straight triangular blocks, a decrease in the peak load, compared to the reference assembly, can be observed. Indeed, the load vs. displacement curve departs from the linear elastic region at relatively low deflections, which may be attributed to the increased ability of the central block to slip relative to the surrounding blocks of the assembly.

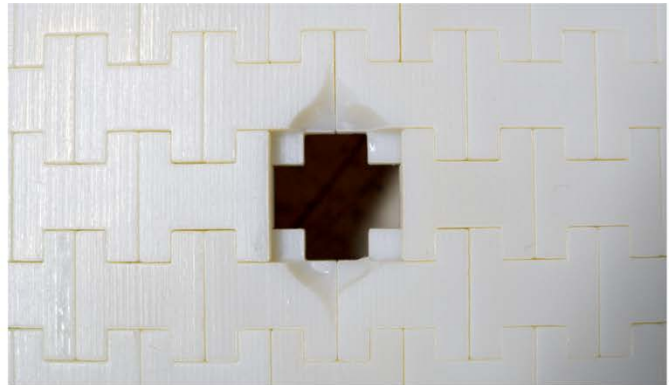
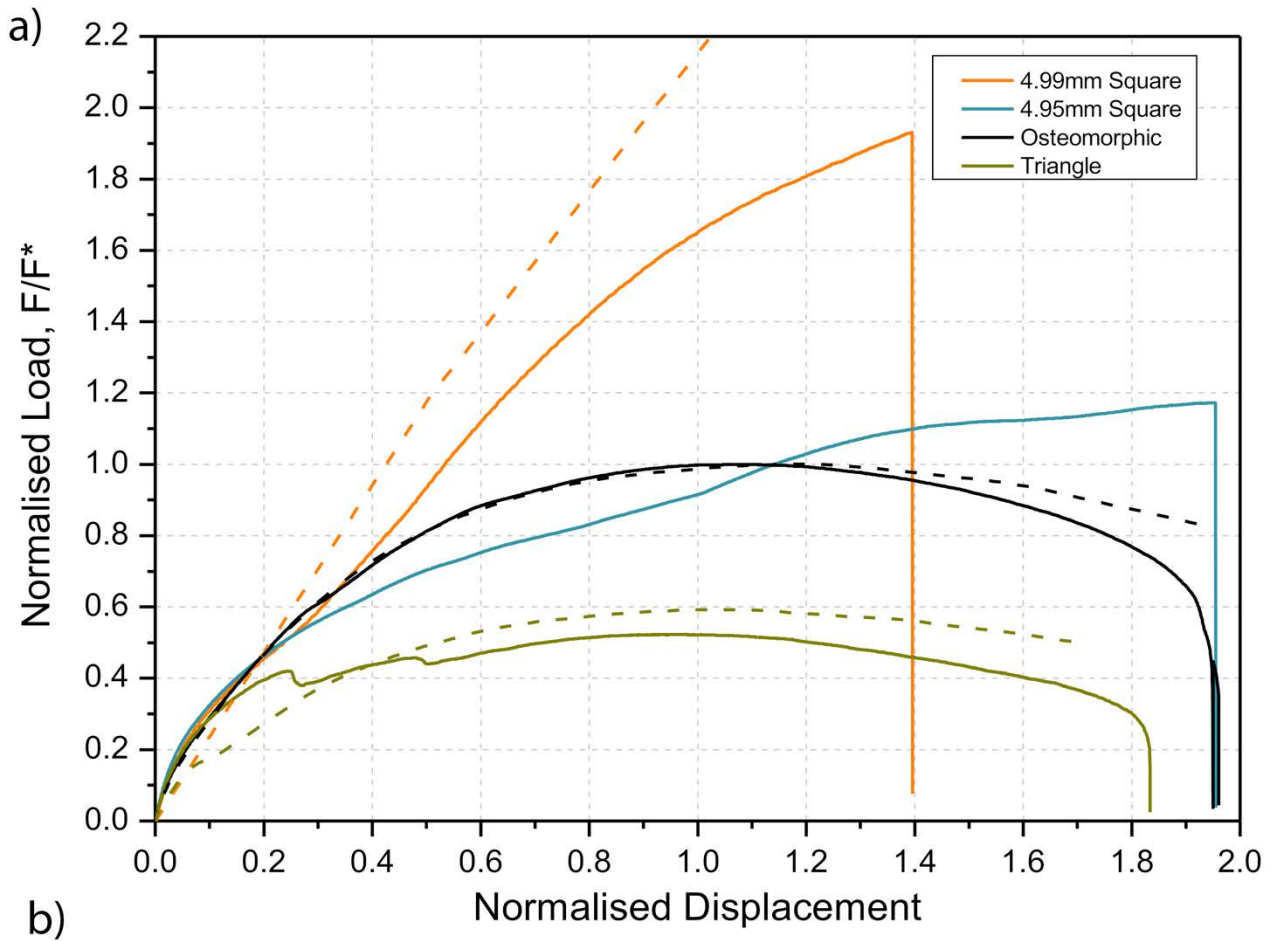


Figure 5.7 - a) Normalised load-displacement curves for assemblies of interlocked blocks with non-planar surfaces. The load and the displacement have been normalised in the same manner as in Figure 5.4. The solid lines correspond to the experimental curves and dashed lines to the computational curves. b) Damage to osteomorphic and square assemblies after mechanical testing

For all samples, nearly the same initial region (up to about 0.12 normalised displacement) is observed. This indicates that loading at low strains is not geometry-dependent (as observed earlier for the hierarchically interlocked samples). As shown in Chapter 4, the initial response to loading is governed by other variables, such as block size, magnitude of the coefficient of friction, material properties, and boundary conditions. This is also supported by previous studies by Schaare et al. [13] for assembly parameters and Khandewal et al. [86, 104] for size parameters. It is only after this initial deformation stage that the geometry becomes critical. This effect is demonstrated in Figure 5.7 a, which shows a similar initial stiffness for the different assemblies tested, while displaying varying peak loads. Consequently, for a given set of conditions as outlined in Chapter 4, the initial stiffness can be approximated. Following this, geometry modifications can be implemented to control the mechanical response and deformation mechanics.

It appears that after the initial stages of displacement in the ca. 0.2 normalised displacement region, the effects of sliding and tilting/bending become important to various degrees dependent on geometry. Around this transition region, the load on the H+ assembly continues to rise, and thus presumably only tilting/bending occurs. The load on the reference osteomorphic assembly is also still increasing, however at approximately 0.25 normalised displacement this growth begins to slow down, as the sliding sets in and acts concurrently with tilt/bend. Finally, the triangular block assembly exhibits a significant load decrease at around 0.25 normalised displacement, and another at 0.5 normalised displacement. These drops in load appear to be related to the slip mechanism discussed above, and their presence seems to correspond to a transition from static to kinetic friction – a hypothesis that would require further study to confirm. The load-displacement curve of the triangle geometry is much flatter and has a lower peak load compared to the assemblies with the other two geometries. From a value of the normalised displacement approximately in the range of 0.4 – 1, the H+ block assembly keeps showing an increase in load, while significant deformation softening is seen for the other two geometries, with the triangle block assembly reaching its peak load at 0.95 normalised displacement - a slightly lower value than the one for the reference, cosine block assembly (1.05).

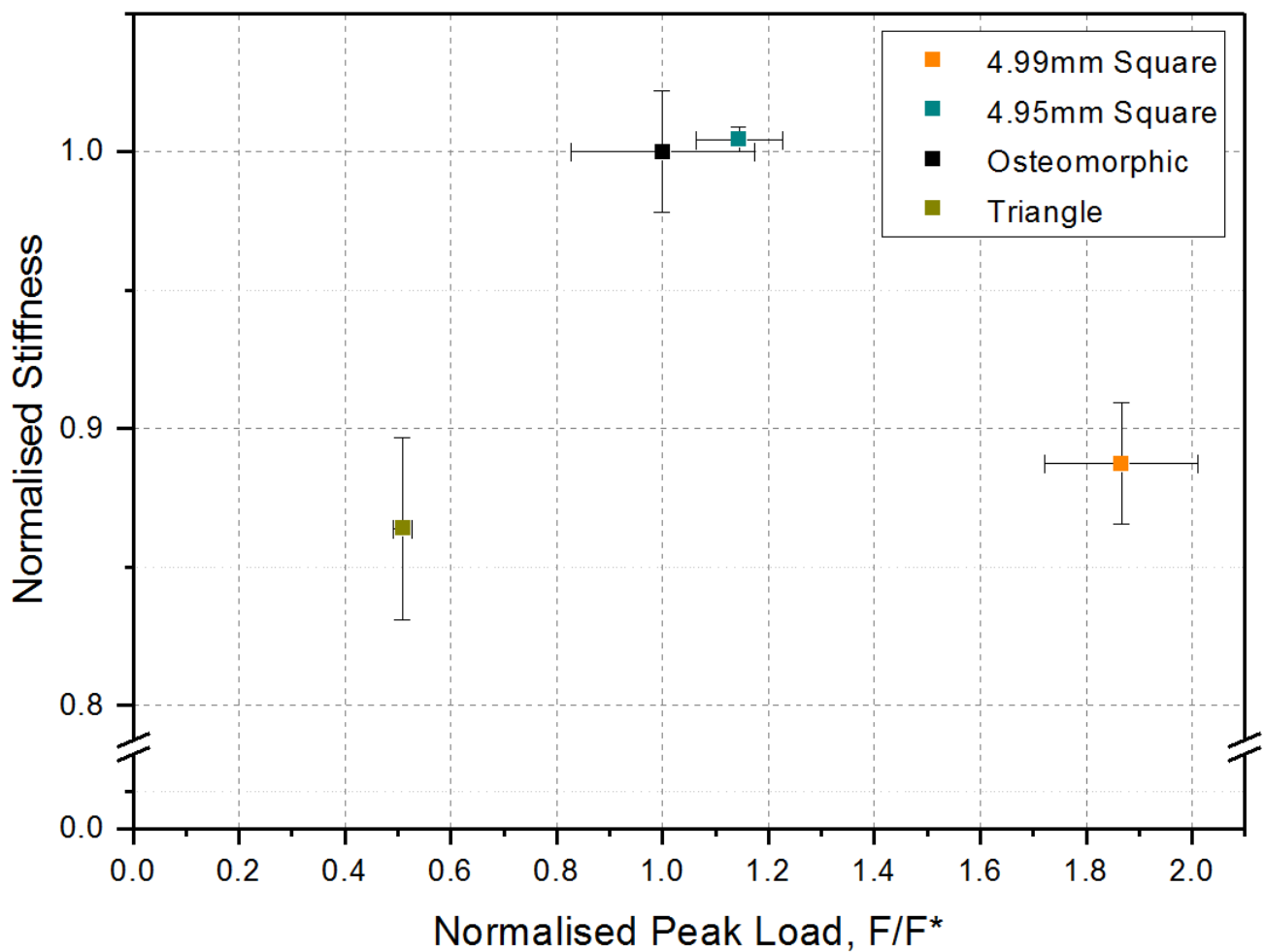


Figure 5.8 – Experimental peak load and stiffness for assemblies with modified geometry, normalised with respect to the peak load and stiffness of a reference assembly of osteomorphic blocks. The error bars indicate the scatter in the data. Stiffness is taken as the tangent at 0.01 normalised displacement

After a peak, a gradual decrease in load is observed for the osteomorphic and straight triangle block assemblies until their failure occurs at 0.195 and 0.183 normalised displacement, respectively. In contrast, the H+ assembly fails in a more brittle manner (Figure 5.7 b). The point at which failure occurs depends upon the tightness of fit (4.99 mm vs. 4.95 mm block size), as does the peak load and the accompanying displacement. The brittle failure of the H+ assembly was found to be confined to five blocks in the middle (the central block and the four adjacent ones). A greater amount of local plastic deformation was also detected in the H+ blocks at the indentation point on the central block and its neighbours as compared to other assemblies (Figure 5.7 b). In addition to increased peak load,

enhanced energy absorption or toughness modulus, as represented by the area below the load-displacement curve, was observed for the two H+ block assemblies. This might be associated with increased plastic deformation or propensity for damage of the blocks – a proposition that needs to be tested in future experiments on different materials. We note, however, that blocks of the osteomorphic and straight triangle assemblies exhibited only small amounts of damage at failure (Figure 5.7 b).

Figure 5.7 a also shows computational results for the three different geometries considered. The experimental and computational results for osteomorphic block assembly are in very good agreement and diverge only slightly at the point of final failure, likely due to the exclusion of damage and plasticity from the simulation. The results for the square block assembly also provide reasonable agreement, the simulation slightly overestimating the load, again most probably due to some plastic deformation of the material not considered in the simulations. Finally, there is a greater discrepancy between the computational and experimental results for the triangular block assembly. This could be attributed to differences in the interface behaviour, primarily the difference in static and kinetic friction occurring at a normalised displacement of about 0.1. The penalty-based interaction of the simulation does not account for this, with negligible static friction observed. Overall, however, the simulations agree well with the experiments, at least qualitatively and semi-quantitatively, which means that they capture well the mechanics of the assembly, as shown in Figure 5.6. Furthermore, it should be noted that the simulations are the only tool for validating our hypotheses related to different mechanisms of interaction of the interfaces.

The systems with modified geometry are also included in Figure 5.6 which displays the slip behaviour of the central blocks under loading based on FEA results. We observe similar trends to those stated in the foregoing section, with a clear correlation between load bearing capacity and slip. In Figure 5.6a, at normalised displacement of 1.0, we observe that the osteomorphic sample has experienced approximately 0.23 slip while the triangle assembly has undergone 0.35, and the square sample less than 0.05 slip. Additionally, the images presented in Figure 5.6b show visually the different slip characteristics of the different assemblies and exhibit a large displacement of the central block observed in the triangle

and osteomorphic assemblies at 1.0 normalised displacement. By contrast, the square sample shows negligible slip at this displacement.

5.4 Discussion

The results presented here link the effect of geometry to deformation mechanics and hence mechanical properties for topological interlocking assemblies. Previous numerical examples from Yong [98] investigated some variations in the amplitude of osteomorphic surface curvature, which modified the initial mechanical response (prior to peak force) under point loading, however did not relate these results to any mechanism other than an increased ability to transfer load. Additionally, Mirkhalaf et al. [105] modified the interlocking angles of an assembly of glass truncated tetrahedra under impact loading from 0° to 10° . All samples showed a large increase in the impact energy when compared to monolithic glass, however above an interlocking angle of 2.5° there was little change in the impact energy of the various assembly.

Previous studies by Brugger et al. [106, 108] and Duguè et al. [103] refer to a “master curve” where for a fixed geometry the same shape of the load-displacement curve is achieved, regardless of variations of material properties, block size etc. The present study highlights the ability to modify this behaviour by geometry variations, showing that a master curve is only valid for a single geometry. The results presented here show that by manipulating the ability of the constituent blocks of topological interlocking assemblies to slip relative to one another, better control of the mechanical response of this class of materials can be obtained.

The hierarchical interlocking results suggest that the effect of slip is critical to the overall performance of the assembly, as it appears that by delaying the onset of significant slip, the overall peak load can be increased. This hypothesis was tested by designing blocks (H+ blocks) that would suppress slip entirely. Indeed, we observed that no softening of topological interlocking assemblies occurs when slip is absent, hereby directly linking softening with slip

in topological interlocking assemblies for the first time. This is an important finding, and one that will enable better design of these types of structures moving forward.

In the current chapter, blocks surface geometry as well as the block geometry, were designed specifically to explore how the shape of interface between blocks can be used to control the deformation mechanics, and hence the mechanical properties. In Chapter 4, the manipulation of the interaction between the blocks was achieved by modifications to the coefficient of friction (amongst other parameters). Other techniques to manipulate these interactions are explored in Chapter 6, namely the use of a soft interfacial layer between blocks to adjust the mechanical characteristics.

An important outcome of our study is the recognition that the mechanical response of ensembles of topologically interlocked blocks is determined by different modes of block interaction, including tilt/bend, slip, and plastic deformation, and that the relative contributions of these modes depend on the block geometry.

5.5 Conclusions

This work provides crucial insight into the mechanical response of topological interlocking assemblies under point loading. The key outcomes of the work can be summarised as follows. A secondary surface geometry was introduced to non-planar blocks to create an additional interlocking effect between neighbouring blocks at a new length scale, referred here as hierarchical interlocking. Experimental results suggest that the hierarchical features associated with patterning of the interlocking block surfaces cause a delay of the onset of slip of the central block under concentrated load and an attendant increase in the maximum load bearing capacity of the overall assembly. This concept was further tested by designing and testing new topological interlocking blocks, termed the H+ block, which ruled out slip. The tests showed that without slip, topological interlocking assemblies with a sufficient global constraint, could not “soften” – linking the two mechanisms for the first time.

Computational results demonstrated that the slip mechanism is correlated with the mechanical behaviour of these geometrically complex assemblies.

In summary, this study showed that geometrical modifications to the original osteomorphic block and patterning of the block surfaces provided a way to manipulate the deformation mechanisms of topologically interlocking assemblies, thereby controlling the mechanical response under point loading. These new insights gained from the computational modelling and experimental data enable design of topological interlocking structures with tailored mechanical properties in the future.

6. Mechanical Performance of Bioinspired Hybrid Structures Utilising Topological Interlocking Geometry

6.1 Introduction

Previous chapters in this thesis have highlighted the importance of the interface between topological interlocking on the mechanical response of the overall assembly. In Chapter 4, a link between the coefficient of friction and the deflection to peak load suggested an interesting relationship between the block interface and the deformation mechanisms. This connection was explored further in Chapter 5 via modifications to the geometry of the building blocks themselves and their surface morphology, showing that these modifications could directly affect deformation mechanisms, and hence the mechanical response of these assemblies. Indeed, the relationship between block interface and mechanical performance in the context of topological interlocking provides many potential avenues of controlling the properties of the assemblies.

One such opportunity lies in structural composites inspired by bone and nacre which have emerged as exemplars for guiding materials design of fracture-resistant, rigid hybrid materials. In particular, the intricate structure of nacre, which combines a hard majority phase with a small fraction of a soft phase, achieves superior mechanical properties compared to its constituents and has generated much interest [8, 52, 137]. In this work, the concepts of topological interlocking and soft interfacial materials (based off the analogous nacre) will be used to create new hybrid materials, with fine architectural control possible by using additive manufacturing. The *three-dimensional* osteomorphic block geometry offers itself as a basis for such design, as it resembles the natural surface waviness found in the

aragonite platelets in nacre. This waviness creates a simple form of mechanical interlocking (a mechanism separate from the topological interlocking mainly considered here) between the platelets that plays an important role in the mechanical behaviour of nacre.

In this chapter, synthetic hybrid structures are designed and manufactured using state-of-the-art 3D printing technology, permitting the integration of multiple materials with widely contrasting mechanical properties. The use of multi-materials is hypothesised to greatly affect the mechanical response of topologically interlocked assemblies.

This chapter will firstly present multi-material assemblies similar in size and shape to those previously reported in Chapters 4 and 5, and which will also be tested in a similar manner, that is, concentrated out-of-plane loading. The design of the fabricated hybrid structures was guided by work from the previous chapters.

Following this, mode I tensile testing will be employed to investigate the mechanical properties relating to crack propagation within these assemblies. Previous work in this area has primarily focussed on structures for which the shape of the individual blocks did not vary in the direction normal to the plane of assembly, essentially considering two dimensions [16, 57, 59, 79, 138]. This work extends these concepts by using building blocks with more complex geometries, allowing for shape variation in the direction *normal* to the block plane.

Below, the results of two types of experimental investigations of the mechanical behaviour of the novel topological interlocking structures fabricated by additive manufacturing are reported. Also presented are the outcomes of computational work carried out to support the Mode I tensile experiments and better understand the mechanical response of the nacre-inspired structures with topologically interlocked hard building blocks.

6.2 Design and Motivation

The chapter comprises two primary sections, relating to the different modes of deformation:

- 1) Out-of-plane loading of multi-material structures, based upon the designs previously reported in Chapters 4 and 5,
- 2) Mode I tensile testing of specially designed hybrid materials.

Both sections use the same additively manufactured component materials as those previously used in Chapters 3 to 5. VeroWhitePlus (VW+) was once again employed as the primary stiff material, with the rubber-like material TangoBlackPlus (TB+) used as the soft, compliant phase (more detail on the material properties can be found in Chapter 3).

Fabrication and testing of specimens under out-of-plane point loading was conducted as in Chapters 4 and 5. The blocks had dimensions of 20 mm x 20 mm x 10 mm and were assembled into plates with dimensions of 160 mm x 150 mm, which were loaded by a point indenter with a 7mm diameter. A set of individual blocks were printed with a coated surface layer with varying thicknesses, from 0.5 mm to 0.05mm, to determine the thinnest achievable soft phase coating of the interfacing surfaces, as shown in Figure 6.1a. The optimum thickness of 0.4 mm was selected, as it provided the block with a consistent thickness of soft phase coating. While a thinner soft phase coating was achievable, due to the curved geometry of the block the coating was found to vary in thickness, with certain sections of the surface coating not able to be manufactured by the printer due to resolution limits. This effect is due to the varying surface angles of the block in relation to the print bed. These surfaces are often referred to as the “upskin” and “downskin” of an additively manufactured part, which is a common phenomenon observed in the additive manufacturing process leading to variation in design vs fabricated samples [139]. The individual blocks were assembled into a plate and held in place by a frame, as used previously.

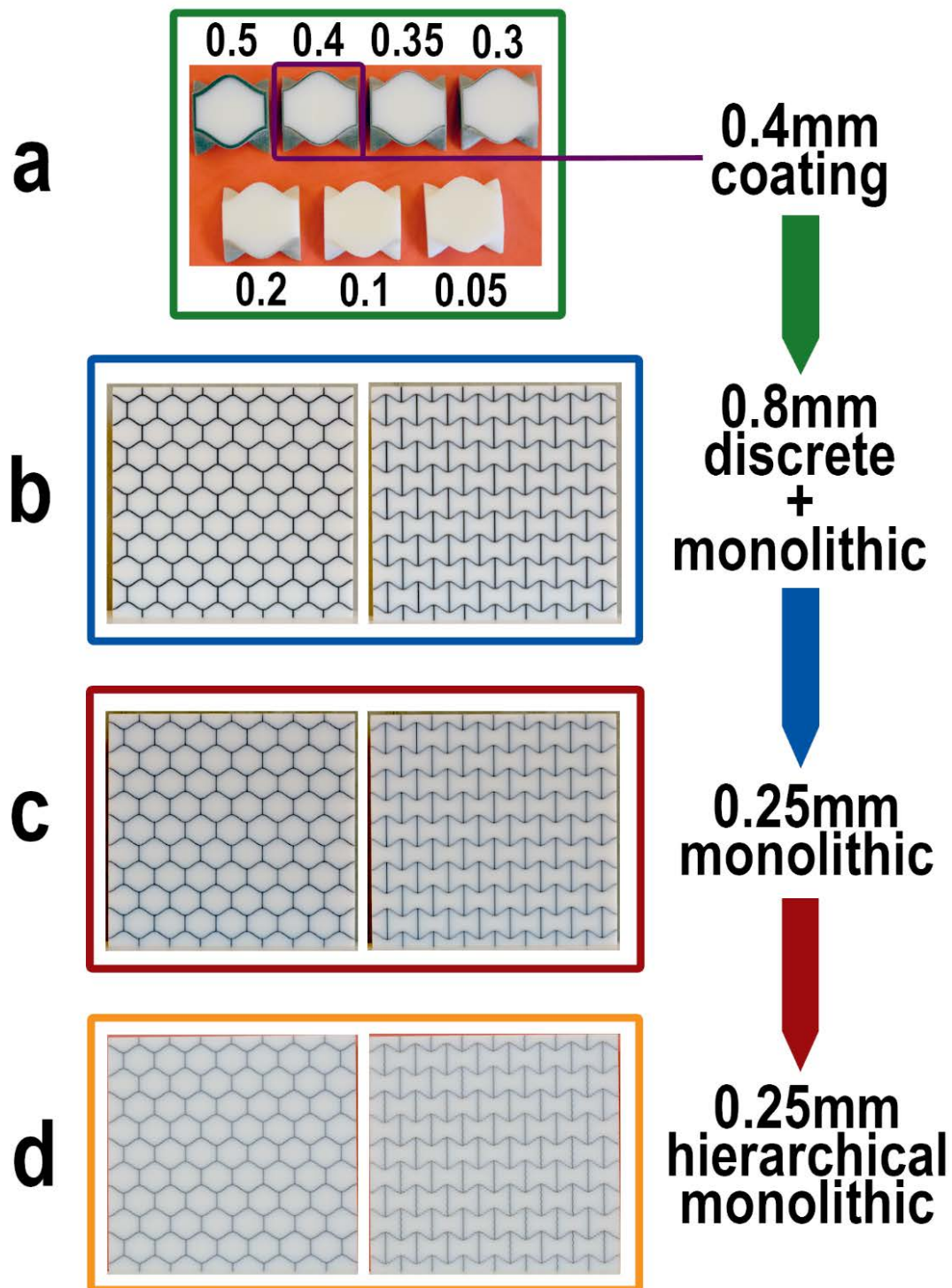


Figure 6.1 – Outline of geometries and assemblies tested in section 6.3, all images show printed samples, white = stiff, black = soft. a) multiple individual osteomorphic blocks with a soft phase coating on interlocking interfaces, varying in thickness between 0.05 mm – 0.5 mm. Coating thickness of 0.4 mm was selected as an optimum one. Block size 20 mm x 20 mm x 10 mm. b) assemblies with a soft interface layer of 0.8 mm between blocks, achieved

either through discrete blocks with 0.4 mm coating or single piece printed assembly. c) single piece assembly with minimum achievable interface thickness of 0.25 mm. d) monolithic plate with hierarchical interlocking geometry from Chapter 5 with 0.25 mm soft interface. b) to d) assembly size approx. 160 mm x 150 mm, small variation with different thickness interface

A monolithic version of this assembly was designed and printed to serve as a comparison between discrete and continuous multi-material structures (Figure 6.1b). The thickness of the soft interface in a continuous specimen was then minimised, with a thickness of 0.25 mm found to give a consistent result when embodied in a monolithic design (Figure 6.1c). This difference between discrete and continuous achievable soft phase thickness is believed to be a function of the material jetting process, whereby the “upskin” and “downskin” angles of the discrete block are not present in a continuous sample, which is enclosed by stiff material.

Finally, in Section 6.3, a multi-material version of the “all” surface hierarchical structure presented in Chapter 5 was designed and fabricated with a 0.25 mm soft phase thickness (Figure 6.1d). This sample utilises two bioinspired concepts (structural hierarchy and soft-and-hard phase composition) in order to compare the effect of hierarchical interlocking geometry in this multi-material study.

The second part of the study, utilising Mode I tensile testing, involved designing and fabricating specimens in the form of flat panels with the soft phase comprising approximately 13.5% by volume, with an in-plane thickness of 250 μm . The dimensions of the samples were 64.75 mm x 58.5 mm and 3.125 mm in thickness. The specimens were fabricated with 10 blocks along the tensile direction and 24 blocks across the specimen. The four block geometries presented in Figure 5.2 had the same dimensions and the printed blocks were of the same volume.

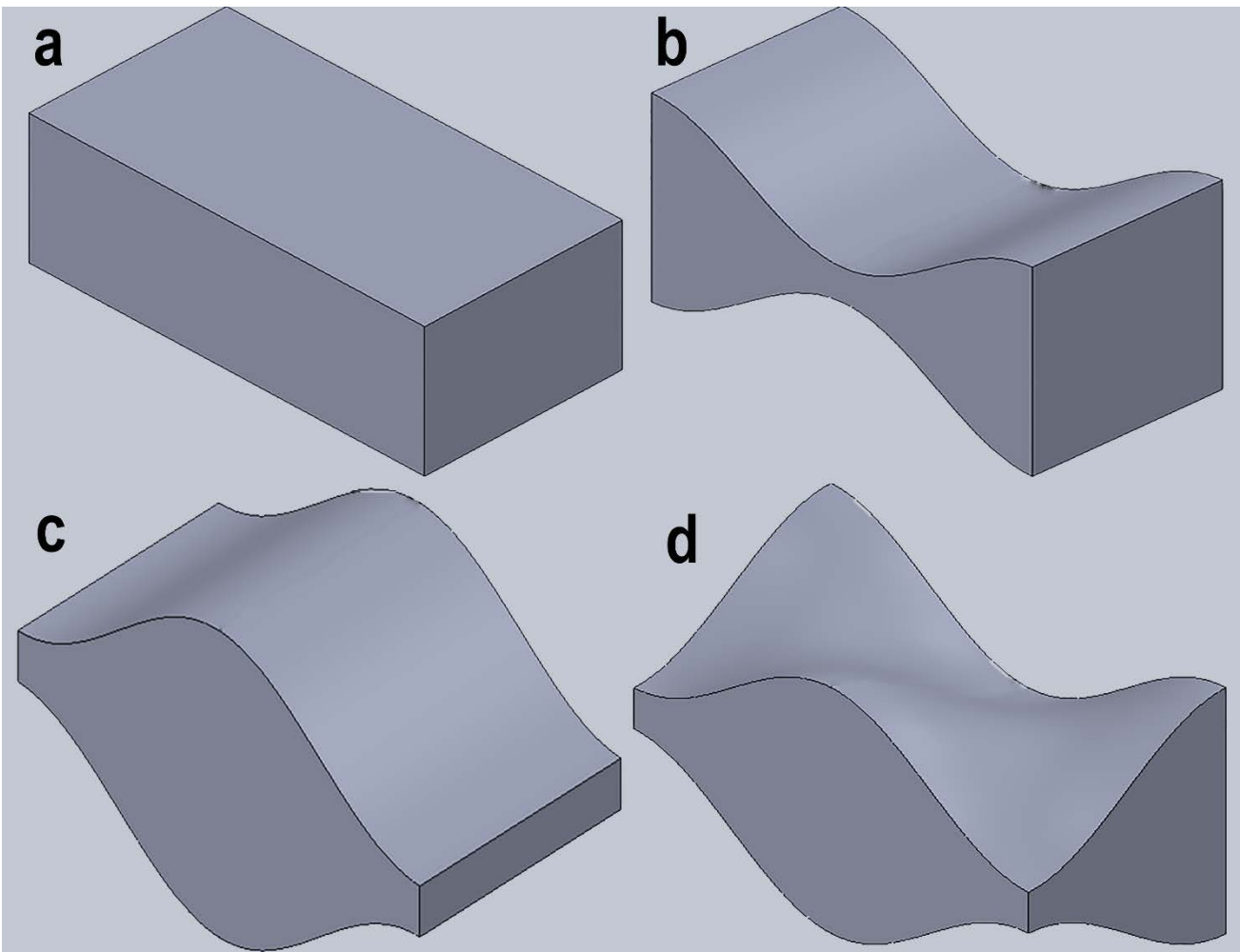


Figure 6.2 – Principal building block geometries used in specimens for testing in Section 6.3.2. (a) rectangle or standard brick used as a reference in the brick-and-mortar structures printed; (b) “hourglass” and (c) “smooth honeycomb” represent the two opposite faces of the osteomorphic block shown in (d). The size of each block pictured is 6.25 mm in length and 3.125 mm in width. Note that the cross-sections of the blocks in figures (b) and (c) do not change along the straight lines drawn in the figures. Assemblies based on these geometries are therefore referred to as two-dimensional. By contrast, the cross-section of the osteomorphic block (d) transforms along the direction normal to its face: a crest at the front face corresponds to a minimum at the back face. The shape presented in (d) provides the structure with the three-dimensionality that is crucial for its mechanical performance

Mechanical characterisation involved single edged notched tensile (Mode I) testing of the specimens in triplicate at a minimum for each geometry. The samples were printed with

notches (9.745 mm by 0.79 mm), without the need for additional cutting prior to testing. Failure of the specimens always occurred at the notch tip, which indicated that the printed notch was sufficiently sharp. The specimens were tested using an Instron 4505 testing machine with a 20 kN static load cell. The samples were printed with specifically designed “knurled” VW+ sections at either end of the architected sample region. The size and shape of these knurled sections were intended to minimise slippage in the machine’s grips when applying the tensile load. Testing was conducted with 3 mm/min displacement rate. It is important to note that these testing conditions did not follow any established standard; rather, the experimental procedure used by Dimas et al. [16] in their study of brick-and-mortar structures was adopted.

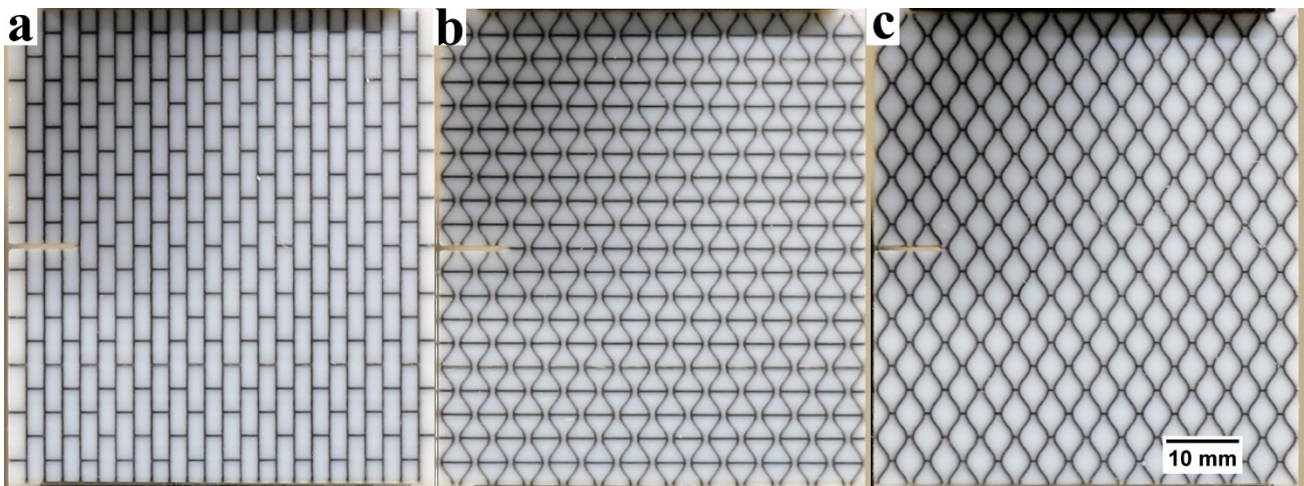


Figure 6.3 - Images of additively manufactured specimens used for Mode I fracture testing. The dimensions of specimens are 64.75 mm x 58.5 mm with a thickness of 3.125 mm. The volume fraction of the soft phase is approximately 13.5 ± 0.1 % for all samples. (a) Bricks-and-mortar sample, representing a simplified nacre structure; (b) and (c) “hourglass” and “smooth honeycomb” samples: the respective motifs of the surface tessellations of these samples correspond to the two opposite faces of an osteomorphic block, as seen in Figure 5.2d. Further details of the samples are given in Section **Error! Reference source not found.** Note that the sample consisting of interlayered interlocked osteomorphic blocks, which was also tested, is not shown, as it appears identical to the samples in (b) or (c) depending on which side is viewed

6.3 Results

6.3.1 *Out-of-plane Loading*

The results of concentrated point loading of the various multi-material specimens are presented in Figure 6.4. This plot shows the results for a reference assembly (as used previously in Chapters 4 and 5) in dark yellow, as well as the solid plate results in black to give context to the multi-material results. The green curve shows the effect of the soft phase surface layer on the discrete blocks, which is seen to cause a significant decrease in peak load (110 N) and stiffness (47 N/mm) as compared to the reference assembly (495 N and 171 N/mm, respectively). The continuous or monolithic version of this assembly, represented by the blue curve, shows an increase in peak load (305 N) and stiffness (125 N/mm), compared to the discrete assembly, although it is still significantly lower than for the single-material reference assembly. The shape of the blue curve is quite different from that for the reference assembly, with the peak load being reached at a much lower displacement (approximately 4 mm vs 11 mm, respectively) and a larger softening region is observed.

The effect of the interfacial layer thickness is represented in the difference between the red (0.25 mm) and blue (0.8 mm) curves in Figure 6.4. The red curve displays a large increase in peak load (1151 N) and stiffness (567 N/mm) compared to both the reference assembly and a similar monolithic sample with a thicker interfacial soft layer. The increase in peak load for the 0.25 mm monolithic specimen over the reference assembly and a 0.8 mm monolithic sample is substantial, more than doubling and tripling the peak load, respectively. The shape of the red curve is also similar to that of the blue curve, with peak load occurring at approximately 3.5 mm displacement followed by a drop in load and a large softening region.

The addition of the hierarchical interlocking geometry leads to a significant increase in peak load (1810 N), as shown by the orange curve in Figure 6.4, over the standard osteomorphic geometry (shown in red). This increase in peak load however, is not accompanied by a significant increase in the stiffness, which is only slightly higher (653 N/mm). This supports

the results presented in Chapter 5 related to the effect of hierarchical interlocking on the mechanical properties of discrete assemblies of osteomorphic blocks.

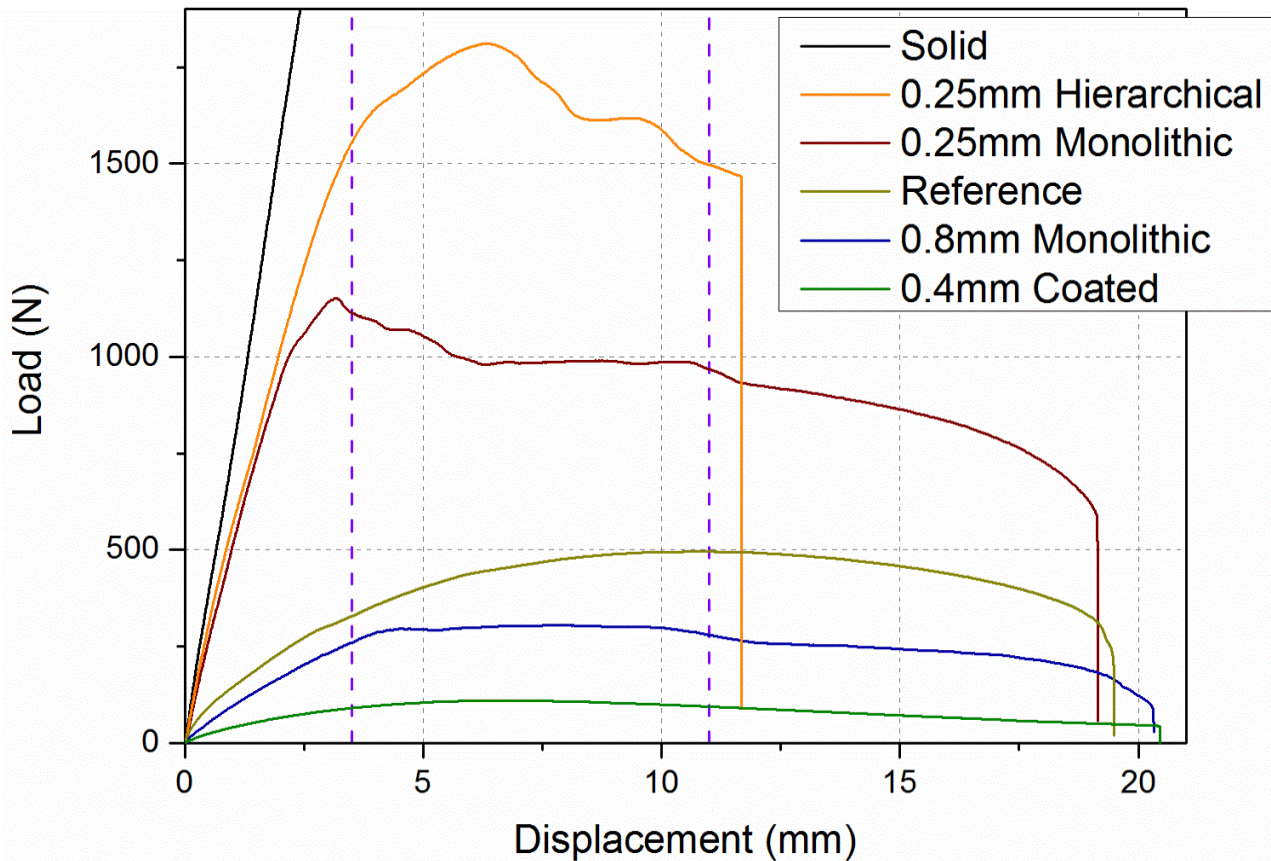


Figure 6.4 – Plot of load vs displacement for out-of-plane loading of various multi-material assemblies. Reference assembly (as used in Chapter 4) shown in dark yellow. Discrete blocks coated with 0.4mm soft phase sample shown in green, with monolithic comparison (0.8mm soft phase) shown in blue. Monolithic sample with 0.25mm thick soft phase shown in red, with hierarchical comparison (same soft phase) shown in orange. Dotted purple lines are referred to in discussions below

The failure of the monolithic hierarchical structure occurs at a displacement (approximately 12 mm) which is significantly smaller, when compared to the other assemblies (approximately 20 mm). This is characterised by failure through the stiff phase of the structure, as shown in Figure 6.5c. This type of crack propagation does not occur in the other samples (Figure 6.5a and b), with ductile-like damage to the soft phase observed instead.

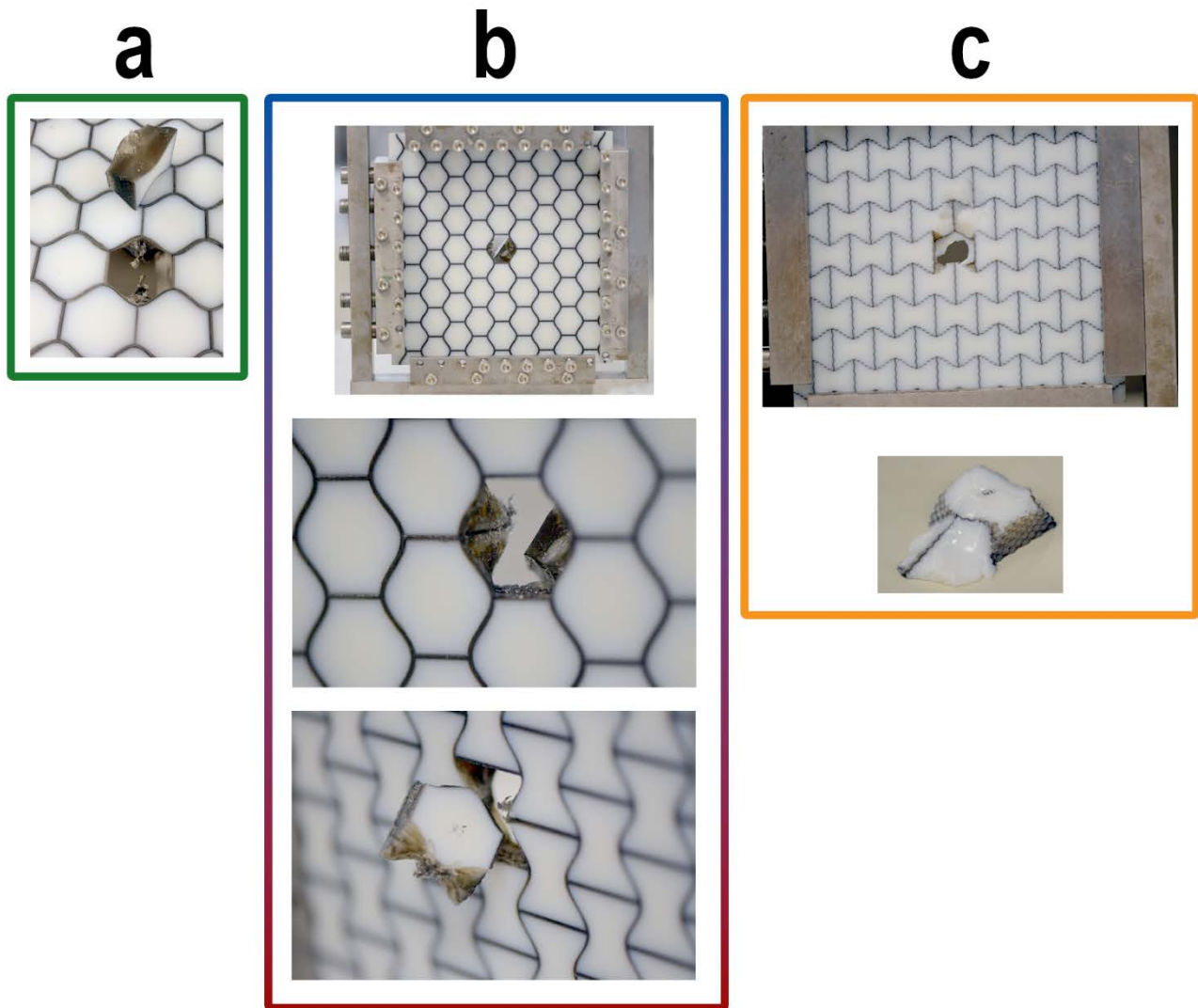


Figure 6.5 – Selection of post-failure specimens. a) and b) shows damage to soft phase coating between blocks, while c) shows that cracking was able to propagate through the stiff phase leading to an earlier failure compared to other geometries

Indeed, the shape of the monolithic specimens (shown in blue, red and orange in Figure 6.4) shows a different loading profile, when compared to the discrete assemblies. In these monolithic structures we observe, earlier displacement to peak load, followed by a sharp decrease in load, compared to the reference assembly. In Chapter 5, where the deformation mechanisms of tilt/bend, slip and damage were discussed, it was hypothesised that at the approximate displacement highlighted by the first dotted purple line (roughly 3.5 mm), the first instance of “slip” between the central block and neighbouring blocks can be observed.

The initial tearing of the soft phase (c.f. Figure 6.5b) resulted in a more drastic decrease in load than the relative smoothness of the stiff, discrete assembly. In the hierarchical structure, the displacement at which this occurs is at a greater displacement (approximately 7mm) due to the additional interlocking of the surfaces, discussed in more detail in Chapter 5.

At approximately 11.5 mm displacement, we observe multiple changes in the different loading curves in Figure 6.4:

- the reference assembly reaches the peak load;
- the two non-hierarchically interlocked monolithic specimens show a noticeable drop in load;
- the hierarchical sample fails.

These three observations, taken together, suggest a critical mechanism is occurring at this displacement, which is slightly greater than the thickness of the structures (10 mm). Previously in Chapter 5, this was suggested to be a result of the slip mechanism becoming dominant compared to the tilting/bending mechanism. The above results appear to support this hypothesis, as we would expect the soft phase to give rise to more significant drops in load due to the relative “stickiness” (i.e. higher coefficient of friction) of the soft phase, when compared to the stiff material in the reference assembly. The sudden, brittle failure of the hierarchically interlocked specimens indicates that the force required for the blocks to slip past one another in this design generates a stress greater than the strength of VW+, leading to failure through the stiff blocks. The combination of hierarchical interlocking and interfacial soft phase has a similar effect on the H+ blocks (presented in Chapter 5), whereby most of the slip is suppressed. As this failure occurs at approximately the same displacement as the other observations mentioned above, it seems to indicate that the slip begins playing a greater role in deformation at this stage of loading. This hypothesis would require further work to be confirmed, however it certainly supports the mechanisms proposed earlier in Chapters 4 and 5.

6.3.2 *Mode I Tensile Loading*

The experimental setup for the second study differs slightly from that described in the previous section, with four principal geometries selected for testing, as shown in Figure 5.2. The brick-and-mortar design (Figure 5.2a) emulating nacre was used as a reference due to recent interest it has garnered [50]. However, the main focus of this study is on the effect of three-dimensional interlocking offered by the *osteomorphic* design (Figure 5.2d). In order to verify the ability of 3D design of a building block to enhance mechanical properties of the assembly, two other types of block shape were also developed, based on the surface profiles of the two opposing faces of the osteomorphic block. These are termed “hourglass” (Figure 5.2b) and “smooth honeycomb” (Figure 5.2c). The hourglass design in particular bears some resemblance to the “dovetail” features found in nacre [57]. The dimensions of the building blocks were kept constant across specimens, with an aspect ratio of approximately 2.9. It is important to note that the dimensions selected did not reflect the aspect ratios and stiff-to-soft volume fraction ratios found in nacre, nor are they the focus of this work. While other works have addressed the optimisation of these parameters, [60, 140] the present study concentrated on the shape of the stiff blocks as a means to improve the mechanical performance of the assembly over the nacre-inspired structure.

Mode I fracture tests were conducted on 3D printed notched specimens (Figure 5.4) which combine the stiff (VW+) and the soft (TB+) materials, in a nacre-like fashion. The geometry of these assemblies was motivated by the work by Dimas et al. [16] on brick-and-mortar and related two-dimensional bioinspired structures. The new block in this study was the specially-designed shape of the hard blocks described above. The details of the printing process and the materials used are outlined in the Chapter 3.

Mechanical testing of these specimens returned results (Figure 6.6) which showed the osteomorphic design to have improved mechanical properties. Indeed, the stress-strain curves for the geometries tested demonstrate the osteomorphic block to have an increased strength, ductility and modulus of toughness when compared to the simple brick-and-mortar (Figure 5.4a) or nacre-like samples (Figure 5.4b and c). The hourglass geometry results also show a large increase in peak stress. It should be noted that our stress-strain results

for brick-and-mortar structure are in reasonable agreement with those previously reported, with an allowance for differences in the experimental procedure and the aspect ratios of stiff blocks [16]. Hourglass and osteomorphic samples exhibit very similar values of peak stress. This suggests that interlocking in the direction of loading of the hourglass assembly (along the long axis of the blocks) is the predominant mechanism that leads to a high peak stress. Indeed, interlocking of the hourglass blocks in this orientation hinders slipping of the blocks in a similar (albeit not identical) way to the interlocking of osteomorphic blocks.

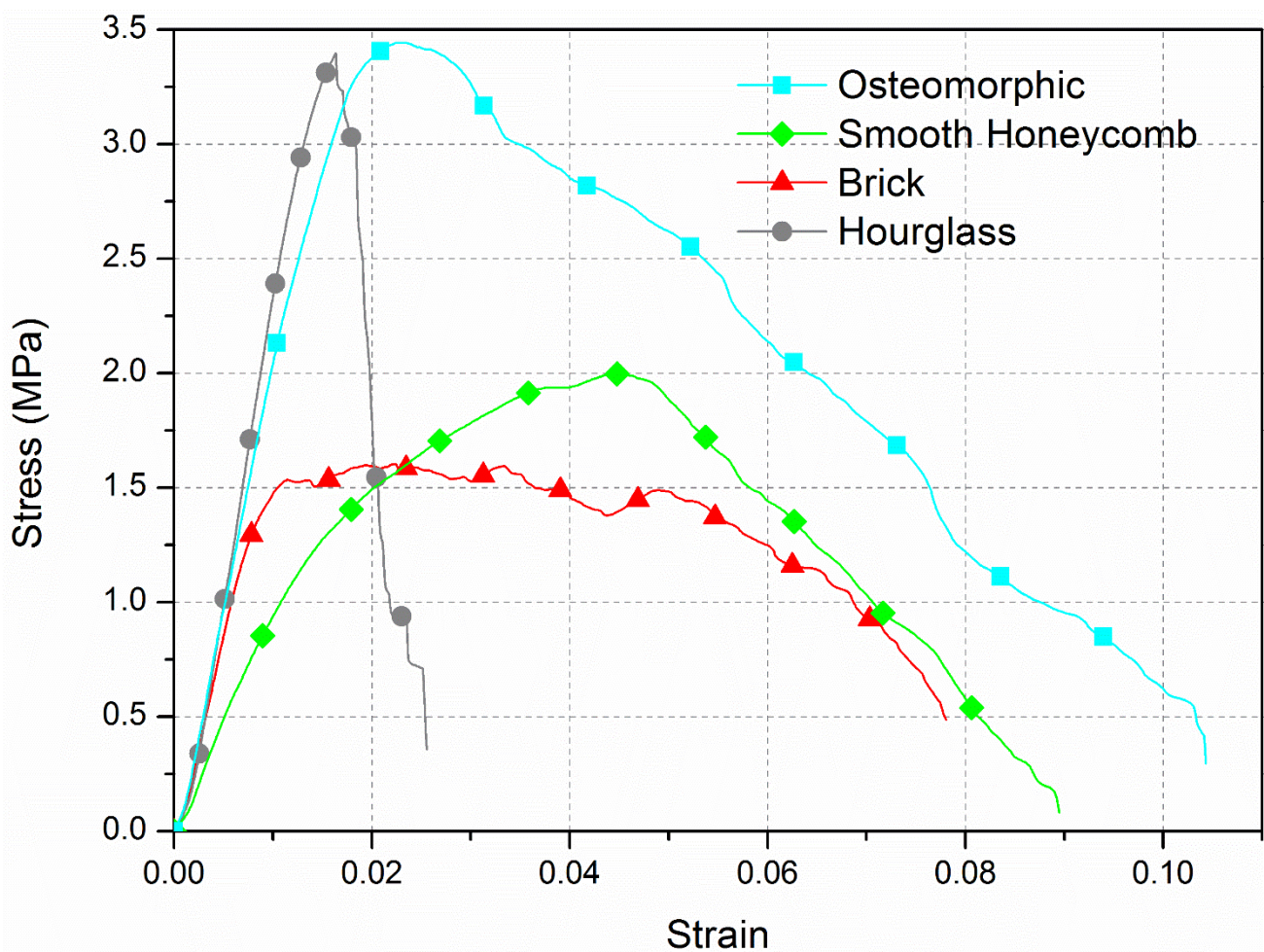


Figure 6.6 – Comparison of representative stress-strain curves for the four geometries. This plot illustrates the increase in peak stress, strain at failure, and modulus of toughness of the osteomorphic specimen, as compared to the bricks-and-mortar structure. The effect of the high peak load appears to be associated with interlocking, as it is the greatest for the “hourglass” and the “osteomorphic” cases – both involving interlocking

As evident from Figure 6.6, a near doubling of both the peak stress and the elongation to failure can be observed, the osteomorphic structure exhibiting a superior performance compared to that of the brick-and-mortar structure. Figure 6.7 shows a plot of modulus of toughness (as measured by the area under the stress-strain curve) vs. peak stress. It can be seen that the assemblies made from osteomorphic blocks exhibit improvement in both modulus of toughness and peak stress over the traditional brick-and-mortar design.

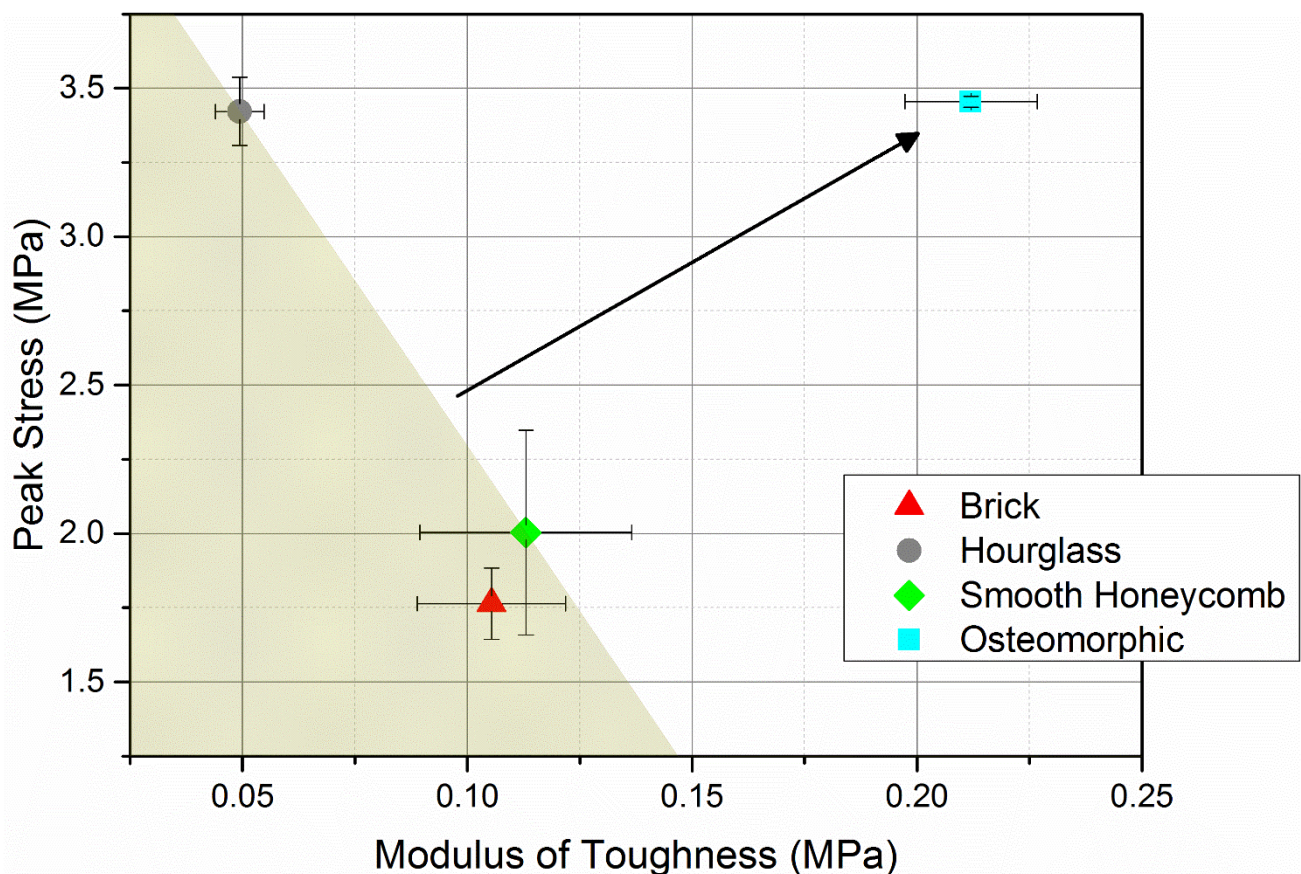


Figure 6.7 – Plot of modulus of toughness (as measured by the area under the stress-strain curve) vs. peak stress. Doubling of both modulus of toughness and peak stress achieved with the osteomorphic geometry is seen. Improvement of both characteristic properties due to the osteomorphic design is highlighted by the arrow. The shaded area highlights the improved mechanical properties due to the “combination” of hourglass and smooth honeycomb geometries

The fracture paths in the samples tested are shown in Figure 5.7 . These images reveal that failure surfaces of osteomorphic, brick-and-mortar, and smooth honeycomb structures follow a similar fracture path. This suggests that the fracture path itself is not a sole factor in the improved modulus of toughness of the osteomorphic sample, as the mechanical responses for these designs vary significantly. These fracture patterns are relatively simple as compared to those in natural nacre, with less changes of direction or zigzagging, as one could expect from the lower aspect ratio of the building blocks in our synthesised structures. Delocalisation of stress around the crack tip was observed in all specimens (Figure 5.7) except for the hourglass shape with its concave geometry. The hourglass geometry is unable to provide resistance to the concentration of the tensile stress around the thin waist of a block, leading to early fracture of these blocks (stiff phase). Indeed, failure through the soft phase, rather than the interface between the soft and stiff phases (delamination), was observed for all specimens, except for the hourglass ones.

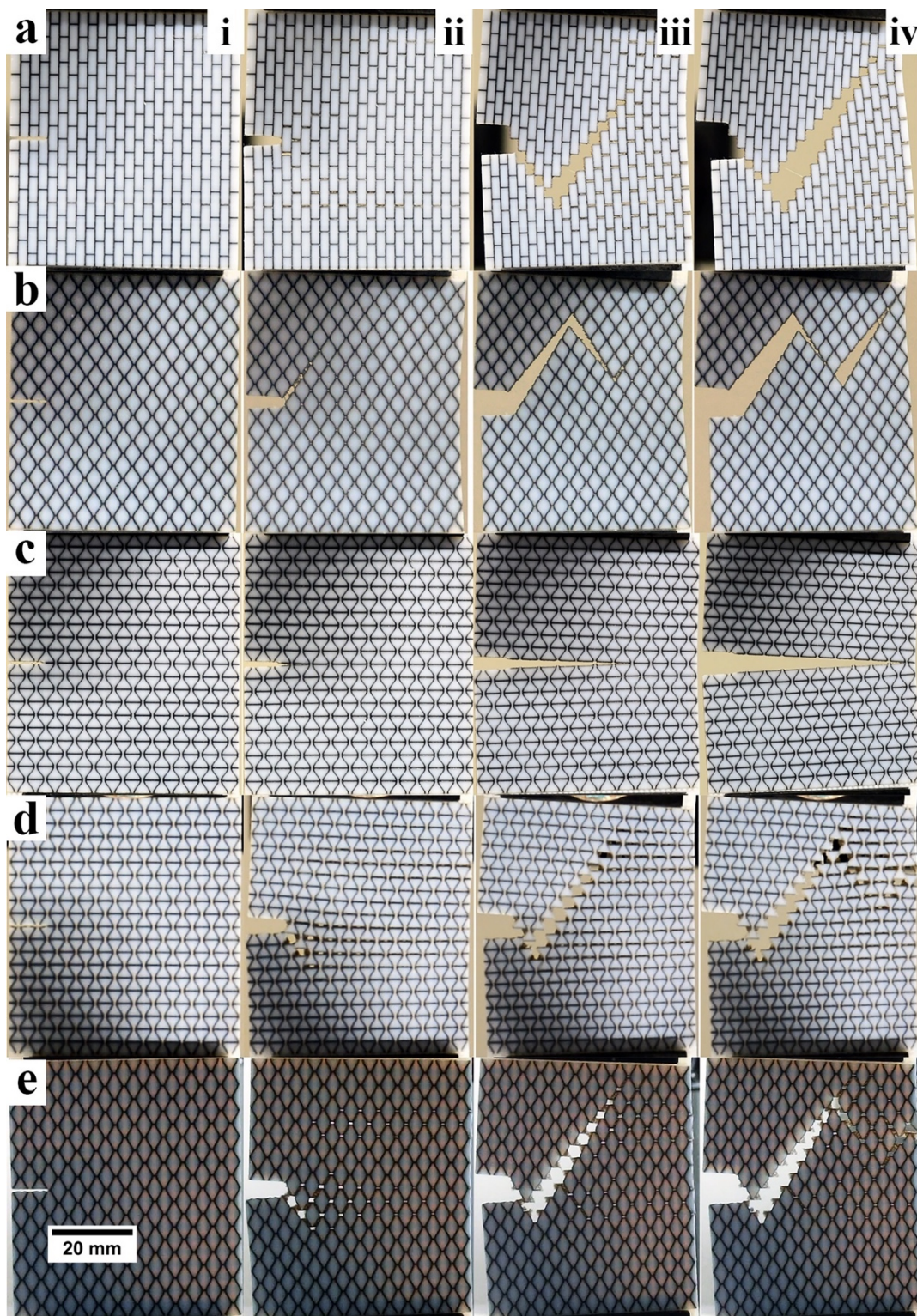


Figure 6.8 - Images of fracture sequence during experimental testing for a) brick-and-mortar, b) smooth honeycomb, c) hourglass, d) osteomorphic – hourglass side, e) osteomorphic – smooth honeycomb. The images represent the four characteristic stages of fracture i) initial state, ii) crack initiation, iii) crack propagation, iv) failure. Areas of stress delocalization are

observed in all samples except c). Of particular note are these areas observed in the ii) stage of testing. Similarities in fracture paths is also observed in iv) for all samples except c)

Computational work was undertaken to gain a qualitative insight into some of the observed experimental results and the mechanisms involved. Three-dimensional finite element simulations were conducted to investigate the stress distribution in the area around the crack initiation site, as it was of particular interest for the mechanical performance of the specimens (Figure 5.8). This critical area focussed on two geometries that exhibit interlocking capabilities, viz. hourglass and osteomorphic. The scope of this work was not to precisely simulate the actual experimental testing, but rather to gain a qualitative insight into the stress distributions in ensembles of interlocked blocks at the initial stages of experimental testing, i.e. at the onset of brittle failure in the hourglass specimen. This was achieved by applying a tensile load of a magnitude similar to that at which brittle failure occurred experimentally in the hourglass geometry (involving an approximately 1mm displacement), to a notched planar assembly of interlocked blocks from around the crack initiation site (a region highlighted in Figure 5.8a, b and c). The soft phase was not included in the simulations, as the primary focus of the numerical work was limited to the analysis of stress distributions around the potential crack initiation site, which led to brittle failure in hourglass assemblies but not in osteomorphic ones. The latter failed through the soft phase, as the stress concentration zone was confined to a small volume at the edge of an block, see below. Due to the lack of adequate models at this scale, particularly for the soft phase, simulation of the mechanical responses of the hybrid materials was beyond the scope of this work and will be the subject of proposed future research. The blocks were modelled as linear elastic materials with an elastic modulus $E = 1.8 \text{ GPa}$ and Poisson's ratio $\nu = 0.39$, as derived from previous experimental work. The coefficient of friction between the blocks was set at a high value, $\mu = 1.0$, to emulate the 'stickiness' effect of the soft, elastomeric matrix. The simulations did not proceed to the stage of crack propagation, where the cohesive effect of the soft phase predominates. This high coefficient of friction thus acts to approximate the initial relative movement of the stiff blocks.

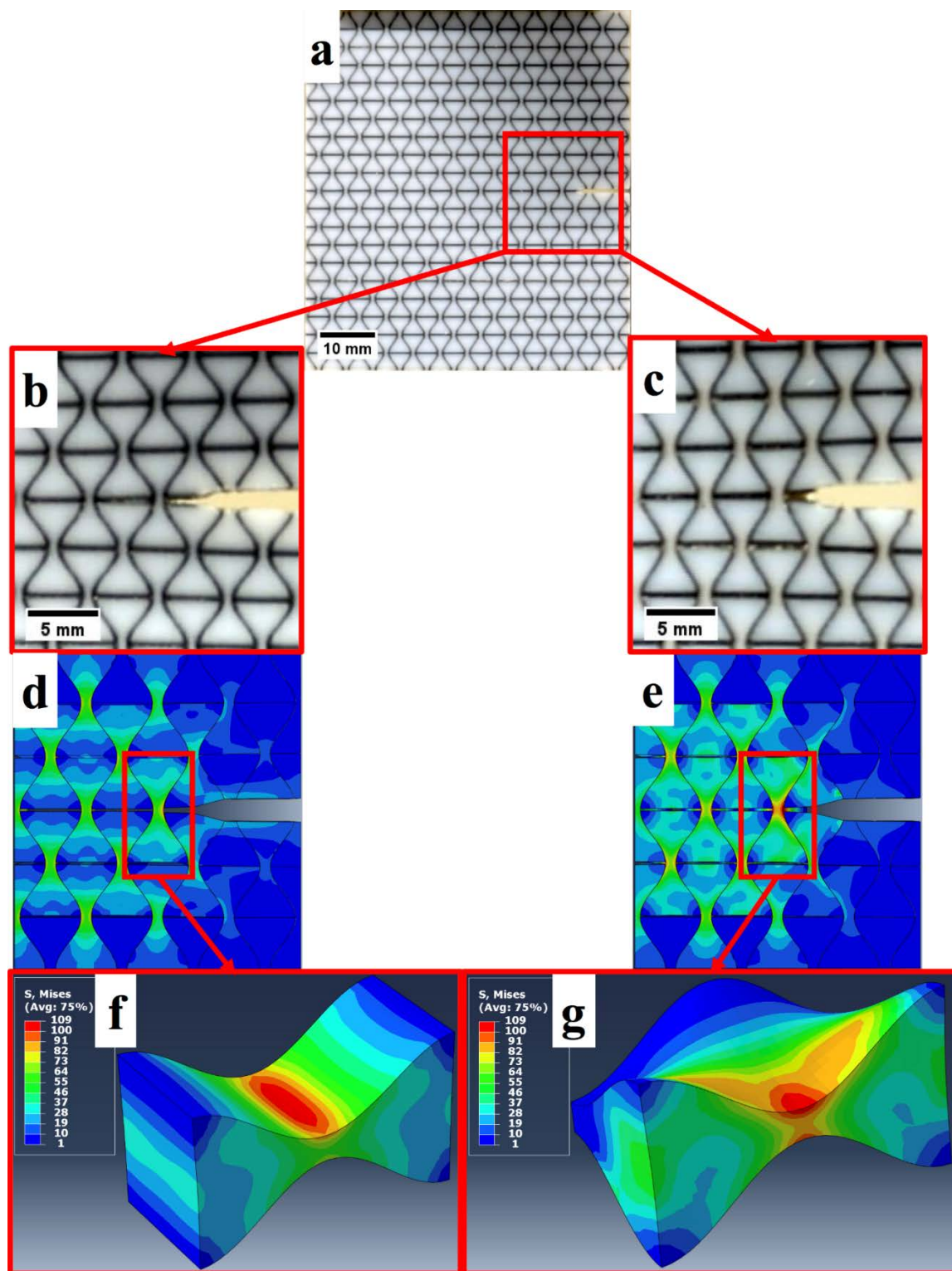


Figure 6.9 – Overview of computational work: a) initial state of experimental specimen with crack initiation site highlighted in red, experimental crack initiation site of hourglass (b) and osteomorphic (c) specimens before brittle failure, FEA simulations showing the von Mises equivalent stress distribution at a crack initiation site for hourglass (d) and osteomorphic (e)

specimens with central block highlighted in red, FEA simulations showing von Mises equivalent stress distribution for a central block at the crack tip for hourglass (f) and osteomorphic (g) geometries. These images illustrate the areas of stress concentration for the two geometries with interlocking features. The stress concentration in the “hourglass” block (f) extends through the entire depth of the specimen which results in its brittle failure. The 3D nature of the osteomorphic block (g) restricts the stress concentration to one side of the block, which reduces the likelihood of a crack propagation through the stiff phase

The distributions of the von Mises equivalent stress are presented for the block in front of the initial crack tip highlighted in Figure 5.8f and g. The figure illustrates the occurrence of stress concentration around the central region of the blocks. For the same level of displacement of the loading frame, the maximum stresses that develop in the hourglass block (Figure 5.8f) and in an osteomorphic block (Figure 5.8g) are found to be nearly identical (109 MPa). The main difference observed between the two geometries is that the stresses propagate through the depth of the hourglass block, while the stresses in an osteomorphic block are concentrated on one side or an edge of the block, cf. Figure 5.8. This appears to be the likely reason for greater resistance of the hard phase in the osteomorphic assembly to brittle failure, promoting failure through the soft phase. Figure 5.8e shows greater localisation of stress at the neck region of the osteomorphic blocks compared to the hourglass ones (Figure 5.8d). It is important to note that these stresses do not propagate through the depth of the osteomorphic blocks and are instead confined to a small area at the edge of the blocks, which appear not to lead to brittle failure. Further computational work to substantiate this proposition is needed. This would require the implementation of an adequate full-scale three-dimensional constitutive model with both hard and soft phases, one which accounts for damage evolution in both phases and is currently under development.

6.4 Discussion

Two sets of designs are presented in this work, both of which highlight the added benefit of combining topological interlocking and multi-material design. The Mode I fracture testing samples (except the brick specimen) displayed a larger interlocking angle between the hard phase blocks than that observed in nacre [50]. As mentioned above, the waviness of the surfaces of the aragonite platelets gives rise to a certain level of mechanical locking. The “waviness” of the topologically interlockable blocks is principally of a different kind. First, it is an inherent block of the structure that provides periodicity of tessellation of a plate into discrete blocks and ensures its very integrity. Second, it has a much greater amplitude than the irregular waviness of the aragonite platelets in the nacre structure. It should be noted that the magnitude of the undercut of the mating osteomorphic blocks can be varied without a change of the topology of interlocking. Our results strongly suggest that the superior performance of the osteomorphic design is related to this specialised block geometry. The curved contact surfaces of the blocks, particularly the concavo-convex surfaces of the osteomorphic ones, and the periodic nature of their arrangement result in thicker and thinner parts of the blocks facing each other at their opposite sides, helping resist premature fracture. Essentially, the advantageous effect of 2D in-plane interlocking of the dovetail kind (as found in natural nacre) [57] or hourglass geometries is retained in 3D interlocking assemblies, with an additional benefit of interlocking in the direction *normal* to the plane of assembly. Importantly, the 3D nature of the block geometry inhibits fracture of the rigid phase and promotes failure development through the soft phase, thus enhancing the overall modulus of toughness. Indeed, the soft phase in this work demonstrates similar characteristics to those previously noted in nacre, nacre-like materials and sutures, such as cushioning [138], stress delocalisation [31] and crack bridging [47].

Barthelat [50] noted that control of a number of variables (including block waviness and thickness of the panel assembled from the blocks) in simple interlocked nacre-like structures was necessary to balance opposing tensile and compressive forces within stiff blocks, thus hindering early fracture of the stiff phase. This brittle failure clearly needs to be avoided, and the 3D block geometries described in this work provide an avenue to achieve this. This presents new possibilities to extend the properties space of materials, due to the benefits of

a high degree of interlocking (high peak stress), while shifting the failure zone into the soft phase thus achieving large strains at failure.

In relation to the out-of-plane loading of the multi-material specimens, the advantage of using a soft interfacial layer is clear in the monolithic form with a significant increase in mechanical performance observed, similar to that observed by Mirkhalaf et al. [105] when incorporating a rubber phase with glass blocks. Importantly, all samples except the hierarchically interlocking sample, displayed similar displacement to failure as for the reference sample, even in monolithic form. However, the discrete blocks with a soft coating show a large decrease in mechanical performance, most likely due to the failure, in the form of delamination occurring between the soft and hard interface of the block itself, rather than between the soft layers of neighbouring blocks. Another potential explanation could be related to a “cushioning” effect of the soft phase, resulting in larger compliance and decreased load bearing capacity [138]. This is not observed in the monolithic (or Mode I) samples where failure occurs cohesively, through the soft phase only.

Modifications to the interfacial thickness of the out-of-plane samples also highlighted the importance of geometrical control over the fabrication process. The thinner interfacial layer showed a marked improvement over the thicker sample. The lower fraction of soft phase lead to a distinct improvement, which would be expected to continue to a certain lower limit, defined by the current manufacturing technology. Exploring this limit further, could be of interest as manufacturing techniques continue to improve.

The materials considered in this study are not intended to represent a structure with optimised mechanical response. Indeed, it is reasonable to expect a combination of a hard and soft materials with a larger ratio of elastic moduli to perform better [140]. Instead, the focus on geometrical design, particularly within the framework of multi-material design, is proposed to explore improved mechanical performance of this class of hybrid materials.

6.5 Conclusions

This chapter was concerned with investigating the effect of topological interlocking and multi-material design on the mechanical performance of bioinspired materials. Our results demonstrate that by adding a soft phase and combining a biomimetic approach with the concept of topological interlocking, hybrid structures with superior mechanical properties can be achieved. The potency of this promising design approach was explored through experimental results obtained under both out-of-plane concentrated point loading and Mode I notched tensile testing. Additive manufacturing was employed as the enabling technology to create hybrid structures comprised by hard blocks with intricate interlocking surfaces interleaved with soft layers.

Out-of-plane testing revealed the potential mechanical improvements of multi-material design with monolithic structures, in particular, displaying distinct advantages over single material design. Displacement to failure of monolithic specimens was maintained, compared to discrete single material assemblies, whilst significantly improving the peak load and stiffness, when the soft matrix phase is sufficiently thin (i.e. approximately 0.25mm). Experimental testing of the multi-material structures also supported previous observations in regard to the deformation mechanisms of topological interlocking structures, namely linking slip and tilt/bend to the mechanical behaviour.

Mode I tensile testing showed that the three-dimensional concavo-convex surfaces used in the interlocking osteomorphic blocks to be superior to the two-dimensional locking geometry, analogous to the tablet-level waviness observed in nacre. It was demonstrated that topological interlocking opens up a new avenue to enhancing the mechanical performance of the composite structures by preventing the brittle failure through the stiff and brittle blocks. Our results provided a clear demonstration that by introducing an interlocking-generating shape variation of the hard building blocks in the direction normal to the plane of assembly, further improvements in the mechanical properties of brick-and-mortar based structures are

possible. Thus, the present work highlighted the additional benefits topological interlocking can bring to bioinspired materials.

7. Conclusions and Future Work

7.1 Conclusions

In this thesis, the principles which underpin the class of architected materials known as *topological interlocking* were explored through the characterisation of mechanical properties and deformation mechanics, as well as through the design, testing and analysis of novel, bioinspired architected structures.

Overall, the thesis has sought to provide a much greater understanding of the effect of the intrinsic material characteristics, such as the elastic modulus and coefficient of friction, and the extrinsic parameters, including constraining forces and the size and geometry parameters, on the mechanical properties of interlocking block ensembles. The regularities in the mechanical response established can serve as a guide in the design of future topological interlocking structures. A link between the deformation mechanisms of topological interlocking assemblies and the resultant mechanical response has been formulated on this basis in the form of mathematical equations which can be used to predict the mechanical response of topological interlocking materials and structures. This involves the ability to modify these mechanisms by varying the material the blocks are made from and some of the extrinsic parameters of the assemblies, and therefore predict and tailor their mechanical response. The important role of the interfaces of the topological interlocking blocks in this response, explored through manipulating friction, block geometry and the properties of the soft interlayer phase, opens up interesting possibilities in this regard.

In a broad sense, the thesis has provided a greater understanding of topologically interlocked materials by examining the governing variables, with a particular focus on the mechanical properties. The interface and geometry provide the greatest insights into the

deformation mechanisms, and how these mechanisms lead to the resultant mechanical response.

The detailed contributions of this research are summarised as follows:

7.1.1 Characterisation of Mechanical Properties

A numerical finite element model was developed, supported by experimental data, to investigate multiple variables known to affect the mechanical response of planar, topologically-locked assemblies under concentrated point loading. The key outcomes include the characterisation of relationships between multiple variables, specifically addressing, various mechanical properties for non-planar blocks in planar assemblies. While previous attempts to develop such trends have been made, they have generally been limited in scope, focussing on a small number of variables or properties. In this work, the greatest number of variables and properties have been linked together, providing the broadest picture yet to characterise the mechanical response of this class of material. Further efforts in this area, could aim to support these results with focuses on alternative geometries or investigative methods.

Using this model, it was established that the three assembly variables (elastic modulus, coefficient of friction and lateral pre-load) are directly correlated with mechanical properties of the assembly, such as stiffness and load bearing capability. The relationships are described empirically across a broad input range. The elastic modulus of the block material was found to have the greatest effect on the stiffness and peak force for the variables, with a strong logarithmic relationship observed, although increases to the friction and pre-load also leads to approximately linear increases in the above properties. The deflection to peak load and at failure – the key characteristics of the mechanical response of the assembly – were shown to be generally independent of these parameters. The exception to this was the influence of coefficient of friction, which showed a clear positive trend with deflection to peak load, suggesting that the interface between the blocks has the potential to modify the

characteristic shape of the load-deflection curve through control of the deformation mechanisms.

The effect of size was also investigated (keeping all other variables constant) showing that increases to the block size and assembly size increased the stiffness and peak load following a power law. This dependence is similar to the previously-reported trends observed by Khandelwal et al. [104]. Despite the assembly characteristics being different from those previously reported, the observed trends hold for a different interlocking geometry and show the general nature of the behaviour. Increases to the block size and assembly size were also shown to increase the deflection to peak force and failure to a weak power law, the first time such quantifiable characterisation has been presented.

The results also agreed with the previously-reported clear monotonic positive relationship between stiffness and peak force. Finally, the results were rationalized via the use of an Artificial Neural Network (ANN) which provided the quantified relative effects of five variables (elastic modulus, lateral load, coefficient of friction, block size and assembly size) on the mechanical response in the form of weighted equations as a function of all variables. These effects were also visualised to highlight the overall trends, and as a result give a clear indication of the ability to map the mechanical response in relation to several of the key parameters. Indeed, this model provides a framework to design and tailor one or more mechanical property based on up to five different intrinsic and extrinsic assembly variables. As an example, using the ANN for a given material and friction, a lateral load, block size and assembly size can be selected to give a desired combination of peak load and deflection to failure.

Overall, insight and significant evidence into the effects of a number of variables were presented for planar assemblies of non-planar blocks under concentrated point loading with a controlled, predictable mechanical response in terms of load bearing capability, flexural stiffness, deflection to peak load and deflection to failure.

7.1.2 *Geometry variation and hierarchical structure*

The concept of structural hierarchy was combined with topological interlocking to create hierarchically interlocked structures in three dimensions. This was introduced in the form of a secondary, interlocking surface morphology, one length scale smaller than the block. These interlocking features comprised of pyramidal geometries with alternating normal directions, in to, and out of, the block. The role of non-planar block geometries in the mechanical response of topologically interlocked ensembles was also studied. A key conclusion was the understanding of the roles of slip (the relative movement of the block under load with its neighbouring blocks) and tilt/bend (the overall movement of the assembly). This was shown via modifications to the interactions of blocks in the form of geometrical surface variations, termed as “hierarchical interlocking”, which led to an increase in peak load bearing capability. This effect occurs by delaying the onset of the slip between the central components, a hypothesis explored by modifying the non-planar block geometry to suppress slip. These blocks were designed to utilise right-angled, square topology, here termed as “H+ blocks” (due to the geometry of the two alternating sides of the block) to cease any sliding between neighbouring blocks. When tested, these blocks showed no softening region. This suggested that softening in topological interlocking assemblies is directly related to slip of the central block, a theory supported by computational results. This was further supported via block geometries which were expected to slip to greater extent, having a lower load bearing capacity and larger softening region. Taken together, these results highlight the ability to control the failure mechanisms (namely slip) via modifications to the block (and surface) geometry, and hence control the mechanical response of topological interlocking planar assemblies.

7.1.3 *Bioinspired, multi-material structures*

The effect of topological interlocking and bioinspired multi-material design was explored in the context of mechanical performance in Chapter 6. The biological model was achieved through the design of interlocking ensembles of blocks, with the nacre-like soft matrix phase between the rigid blocks. Such novel three-dimensional structures with intricate

architected geometries and soft interlayers were fabricated using additive manufacturing and tested by concentrated point loading and Mode I tensile loading, using a combination of experimental and numerical techniques.

The results of the out-of-plane loading experiments and modelling showed that by including a thin soft phase matrix between stiff topological interlocking blocks, a significant increase in the mechanical properties, particularly ductility and energy absorption, can be achieved during out-of-plane loading due to the requirement for cohesive fracture of the thin soft phase, as opposed to the frictional effects of discrete blocks in an assembly. Specifically, a similar displacement to failure can be achieved with a large increase in peak load bearing capacity. Additionally, the concepts of hierarchical interlocking (as introduced in Chapter 5) and multi-material design are combined and fabricated monolithically, displaying a larger load bearing capacity. Fracture through the stiff phase is observed at an earlier displacement due to the inability for slip to occur, supporting previous observations from earlier chapters, that slip and tilt/bend control the mechanical response of these assemblies.

The benefits of using topologically interlocked multi-material structures to increase the fracture toughness was assessed using Mode I tensile testing. Specially designed specimens (based on previous studies [16]) were also used to investigate the fracture mechanisms of multi-material structures utilising topological interlocking. This testing demonstrated the added benefits of designing in three dimensions, specifically for improvements in the mechanical properties. In particular, a significant increase in stiffness and peak load bearing capability of an assembly of topologically interlocked blocks was observed, combined with a large deflection to failure. This was achieved through the increased ability for the three-dimensional design of topological interlocking geometries to resist failure through the stiff blocks when compared with the traditional two-dimensional brick and mortar designs. The osteomorphic geometry did not allow stress concentrations to occur through the entire thickness of the specimen, suppressing the ability for crack propagation through the stiff phase. These intricate structures were demonstrated to provide a promising avenue for future development of hybrid materials, due to the relatively unexplored combination of multi-material *and* three-dimensional interlocking design.

7.2 Future Work

There remain multiple areas which offer exciting opportunities to continue the research covered in this thesis. Indeed, many of the topics discussed in this thesis provide a strong foundation for materials design efforts based on topological interlocking with blocks of biomimetics. Promising potential prospects of design using topological interlocking are outlined below.

7.2.1 Geometrical optimisation

In this thesis, the effect of geometry was explored in the context of non-planar blocks and surface modifications (i.e. hierarchical interlocking), revealing information about the deformation mechanisms and how they can be manipulated to affect the mechanical response. While this study touched on some key geometries, there remain a very large number of possible geometries.

Particular areas of interest would include:

- Interplay between different size scales and ratios in the context of hierarchy. For example, how does changing the ratio of surface feature size to block size effect the mechanical response? Additional levels of hierarchy are also of interest, that is, how does the *number* of levels of hierarchy effect the mechanical response. Similar work conducted by Mirzaeifar et al. [79] showed improved defect tolerance for two-dimensional multi-material structures, similar benefits may exist for other classes of architected materials.
- Linking geometry directly with mechanical response. Can we gain greater control over the mechanical response via more subtle changes to the geometry? This would extend the work of Chapter 5, where the block geometry was modified to via changes in the osteomorphic curve function (ie. square and triangular curves). For example, a parametric study on the effect of curve functions and variables on non-planar blocks could reveal a much stronger connection between geometry

and mechanical response. An analytical study into this effect may also prove insightful.

- Various platonic body-based assemblies, beyond cubes and tetrahedral, which have not been explored yet. Comparing and contrasting these geometries could reveal further information regarding the similarities and differences in the mechanics of the respective assemblies and further novel designs. Difficulties arise in comparing dissimilar geometries, however options to do so include constant interacting surface area, volume or total area.
- Asymmetrical geometries could provide an avenue for highly tailored mechanical responses by providing directionality during loading. This could focus on surfaces with directionality in relation to loading direction, e.g. directional ridges or teeth on the block surface [66-68], or modifications to the block geometry, e.g. two *different* non-planar functions on either side of the osteomorphic block, to allow more or less slip on either side, while still facilitating interlocking.

7.2.2 *Interfacial design*

The role of the interface in the mechanical response was a key theme throughout this work, and there remains multiple avenues left to explore within this area. These include:

- Exploring the role of the rubber-like soft phase from Chapter 6, particularly modelling the damage and mechanical behaviour in three dimensions under multiple failure modes. Understanding this behaviour will provide more informed design criteria.
- The achievable resolution, and therefore attainable feature size, of additive manufacturing (and other techniques) is improving, and thus the ability to research the interplay between topology, surface roughness and friction becomes far more interesting. For instance, how can we modify these surface interactions using geometrical design at increasingly small scales and how does that affect the overall properties? External stimuli such as light and temperature could also be utilised to modify the mechanical properties.

- Designing specific combinations of materials for tailored interface response is also largely unexplored in this context. In particular, the relationship between material and geometry for two (or more) sets of materials could be exploited to further push the field of hybrid/architecture materials. Indeed, a key benefit of topological interlocking is ability to combine dissimilar materials, utilising responsive materials [93] would enable multi-functional hybrids with tuneable responses.

7.2.3 *Topological interlocking design utilising computational techniques*

Multi-material hybrid structures were investigated in this work and are an area of broad interest across the materials engineering spectrum. Computational techniques such as topology optimization and machine learning have recently come to the fore in the role of mechanical and materials design [119, 141-144].

Potential areas of where this concept could be exploited include:

- Utilising topological interlocking with recent advances in topology optimisation to create assemblies with optimal block geometry [145] for specific loading applications. Given the complex 3D nature of topological interlocking, computational challenges exist, however with simplified design objectives, geometry, size and loading conditions, the computational feasibility is much greater.
- Exploring further topological interlocking structures via machine learning. Deep learning algorithms are becoming increasingly advanced in the field of three dimensional geometries [146] able to learn and *generate* new structures on a rewards-based feedback loop [147]. For example, existing topological interlocking geometries would act as an input to the system, with different geometries assigned different weighting based on certain criteria (e.g. “H+” block has a high no-slip weighting). The system is then able to generate its own topologies based on those inputs before the newly generated geometries are scored by humans for

further feedback. A system such as this could be utilised to broaden the design space of hybrid structures to consider new geometries.

References

1. Ashby, M.F. and Y.J.M. Bréchet, *Designing hybrid materials*. Acta Materialia, 2003. **51**(19): p. 5801-5821.
2. Barthelat, F., *Architected materials in engineering and biology: fabrication, structure, mechanics and performance*. International Materials Reviews, 2015. **60**(8): p. 413-430.
3. Meyers, M.A., P.Y. Chen, M.I. Lopez, Y. Seki and A.Y. Lin, *Biological materials: a materials science approach*. J Mech Behav Biomed Mater, 2011. **4**(5): p. 626-657.
4. Khandelwal, S., T. Siegmund, R.J. Cipra and J.S. Bolton, *Adaptive mechanical properties of topologically interlocking material systems*. Smart Materials and Structures, 2015. **24**(4): p. 045037.
5. Carlesso, M., A. Molotnikov, T. Krause, K. Tushtev, S. Kroll, K. Rezwan and Y. Estrin, *Enhancement of sound absorption properties using topologically interlocked elements*. Scripta Materialia, 2012. **66**(7): p. 483-486.
6. Molotnikov, A., Y. Estrin, A.V. Dyskin, E. Pasternak and A.J. Kanel-Belov, *Percolation mechanism of failure of a planar assembly of interlocked osteomorphic elements*. Engineering Fracture Mechanics, 2007. **74**(8): p. 1222-1232.
7. Dunlop, J.W.C. and P. Fratzl, *Biological Composites*. Annual Review of Materials Research, 2010. **40**(1): p. 1-24.
8. Espinosa, H.D., J.E. Rim, F. Barthelat and M.J. Buehler, *Merger of structure and material in nacre and bone – Perspectives on de novo biomimetic materials*. Progress in Materials Science, 2009. **54**(8): p. 1059-1100.
9. Malik, I.A., M. Mirkhalaf and F. Barthelat, *Bio-inspired “jigsaw”-like interlocking sutures: Modeling, optimization, 3D printing and testing*. Journal of the Mechanics and Physics of Solids, 2017. **102**: p. 224-238.
10. McKittrick, J., P.Y. Chen, L. Tombolato, E.E. Novitskaya, M.W. Trim, G.A. Hirata, E.A. Olevsky, M.F. Horstemeyer and M.A. Meyers, *Energy absorbent natural*

- materials and bioinspired design strategies: A review*. Materials Science and Engineering: C, 2010. **30**(3): p. 331-342.
11. Fratzl, P., O. Kolednik, F.D. Fischer and M.N. Dean, *The mechanics of tessellations - bioinspired strategies for fracture resistance*. Chemical Society Reviews, 2015.
 12. Fratzl, P. and R. Weinkamer, *Nature's hierarchical materials*. Progress in Materials Science, 2007. **52**(8): p. 1263-1334.
 13. Schaare, S., *Charakterisierung und Simulation topologisch verzahnter Strukturen*, in *Fakultät für Natur- und Materialwissenschaften*. 2008, Technischen Universität Clausthal: Clausthal-Zellerfeld.
 14. Khandelwal, S., *Hybrid And Smart Topologically Interlocking Materials*. 2013, Purdue University.
 15. Dugué, M., *Expériences et simulations de matériaux autobloquants*. 2013.
 16. Dimas, L.S., G.H. Bratzel, I. Eylon and M.J. Buehler, *Tough Composites Inspired by Mineralized Natural Materials: Computation, 3D printing, and Testing*. Advanced Functional Materials, 2013. **23**(36): p. 4629-4638.
 17. Ashby, M.F., *Materials Selection in Mechanical Design (4th Edition)*. Elsevier.
 18. Kromm, F.X., J.M. Quenisset, R. Harry and T. Lorriot, *An Example of Multimaterials Design*. Advanced Engineering Materials, 2002. **4**(6): p. 371-374.
 19. Bouaziz, O., Y. Bréchet and J.D. Embury, *Heterogeneous and Architected Materials: A Possible Strategy for Design of Structural Materials*. Advanced Engineering Materials, 2008. **10**(1-2): p. 24-36.
 20. Bréchet, Y. and J.D. Embury, *Architected materials: Expanding materials space*. Scripta Materialia, 2013. **68**(1): p. 1-3.
 21. Fleck, N.A., V.S. Deshpande and M.F. Ashby, *Micro-architected materials: past, present and future*. Proceedings of the Royal Society A: Mathematical, Physical and Engineering Sciences, 2010. **466**(2121): p. 2495-2516.
 22. Krauss, S., E. Monsonneg-Orran, E. Zelzer, P. Fratzl and R. Shahar, *Mechanical Function of a Complex Three-Dimensional Suture Joining the Bony Elements in the Shell of the Red-Eared Slider Turtle*. Advanced Materials, 2009. **21**(4): p. 407-412.
 23. Naleway, S.E., M.M. Porter, J. McKittrick and M.A. Meyers, *Structural Design Elements in Biological Materials: Application to Bioinspiration*. Advanced Materials, 2015. **27**(37): p. 5455-5476.

24. Wegst, U.G., H. Bai, E. Saiz, A.P. Tomsia and R.O. Ritchie, *Bioinspired structural materials*. Nat Mater, 2015. **14**(1): p. 23-36.
25. Ashby, M.F., *Hybrids to fill holes in material property space*. Philosophical Magazine, 2005. **85**(26-1): p. 3235-3257.
26. Meyers, M.A., P.-Y. Chen, A.Y.-M. Lin and Y. Seki, *Biological materials: Structure and mechanical properties*. Progress in Materials Science, 2008. **53**(1): p. 1-206.
27. Srinivasan, A.V., G.K. Haritos, F.L. Hedberg and W.F. Jones, *Biomimetics: Advancing Man-Made Materials Through Guidance From Nature - An Update*. Applied Mechanics Reviews, 1996. **49**(10S): p. S194-S200.
28. Chen, P.-Y., E. Novitskaya, M.I. Lopez, C.-Y. Sun and J. McKittrick, *Toward a better understanding of mineral microstructure in bony tissues*. Bioinspired, Biomimetic and Nanobiomaterials, 2014. **3**(2): p. 71-84.
29. Buehler, M.J., *Materials by Design-A Perspective From Atoms to Structures*. MRS Bulletin, 2013. **38**(2): p. 169-176.
30. Sanchez, C., H. Arribart and M.M. Giraud Guille, *Biomimetism and bioinspiration as tools for the design of innovative materials and systems*. Nature Materials, 2005. **4**(4): p. 277-288.
31. Meyers, M., A.M. Lin, Y. Seki, P.-Y. Chen, B. Kad and S. Bodde, *Structural biological composites: An overview*. JOM Journal of the Minerals Metals and Materials Society, 2006. **58**(7): p. 35-41.
32. Fratzl, P., *Biomimetic materials research: what can we really learn from nature's structural materials?* Journal of the Royal Society Interface, 2007. **4**(15): p. 637-642.
33. Mayer, G., *New classes of tough composite materials—Lessons from natural rigid biological systems*. Materials Science and Engineering: C, 2006. **26**(8): p. 1261-1268.
34. Weinkamer, R. and P. Fratzl, *Mechanical adaptation of biological materials — The examples of bone and wood*. Materials Science and Engineering: C, 2011. **31**(6): p. 1164-1173.
35. Gu, G.X., M. Takaffoli, A.J. Hsieh and M.J. Buehler, *Biomimetic additive manufactured polymer composites for improved impact resistance*. Extreme Mechanics Letters, 2016.

36. Montero, C., B. Clair, T. Alméras, A.v.d. Lee and J. Gril, *Relationship between wood elastic strain under bending and cellulose crystal strain*. Composites Science and Technology, 2012. **72**(2): p. 175-181.
37. Amada, S., T. Munekata, Y. Nagase, Y. Ichikawa, A. Kirigai and Y. Zhifei, *The Mechanical Structures of Bamboos in Viewpoint of Functionally Gradient and Composite Materials*. Journal of Composite Materials, 1996. **30**(7): p. 800-819.
38. Qin, Z., L. Dimas, D. Adler, G. Bratzel and M.J. Buehler, *Biological materials by design*. Journal of Physics Condensed Matter, 2014. **26**(7): p. 073101.
39. Sun, J. and B. Bhushan, *Hierarchical structure and mechanical properties of nacre: a review*. RSC Advances, 2012. **2**(20): p. 7617.
40. Li, X.W., H.M. Ji, W. Yang, G.P. Zhang and D.L. Chen, *Mechanical properties of crossed-lamellar structures in biological shells: A review*. J Mech Behav Biomed Mater, 2017. **74**: p. 54-71.
41. Launey, M.E., E. Munch, D.H. Alsem, H.B. Barth, E. Saiz, A.P. Tomsia and R.O. Ritchie, *Designing highly toughened hybrid composites through nature-inspired hierarchical complexity*. Acta Materialia, 2009. **57**(10): p. 2919-2932.
42. Lin, A. and M.A. Meyers, *Growth and structure in abalone shell*. Materials Science and Engineering: A, 2005. **390**(1-2): p. 27-41.
43. Luz, G.M. and J.F. Mano, *Biomimetic design of materials and biomaterials inspired by the structure of nacre*. Philosophical Transactions of the Royal Society of London, Series A, 2009. **367**(1893): p. 1587-1605.
44. Wegst, U.G.K. and M.F. Ashby, *The mechanical efficiency of natural materials*. Philosophical Magazine, 2004. **84**(21): p. 2167-2186.
45. Wang, R. and H.S. Gupta, *Deformation and Fracture Mechanisms of Bone and Nacre*. Annual Review of Materials Research, 2011. **41**(1): p. 41-73.
46. Espinosa, H.D., A.L. Juster, F.J. Latourte, O.Y. Loh, D. Gregoire and P.D. Zavattieri, *Tablet-level origin of toughening in abalone shells and translation to synthetic composite materials*. Nature Communications, 2011. **2**: p. 173.
47. Barthelat, F. and H.D. Espinosa, *An Experimental Investigation of Deformation and Fracture of Nacre—Mother of Pearl*. Experimental Mechanics, 2007. **47**(3): p. 311-324.
48. Rabiei, R., S. Bekah and F. Barthelat, *Failure mode transition in nacre and bone-like materials*. Acta Biomaterialia, 2010. **6**(10): p. 4081-4089.

49. Wang, R.Z., Z. Suo, A.G. Evans, N. Yao and I.A. Aksay, *Deformation mechanisms in nacre*. Journal of Materials Research, 2001. **16**(09): p. 2485-2493.
50. Barthelat, F., H. Tang, P. Zavattieri, C. Li and H. Espinosa, *On the mechanics of mother-of-pearl: A key feature in the material hierarchical structure*. Journal of the Mechanics and Physics of Solids, 2007. **55**(2): p. 306-337.
51. Bonderer, L.J., A.R. Studart and L.J. Gauckler, *Bioinspired Design and Assembly of Platelet Reinforced Polymer Films*. Science, 2008. **319**(5866): p. 1069-1073.
52. E. Munch, M.E.L., D. H. Alsem, E. Saiz, A. P. Tomsia, R. O. Ritchie, *Tough, Bio-Inspired Hybrid Materials*. Science, 2008. **322**: p. 1516-1520.
53. Munch, E., E. Saiz, A.P. Tomsia and S. Deville, *Architectural Control of Freeze-Cast Ceramics Through Additives and Templating*. Journal of the American Ceramic Society, 2009. **92**(7): p. 1534-1539.
54. Launey, M.E., E. Munch, D.H. Alsem, E. Saiz, A.P. Tomsia and R.O. Ritchie, *A novel biomimetic approach to the design of high-performance ceramic-metal composites*. Journal of the Royal Society Interface, 2010. **7**(46): p. 741-753.
55. Libanori, R., F.H.L. Münch, D.M. Montenegro and A.R. Studart, *Hierarchical reinforcement of polyurethane-based composites with inorganic micro- and nanoplatelets*. Composites Science and Technology, 2012. **72**(3): p. 435-445.
56. Wegst, U.G., M. Schecter, A.E. Donius and P.M. Hunger, *Biomaterials by freeze casting*. Philosophical Transactions of the Royal Society Series A, 2010. **368**(1917): p. 2099-2121.
57. Barthelat, F. and D. Zhu, *A novel biomimetic material duplicating the structure and mechanics of natural nacre*. Journal of Materials Research, 2011. **26**(10): p. 1203-1215.
58. Slesarenko, V., N. Kazarinov and S. Rudykh, *Distinct failure modes in bio-inspired 3D-printed staggered composites under non-aligned loadings*. Smart Materials and Structures, 2017. **26**(3): p. 035053.
59. Valashani, S.M. and F. Barthelat, *A laser-engraved glass duplicating the structure, mechanics and performance of natural nacre*. Bioinspir Biomim, 2015. **10**(2): p. 026005.
60. Barthelat, F., *Designing nacre-like materials for simultaneous stiffness, strength and toughness: Optimum materials, composition, microstructure and size*. Journal of the Mechanics and Physics of Solids, 2014. **73**: p. 22-37.

61. Gu, G.X., F. Libonati, S. Wettermark and M.J. Buehler, *Printing Nature: Unraveling the Role of Nacre's Mineral Bridges*. Journal of the Mechanical Behavior of Biomedical Materials, 2017.
62. Lin, E., Y. Li, J.C. Weaver, C. Ortiz and M.C. Boyce, *Tunability and enhancement of mechanical behavior with additively manufactured bio-inspired hierarchical suture interfaces*. Journal of Materials Research, 2014. **29**(17): p. 1867-1875.
63. Achrai, B. and H.D. Wagner, *Micro-structure and mechanical properties of the turtle carapace as a biological composite shield*. Acta Biomaterialia, 2013. **9**(4): p. 5890-5902.
64. Achrai, B., B. Bar-On and H.D. Wagner, *Bending mechanics of the red-eared slider turtle carapace*. Journal of the Mechanical Behaviour of Biomedical Materials, 2014. **30**: p. 223-233.
65. Chen, I.H., W. Yang and M.A. Meyers, *Leatherback sea turtle shell: A tough and flexible biological design*. Acta Biomaterialia, 2015. **28**: p. 2-12.
66. Li, Y., C. Ortiz and M.C. Boyce, *Stiffness and strength of suture joints in nature*. Phys Rev E Stat Nonlin Soft Matter Phys, 2011. **84**(6 Pt 1): p. 062904.
67. Li, Y., C. Ortiz and M.C. Boyce, *A generalized mechanical model for suture interfaces of arbitrary geometry*. Journal of the Mechanics and Physics of Solids, 2013. **61**(4): p. 1144-1167.
68. Li, Y., C. Ortiz and M.C. Boyce, *Bioinspired, mechanical, deterministic fractal model for hierarchical suture joints*. Phys Rev E Stat Nonlin Soft Matter Phys, 2012. **85**(3 Pt 1): p. 031901.
69. Lin, E., Y. Li, C. Ortiz and M.C. Boyce, *3D printed, bio-inspired prototypes and analytical models for structured suture interfaces with geometrically-tuned deformation and failure behavior*. Journal of the Mechanics and Physics of Solids, 2014. **73**: p. 166-182.
70. Chen, I.H., W. Yang and M.A. Meyers, *Leatherback sea turtle shell: A tough and flexible biological design*. Acta Biomaterialia, 2015. **28**: p. 2-12.
71. Meyers, M.A., J. McKittrick and P.-Y. Chen, *Structural Biological Materials: Critical Mechanics-Materials Connections*. Science, 2013. **339**(6121): p. 773-779.
72. Studart, A.R., *Towards high-performance bioinspired composites*. Advanced Materials, 2012. **24**(37): p. 5024-5044.

73. Meza, L.R., A.J. Zelhofer, N. Clarke, A.J. Mateos, D.M. Kochmann and J.R. Greer, *Resilient 3D hierarchical architected metamaterials*. Proc Natl Acad Sci U S A, 2015. **112**(37): p. 11502-11507.
74. Zheng, X., W. Smith, J. Jackson, B. Moran, H. Cui, D. Chen, J. Ye, N. Fang, N. Rodriguez, T. Weisgraber and C.M. Spadaccini, *Multiscale metallic metamaterials*. Nat Mater, 2016. **15**(10): p. 1100-1106.
75. Qin, Z., B.G. Compton, J.A. Lewis and M.J. Buehler, *Structural optimization of 3D-printed synthetic spider webs for high strength*. Nat Commun, 2015. **6**: p. 7038.
76. Gong, J., H. Lin, J.W. Dunlop and J. Yuan, *Hierarchically Arranged Helical Fiber Actuators Derived from Commercial Cloth*. Advanced Materials, 2017.
77. Zhang, Y., H. Yao, C. Ortiz, J. Xu and M. Dao, *Bio-inspired interfacial strengthening strategy through geometrically interlocking designs*. J Mech Behav Biomed Mater, 2012. **15**: p. 70-77.
78. Niebel, T.P., D. Carnelli, M.R. Binelli, R. Libanori and A.R. Studart, *Hierarchically roughened microplatelets enhance the strength and ductility of nacre-inspired composites*. J Mech Behav Biomed Mater, 2016. **60**: p. 367-377.
79. Mirzaeifar, R., L.S. Dimas, Z. Qin and M.J. Buehler, *Defect-Tolerant Bioinspired Hierarchical Composites: Simulation and Experiment*. ACS Biomaterials Science & Engineering, 2015. **1**(5): p. 295-304.
80. Launey, M.E., M.J. Buehler and R.O. Ritchie, *On the Mechanistic Origins of Toughness in Bone*. Annual Review of Materials Research, 2010. **40**(1): p. 25-53.
81. Estrin, Y., A.V. Dyskin and E. Pasternak, *Topological interlocking as a material design concept*. Materials Science and Engineering: C, 2011. **31**(6): p. 1189-1194.
82. Dyskin, A.V., Y. Estrin, A.J. Kanel-Belov and E. Pasternak, *Toughening by Fragmentation—How Topology Helps*. Advanced Engineering Materials, 2001. **3**(11): p. 885-888.
83. Dyskin, A.V., Y. Estrin, A.J. Kanel-Belov and E. Pasternak, *Topological interlocking of platonic solids: A way to new materials and structures*. Philosophical Magazine Letters, 2003. **83**(3): p. 197-203.
84. Dyskin, A.V., Y. Estrin, E. Pasternak, H.C. Khor and A.J. Kanel-Belov, *Fracture Resistant Structures Based on Topological Interlocking with Non-planar Contacts*. Advanced Engineering Materials, 2003. **5**(3): p. 116-119.

85. Krause, T., A. Molotnikov, M. Carlesso, J. Rente, K. Rezwani, Y. Estrin and D. Koch, *Mechanical Properties of Topologically Interlocked Structures with Elements Produced by Freeze Gelation of Ceramic Slurries*. Advanced Engineering Materials, 2012. **14**(5): p. 335-341.
86. Schaare, S., A.V. Dyskin, Y. Estrin, S. Arndt, E. Pasternak and A. Kanel-Belov, *Point loading of assemblies of interlocked cube-shaped elements*. International Journal of Engineering Science, 2008. **46**(12): p. 1228-1238.
87. Martini, R., Y. Balit and F. Barthelat, *A comparative study of bio-inspired protective scales using 3D printing and mechanical testing*. Acta Biomaterialia, 2017.
88. Kanel-Belov, A., A. Dyskin, Y. Estrin, E. Pasternak and I. Ivanov-Pogodaev, *Interlocking of convex polyhedra: towards a geometric theory of fragmented solids*. Moscow Mathematical Journal, 2010. **10**(2): p. 337-342.
89. Fallacara, G., *Stereotomy-Stone Architecture and New Research*. 2012: Presses des Ponts et Chaussées <http://www.presses-des-ponts.fr/>.
90. Glickman, M., *The G-Block System of Vertically Interlocking Paving*, in *Second International Conference of Concrete Block Paving*. 1984: Delft.
91. Molotnikov, A., R. Gerbrand, O. Bouaziz and Y. Estrin, *Sandwich Panels with a Core Segmented into Topologically Interlocked Elements*. Advanced Engineering Materials, 2013. **15**(8): p. 728-731.
92. Feng, Y., T. Siegmund, E. Habtour and J. Riddick, *Impact mechanics of topologically interlocked material assemblies*. International Journal of Impact Engineering, 2015. **75**: p. 140-149.
93. Molotnikov, A., R. Gerbrand, Y. Qi, G.P. Simon and Y. Estrin, *Design of responsive materials using topologically interlocked elements*. Smart Materials and Structures, 2015. **24**(2): p. 025034.
94. Djumas, L., A. Molotnikov, G.P. Simon and Y. Estrin, *Enhanced Mechanical Performance of Bio-Inspired Hybrid Structures Utilising Topological Interlocking Geometry*. Sci Rep, 2016. **6**: p. 26706.
95. Tessmann, O. and M. Becker. *Extremely heavy and incredibly light : Performative assemblies in dynamic environments*. in *Proceedings of the 18th International Conference on Computer-Aided Architectural Design Research in Asia, CAADRIA*. 2013. Singapore: CAADRIA and CASA.

96. Weizmann, M., O. Amir and Y.J. Grobman, *Topological interlocking in buildings: A case for the design and construction of floors*. Automation in Construction, 2016.
97. Mirkhalaf, M. and F. Barthelat, *Nacre-like materials using a simple doctor blading technique: Fabrication, testing and modeling*. J Mech Behav Biomed Mater, 2016. **56**: p. 23-33.
98. Ta, D.Y.H., *Utilisation of Topologically-Interlocking Osteomorphic Blocks for Multi-Purpose Civil Construction*, in *School of Civil & Resource Engineering*. 2011, University of Western Australia.
99. Khandelwal, S., T. Siegmund, R.J. Cipra and J.S. Bolton, *Transverse loading of cellular topologically interlocked materials*. International Journal of Solids and Structures, 2012. **49**(18): p. 2394-2403.
100. Siegmund, T., F. Barthelat, R. Cipra, E. Habtour and J. Riddick, *Manufacture and Mechanics of Topologically Interlocked Material Assemblies*. Applied Mechanics Reviews, 2016. **68**(4): p. 040803.
101. Estrin, Y., *Negative stiffness of a layer with topologically interlocked elements*. Scripta Materialia, 2004. **50**(2): p. 291-294.
102. Schaare, S., W. Riehemann and Y. Estrin, *Damping properties of an assembly of topologically interlocked cubes*. Materials Science and Engineering: A, 2009. **521-522**: p. 380-383.
103. Dugué, M., M. Fivel, Y. Bréchet and R. Dendievel, *Indentation of interlocked assemblies: 3D discrete simulations and experiments*. Computational Materials Science, 2013. **79**: p. 591-598.
104. Khandelwal, S., T. Siegmund, R.J. Cipra and J.S. Bolton, *Scaling of the Elastic Behavior of Two-Dimensional Topologically Interlocked Materials Under Transverse Loading*. Journal of Applied Mechanics, 2013. **81**(3): p. 031011.
105. Mirkhalaf, M., J. Tanguay and F. Barthelat, *Carving 3D architectures within glass: Exploring new strategies to transform the mechanics and performance of materials*. Extreme Mechanics Letters, 2016.
106. Brugger, C., M.C. Fivel and Y. Bréchet, *Numerical Simulations of Topologically Interlocked Materials Coupling DEM Methods and FEM Calculations: Comparison with Indentation Experiments*. MRS Proceedings, 2011. **1188**.

107. Autruffe, A., F. Pelloux, C. Brugger, P. Duval, Y. Bréchet and M. Fivel, *Indentation Behaviour of Interlocked Structures Made of Ice: Influence of the Friction Coefficient*. Advanced Engineering Materials, 2007. **9**(8): p. 664-666.
108. Brugger, C., Y. Bréchet and M. Fivel, *Experiments and Numerical Simulations of Interlocked Materials*. Advanced Materials Research, 2008. **47-50**: p. 125-128.
109. Timoshenko, S.P. and S. Woinowsky-Krieger, *Theory of plates and shells*. 1959: McGraw-hill.
110. Warren, C.Y., G.B. Richard and M.S. Ali, *Flat Plates*, in *Roark's Formulas for Stress and Strain, Eighth Edition*. 2012, McGraw Hill Professional, Access Engineering.
111. Truby, R.L. and J.A. Lewis, *Printing soft matter in three dimensions*. Nature, 2016. **540**(7633): p. 371-378.
112. Gibson, I., D. Rosen and B. Stucker, *Additive Manufacturing Technologies: 3D Printing, Rapid Prototyping, and Direct Digital Manufacturing (Second Ed.)*. Second Edition ed. 2015: Springer New York.
113. Kokkinis, D., M. Schaffner and A.R. Studart, *Multimaterial magnetically assisted 3D printing of composite materials*. Nat Commun, 2015. **6**: p. 8643.
114. Compton, B.G. and J.A. Lewis, *3D-Printing of Lightweight Cellular Composites*. Advanced Materials, 2014: p. n/a-n/a.
115. Stratasys. *PolyJet Technology*. 2015 [cited 2015 November, 2015]; PolyJet Technology]. Available from: <http://www.stratasys.com/3d-printers/technologies/polyjet-technology>.
116. Studart, A.R., *Additive manufacturing of biologically-inspired materials*. Chemical Society Reviews, 2016. **45**(2): p. 359-376.
117. Wang, L., J. Lau, E.L. Thomas and M.C. Boyce, *Co-continuous composite materials for stiffness, strength, and energy dissipation*. Advanced Materials, 2011. **23**(13): p. 1524-1529.
118. Wen, L., J.C. Weaver and G.V. Lauder, *Biomimetic shark skin: design, fabrication and hydrodynamic function*. Journal of Experimental Biology, 2014. **217**(Pt 10): p. 1656-1666.
119. Gaynor, A.T., N.A. Meisel, C.B. Williams and J.K. Guest, *Multiple-Material Topology Optimization of Compliant Mechanisms Created Via PolyJet Three-Dimensional Printing*. Journal of Manufacturing Science and Engineering, 2014. **136**(6): p. 061015.

120. Bafekrpour, E., A. Molotnikov, J.C. Weaver, Y. Brechet and Y. Estrin, *Responsive materials: a novel design for enhanced machine-augmented composites*. Sci Rep, 2014. **4**: p. 3783.
121. Bafekrpour, E., A. Dyskin, E. Pasternak, A. Molotnikov and Y. Estrin, *Internally architected materials with directionally asymmetric friction*. Sci Rep, 2015. **5**: p. 10732.
122. Ge, Q., C.K. Dunn, H.J. Qi and M.L. Dunn, *Active origami by 4D printing*. Smart Materials and Structures, 2014. **23**(9): p. 094007.
123. Libonati, F., G.X. Gu, Z. Qin, L. Vergani and M.J. Buehler, *Bone-Inspired Materials by Design: Toughness Amplification Observed Using 3D Printing and Testing* Advanced Engineering Materials, 2016. **18**(8): p. 1354-1363.
124. Sen, D. and M.J. Buehler, *Atomistically-Informed Mesoscale Model of Deformation and Failure of Bioinspired Hierarchical Silica Nanocomposites*. International Journal of Applied Mechanics, 2010. **02**(04): p. 699-717.
125. Sen, D. and M.J. Buehler, *Structural hierarchies define toughness and defect-tolerance despite simple and mechanically inferior brittle building blocks*. Sci Rep, 2011. **1**: p. 35.
126. Cranford, S. and M.J. Buehler, *Materiomics: biological protein materials, from nano to macro*. Nanotechnol Sci Appl, 2010. **3**: p. 127-148.
127. Zienkiewicz, O.C., R.L. Taylor and J.Z. Zhu, *9 - Discrete element methods*, in *The Finite Element Method Set (Sixth Edition)*. 2005, Butterworth-Heinemann: Oxford. p. 245-277.
128. Huebner, K.H., D.L. Dewhurst, D.E. Smith and T.G. Byrom, *The finite element method for engineers*. 2008: John Wiley & Sons.
129. Kasabov, N.K., *Foundations of Neural Networks, Fuzzy Systems, and Knowledge Engineering*. 1996: MIT Press.
130. Ge, Q., H.J. Qi and M.L. Dunn, *Active materials by four-dimension printing*. Applied Physics Letters, 2013. **103**(13): p. 131901.
131. Gent, A.N. *On the relation between indentation hardness and Young's modulus*. 1958. Institution of Rubber Industry - Transactions.
132. Ashby, M., *Designing architected materials*. Scripta Materialia, 2013. **68**(1): p. 4-7.

133. ABAQUS, *Quasi-Static Analysis with Abaqus/Explicit*, in *Documentation 6.14* 2015, Dassult Systèmes: Providence, RI, USA.
134. Dyskin, A.V., Y. Estrin, A.J. Kanel-Belov and E. Pasternak, *A new principle in design of composite materials: reinforcement by interlocked elements*. Composites Science and Technology, 2003. **63**(3–4): p. 483-491.
135. Dyskin, A., E. Pasternak and Y. Estrin, *Mortarless structures based on topological interlocking*. Frontiers of Structural and Civil Engineering, 2012. **6**(2): p. 188-197.
136. Estrin, Y. and Y. Bréchet, *On a model of frictional sliding*. pure and applied geophysics, 1996. **147**(4): p. 745-762.
137. Meyers, M.A., A.Y. Lin, P.Y. Chen and J. Muyco, *Mechanical strength of abalone nacre: role of the soft organic layer*. J Mech Behav Biomed Mater, 2008. **1**(1): p. 76-85.
138. Mirkhalaf, M., A.K. Dastjerdi and F. Barthelat, *Overcoming the brittleness of glass through bio-inspiration and micro-architecture*. Nat Commun, 2014. **5**: p. 3166.
139. Bourell, D., J.P. Kruth, M. Leu, G. Levy, D. Rosen, A.M. Beese and A. Clare, *Materials for additive manufacturing*. CIRP Annals, 2017. **66**(2): p. 659-681.
140. Begley, M.R., N.R. Philips, B.G. Compton, D.V. Wilbrink, R.O. Ritchie and M. Utz, *Micromechanical models to guide the development of synthetic 'brick and mortar' composites*. Journal of the Mechanics and Physics of Solids, 2012. **60**(8): p. 1545-1560.
141. Eschenauer, H.A. and N. Olhoff, *Topology optimization of continuum structures: A review*. Applied Mechanics Reviews, 2001. **54**(4): p. 331.
142. Clausen, A., F. Wang, J.S. Jensen, O. Sigmund and J.A. Lewis, *Topology Optimized Architectures with Programmable Poisson's Ratio over Large Deformations*. Advanced Materials, 2015.
143. Nguyen, T.N., T. Siegmund, W. Tsutsui, H. Liao and W. Chen, *Bi-objective optimal design of a damage-tolerant multifunctional battery system*. Materials & Design, 2016. **105**: p. 51-65.
144. Gu, G.X., S. Wettermark and M.J. Buehler, *Algorithm-driven design of fracture resistant composite materials realized through additive manufacturing*. Additive Manufacturing, 2017.
145. Hinze, T., L.L. Weber and U. Hatnik. *Walking Membranes: Grid-Exploring P Systems with Artificial Evolution for Multi-purpose Topological Optimisation of*

- Cascaded Processes*. in *Membrane Computing*. 2017. Cham: Springer International Publishing.
146. Leonardo, M.-D.-L. and C. Oscar Javier Begambre, *Multi-Objective Heuristic Computation Applied to Architectural and Structural Design: A Review*. International Journal of Architectural Computing, 2013. **11**(4): p. 363-392.
147. Kononenko, O. and I. Kononenko, *Machine Learning and Finite Element Method for Physical Systems Modeling*. arXiv:1801.07337, 2018.